

Université
de Toulouse

THÈSE

En vue de l'obtention du

DOCTORAT DE L'UNIVERSITÉ DE TOULOUSE

Délivré par :

Institut National Polytechnique de Toulouse (INP Toulouse)

Discipline ou spécialité :

Surfaces Interfaces Continentales Hydrologie

Présentée et soutenue par :

M. SYLVAIN PASQUIER

le lundi 25 septembre 2017

Titre :

Modeling two-phase flows in columns equipped with structured packings: a multiscale porous medium approach.

Ecole doctorale :

Sciences de l'Univers de l'Environnement et de l'Espace (SDUEE)

Unité de recherche :

Institut de Mécanique des Fluides de Toulouse (I.M.F.T.)

Directeur(s) de Thèse :

M. MICHEL QUINTARD

Rapporteurs :

M. DIDIER LASSEUX, UNIVERSITÉ DE BORDEAUX

M. LUDOVIC RAYNAL, IFPEN

Membre(s) du jury :

Mme VERONIQUE ROIG, INP TOULOUSE, Président

M. FLORIAN FICHOT, CEA CADARACHE, Membre

M. MICHEL QUINTARD, INP TOULOUSE, Membre

Modeling two-phase flows in columns equipped with structured
packings: a multiscale porous medium approach

Sylvain Pasquier

October 24, 2017

Résumé

La technologie la plus utilisée pour séparer les principaux composants de l'air est aujourd'hui la distillation en colonne à garnissage structuré. Ce procédé se caractérise par un écoulement gaz-liquide contre-courant au sein d'une structure constituée de plaques corruguées placées parallèlement et agencées en packs. La description d'un tel procédé est rendue difficile par les très grandes dimensions du système et par la complexité des phénomènes à la petite échelle. La méthode de la prise de moyenne volumique, utilisée pour les problèmes de changement d'échelle en milieu poreux, est utilisée pour décrire le système à une échelle qui permet une résolution. Le travail est organisé en trois étapes.

Dans un premier temps, pour les débits modérés, une méthode est proposée pour évaluer la perte de charge au sein de la structure en prenant en compte des rugosités de structure ou créées par des instabilités du film liquide. A ce stade, l'effet de la surface rugueuse est caractérisé par une condition limite effective. Le problème aux limites effectif pour la phase gaz est ensuite moyenné en volume pour obtenir un système d'équations à grande échelle. Le bilan de quantité de mouvement à grande échelle est une loi de Darcy généralisée aux écoulements inertiels, dans laquelle les paramètres effectifs contiennent les effets des instabilités de surfaces de la petite échelle.

La seconde étape est dédiée à l'interaction entre les deux phases à plus hauts débits. On montre que des modèles qui incluent explicitement des termes croisés à grande échelle permettent de décrire l'écoulement au sein du garnissage à grands nombres de Reynolds. Plus généralement, ces modèles, peu utilisés dans la littérature sur les milieux poreux, s'avèrent adaptés pour les écoulements dans les milieux très perméables, pour lesquels des variations importantes de la perte de charge et des saturations sont observées.

Enfin, on s'intéresse à la description de la distribution de la phase liquide au sein de la structure de garnissage. Une approche multiphasique, où la phase liquide est séparée en plusieurs pseudo-phases, est adaptée pour modéliser l'anisotropie de l'écoulement. Deux méthodes impliquant une approche à deux pseudo-phases et une approche à quatre pseudo-phases pour la phase liquide sont comparées. Cette dernière méthode est notamment utile pour décrire des régimes d'écoulement très différents, et permet de capturer à grande échelle les chemins préférentiels suivis par le film liquide au sein du garnissage.

Abstract

Distillation in columns equipped with structured packings is today the most used technology for separating air in its primary components. This process is characterized by a counter-current gas-liquid flow in a structure made of parallel corrugated sheets arranged in packs. The description of such system is constrained by the large dimensions of the columns and by the complexity of the local-scale phenomena. This leads to consider a strategy of upscaling, based on the volume averaging method, to describe the system at a scale at which a resolution is possible. The work is organized in three steps.

As a first step, considering moderate flow rates, a methodology of upscaling is developed to predict the pressure drop in the flow of the gas phase taking into account small scale roughnesses due to the structure itself or perturbations of the liquid film. At this stage, the effect of this rough surface is characterized by an effective boundary condition. The boundary value problem for the flow of the gas phase is volume averaged in order to derive a system of equations at large scale. The resulting momentum balance is a generalized Darcy's law for inertial flows, involving effective parameters accounting for the roughness at the microscale.

The second step of this work focuses on the interaction between the two phases at higher flow rates. It is shown that models involving non-standard macroscopic cross-terms are more prone to describe the flow in packings at high Reynolds numbers than the models usually used in porous media sciences. More generally, these models are shown to characterize accurately processes in highly permeable media, where drastic changes of pressure drop and retention are observed.

We finally study the distribution of the liquid phase in the structured packing. It is shown that a specific approach involving a multiphase model with liquid decomposition is required to capture the anisotropy generated in the flow of the liquid phase. Two methods involving two pseudo-phases and four pseudo-phases for the liquid phase are compared. This last method captures a number of very different distribution regimes in the column and offers additional flexibility to describe preferential paths of the liquid.

Remerciements

Le travail de recherche présenté dans ce manuscrit a été effectué à l’Institut de Mécanique des Fluides de Toulouse, au sein du Groupe d’Etude des Milieux Poreux. Il a été effectué en collaboration (CIFRE) avec le Centre de Recherche Paris-Saclay d’Air Liquide, à Jouy-en-Josas.

Je tiens à remercier en tout premier lieu Michel Quintard, qui a été mon directeur de thèse, et qui a su me faire profiter de toute son expérience dans l’encadrement d’un travail scientifique. J’ai souvent été impressionné par la capacité de Michel à s’investir pleinement dans les nombreux projets auxquels il participe, que ce soit pour faire bénéficier de son expertise, ou pour remplir, au quotidien, les tâches les plus laborieuses de la vie de chercheur. Merci pour la patience dont il a fallu faire preuve durant les nombreuses (et parfois longues !) réunions que l’on a pu avoir, quand on “faisait le point” sur l’avancée de la thèse. Je crois avoir acquis auprès de Michel des méthodes d’organisation dans le travail qui me serviront longtemps.

Je souhaite aussi remercier chaleureusement Yohan Davit, qui a encadré ma thèse, et qui a vécu au plus près mes années passées à l’IMFT. Je ne crois pas qu’on puisse se représenter facilement l’investissement de Yohan pour ma thèse, tant il a été important. Jamais avare en conseils et toujours disponible pour discuter de mon travail, il a pu m’aider à m’y retrouver quand je n’y voyais plus très clair, et m’a patiemment formé (avec une persévérance peu commune !) à la science des milieux poreux. Là encore, j’ai été impressionné par l’énergie et la passion que tu mets dans ton travail au quotidien.

J’ai aussi été amené, ponctuellement, à travailler au centre de recherche d’Air Liquide à Jouy-en-Josas. C’est un lieu que je connais bien car j’y ai effectué mon stage de Master, et j’ai eu plaisir à y retourner pendant la thèse, pour des réunions de travail ou pour mettre en place le modèle en conditions industrielles. Je remercie Guillaume Mougin, mon directeur de thèse du côté industriel, pour la qualité des échanges que nous avons eu lors de mes passages au Centre, ils m’ont toujours aidé à mettre mon travail en perspective. Merci aussi à Kateryna Voronetska, au côté de qui je travaillais au Centre, et bien souvent depuis l’IMFT par téléphone. Il fallait bien du courage pour interpréter les documents que je t’envoyais, pas toujours bien faits, et pour “faire tourner” mes codes, pas toujours bien fonctionnels au moment où il le fallait ! Cela aura été un plaisir de travailler avec toi. Merci aussi à Sébastien Cadalen, Mikaël Wattiau, Thierry Désaleux, pour leur expertise et leur aide lors de mes passages au Centre, ainsi qu’à Christine Dervin. Un salut aussi à mes collègues du centre, que j’aurais peu eu le temps de cotoyer durant ma thèse, mais que je prenais toujours plaisir à retrouver lors de mes passages.

Je remercie Didier Lasseux et Ludovic Raynal d’avoir accepté de rapporter mon manuscrit de thèse, malgré la période estivale. Je remercie aussi Véronique Roig et Florian Fichot d’avoir accepté d’être examinateur de la thèse.

Je tiens, enfin, et surtout, à remercier tous mes collègues au sein du Groupe d’Etude des Milieux Poreux, doctorants, post-doctorants ou permanents, anciens ou actuels. La bonne ambiance au quotidien, l’entraide au sein du groupe, les moments partagés en salle de pause, ont été déterminants pendant la thèse. Merci à Frédéric, Martin, Myriam, Yohan, Hamza, Tawfik, Romain, Ruddy, Jianwei, Chen, Laeticia, Ange, Mauricio, Benjamin, Jacques, Laetitia, Antoine, Amy, Pauline, Edith, Adlan, Maxime, Vincent, Pierre, et à tous ceux que j’oublie probablement. Un clin d’oeil particulier à Jianwei, avec qui j’ai partagé mon bureau pendant ma première partie de thèse, et à Romain et Hamza, mes “co-bureaux” par la suite. Ils ont beaucoup contribué à la réussite de cette thèse.

Pour finir, je tiens à remercier ma famille, qui est venue en nombre assister à ma soutenance, curieuse de découvrir ce qui se cache derrière la “mécanique des fluides”, un terme qui fait partie du vocabulaire familial depuis un bon moment. Mes parents, qui m’ont toujours soutenu dans la poursuite de mes études, Jérôme, Delphine, papi et mamie Babonneau, Valérie, Hubert, Cécile, Jojo, Christine, Gui, Sylvie, Jean-Luc, Maud,

Johan et Quentin. Marius, aussi !

Contents

1	Introduction	1
1.1	Distillation in columns equipped with structured packings	2
1.1.1	The distillation process	2
1.1.2	Equipment of structured packings	3
1.1.3	A multi-scale process	4
1.1.4	The physics of the gas-liquid flow	6
1.1.5	General issues and objective of this work	9
1.2	State of the art for separation processes in structured packings	10
1.2.1	Estimation of the pressure drop	10
1.2.2	Characterization of the liquid phase	11
1.2.3	Upscaling approaches	11
1.2.4	Modeling of mass transfer	13
1.3	Organization of the manuscript	14
2	Methodology: upscaling in porous media	16
2.1	Scales of description	17
2.2	Boundary value problem at pore-scale	18
2.3	Definitions and theorems	21
2.3.1	Spatial and temporal averaging	21
2.3.2	Theorems for the volume averaging method	23
2.3.3	Decomposition in average plus perturbations	24
2.4	The method of volume averaging	25
I	Monophasic modeling	27
3	Gas phase as a one-phase flow: impact of a rough surface	28
3.1	Introduction	29
	Paper: Modeling flow in porous media with rough surfaces: effective slip boundary conditions and application to structured packings	32
3.2	Introduction	33
3.3	Derivation of an effective slip condition	34
3.3.1	Micro-scale transport equations	34
3.3.2	Domain decomposition and effective slip	35
3.4	Upscaling at the Darcy-scale via volume averaging	39

3.4.1	Notations	39
3.4.2	Temporal averaging	39
3.4.3	Spatial averaging	40
3.5	Results	42
3.5.1	Methods	42
3.5.2	Case 1: Application to a channel with sinusoidal walls	45
3.5.3	Case 2: Application to an array of rough cylinders	46
3.5.4	Case 3: Application to structured packings	52
3.6	Conclusion	58
 II Multiphase modeling		60
 4 Two-phase flow in highly permeable media: models with cross terms		62
4.1	Introduction	63
4.2	Two-phase flow model at macroscale: step by step method	64
4.2.1	Step 1: Mathematical problem at pore-scale	64
4.2.2	Step 2: volume averaging	65
4.2.3	Step 3: Problem on the deviations	66
4.2.4	Step 4: Approximation of the perturbations	71
4.2.5	Step 5: Closure at macroscale	71
	Paper: Modeling two-phase flow of immiscible fluids in porous media: Buckley-Leverett theory with explicit coupling terms	75
4.3	Introduction	76
4.4	Methods	77
4.4.1	Models and assumptions	77
4.4.2	Buckley-Leverett theory	79
4.4.3	Boundary, initial conditions and fluids	83
4.4.4	Closures for the effective parameters	83
4.5	Results	85
4.5.1	Case 1: Drainage: water/air flow in a particle bed	85
4.5.2	Case 2: Imbibition: air/water flow in highly permeable media	89
4.5.3	Case 3: Imbibition: oil/water flow in low permeability media	92
4.6	Conclusion	94
 5 Extension to the inertial regime and application to structured packings		96
	Paper: Momentum exchange drives immiscible two-phase flows within highly permeable porous media	98
5.1	Introduction	99
5.2	The fundamental physics of two-phase flow in porous media	100
5.2.1	Mathematical system at the pore-scale	100
5.2.2	Flow regimes: low vs high permeability	100
5.3	Continuum-scale models for two-phase flows	102
5.3.1	Empirical models for highly permeable porous media	102
5.3.2	Semi-heuristic model for highly permeable porous media	103
5.3.3	Simplified one-dimensional model	107
5.4	Semi-analytical and numerical methods	108

5.4.1	Buckley-Leverett theory	108
5.4.2	Finite-volume solver	109
5.5	Results	111
5.5.1	Case 1: creeping flows	111
5.5.2	Case 2: co-current flows within particle beds	113
5.5.3	Case 3: counter-current flows within structured packings	119
5.6	Conclusion	128
6	Distribution of the liquid phase	130
6.1	Previous approaches in the literature	131
6.1.1	Liquid “splitting”	132
6.1.2	One-phase flow in a bi-structured medium	133
6.2	Modeling strategy based on liquid splitting	134
6.2.1	Mass and momentum transport	135
6.2.2	Liquid exchange between the pseudo phases	138
6.2.3	Internal boundaries and rotation of the packs	139
6.2.4	Reduction toward a two-liquids approach	140
6.3	Numerical method	141
6.4	Results	142
6.4.1	Case 1: two pseudo-liquids in a two-pack column	142
6.4.2	Case 2: two and four liquids models between two sheets	144
7	Conclusion and perspectives	152
	Conclusion	152
A	Appendix - Chapter 3	156
A.1	Spatial averaging	156
A.1.1	Mathematical problem governing the deviations	158
A.1.2	Closure problem	158
A.2	Visualisation of the grids	159
B	Appendix - Chapter 4	161
B.1	Closure problems: two-phase flows	161
C	Appendix - Chapter 6	163

Introduction en Français

L'air pur est composé à 72.12% en azote, à 20.95% en oxygène, à 0.93% en argon, et dans des proportions très faibles en gaz rares, dont le néon, l'hélium, le krypton, le xénon, ou encore l'hydrogène. La séparation de l'air en ses constituants principaux s'effectue au sein d'usines de séparation (Air separation units, ASU), où sont réalisées les différentes étapes nécessaires au procédé. Ce procédé constitue aujourd'hui un secteur industriel majeur à travers le monde, du fait de la demande en oxygène, azote, ou argon, en grande quantité et dans des secteurs industriels très divers. La production en oxygène atteint par exemple plus d'un million de tonnes par jour à travers le monde. Son application la plus connue se situe dans le domaine de la santé, où il est utilisé pour améliorer les conditions respiratoires. L'utilisation principale de l'oxygène, cependant, et en quantité industrielle, est en tant que comburant, pour de nombreuses applications dont la sidérurgie et la métallurgie, où il est associé à des gaz combustibles pour améliorer les rendements. Ses propriétés d'oxydation sont aussi largement utilisées dans les industries chimique et pétrochimique. L'azote, pour sa part, est principalement utilisé en tant que gaz inerte dans de très nombreux secteurs, notamment dans l'industrie pétrolière pour prévenir les risques de combustion. Il est aussi utilisé en tant que liquide cryogénique dans le domaine de la santé. L'argon, enfin, possède lui aussi la propriété d'être très peu réactif, et est donc utilisé principalement en tant que gaz inerte.

La séparation des principaux composants de l'air sur le site d'une usine de séparation est réalisée par un procédé de *distillation*, au sein de colonnes de très grandes dimensions, pouvant mesurer plusieurs dizaines de mètres de haut et plusieurs mètres de diamètre. Le procédé de distillation repose sur le fait que l'oxygène et l'azote possèdent des points d'ébullition qui sont différents : l'azote se liquéfie à -195.8°C alors que l'oxygène se liquéfie à -183°C , à pression atmosphérique. A température intermédiaire entre ces deux valeurs, le mélange azote-oxygène se compose donc de deux phases, une phase chargée en oxygène qui est sous forme liquide et une phase chargée en azote qui est sous forme gazeuse. De manière à obtenir deux phases avec un très haut degré de pureté en oxygène et en azote respectivement, on fait s'écouler le mélange au sein d'une structure particulière, qui est le *garnissage structuré*. Cet équipement permet notamment de maximiser la surface d'échange entre les deux phases. Il est constitué de fines feuilles métalliques corruguées (~ 0.1 cm d'épaisseur), placées parallèlement et agencées en packs (~ 20 cm de hauteur). Les deux phases sont par ailleurs placées à contre-courant, de manière à générer un cisaillement fort et à optimiser le transfert de matière à l'interface. La phase liquide chargée en oxygène s'écoule ainsi par gravité le long du garnissage sous la forme d'un film mince, quand la phase gaz chargée en azote remonte la colonne. L'équipement de garnissage structuré est aujourd'hui présent dans la plupart des colonnes de distillation à travers le monde, et est utilisé plus largement pour les procédés de séparation à grande échelle dans l'industrie chimique, dont entre autres le traitement du CO_2 (absorption) ou des procédés de raffinage dans l'industrie pétrolière. Il a remplacé, peu à peu, à partir des années 1980, des équipements constitués de plateaux horizontaux ("trays") ainsi que les garnissages "vrac", constitués de petits éléments généralement sous la forme d'anneaux. Les plateaux et le garnissage vrac sont encore utilisés dans l'industrie chimique mais possèdent un rendement plus faible et des pertes de charge plus élevées pour la distillation de l'air en grande quantité. La production en oxygène et en azote purs dans une colonne équipée de garnissage structuré atteint aujourd'hui 50 à 5000 tonnes par jour, en fonction des besoins spécifiques à proximité d'un site de production.

La compréhension de l'écoulement associé au procédé de distillation, sa description au sein de l'équipement de garnissage structuré, sont l'objet de cette étude. Une meilleure compréhension du procédé est motivée par le coût de production très élevé, lié notamment au fonctionnement en condition cryogénique. L'enjeu consiste à optimiser le transfert de matière entre la phase chargée en azote et la phase chargée en oxygène, tout en limitant la perte de charge, qui peut devenir très élevée du fait des dimensions de la colonne. Il s'agit

notamment de limiter les effets de maldistribution de la phase liquide au sein du garnissage et de contrôler le caractère instable de l'écoulement liquide-gaz, qui, bien qu'il favorise le transfert de matière, génère de la perte de charge et donc des coûts de fonctionnement. A des régimes d'écoulements trop forts, le cisaillement du film liquide par la phase gaz provoque l'arrachage du film sous forme de gouttes, et mène à un phénomène d'engorgement de la colonne. Ce phénomène se caractérise par une augmentation très forte de la perte de charge et par une chute de l'efficacité du transfert.

Le projet de recherche global, dont fait partie cette étude, est ainsi de prédire l'efficacité du transfert et le coût énergétique associé, pour une géométrie de garnissage donnée, et pour des conditions opératoires données. Le travail de modélisation est aussi et surtout une alternative à la mise en place de mesures expérimentales. Il s'agit donc de résoudre un modèle de transport des espèces chimiques au sein de la structure de garnissage pour différents régimes d'écoulement. A l'heure actuelle, cependant, la complexité de l'écoulement à la petite échelle et le facteur d'échelle très élevé entre les petites et les grandes échelles du procédé rendent la résolution numérique des équations de transport des espèces inenvisageable. En réalité, la résolution de l'écoulement contre-courant gaz-liquide à l'échelle d'un petit volume de garnissage de l'ordre du centimètre représente aujourd'hui un calcul très lourd, et les méthodes numériques sont encore incertaines. Il est donc judicieux de s'orienter vers des méthodes de *changement d'échelle*. Ces méthodes permettent de faire un transfert de l'information des petites échelles vers les grandes échelles et donc de décrire le système avec une résolution moins élevée. Dans le cas présent, il s'agit de traiter la colonne à garnissage comme un milieu poreux. Les milieux poreux sont en effet typiquement des milieux qui impliquent des phénomènes physiques à des échelles très différentes et pour lesquels les techniques de changement d'échelle sont très utilisées. On utilise dans ce travail la méthode de la prise de moyenne volumique, qui consiste à moyennner en espace le problème mathématique qui définit le système à l'échelle du pore, et donc à obtenir un modèle dit à *grande échelle*. Les lois ainsi obtenues contiennent l'information de la petite échelle, dite *filtrée*, via des paramètres effectifs. Ces paramètres sont déterminés par une résolution de problèmes de fermetures à l'échelle d'une cellule unitaire représentative du système. L'idée générale du changement d'échelle est ainsi, d'une part, de résoudre un problème mathématique sur un petit élément représentatif milieu, et, d'autre part, de résoudre un modèle moyenné sur un maillage du domaine nettement moins raffiné que si la physique à la petite échelle était résolue.

Des méthodes de changement d'échelle ont déjà été utilisées dans la littérature sur les procédés de séparation en colonne à garnissage structuré, mais les modèles développés restent à l'heure actuelle incomplets. Ce travail s'inscrit donc dans la continuité des travaux réalisés jusqu'à présent. Il est réalisé en collaboration entre le Groupe d'Etude des Milieux Poreux (GEMP) de l'Institut de Mécanique des Fluides de Toulouse (IMFT) et le Centre de Recherche Paris-Saclay d'Air Liquide. Le chapitre 1 est consacré à l'introduction du procédé de distillation et à l'état de l'art de la recherche sur ce procédé. Le chapitre 2 est consacré à l'introduction des méthodes de changement d'échelle dans les milieux poreux. Dans le chapitre 3, un modèle est développé pour la phase gaz pour les débits modérés, où l'impact de rugosités de surface est pris en compte. Les chapitres 4 et 5 sont dédiés à l'étude de modèles diphasiques pour décrire l'écoulement gaz-liquide à plus hauts débits, où l'interaction entre phases est importante. Enfin, dans le chapitre 6, on étudie des approches où la phase liquide est décomposée en plusieurs pseudo-phases, de manière à mieux représenter l'anisotropie de l'écoulement liquide au sein du garnissage structuré.

Chapter 1

Introduction

Contents

1.1	Distillation in columns equipped with structured packings	2
1.1.1	The distillation process	2
1.1.2	Equipment of structured packings	3
1.1.3	A multi-scale process	4
1.1.4	The physics of the gas-liquid flow	6
1.1.5	General issues and objective of this work	9
1.2	State of the art for separation processes in structured packings	10
1.2.1	Estimation of the pressure drop	10
1.2.2	Characterization of the liquid phase	11
1.2.3	Upscaling approaches	11
1.2.4	Modeling of mass transfer	13
1.3	Organization of the manuscript	14

1.1 Distillation in columns equipped with structured packings

1.1.1 The distillation process

The atmospheric air is predominantly composed of nitrogen at 72.12%, of oxygen at 20.95%, and of argon at 0.93%; the remaining consists of traces of rare gases, including neon, helium, krypton, xenon and hydrogen. Air separation units (ASU), or air separation plants, are used to separate the air into its primary components: nitrogen, oxygen, and sometimes argon. The primary components of air are utilized in a large variety of fields. Oxygen is used to enhance furnaces in metal production and coal gasification, for the treatment of waste water, or for medical purposes. Nitrogen is mainly used for its inerting property, in chemical and petroleum industries, and also as a cryogenic liquid. Argon is also mainly used for its inerting property. The demand for these pure components has increased substantially over the last century and is today a major industrial sector around the world. The production in oxygen, for instance, reaches today one million ton per day.

Separating air in its primary components was first realized separately by Carl von Linde and Georges Claude at the end of the 19th century, using the Joule-Thomson refrigeration effect. The general principle is still the same today, although technologies and the quantities produced have changed considerably. It consists in distilling oxygen and nitrogen based on their distinct boiling temperatures: the boiling point of oxygen (-183°C at atmospheric pressure conditions) is higher than that of nitrogen (-195.8°C). The distillation is operated in industrial columns of very large dimensions, up to tens of meters high, and several meters in diameters. The ASU, as the one depicted in Fig. 1.1, are today present in many countries to respond to the high demand in pure chemical components. They are sometimes installed directly in industrial sites in order to supply directly the gases produced. The oxygen production capacity of a plant varies from 50 tons up to 5000 tons per day, depending on the specific needs.

Before proceeding to the distillation of the air and separating oxygen from nitrogen, a number of preliminary steps are realized [8]. The air extracted from the atmosphere is initially compressed up to around 6 bar, resulting in an increase of temperature. It is then cooled down using a heat-exchanger to return to ambient temperature. Given the very low boiling points of oxygen and nitrogen, the main step of the process consists in cooling the air down to very low temperatures. At this stage, however, the air is composed of many impurities, including vapor water, carbon dioxide, sulfur compounds, and hydrocarbons, such as acetylene and ethylene. These components would freeze at very low temperature and must be removed before the main cooling step. This purification is made through adsorption. The air, which is now compressed and cleaned, is finally cooled down to its dew point, in order to proceed to the distillation. The cooling, again, is done by heat-exchangers.

At cryogenic temperature the nitrogen/oxygen mixture is made of a liquefied part enriched in oxygen and of a vaporized part enriched in nitrogen. To obtain a separated mixture with pure components, i.e. a pure oxygen phase (liquid) and a pure nitrogen phase (vapor), the process is based on two principles. On the one hand, the contact area between the two phases is maximized by a suitable structure which will be described in the following, and, on the other hand, the two phases are operated counter-currently in order to favor the mass transfer. The liquefied phase streams down by gravity through the column and gets enriched in oxygen, as oxygen is less volatile than nitrogen, while the vapor phase ascends the column and gets enriched in nitrogen. The counter-current flow generates a shear-stress which favors the interfacial transfer of chemical species. The purity of the liquid oxygen and gaseous nitrogen can thus reach 99.9%. To improve the production of oxygen, Carl von Linde suggested in 1910 to use a double column configuration. One of the two columns is at high pressure (~ 6 bar), and is used to provide an intermediate reflux of oxygen and nitrogen streams to the low pressure column (~ 1.4 bar). This is in this low pressure column that the pure

components are therefore recovered. This configuration is still the one used today.



Figure 1.1 – Industrial site of an Air Separation Unit (ASU)

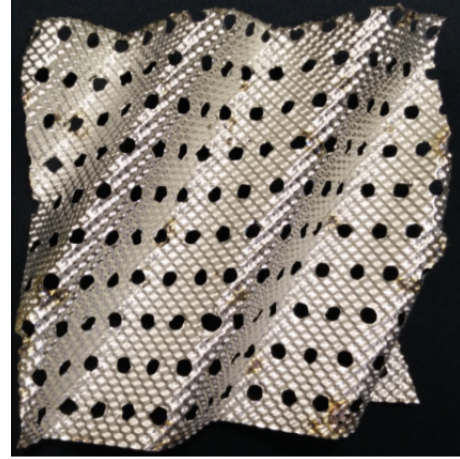
1.1.2 Equipment of structured packings

Distillation columns are equipped with devices called contactors and especially engineered to ensure a maximal surface of contact between the liquid and the vapor phases. The contactors were initially *trays*, consisting in a succession of horizontal plates throughout the column. The development of *structured packings*, in the 1960s, represented a major breakthrough to separate components in industrial quantities, as it enhances the contact area between the phases and limits the pressure drop compared to trays. The pressure drop is for instance reduced by five to ten compared to columns equipped with trays [8]. To date, this is the most efficient equipment and it is used in the industry worldwide for the distillation of air, as well as for other separation processes, such as the captation of CO₂, or oil refining.

Structured packings are composed of parallel corrugated sheets arranged in packs. The corrugated sheets are thin metal sheets of thickness ~ 0.1 mm that can be either smooth or textured. A picture of a pack of structured packings and a zoom on a corrugated sheet are given in Fig. 1.2. A column of distillation is filled with a succession of packs, which stand approximately 20 cm high and are successively rotated by 90°. Structured packings therefore combine both a very large surface area (packing area, up to $750 \text{ m}^2/\text{m}^3$) and a large void space (up to ~ 0.95). The large surface of the packings maximizes the contact area between the two phases, as the liquid phase streams down as a thin film on the corrugated sheets. The extremely large porosity also maintains a reasonable pressure loss across the industrial scale columns, therefore reducing energy costs. The successive reorientation of the packs also redistributes the liquefied phase streaming down in the column and contributes to its good distribution.



(a)



(b)

Figure 1.2 – Pictures of structured packings - a) a pack (BX Gauze packing from Sulzer) b) an element of corrugated sheet (picture from Izož [86]).

1.1.3 A multi-scale process

The distillation process in columns equipped with structured packings is a *multi-scale* process. One can distinguish the macroscale, which is associated to the dimensions of the columns, from the microscale, which is the scale of a small pattern of corrugations (see Fig. 1.3). These two scales are distinct by several orders of magnitude. While industrial columns are often up to ten meters high, the amplitude and wavelength of the corrugations are about one centimeter. Corrugated sheets are also often engineered with a small surface texture. This rough texture is used to enhance the wetting of the sheets, and its amplitude is generally below the millimeter. Such a texture is represented in Fig. 1.3. Even smaller scales are also at play when one considers the gas-liquid flow. The thickness of the liquefied film enriched in oxygen is for instance about several hundreds of micrometers, i.e. an order of magnitude below the size of a small pattern of packings.

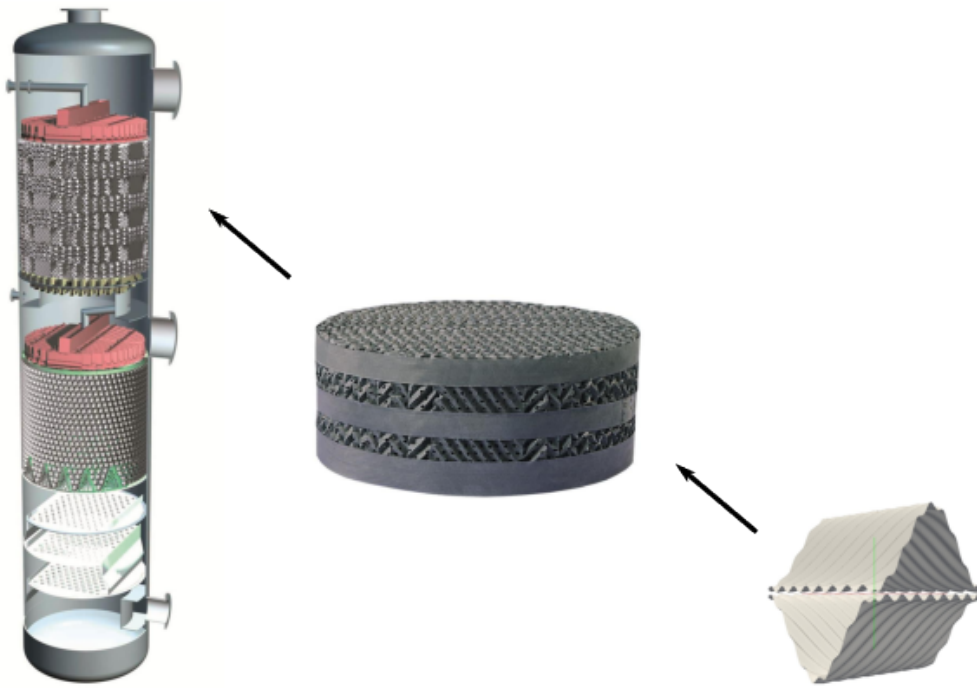


Figure 1.3 – Representation of the different scales at play - from microscale (crossing element of packing) to macroscale (scale of the column)

These numerous scales are in fact reminiscent of multi-scale processes in porous media. A structured packing actually constitutes a very singular porous medium whose characteristics can be enumerated as follows

- a very high porosity level, which varies depending of the type of packing, up to ~ 0.95 , and which leads to a high permeability, $> 1 \times 10^{-7} \text{ m}^2$.
- an ordered porous medium, made of a repetitive pattern (see Fig. 1.3).
- a strong anisotropy due to the arrangement in parallel corrugated sheets and to the reorientation of the packs.
- symmetrical features: given two parallel corrugated sheets, their corrugations are symmetrical compared to the vertical axis of the column (angle $\pm\theta$, see Fig. 1.4 or Fig. 1.2).

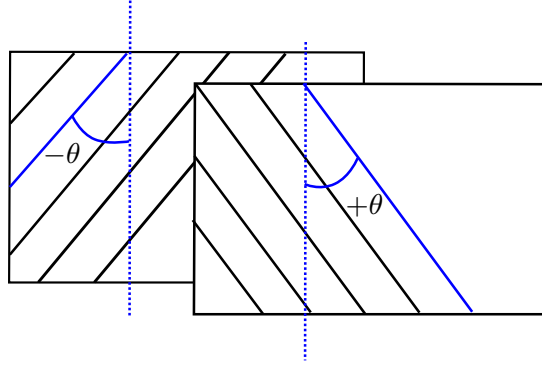


Figure 1.4 – Representation of two parallel corrugated sheets ; the inclination of the corrugations is respectively $+\theta$ and $-\theta$ compared to the axis of the column.

Considering this last symmetrical feature, Soulaine et al. in [162] suggest that a structured packing can be treated as a “bi-structured medium”. By definition, a bi-structured medium exhibits two distinct flow behaviors at the macroscale corresponding to two distinct regions at the microscale. Here, the opposite orientation of the corrugations guides the liquid film in two opposite directions. This question is further discussed in this work.

1.1.4 The physics of the gas-liquid flow

The distillation process therefore constitutes a counter-current gas-liquid flow in a highly permeable media. On the one hand, the liquid phase flows as a thin gravity film along the corrugated sheets. This is a laminar (but inertial) flow, with a Reynolds number below $Re_l = 200$. For a given phase i , the Reynolds number is defined such as

$$Re_i = \frac{\rho_i U_i l_i}{\mu_i}, \quad (1.1)$$

where ρ_i and μ_i are the density and the viscosity of the phase i , U_i its characteristic velocity and l_i a characteristic length scale. For the liquid film, l_i generally refers to the thickness of the liquid film. The thin film wets the major part of the corrugated sheets, resulting in a large contact area between the liquid and the gas. The *effective area* a_e , which is defined as the interfacial area between the liquid and the gas phases, is often introduced to quantify this surface. This is a key parameter as the global mass transfer directly relies on it. The efficiency of a given design of packing is then assessed by evaluating a_e/a_p , which is the ratio of the effective area to the *packing surface area* a_p of the packing defined by the total area of the corrugated sheets. This ratio informs on the wetting of the liquid phase for a given type of packing. It was shown to be a function of the liquid flow rate, of geometrical features, and of the physical properties of the phases [174, 1, 183, 2]. It is generally below 1 for moderate flow rates and higher than 1 for high flow rates, although it depends on numerous parameters. Coarse packings (small packing surface area a_p) are, for instance, shown to favor high ratios a_e/a_p compared to dense packings (high packing surface area a_p). Wang et al. [2] indicate that it is likely due to maldistribution and insufficient wetting in the latter case, while coarse packings favor surface instabilities and therefore increase the effective area. The wettability and interfacial tension of the liquid phase also play a central role. The correlation between surface tension and wettability is complex, while it can be roughly evaluated at looking at the *spreading coefficient* [68] defined by

$$S_p = \gamma_{sg} - (\gamma_{sl} + \gamma_{lg}) \quad (1.2)$$

where the liquid-gas interfacial tension is later denoted γ . When $S_p > 0$, the liquid wets the surface completely while when $S_p < 0$, partial wetting occurs. Low surface tension liquids are more prone to flow as thin liquid films, while high surface tension fluids will tend to generate triple lines and only partially wet the structure. In the air distillation process, the liquefied phase is generally assumed to perfectly wet the structure and to flow as a uniform and thin liquid film, due to its very low surface tension.

The preponderance of some effects on others is quantified using well-known dimensionless numbers. The Capillary Ca and Bond Bo numbers compare respectively the relative importance of capillary effects on viscous and gravity effects. They read respectively

$$Ca_i = \frac{\mu_i U_i}{\gamma}, \quad Bo_i = \frac{(\rho_i - \rho_j) g l_i^2}{\gamma}, \quad (1.3)$$

(respectively Ca_j and Bo_j for the phase j), and γ the surface tension between i and j . A Weber number is also sometimes introduced to assess the relative influence of inertial effects compared to capillarity, but it is contained in the definitions of the Reynolds and Capillary numbers since

$$We_i = \frac{\rho_i U_i^2 l_i}{\gamma} = Re_i Ca_i. \quad (1.4)$$

Estimations of upper bounds for the Bond and Capillary numbers for the liquid phase (oxygen phase) in structured packings are about $Bo_w \sim 50$ and $Ca_w \sim 2 \times 10^{-3}$, which are large values for two-phase flows in porous media. These estimations indicate that the capillary effects do not play a central role in the distillation process in a column equipped with structured packings. This is due to the high permeability of the structure, which is in contrast with many porous media involving two-phase flows, and to the low surface tension of the couple of fluids in cryogenic conditions.

The liquid film in the distillation process is also characterized by the development of trains of waves at its surface, whose amplitude can be up to five times the thickness of the liquid film. A typical profile of soliton-like waves is shown in Fig. 1.5. These instabilities tend to increase the effective surface a_e and therefore to enhance the mass transfer between the two phases. It also impacts the pressure drop in the column as it generates further dissipation effects at the interface between the two phases. These instabilities are seen in Chapter 3 as a roughness for the flow of the gas phase.

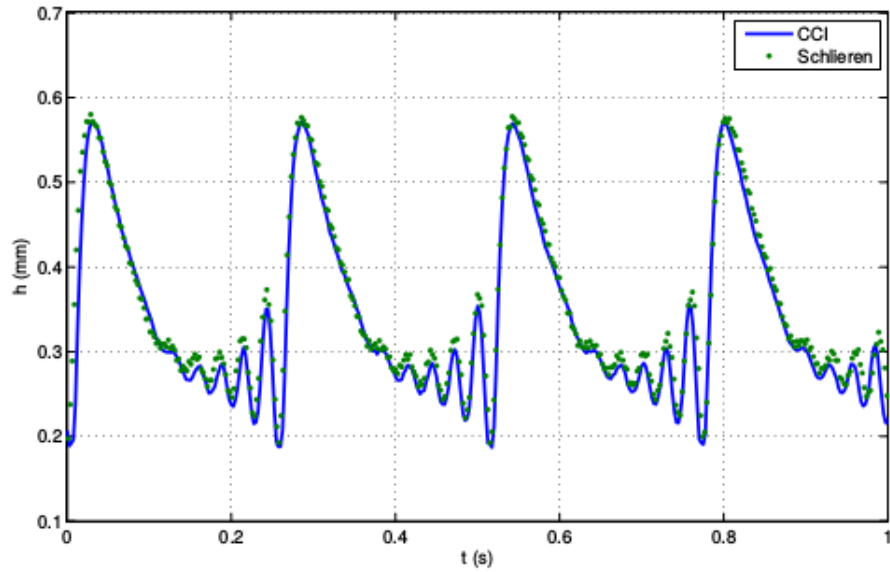


Figure 1.5 – Wave profile of two-dimensional travelling waves at the surface of a liquid film in an inclined plate - experiment from Kofman (2014) [94].

In contrast with the liquid phase, the gas phase occupies much of the void space in the structure and ascends the column. While the liquid flow is laminar, the gas flow is turbulent at high flow rates, with a Reynolds number up to 20000 for the highest flow rates. The interfacial shear-stress due to the high flow rate reinforces the development of soliton-like waves at the surface of the liquid film, which causes an increase of the pressure drop and tends to retain the liquid in the column. The regime corresponding to a little interaction between the two phases is referred to as the pre-loading regime (low flow rates), while the regime corresponding to a significant interaction is referred to as the loading regime (high flow rates). An excessive shear-stress between the two phases leads to the well-known phenomenon of *flooding*. The liquid is strongly retained by the counter-current gas phase and accumulates drastically at the interfaces between the packs. This produces a drastic increase of the pressure drop and of the global liquid retention in the column. The different regimes (pre-loading, loading, flooding) are seen in Fig. 1.6 in the experimental results from Sues and Spiegel (1992) [167]. These results show the typical trend of the pressure drop and of the liquid saturation in separation processes in structured packings, for increasing gas and liquid flow rates.

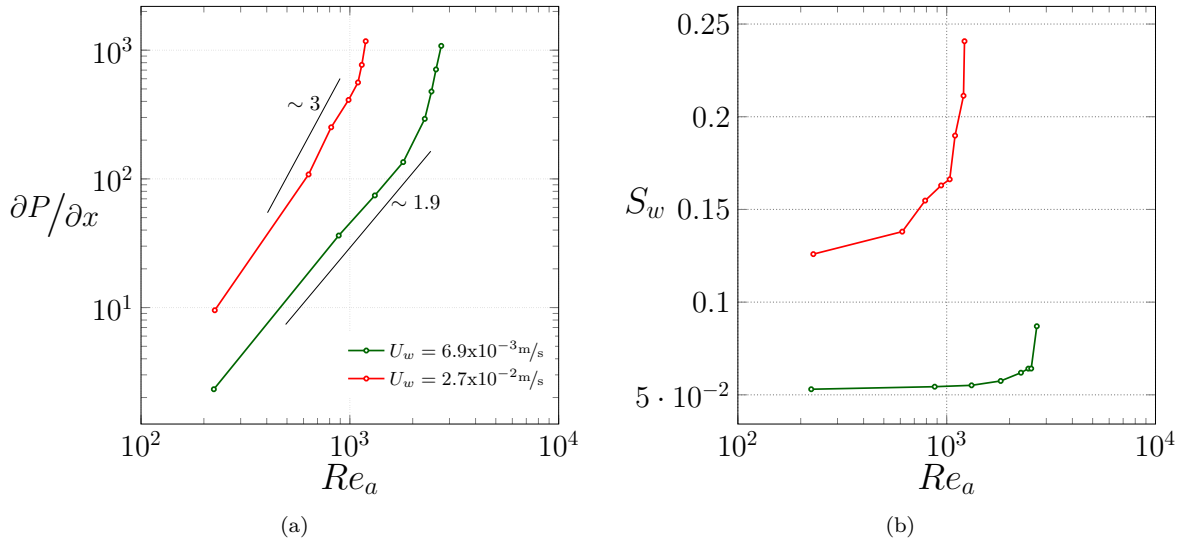


Figure 1.6 – Experimental data in columns equipped with structured packings - Suess and Spiegel (1992) [167] - a) pressure drop and b) liquid saturation, as a function of the gas Reynolds number .

1.1.5 General issues and objective of this work

While the equipment of structured packings is, to date, the most efficient and mature method to produce pure air components in large quantities, it is also energy intensive. Therefore, the main reason for a constant innovation of the equipment is the demand to minimize the operating costs. The choice of an equipment of structured packings relies on a compromise between

- the *efficiency*: to obtain pure components in large quantities and in the smallest columns.
- the *capacity*: to operate over a large range of flow rates without excessive destabilization of the vapor/liquid flow (flooding).

The physical phenomena that limit both efficiency and capacity are well known. On the one hand, maldistribution effects of the liquid phase are limiting the surface of exchange between the two phases. On the other hand, the interfacial shear-stress between the gas and the liquid film, although it generally benefits to the mass transfer, may increase pressure drop (energy cost) and lead to the flooding of the column at high flow rates.

The present work aims at contributing to the global objective of *modeling* the distillation process. Given the high operating cost of the separation processes in structured packings, even little improvements of the efficiency would decrease significantly the global cost. Developing models of the process (phases distribution, pressure drop, mass transfer, etc) is therefore essential in order to be predictive of the transfer for a given design of packings. In the last forty years, a constant progress has been realized on the design in order to reduce the pressure drop and to increase the global efficiency. These improvements have been largely achieved through experimental tests of new designs. Such experiments are however heavy to implement and expensive. The alternative method therefore consists in a modeling strategy. Much research has been dedicated to this aim in the last decades. Spiegel and Meier [164] (2003) and Olujic [124] (2009) suggested a number of research orientations, or “road-map” to follow. This road-map is largely devoted to both experimental imagery and

numerical modeling. The development of upscaling methods is also an important objective in order to reduce the computational costs of the modeling procedure. Such methods allow to model the process without solving the smallest scales at play for large dimension systems, which is impossible at this stage. The volume averaging method is such a method and is described later in this work. The derivation of a predictive model, for a given design of packings, would represent a major tool to enhance the process. One can speculate, perhaps over a ten year horizon, that the resolution of the process will be a daily work for an engineer in the chemical industry.

The next section is dedicated to a review of the significant works devoted to the separation processes in structured packings in the last decades.

1.2 State of the art for separation processes in structured packings

1.2.1 Estimation of the pressure drop

A key issue of separation processes in columns is to limit pressure drop. Many research works have therefore been focused on the estimation of this property. The first models for the *dry pressure drop* were 1D correlations between the gas flow rate and the pressure drop, based on well-known relationships used in porous media such as Ergun's laws. *Dry* pressure drop refers to a one-phase flow in the column for the gas phase, i.e. the liquid is not considered. It consists in polynomial functions of the gas flow rate, where the polynomial coefficients are known as the Ergun coefficients and are determined through experiments (Bravo et al. [28], Stichlmair et al. [166], Rocha et al. [145], Billet and Schultes [25]). The *wet pressure drop*, conversely, accounts for the presence of the liquid and is often determined by weighting the void-space according to the space that is occupied by the film. These 1D laws were the first models used to characterize gas-liquid flows in structured packings, but a certain degree of empiricism was involved, and the requirement for global experiments makes their use prohibitive.

In the last decades, as in many engineering fields, the development of numerical methods in fluid dynamics represented a major breakthrough to better characterize the flow in structured packings. Contrary to lab experiments, computational fluid dynamics (CFD) allows to conduct *local* analysis of the flow, i.e. in small part of the domain which is considered representative. Such simulations can be easily repeated for various designs, and therefore represent a significant reduction of both cost and time. Petre et al. [129] (2003) were the first to introduce the concept of REV for structured packings. Given the non-classical geometry of the global structure (multiple packs, successive rotations), they first suggest to consider *multiple* representative unit cells. Apart from the entrance and exit regions of the columns, two local regions are distinguished, including the smallest pattern of two parallel corrugated sheets and the region of transition between two packs. These different areas are seen as independent sources of dissipation and therefore of pressure drop. Then, simulations of the gas phase in the two regions provide the friction coefficients and then gives an estimation of the pressure drop as a function of the flow rate. Ever since, CFD tools have been used in many works to estimate the pressure drop in various designs of corrugated sheets. The modeling of the turbulence is generally based on a RANS approach (temporal averaging), and so far, a more precise description of the gas flow in the column has not been published (LES or DNS approaches). Calculations are often conducted in a single crossing element of packings [163, 153], but simulations over large scale packs have also been conducted [125, 121]. These large scale simulations, however, are based on RANS approaches which smooth the potential macroscale vortices of the flow.

1.2.2 Characterization of the liquid phase

The distribution of the liquid phase in the column is also a major issue, since it directly determines the size of the surface of exchange between the two phases and the transport of the chemical species. The simplest modeling approach consists in seeing the liquid phase as a liquid film flowing on an inclined plate. In the creeping regime, the thickness and the velocity profile can be calculated analytically using the theory of Nusselt (1916). This method was often used in order to estimate the liquid saturation in the column for a given flow rate [28, 25, 145]. It is however limited as it does not account for the corrugations of the sheets. The development of numerical tools on one hand, and of non-invasive techniques of visualization on the other hand, allowed to better apprehend the liquid modeling.

The development of CFD tools for engineering practice, in the 1990s, introduced a new option to obtain more precise information on the liquid film. One approach, proposed initially by Szulczewska et al. [169] (2003) and used extensively ever since, is to estimate the thickness of the liquid film through a 2D VOF (volume of fluid) simulation along a corrugated 2D wall [142, 141, 54, 69, 151]. The liquid saturation that is obtained allows to weight the pressure drop in the structure, which is initially determined using the methodology detailed in the previous section. Similar simulations in the real 3D geometry, using VOF methods, is today difficult to achieve, even in absence of counter-current flow. The work from Haroun et al. [70] (2014) is so far one of the only attempt of a VOF simulation in a geometry of corrugated sheet in 3D. A single sheet is used, as the physics at play at the contact points between two sheets complicates the simulation. The works of Sun et al. [168] and Liu et al. [109], between two sheets, can also be cited, although the numerical results are not clearly described. Yet much numerical work remains to be done before the counter-current flow in packings can be conducted in 3D. New methods involving, on one hand, an integral model for the liquid film with polynomial solutions [49], and, on the other hand, a DNS simulation in the gas phase, were recently proposed to characterize gas-liquid flows involving a separation of scales between the two phases and a high interfacial shear stress [104]. It enables to capture accurately the gravity-waves developing at the surface of the liquid and it limits the computational cost as it avoids to resolve the Navier-Stokes equations in the film. So far, the application is however restricted to test geometries.

Experiments were also proposed to better understand the flow of the liquid phase. The development of non-invasive techniques of visualization greatly contributed to the characterization of the liquid phase in structured packings. The use of tomography imagery, based either on x-ray or gamma-ray methods, represented a major breakthrough to characterize the distribution of the liquid. It provided new information on the global behavior of the liquid phase [27, 65, 114, 181, 61, 154]. It was seen for instance that the liquid phase is much more affected by the anisotropy of the structure than the gas phase. It is also proved that some liquid is retained locally at the contact points between two corrugated sheets, and is therefore redirected constantly. Mahr and Mewes [114] (2007), using tomography between two corrugated sheets with a single injection point, showed that the liquid tends to flow in preferential flow paths due to the corrugations. So far, however, the spatial and temporal resolutions of the tomography methods restrain the access to a quantitative estimation of the saturations or to dynamical behaviors.

1.2.3 Upscaling approaches

The development of upscaling strategies, finally, represents a key aspect of the research on separation processes with structured packings. Following methods used in porous media, the idea is to distinguish a micro and a macro scales and to characterize the system at the largest scale based on limited information from the small scale. The models constitute a set of equations on averaged fields, such as the averaged velocity or the averaged pressure. Such a technique allows to solve the model on a grid with a much lower resolution

than if the physical phenomena at the smallest scales were solved. To a certain extent, the CFD approaches introduced earlier rely on upscaling methods, as a local information (simulation of the flow in a unit-cell) is used to characterize the system at large scale. Most often, however, the structure of the law at the macroscale (generally Ergun laws) does not result from an upscaling strategy.

Iliuta et al. [83] (2004) derived a system of partial differential equations for the flow at macroscale, using a method inspired from the volume averaging method. The model is also referred as the Euler-Euler method, and implies a number of *frictions forces* in the momentum balance, which characterize the fluid/solid and fluid/fluid interfacial effects. This model was further extended to include the distribution of the liquid phase within the structure [62], through the use of an additional dispersion force in the momentum balance, forcing the flow radially. The magnitude of the dispersion force is determined through a dispersion coefficient, which is for instance calibrated experimentally. This model allows to represent the global plume of the liquid phase along multiple packs, but does not capture the preferential flow paths along two parallel corrugated sheets.

Mahr and Mewes [114] (2007) also used the volume averaging method to develop a model for the flow in packings. Similarly to Iliuta et al., the model involves friction forces, and does not rely on simulations of the flow at the small scale. The originality of their model is that they consider a two-equation model for the liquid phase at the macroscale. Based on their tomography image (see previous section), they observe that the double orientation of the corrugations guides the liquid in two opposite directions. They therefore suggested to “split” the liquid phase into two *pseudo* liquid phases, for the two films between two parallel corrugated sheets. The two films flow along two directions inclined at an angle $\pm\theta^*$ with the vertical axis. These directions are controlled by second-order tensors in the momentum balance, guiding the velocity fields along the desired directions. The films can also exchange matter at the contact points between two corrugated sheets, thereby respecting the experimental observations. The system at macroscale involves in the end a set of six equations, for the mass and momentum equations of the three phases gas-liquid-liquid.

Soulaine et al. [162] (2014), in the same spirit, derived a model for a gas-liquid-liquid system at the macroscale. They define the column equipped with structured packings as a bi-structured medium, i.e. a medium which segregates the fluid phases in two preferential directions [160]. They considered first the generic case of a one-phase flow in a bi-structured medium, and established a set of macroscale laws with closures, using the volume averaging method. Their model for structured packings is then conceived as a semi-heuristic extension of the theoretical model emerging from the one-phase flow analysis. It consists in a set of generalized Darcy’s laws with second-order tensors for the momentum transport of the gas and the two pseudo-liquids. The two films are supposed to flow along an effective angle and respectively its opposite with the column axis, following the idea of Mahr and Mewes.

An other interesting approach of upscaling is the work of Soulaine and Quintard [163] (2014). They derive a model for the gas phase based on the volume averaging method with closures. The model is a generalized Darcy’s law (or generalized Forchheimer’s law) in the inertial and turbulent regime. The originality of this work is to account for the turbulence effects via an initial RANS simulation on an unit-cell. This simulation provides the field of the so-called apparent viscosity in turbulence modeling. This field is further used in the closure problem of the volume averaging method to account for the turbulence effects. Contrary to the works described so far, also, the approach relies on the resolution of a closure problem at the local scale.

Other macroscale modeling approaches have been suggested in the literature, including the model from Aroonwilas and Tontiwachwuthikul [14, 13] (2000), used further by Sun et al. [168] and Liu et al. [109] (2016). The modeling strategy is based on a network modeling, meaning that the contact points between the corrugated sheets constitute a grid of nodes which is the base of the network. At each node, the liquid is able to flow in a number of different directions representing the different flow paths of the liquid. This

distribution is assessed via probability functions in [14, 13] and via numerical simulation of the film (VOF) between two corrugated sheets in [168, 109].

We have seen here that different approaches were employed in the literature to derive a large scale model for the separation process in structured packings. One should however distinguish the heuristic approaches from approaches emerging from more theoretical basis. As we will see in the manuscript, rigorous methods can be difficult to conduct due to the complexity of the flow at the local scale, leading to the development of semi-heuristic approaches. Two observations can be made, though. Upscaling strategies, such as the volume averaging method, provides some physical coherence to the mathematical structure of the model at the large scale. Also, if a closure can be derived, this method relies on the resolution of closure problems over a representative volume of the column, meaning that there is a transfer of information from the micro to the macroscale.

1.2.4 Modeling of mass transfer

Last but not least, an important aspect of the modeling strategy is to estimate the transport of chemical species between the two phases (mass transfer). It consists in the estimation of the transfer rate of a component A from a phase to an other. In the distillation process, the component A refers either to the oxygen or to the nitrogen of the oxygen/nitrogen mixture. Multiple approaches with different levels of complexity were used to model the mass transfer. Assuming that the system can be associated to a two-film flow with a plane interface, a number of models estimate the efficiency of the mass transfer of a component A via the calculation of a global mass transfer coefficient K_A [170]. This coefficient is seen as a global resistance to the transfer ($1/K_A$), i.e. corresponds to the resistance in series in the liquid and the gas phase. The study therefore consists in the determination of the mass transfer coefficients in the two phases, generally referred as k_{l_A} and k_{g_A} , with $1/K_A = 1/k_{l_A} + 1/k_{g_A}$. The model from Lewis and Whitman (1924) [107] is extensively used in chemical engineering. In this theory, mass transfer occurs in thin layers at the interface between the two phases, and is assumed to be controlled by diffusion. The mass transfer coefficients k_{l_A} and k_{g_A} are therefore proportional to the diffusion coefficients in the two phases. This approach is not always physically realistic but is appreciated for its simplicity. Other approaches are the penetration theory of Higbie (1935) [75], and the surface renewal theory of Danckwerts (1970) [40]. These two models are proved to be more realistic than the model of Lewis and Whitman and are also very common in engineering practice.

These models of films (global mass transfer coefficient K_A) formed the basis to derive mass transfer models for the separation processes in structured packings. The first of these models is due to Bravo et al. (1985) [28] and consists in correlations for the mass transfer coefficients k_{l_A} and k_{g_A} . These correlations are function of the flow rates and of the thickness of the liquid film. Similar models are those of Billet and Schultes (1993) [25] and Rocha et al. (1996) [147], where the effective area of exchange a_e is also included. More recently, a large number of works were dedicated to the determination of correlations for the mass transfer coefficients and the effective area, including the experimental works of Tsai et al. and Wang et al. [174, 1, 2, 183] (2009-2016). These correlations characterize the impact of the physical properties of the fluids, the flow rates, or geometrical features (design of the corrugated sheets) on mass transfer. An interesting new approach by Wang et al. [2, 183] (2014) consists for instance in introducing the concept of mixing point density, which is the number of contact points between the corrugated sheets per cubic meter. It is shown to be positively correlated to the mass transfer, which is attributed to the local redistributions of the liquid induced by the contact points, as it tends to enhance the mixing with the gas phase.

The approaches introduced so far rely on the assumption that the two-phase flow can be associated to a two-film flow with a plane interface. More accurate models consist in modeling the transport of the chemical

species in the column through conservation equations on the mass fractions of the species. This implies, also, to determine the flow of the fluid phases (velocity fields, position of the interface), which explains the extensive work dedicated to the characterization of the mass and momentum transport via upscaling strategies (previous section). The first models for the transport of the chemical species within structured packings are due to Aroonwilas and Tontiwachwuthikul [14, 13] (2000), following their model for the transport of mass and momentum. Soulaire et al. (2011) [161], following previous approaches [133, 37], proposed a model for the transport of species in a laminar two-phase flow in porous media, using the volume averaging method. The macroscale model involves effective coefficients (including dispersion coefficients and the mass transfer coefficient), which can be determined through the computing of closure problems. Another recent approach is the model proposed by Pham et al. [130] (2015) for the absorption of CO₂ in a solution of MEA in structured packings. Pham et al. determine the velocity fields and the saturations based on the Euler-Euler model and use a semi-heuristic model for the transport of the chemical species.

1.3 Organization of the manuscript

As explained previously, the aim of the present work is to contribute to the modeling of the distillation process in separation columns. The organization of the manuscript is discussed in this section, as well as the elements of the methodology which constitute novelties compared to previous studies.

The chapter 2 is first dedicated to the methodology used throughout the manuscript, and the document is then organized in two main parts. The first part is dedicated to a one-phase flow modeling approach for the flow of the gas phase, while the second part is dedicated to multiphase modeling approaches.

Monophasic approach In Chapter 3, we develop a strategy of upscaling to derive a macroscale model for the flow of the gas phase in the column. The objective is to derive a predictive model of the pressure drop in the gas phase and to account for rough surfaces which can be small scale roughnesses due to the structure or perturbations which develop at the surface of the liquid film. In this last case, the liquid film is therefore seen as a rigid rough surface by the gas phase, generating further dissipation and therefore affecting the pressure loss. The upscaling method is realized in two steps, which consist in first developing a smooth effective boundary condition replacing the no-slip condition at the rough wall, and then in using the volume averaging method to upscale the resulting effective boundary value problem of the flow of the gas phase. This two-step upscaling strategy is applied in Chapter 3. The originality of this work is on

- the derivation and the use of a Navier condition involving a second-order tensor for the anisotropy of the rough surface. The method is inspired from ideas of mapping used in the volume averaging method.
- the use of the volume averaging method for an inertial one-phase flow with a Navier condition at the walls, although similar works were conducted for a Stokes flow with a Navier condition (scalar coefficient) [102], and for an inertial one-phase flow with a no-slip condition [188].

Multiphasic approach The second part of the manuscript is dedicated to multiphase approaches. The Chapters 4 and 5 are dedicated to the derivation and the study of macroscale models for two-phase flows using the volume averaging method. The novelty in these two chapters is on

- the analysis of models with cross-terms in the viscous regime based on the Buckley-Leverett theory,
- the analysis in the inertial regime using a numerical resolution in OpenFoam.

In chapter 6, finally, we suggest another modeling approach for the liquid film in order to capture the anisotropy of the flow. The method relies on an arbitrary separation of the liquid phase in multiple pseudo-phases. It is shown to be adapted to the description of the preferential flow paths of the liquid film in the column. The novelty in Chapter 6 is on

- the introduction of a model using four pseudo-phases for the flow of the liquid phase.
- the computation of the flow in a column of multiple packs, including the rotation of the packs and the modeling of side effects.

The model developed from Chapter 4 to 6 is solved using a finite-volume solver developed in the open-source software OpenFoam. The solver allows to solve the mass and momentum transport of the liquid-gas flow in a column constituted of multiple packs.

Chapter 2

Methodology: upscaling in porous media

Contents

2.1	Scales of description	17
2.2	Boundary value problem at pore-scale	18
2.3	Definitions and theorems	21
2.3.1	Spatial and temporal averaging	21
2.3.2	Theorems for the volume averaging method	23
2.3.3	Decomposition in average plus perturbations	24
2.4	The method of volume averaging	25

In this chapter, we discuss a number of issues regarding the modeling of processes in porous media. Some elements of vocabulary and general concepts related to porous media sciences are first introduced. Then the volume averaging method, which allows to characterize a process at large scale from microscale fundamental principles, is described.

2.1 Scales of description

A porous medium is a hierarchical system composed of a solid structure and of a saturated fluid phase. The fluid phase means either a single fluid phase or a multi-phase flow, as this is the case for the distillation process. A porous medium is said discretely *hierarchical* in the sense that it is characterized by a discrete set of lengthscales. We generally distinguish a *microscale*, l , from a *macroscale*, L . The microscale corresponds to the pore-scale, or local scale, while the macroscale is associated to the dimensions of the system. The hierarchy of scales reads

$$l \ll L. \tag{2.1}$$

This separation of scales is illustrated in Fig. 2.1.

A system can be either described at the microscale or at the macroscale. The resolution of the boundary value problem at the microscale is however often prohibited as it requires a very fine resolution, even for localized information. Regardless of the process, the pore-scale geometry can be very complex, for instance in rocks involving heterogeneities or fractures. Surface effects, also, can be hard to capture, for instance in case of surface roughnesses or in case of reactive surfaces. For multi-phase flows, the position of the fluid-fluid interfaces should be precisely captured, as well as any related physical phenomena (mass transfer, phase change, etc). Also, beyond the concerns on the accuracy, porous media most of the times involve such large dimensions that an exact description of the whole process is absolutely prohibited.

On the other hand, the system can often be represented as a continuum medium at the macroscale. In this case, the geometry of the system is no longer represented precisely. The system is now characterized at any point of the space by *effective properties*, such as the porosity or the permeability. For a multi-phase process, a given point of the space for instance contains information regarding every single phase. This information can be, among other things, the volume ratio of the space which is occupied by a given phase, as well as its velocity. This representation also means that the interfaces between the fluid phases do not exist anymore, meaning somehow a loss of information.

The separation of the scales is the key element of the *change of scale*. The change of description scale, i.e. from the microscale to the macroscale, can be conducted through a number of different upscaling techniques, which differ in the point of view. These techniques include the volume averaging method [184, 116], the homogenization theory [23], and stochastic approaches [117]. From a well defined boundary value problem at the local scale, they permit to derive a system of partial differential equations at the continuum scale. We use in this study the volume averaging method, which relies on the spatial averaging of the mathematical system at pore-scale.

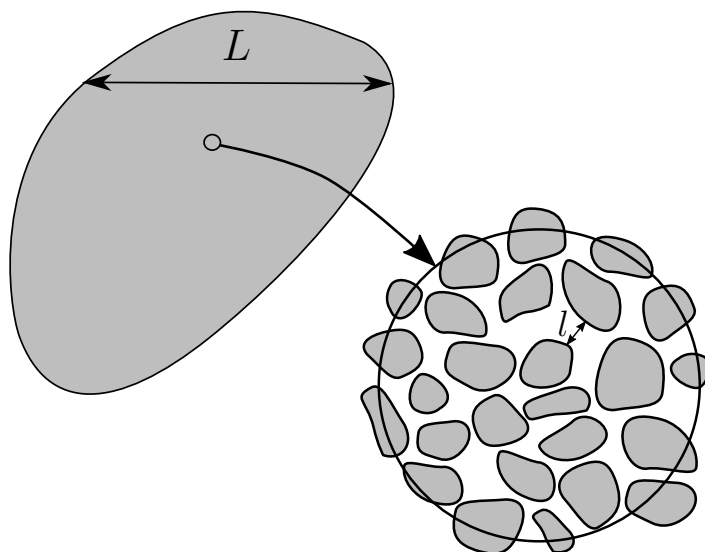


Figure 2.1 – Illustration of the disparate scales in a homogeneous porous medium. l is the lengthscale at microscale and L the lengthscale at macroscale.

2.2 Boundary value problem at pore-scale

Upscaling methods in porous media require to define accurately the boundary value problem of the system at pore-scale. Due to the complexity of the processes at play, this work is sometimes complicated. It implies to describe precisely the topology of the medium, to formulate correctly any transport phenomena, and to define rigorously the boundary conditions of the system. This last point is especially important as boundary effects sometimes play an important role in the process. This is the case when one deals with reactive surfaces, rough surfaces, or when one considers a system involving an interface between a fluid layer and a porous medium. The description of these surfaces and their effects is often complicated. They take place, sometimes, at a smaller scale than the pore-scale, which prevents any numerical resolution. The concept of *effective boundary condition* is therefore often introduced [21] in these cases. This mathematical condition replaces the boundary condition at the interface and mimics the effects actually expected. We propose here, as an example, to introduce the concept of effective condition for a fluid layer over a rough surface. This problem is encountered in very different applications occurring at very different scales, including rough surfaces in microfluidic devices, chemical reactors, or even in geophysics (for instance canopies). This is also the problem which is treated in Chapter 3, when we will consider the boundary value problem for the flow of the gas phase.

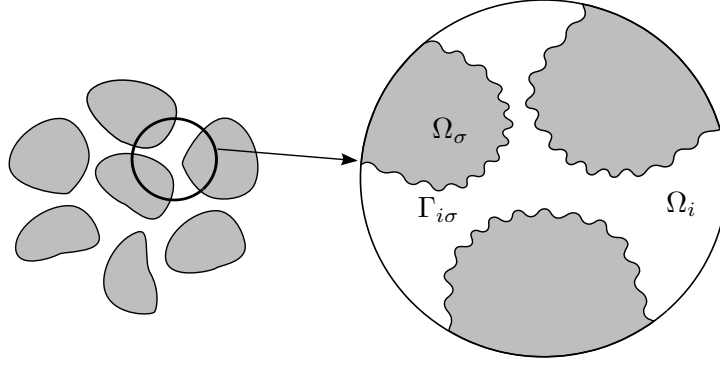


Figure 2.2 – Representation of the pore-scale system with roughness at the surface of the solid part.

A single fluid phase i is considered in a porous domain Ω with a rough surface $\Gamma_{i\sigma}$, as depicted in Fig. 2.2. The boundary value problem for the phase i , including respectively the mass and momentum conservation equations and the no-slip condition at the walls, reads

$$\nabla \cdot \mathbf{u}_i = 0, \quad \text{in } \Omega_i, \quad (2.2a)$$

$$\rho_i \left(\frac{\partial \mathbf{u}_i}{\partial t} + \mathbf{u}_i \cdot \nabla \mathbf{u}_i \right) = -\nabla p_i + \nabla \cdot \left[\mu_i \left(\nabla \mathbf{u}_i + (\nabla \mathbf{u}_i)^T \right) \right] + \rho_i \mathbf{g} \quad \text{in } \Omega_i, \quad (2.2b)$$

$$\mathbf{u}_i = 0 \quad \text{on } \Gamma_{i\sigma}. \quad (2.2c)$$

The complexity of the local pattern at the wall prohibits any numerical resolution of the system Eq. 2.2, or at least complicates it significantly. The derivation of an effective condition is generally conducted based on an approach of decomposition of the domain [5, 179, 84] in two sub-domains, with on one hand a bulk region and on the other hand a thin fluid layer on top of the rough surface. The decomposition domain method consists in approximating the flow locally within the fluid layer, which then allows to derive an effective mathematical relation at the interface between the two subdomains. The configuration with the two subdomains is illustrated in Fig. 2.3. The effective condition is determined following the resolution of a boundary value problem in a small unit-cell in the thin fluid layer. This small unit-cell corresponds to a representative pattern of the rough surface, as the one depicted in Fig. 2.4. The validity of this method relies on a number of assumptions, including a strict separation of scales between the fluid layer and the bulk flow, as well as the fact that the rough wall can be represented by an elementary pattern that repeats periodically. Such a method is actually close to the approaches involving the concept of *mesoscale*, i.e. an intermediate scale between the micro and the macroscale [122].

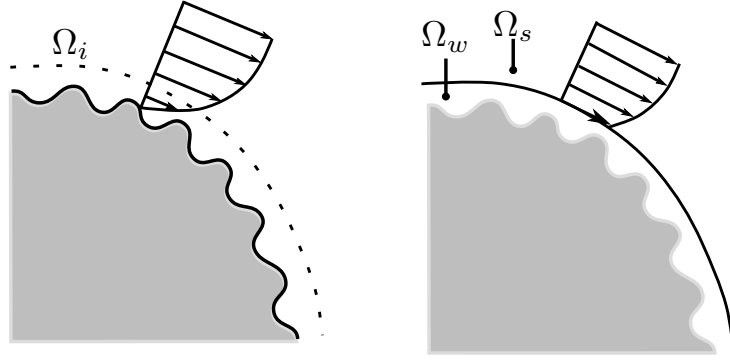


Figure 2.3 – Representation of the concept of effective boundary condition with slip.

In Chapter 3, we derive such a condition in a three-dimensional configuration using ideas of mapping from upscaling strategies in porous media. The effective condition, which is often referred as a Navier condition (or slip condition), reads

$$\mathbf{u}_s = \mathbf{M} \cdot \left[\mathbf{n} \cdot \left(\nabla \mathbf{u}_s + (\nabla \mathbf{u}_s)^T \right) \cdot (\mathbf{I} - \mathbf{nn}) \right] \text{ on } \Gamma_{ws}, \quad (2.3)$$

where \mathbf{M} is a second-order tensor. While the effective coefficient is often a scalar in the literature (slip length), the second-order tensor allows here to characterize anisotropic effects induced by the rough wall. The coefficients of \mathbf{M} are therefore interpreted as slip coefficients in the different directions. These coefficients are computed based on the resolution of local closure problems in a small unit-cell of the repetitive pattern of the rough wall, as the one depicted in the Fig. 2.4. The derivation of the closure problem that we suggest is further explained in Chapter 3.

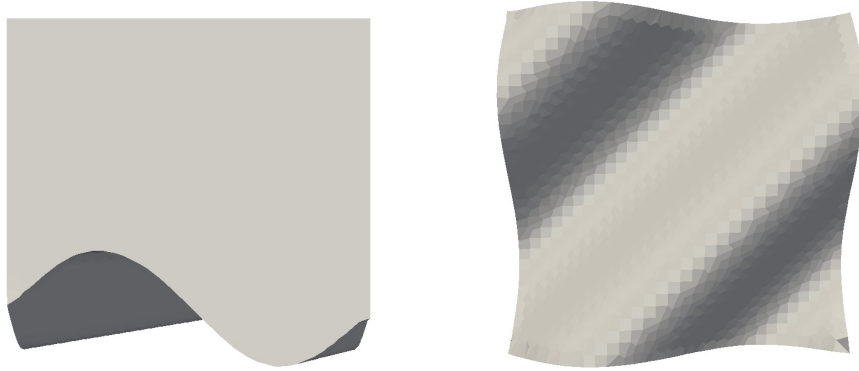


Figure 2.4 – Small domain over a roughness element - side and bottom views

2.3 Definitions and theorems

The averaging of the boundary value problem at the local scale relies on a number of definitions and theorems. This includes the definition of the spatial averaging operators, as well as the definition of a number of theorems and mathematical operations used in the volume averaging method.

2.3.1 Spatial and temporal averaging

The macroscale quantities are defined as the spatial averaging of the microscale quantities within an *averaging volume*. This averaging volume is chosen as a small representative part of the entire domain, called the representative elementary volume (REV). The REV is characterized by the fact that the averaged quantities remain spatially quasi-stationary. It is often conceived as a ball of radius r_0 , as illustrated in Fig. 2.5, whose center is located at a given point \mathbf{x} of the domain Ω . The REV is therefore defined as the domain $\mathcal{V}(\mathbf{x})$ of volume V . A given position within the REV is located by a vector \mathbf{y}_i , which is expressed in a coordinate system whose origin is placed at the center \mathbf{x} . Strictly speaking, the definition of the REV is not the same whether the porous medium is ordered or disordered. For a disordered porous medium, as this is the case in the Fig. 2.5, the radius of the REV must verify the following hierarchy of scales

$$l \ll r_0 \ll L, \quad (2.4)$$

while for an ordered medium with a purely periodic unit-cell, as this is the case in the geometry of structured packing, the following condition applies

$$l \leq r_0 \ll L. \quad (2.5)$$

In the two cases, r_0 is not necessarily chosen as the minimal radius that allows to respect Eqs 2.4 and 2.5 respectively. In other words, the REV is not necessarily chosen as the smallest volume that is representative of the domain Ω . In practical applications, however, it is relevant to limit the computational cost and therefore to limit the size of the REV. For an ordered medium, the size of the minimal REV can be reduced to a simple unit-cell ($l = r_0$) for some specific processes (linear processes, ex. Stokes flow, diffusion). The size of the REV for ordered media is also a well-known question of interest in case of high Reynolds flows and for multiphase flows. This is discussed in the recent works of Jin et al. (2015) [88] and Agnaou et al. [7] (2016), for high Reynolds one-phase flows. This is also an important issue in the present work as the distillation process involves a high Reynolds two-phase flow in an ordered medium.

Further discussion on the concept of REV is available in Davit et al. (2013) [42] and in Davit and Quintard (2017) [44].

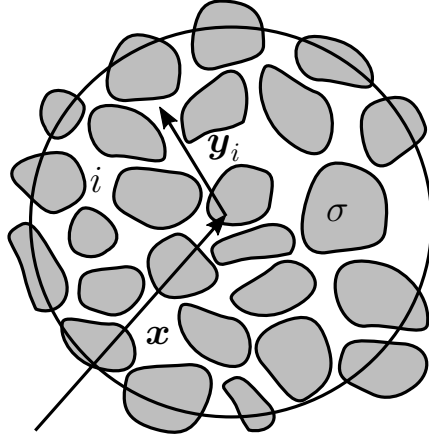


Figure 2.5 – Representation of the representative elementary volume (REV) of the medium

The fluid phase i in Fig. 2.5 occupies the domain $\mathcal{V}_i(\mathbf{x})$, of volume V_i , which is included in the domain $\mathcal{V}(\mathbf{x})$. The volume fraction of the fluid phase, ε_i , is therefore defined as

$$\varepsilon_i = \frac{V_i}{V}. \quad (2.6)$$

In case of one-phase flows, the definition of the volume fraction ε_i is also the definition of the porosity ε of the medium, since $V_i = V_{\text{void}}$

$$\varepsilon = \frac{V_{\text{void}}}{V}. \quad (2.7)$$

In case of multi-phase flows, the saturation S_i of a phase i is defined such that

$$\varepsilon_i = \frac{V_{\text{void}}}{V} \frac{V_i}{V_{\text{void}}} = \varepsilon S_i. \quad (2.8)$$

We define now the spatial and temporal averaging operators. Strictly speaking, the filtering operation of a field ψ_i consists in a convolution product between a kernel function and the field ψ_i . Such an operator generalizes the concept of filtering compared to classical average operators. It is shown to be required in case of purely periodic or quasi-periodic media [137, 136, 44], although it is rarely used. Indeed, the standard definition of the spatial averaging potentially generates anomalous mathematical behaviors when considering Taylor series in the volume averaging method, for instance non-differentiable fields. This is not acceptable as the objective is to construct a system of partial differential equations on the averaged fields. The idea is therefore to choose the adequate kernel function of the convolution that smoothes the behavior of the macroscale fields. Further details can be found in [44] (2017). In this work, for convenience in practical engineering, we use more standard definitions. Two definitions of spatial averaging are utilized in the volume averaging method. The *superficial average*, or phase average of the quantity ψ_i is defined as

$$\langle \psi_i \rangle(\mathbf{x}) = \frac{1}{V} \int_{\mathcal{V}_i(\mathbf{x})} \psi_i dV. \quad (2.9)$$

The superficial average of a velocity field, $\langle \mathbf{u}_i \rangle$, is also sometimes referred as the filtration velocity. The

intrinsic average is defined as

$$\langle \psi_i \rangle^i(\mathbf{x}) = \frac{1}{V_i} \int_{\mathcal{V}_i(\mathbf{x})} \psi_i dV. \quad (2.10)$$

The two definitions are linked through

$$\langle \psi_i \rangle = \varepsilon_i \langle \psi_i \rangle^i. \quad (2.11)$$

The surface average on a surface i, j , denoted $\langle \rangle_{ij}$, is also defined as

$$\langle \psi_i \rangle_{ij}(\mathbf{x}) = \frac{1}{\Gamma_{ij}} \int_{\Gamma_{ij}(\mathbf{x})} \psi_i d\Gamma. \quad (2.12)$$

Temporal fluctuations can also be smoothed out through a temporal averaging. The temporal average of the field $\psi_i(\mathbf{x}, t)$ is defined as

$$\overline{\psi}_i(\mathbf{x}) = \frac{1}{\Delta T} \int_{t-\frac{\Delta T}{2}}^{t+\frac{\Delta T}{2}} \psi_i(\mathbf{x}, \tau) d\tau, \quad (2.13)$$

where ΔT is the integration interval.

2.3.2 Theorems for the volume averaging method

The volume averaging method relies a number of spatial and temporal averaging theorems which are frequently used. These theorems are required as the spatial and temporal derivatives in the mathematical problem at pore-scale become integrals of derivatives as one applies the definitions introduced in the previous section. The spatial averaging of a gradient reads for instance $\langle \nabla \psi_i \rangle$, while one wants to express the mathematical system at macroscale in terms of $\langle \psi_i \rangle$ or $\langle \psi_i \rangle^i$. The point is therefore to interchange differentiation and integration. The averaging and gradient operators are interchanged using

$$\langle \nabla \psi_i \rangle = \nabla \langle \psi_i \rangle + \frac{1}{V} \int_{\Gamma_i} \mathbf{n}_i \psi_i d\Gamma. \quad (2.14)$$

This theorem was introduced independently by Marle (1967) [115] for a one-phase flow in porous media and by Whitaker (1967) [184] for the study of dispersion in porous media. Other demonstrations have been proposed later by Howes and Whitaker (1985) [80] and Quintard and Whitaker [138].

The theorem Eq. 2.14 leads to a relationship which is used extensively in the volume averaging method

$$\nabla \varepsilon_i = -\frac{1}{V} \int_{\Gamma_i} \mathbf{n}_i d\Gamma. \quad (2.15)$$

It is obtained by applying the theorem to a scalar function ψ_i that is 1 in \mathcal{V}_i and 0 everywhere else. The relationship holds whether the phase i is a one-phase flow or part of a multiphase flow. In this latter case, the interface Γ_i is the sum of the interfaces with the phase i , i.e. for instance $\Gamma_i = \Gamma_{i\sigma} \cup \Gamma_{ij}$ for a two-phase flow i, j .

Similarly, the averaging theorem for a divergence operator reads

$$\langle \nabla \cdot \psi_i \rangle = \nabla \cdot \langle \psi_i \rangle + \frac{1}{V} \int_{\Gamma_i} \mathbf{n}_i \cdot \psi_i d\Gamma. \quad (2.16)$$

The theorem of spatial averaging for a temporal derivative differs whether one considers a one-phase flow or a multiphase flow. Considering a two-phase flow i, j , it reads

$$\left\langle \frac{\partial \psi_i}{\partial t} \right\rangle = \frac{\partial \langle \psi_i \rangle}{\partial t} - \frac{1}{V} \int_{\Gamma_{ij}} \mathbf{n}_i \cdot \mathbf{w}_{ij} \psi_i d\Gamma, \quad (2.17)$$

where \mathbf{w}_{ij} is the velocity of the interface Γ_{ij} and where $\mathbf{w}_{i\sigma} = 0$ (non-deformable solid matrix σ). For a one-phase flow i , the theorem Eq. 2.17 reduces to

$$\left\langle \frac{\partial \psi_i}{\partial t} \right\rangle = \frac{\partial \langle \psi_i \rangle}{\partial t}. \quad (2.18)$$

Again, by applying this theorem to a scalar function ψ_i that is 1 in \mathcal{V}_i and 0 everywhere else, a useful relationship can be derived

$$\frac{\partial \varepsilon_i}{\partial t} = \frac{1}{V} \int_{\Gamma_{ij}} \mathbf{n}_i \cdot \mathbf{w}_{ij} d\Gamma. \quad (2.19)$$

2.3.3 Decomposition in average plus perturbations

The volume averaging method uses extensively an important concept which is the decomposition of the local quantity $\psi_i(\mathbf{x})$ in an averaged part and a perturbation

$$\psi_i(\mathbf{x}) = \langle \psi_i \rangle^i(\mathbf{x}) + \tilde{\psi}_i(\mathbf{x}). \quad (2.20)$$

This decomposition is introduced by Gray [63] (1975). A slightly different definition was introduced earlier by Whitaker [185] (1969), using the superficial average $\langle \psi_i \rangle$ instead of the intrinsic average, but the decomposition Eq. 2.20 is usually preferred. An illustration is given in Fig. 2.6.

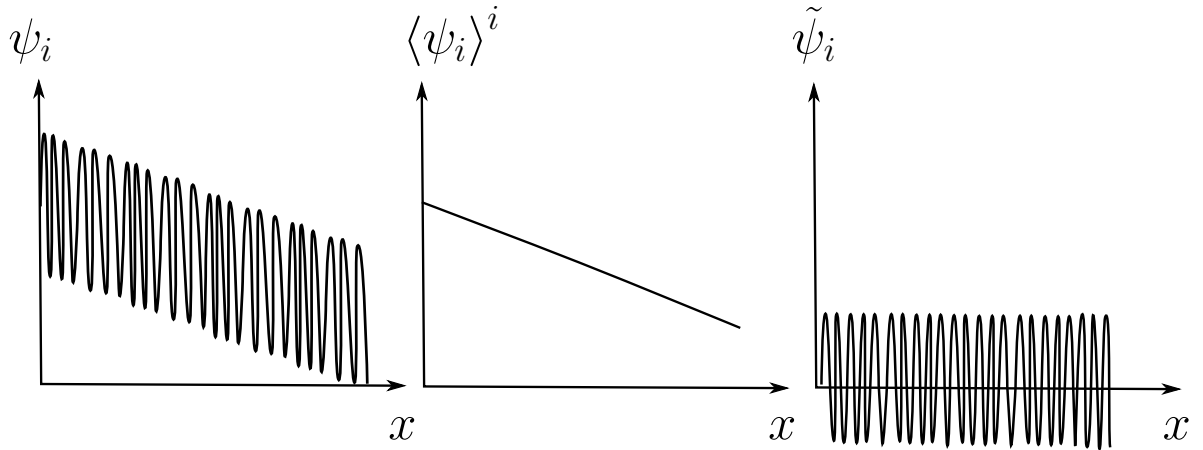


Figure 2.6 – Illustration of the average plus perturbation decomposition. Left: pore-scale signal ; middle: averaged component ; right: perturbations.

This decomposition is used to distinguish the macroscale variations of $\langle \psi_i \rangle^i$ from the microscale variations of $\tilde{\psi}_i$. This especially allows to evaluate the order of magnitudes of certain terms and to simplify the averaged

equations. For instance, in the hypothesis of a clear separation of scales, it is generally assumed that the spatial frequencies of $\langle \psi_i \rangle^i$ are much smaller than those of $\tilde{\psi}_i$. This assumption also leads to the following important approximation

$$\langle \langle \psi_i \rangle^i \rangle^i \sim \langle \psi_i \rangle^i, \quad (2.21)$$

which is also equivalent to

$$\langle \tilde{\psi}_i \rangle^i \sim 0. \quad (2.22)$$

2.4 The method of volume averaging

As evocated earlier, the volume averaging method relies on the spatial averaging of the mathematical problem at pore-scale. The method leads to a set of partial differential equations at the macroscale, which involves a number of effective parameters containing the *filtered information*. These effective parameters make the link between the microscale and the macroscale and are determined through the computation of *closure problems*. The technique relies on sequential steps which can be enumerated as follows

1. Definition of the boundary value problem at the microscale.
2. Averaging of the boundary value problem and decomposition in “average-plus-perturbation”.
3. Derivation of a boundary value problem on the perturbations, using assumptions on the times and length scales for the process under concern.
4. Build approximate relationships for the perturbations.
5. Close the set of equation at macroscale.

1 - Definition of the boundary value problem The rigorous definition of the boundary value problem at pore-scale is very important as it affects the whole procedure. This question was discussed in section 2.2. The boundary conditions especially play a central role in the procedure as they lead to the closure relationships between the micro and the macroscale (see step 4).

2 - Averaging Once the BVP is defined, the averaging operators, the theorems of spatial averaging, as well as the decomposition in average-plus-perturbation are used to establish a new mathematical system at the macroscale. At this stage, this system involves surface integrals on the perturbations, for the interfacial effects between the solid structure and fluids or between different fluids. These integral terms will be the focus of attention for the closure. The following term for instance characterizes the viscous shear-stress and the pressure force at the interface $\Gamma_{i\sigma}$ between a one-phase flow and a solid structure

$$\frac{1}{V_i} \int_{\Gamma_{i\sigma}} \mathbf{n}_{i\sigma} \cdot \left[-\tilde{p}_i \mathbf{I} + \mu_i \left(\nabla \tilde{\mathbf{u}}_i + (\nabla \tilde{\mathbf{u}}_i)^T \right) \right] d\Gamma. \quad (2.23)$$

3 - Derivation of a problem on the perturbations At this stage, the set of equation at the macroscale still involves quantities from the microscale (perturbations, for instance \tilde{p}_i , $\tilde{\mathbf{u}}_i$). The closure is achieved by building relationships for the perturbations as function of the quantities from the macroscale (averaged field). To this end, the strategy consists in studying the boundary value problem that governs the perturbations

at the pore-scale. This BVP is obtained by subtracting the macroscale system of step 2 from the initial boundary value problem. This is roughly illustrated with the relation

$$\tilde{\mathbf{u}}_i = \mathbf{u}_i - \langle \mathbf{u}_i \rangle^i. \quad (2.24)$$

The resulting problem - BVP of the perturbations - still involves a number of averaged quantities, most often at the boundary conditions. These terms actually reflect the exchange of information between the microscale and the macroscale. This is also these terms which lead to the closure.

4 - Approximate representation of the perturbations So far, the step 2 provided a volume-averaged system which is *unclosed*, as it involves averaged quantities and perturbations. Then the step 3 provided a boundary value problem for the perturbations, which still involve some terms from the macroscale. These terms are now seen as *source terms* in the problem on the perturbations. For a linear mathematical problem, it is therefore allowed to build a linear approximation of the perturbations, which for instance reads

$$\tilde{\mathbf{u}}_i = \mathbf{A} \cdot \langle \mathbf{u}_i \rangle^i, \quad (2.25)$$

if $\langle \mathbf{u}_i \rangle^i$ is the macroscopic source term at play. The variable \mathbf{A} is called the closure variable, or mapping variable.

5 - Closed form at macroscale By establishing relationships between the perturbations and the terms at the macroscale, the averaged system from step 2 is therefore closed. It remains however to determine the closure variables that were introduced in the approximation of the perturbations. This is done by introducing the approximate relationships, for instance Eq. 2.25, in the boundary value problem on the perturbations (step 3). By doing so, one now establishes a boundary value problem on the closure variables. This problem is the so-called closure problem. This problem is solved on a spatially periodic unit-cell, which is assumed to represent the porous medium under concern.

Part I

Monophasic modeling

Chapter 3

Gas phase as a one-phase flow: impact of a rough surface

Contents

3.1	Introduction	29
	Paper: Modeling flow in porous media with rough surfaces: effective slip boundary conditions and application to structured packings	32
3.2	Introduction	33
3.3	Derivation of an effective slip condition	34
3.3.1	Micro-scale transport equations	34
3.3.2	Domain decomposition and effective slip	35
3.4	Upscaling at the Darcy-scale via volume averaging	39
3.4.1	Notations	39
3.4.2	Temporal averaging	39
3.4.3	Spatial averaging	40
3.5	Results	42
3.5.1	Methods	42
3.5.2	Case 1: Application to a channel with sinusoidal walls	45
3.5.3	Case 2: Application to an array of rough cylinders	46
3.5.4	Case 3: Application to structured packings	52
3.6	Conclusion	58

3.1 Introduction

The objective of this chapter is to characterize the flow of the gas phase, i.e. to predict both its distribution in the structure and the global pressure drop in the distillation column. The analysis is limited so far to moderate Reynolds numbers, which corresponds to the pre-loading regime in the distillation process. This regime is characterized by a low interaction between the gas and the liquid phase, meaning no significant variation of the liquid film thickness, and no dispersion of the liquid phase in droplets. The modeling strategy relies on the assumption that the thin film can be treated as a *rigid wall*. This assumption is justified by the high ratio between the fluid properties - density, viscosity, and by the strong contrast of the flow rates. It is a method frequently used in the literature [28, 163, 141], as it greatly simplifies the system by decoupling to some extent the resolution of the gas and liquid flows.

The focus is placed here on an issue that has not been studied much in the literature, which is the impact of the hydrodynamic instabilities at the surface of the liquid film on the flow of the gas phase. As referred in section 1.1.4, the film is characterized by waves travelling under the form of soliton-like waves [94]. These trains of waves - which are here seen as *surface roughnesses* - potentially induce significant dissipation effects that must be estimated carefully. The notion of surface roughness can actually be extended to roughnesses of any type, including the small textures sometimes engineered at the surface of the corrugated sheets.

The analysis is developed in a paper which was published recently in Chemical Engineering Science. Beforehand, the modeling strategy is introduced with a special emphasis on the applicability of the method in our case.

Derivation of the effective boundary condition

The problem consists in an inertial, and even turbulent flow, over a three-dimensional rough surface in a highly permeable porous medium. The characterization of the roughness is complex as it involves a local pattern composed of a hump (the highest wave) and possibly small capillary waves, for instance in the case of film instabilities. It is therefore suggested to replace the complex surface by an effective smooth boundary condition, as introduced in section 2.2. This effective boundary replaces the rough wall and mimics its effects locally. It permits to avoid to resolve the flow around the roughnesses, which can represent a high numerical cost as the rough wall is made of complex rough patterns. The derivation of a smooth effective boundary condition has been proposed in the literature in a two-dimensional configuration [6, 179, 84], leading to the derivation of a Navier condition. Such a condition consists in a slip condition and is placed at an effective smooth surface that replaces the rough wall. Multiple methods were developed in the literature for the derivation of the effective condition, implying generally a decomposition of the domain in a bulk domain and a boundary layer over the rough wall [179]. This last method relies on the assumption of a separation of scales between the fields in the bulk flow and the fields in the fluid layer above the rough wall. This is the method used in this study. The effective condition which is derived holds for a three-dimensional pattern that repeats periodically, and reads

$$\mathbf{u}_s = \mathbf{M} \cdot \left[\mathbf{n} \cdot \left(\nabla \mathbf{u}_s + (\nabla \mathbf{u}_s)^T \right) \cdot (\mathbf{I} - \mathbf{nn}) \right] \quad \text{at } \Gamma_{ws}, \quad (3.1)$$

where \mathbf{u}_s is the velocity field in the bulk domain (s as slip) and where Γ_{ws} the interface between the bulk flow and the wall region. The parameter \mathbf{M} is a second-order tensor whose coefficients can be interpreted in terms of slip lengths, similarly to a classical 1D Navier condition. This effective condition can therefore be seen as an extension of the usual Navier condition for a three-dimensional rough pattern at the scale of the

rough wall. It accounts for a potential flow anisotropy induced by the roughness, through the second-order tensor \mathbf{M} . The coefficients of \mathbf{M} are determined by computing a local boundary value problem in the flow layer over a representative elementary pattern of the rough wall.

Given the effective condition Eq. 3.1, the resulting boundary value problem for the flow of the gas phase in the bulk domain consists in mass and momentum conservation equations for a laminar flow. It reads

$$\nabla \cdot \mathbf{u}_s = 0 \text{ in } \Omega_s, \quad (3.2a)$$

$$\rho_\gamma \left(\frac{\partial \mathbf{u}_s}{\partial t} + \mathbf{u}_s \cdot \nabla \mathbf{u}_s \right) = -\nabla p_s + \mu_\gamma \nabla^2 \mathbf{u}_s + \rho_\gamma \mathbf{g} \text{ in } \Omega_s, \quad (3.2b)$$

$$\mathbf{u}_s = \mathbf{M} \cdot \left[\mathbf{n} \cdot \left(\nabla \mathbf{u}_s + (\nabla \mathbf{u}_s)^T \right) \cdot (\mathbf{I} - \mathbf{nn}) \right] \text{ at } \Gamma_{ws}. \quad (3.2c)$$

Applicability of the effective boundary condition method

The decomposition domain method relies on a number of assumptions that must be analyzed carefully in order to understand to what extent it can be applied for practical applications. The constraints can be enumerated as follows

1. a clear separation of scales between the scale of the roughness and the pore-scale is required. Considering the thin liquid film in the distillation process, one estimates the size of the highest wave to be about 5×10^{-4} m and the pore-scale to be about 1×10^{-2} m. An order of magnitude therefore separates the size of the highest soliton and the size of the pore. Similar estimates may be obtained for the case of structured packings with rough sheets, since the size of the roughness is below the millimeter.
2. the rough wall is confined within the viscous boundary layer of the flow. This condition is true if the Reynolds number for the flow of the gas phase remains limited. This condition is not always true for soliton-like waves, but it holds in the laminar regime. This limitation is shown in the paper as a discrepancy is observed for increasing flow rates between the solution obtained from the effective method and the exact solution. Further theoretical developments are therefore required here in order to derive an effective condition which would account for additional inertial effects for a broader range of Reynolds numbers.
3. the roughness is made of a single pattern that repeats periodically. This assumption allows to compute the effective parameter \mathbf{M} over a single element of roughness. It is verified in the distillation process for packings made of rough sheets and also for film roughnesses as the train of waves propagates periodically.
4. the wavelength of the roughness profile must be much smaller than the radius of curvature of the geometry of corrugated sheet. This condition allows to solve the closure problem once for a flat surface and to map it onto the curved surface. This condition imposes to consider train of waves with moderate wavelengths.

Use of the volume averaging method

The second step of the method consists in volume averaging the effective boundary value problem Eq. 3.2. This method follows the methodology of the volume averaging method detailed in the previous chapter.

It leads to the development of a generalized Darcy's law for an inertial flow, also referred to as a Darcy-Forchheimer law. The mass and momentum balances at the macroscale respectively read

$$\nabla \cdot \langle \mathbf{u}_\gamma \rangle = 0, \quad (3.3)$$

$$\langle \mathbf{u}_\gamma \rangle = -\frac{\mathbf{K}_s}{\mu_\gamma} \cdot (\nabla \langle p_\gamma \rangle^\gamma - \rho_\gamma \mathbf{g}) - \mathbf{F}_s \cdot \langle \mathbf{u}_\gamma \rangle, \quad (3.4)$$

where γ refers to the gas phase in the paper. The two effective parameters \mathbf{K}_s and \mathbf{F}_s are respectively the intrinsic permeability tensor and the inertial correction tensor, which are computed numerically via the resolution of a closure problem over a representative cell of the domain Ω_s with spatially periodic conditions. Through these parameters, the momentum transport at the continuum scale includes the effects of the roughness. The method is applied for two 2D configurations including a rough channel and an array of rough beads, and for a 3D geometry of structured packings. In this last configuration, the REV of the structure is assumed to be a single unit-cell of structured packing. This question is discussed in the paper. Further, the analysis is conducted from the Darcean regime and for increasing flow rates up to the onset of the unsteady regime.

Modeling flow in porous media with rough surfaces: effective slip boundary conditions and application to structured packings

Sylvain Pasquier, Michel Quintard and Yohan Davit

Institut de Mécanique des Fluides de Toulouse (IMFT) - Université de Toulouse, CNRS-INPT-UPS, Toulouse France

Published 11 February 2017

Abstract

Understanding and modeling flows in columns equipped with structured packings is crucial to enhance the efficiency of many processes in chemical engineering. As in most porous media, an important factor that affects the flow is the presence of rough surfaces, whether this roughness has been engineered as a texture on the corrugated sheets or is the result of hydrodynamic instabilities at the interface between a gas and a liquid phase. Here, we develop a homogenized model for flows in generic porous media with rough surfaces. First, we derive a tensorial form of an effective slip boundary condition that replaces the no-slip condition on the complex rough structure and captures surface anisotropy. Second, a Darcy-Forchheimer model is obtained using the volume averaging method to homogenize the pore-scale equations with the effective slip condition. The advantage of decomposing the upscaling in these two steps is that the effective parameters at the Darcy-scale can be calculated in a representative volume with smooth boundaries, therefore considerably simplifying mesh construction and computations. The approach is then applied to a variety of geometries, including structured packings, and compared with direct numerical solutions of the flow to evaluate its accuracy over a wide range of Reynolds number. We find that the roughness can significantly impact the flow and that this impact is accurately captured by the effective boundary condition for moderate Reynolds numbers. We further discuss the dependence of the permeability and generalized Forchheimer terms upon the Reynolds number and propose a classification into distinct regimes.

3.2 Introduction

Structured packings are widely used in industrial processes for phase separation such as distillation or post-combustion CO_2 capture. These often consist of parallel corrugated sheets packed together in a way that maintains a large void fraction and surface area, therefore maximizing transfers between phases. Prediction of the pressure drop in columns equipped with such packings is a major concern for users and manufacturers alike. Recent developments in computational fluid dynamics (CFD), along with the advent of high performance computing, are providing the necessary basis to better understand flow in these complex structures and, ultimately, to optimize their design.

Column-scale computations of the flow at the pore-scale, however, is still not feasible. Most simulations focus on a restricted part of the domain, for instance a representative elementary volume (REV) of structured packings. Calculations over a REV are useful to understand the micro-scale physics and evaluate effective parameters that apply to the packing and the column-scale, while being small enough to allow for accurate simulations resolving the smallest scales of the flow. This strategy, inspired from approaches used in porous media sciences, was first introduced by Petre *et al.* in [129], who modeled the gas flow within four REV in the viscous and turbulent regimes. Once effective parameters, such as the permeability tensor, have been evaluated in this REV, the whole column can be treated as a homogenized porous medium. For instance, momentum transport at the column-scale can be described by Darcy-Forchheimer’s law, which can then be solved numerically on a coarse mesh. This approach yields results that are generally more accurate than earlier empirical correlations, such as those proposed by Brunnazi and Paglianti [30], Olujic [123] and Rocha *et al.* [146].

A recent contribution that uses the porous media approach to study flow and pressure drop in gas-liquid distillation columns is the work by Mewes *et al.* [114]. The authors introduced a flow resistance tensor that depends on the velocity magnitude, which can be used to predict the pressure drop for any flow direction. Soullaine and Quintard [163] further investigated anisotropy generated at the micro-scale by inertial flow and proposed an upscaling methodology to determine a correction tensor in the Darcy-Forchheimer’s law. Their conclusion, for 45° inclined corrugations, is that the non-diagonal terms in the effective second-order tensors can be neglected in comparison to the diagonal ones.

In addition to inertial effects and anisotropy, an important factor that affects the gas pressure drop in these columns is the potential presence of rough surfaces. For instance, the corrugated sheets may be textured to increase the efficiency of distillation processes [118] or hydrodynamic instabilities may develop at the liquid-gas interface as a result of the steep flowing angle of the film and the high contrast in velocity between the two phases [191, 49]. Those instabilities, which can manifest as soliton structures, are likely to generate dramatic changes of the pressure drop and contribute to the flooding of the column for a large flow rate of the gas phase [172]. Based on the contrasts in density, viscosity and velocity between the two phases, one often assumes that the gas flow can be treated as a single-phase flow over a rigid rough surface. For this to be accurate, the velocity in the gas phase must be much larger than the velocity in the liquid phase so that we can use a no-slip boundary condition (see also [178] for additional details). The trains of waves can then be treated as a surface roughness for the pressure drop in the gas-phase. This is also consistent with previous works that treat the pressure drop of the gas phase *a posteriori*, by considering the liquid film hold-up for the calculation of the interstitial gas velocity [141].

Here, we propose a multi-scale approach to evaluate the impact of rough surfaces on the macro-scale properties of momentum transport. We develop a systematic methodology for a generic porous medium, independently of the initial nature of the roughness, which is based on the idea that the rough surface can be replaced by an effective boundary condition over a smooth surface, to reduce computation time and limit

issues with the mesh construction. The paper is organized as follows. In Section 2, the pore-scale system of equations is described, along with the domain decomposition method leading to the derivation of an *effective slip boundary condition* that replaces the rough surface. In Section 3, we upscale these equations using the *volume averaging with closure technique* to obtain the macro-scale equations that describe momentum transport along with the closure problems that are used to calculate effective parameters. In Section 4, we apply this generic approach to a variety of geometries including a representative element of structured packings. We evaluate the accuracy of our approach and the impact of the roughness on the effective parameters. Finally, in Section 5, we discuss the limitations of the framework and provide ideas for future improvements.

3.3 Derivation of an effective slip condition

As discussed in the Introduction, the goal of this paper is to develop an upscaling methodology that can be used to evaluate the impact of rough surfaces in porous media. To this end, we will use the method of volume averaging with closure, which has been widely documented since the early work of Whitaker [186]. This method usually yields a macro-scale model involving effective parameters that are computed by solving closure problems over a REV. An important implication of rough surfaces is that computations of the closure problems over a REV may not be tractable if the characteristic amplitude, \mathcal{A} , and wavelength, λ , of the roughnesses are small compared to the pore-scale, l . If this is the case, i.e. if $\frac{\mathcal{A}}{l} \ll 1$ and $\frac{\lambda}{l} \ll 1$, we may need an extremely fine mesh to accurately capture the flow over the roughness, especially if the Reynolds number is larger than unity. Here, we solve this issue by developing an alternative formulation of the pore-scale flow problem, transforming the rough surface into a smooth one. The no-slip condition applying to the complex rough surface is replaced by an effective boundary condition over a smooth surface, therefore limiting the need for a very fine mesh in the vicinity of the surface.

3.3.1 Micro-scale transport equations

We consider the flow of an incompressible fluid γ , within a porous structure with rough walls, as shown in Fig 3.1. Mass and momentum balance are described via the Navier-Stokes equations as

$$\nabla \cdot \mathbf{u}_\gamma = 0, \quad (3.5a)$$

$$\rho_\gamma \left(\frac{\partial \mathbf{u}_\gamma}{\partial t} + \mathbf{u}_\gamma \cdot \nabla \mathbf{u}_\gamma \right) = -\nabla p_\gamma + \nabla \cdot \left[\mu_\gamma \left(\nabla \mathbf{u}_\gamma + (\nabla \mathbf{u}_\gamma)^T \right) \right] + \rho_\gamma \mathbf{g}, \quad (3.5b)$$

$$\mathbf{u}_\gamma = 0 \text{ on } \Gamma_{\gamma\sigma}, \quad (3.5c)$$

where \mathbf{u}_γ , p_γ are the velocity and pressure fields in the rough domain, Ω_γ . ρ_γ and μ_γ are the density and viscosity of the phase γ .

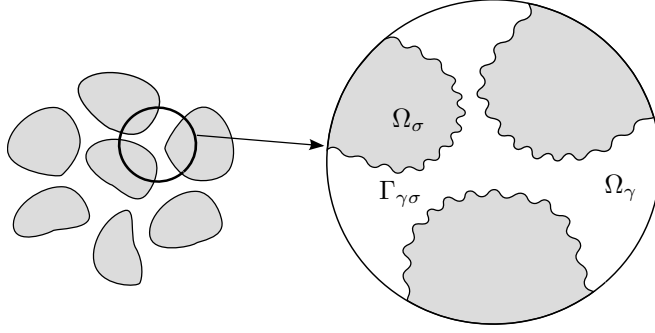


Figure 3.1 – Schematics of a porous medium with rough walls. Ω_σ and Ω_γ are, respectively, the solid and fluid phases. $\Gamma_{\gamma\sigma}$ is the rough surface of the porous medium.

The first step of our methodology is to replace Eqs (3.5a–3.5c) in Ω_γ and on $\Gamma_{\gamma\sigma}$ by an effective mathematical system in an effective domain Ω_s and Γ_{ws} , where the subscript s means “slip”.

3.3.2 Domain decomposition and effective slip

We consider the domain $\Omega_\gamma \subset \mathbb{R}^m$, ($m = 2$ or 3), with the rough boundary $\Gamma_{\gamma\sigma} \subset \mathbb{R}^{m-1}$, as presented in Fig 3.2. The roughness is characterized by an amplitude, \mathcal{A} , and a wavelength, λ . We further use l to represent a characteristic size of the pores. Similarly to the approaches of Achdou *et al.* [5, 6], Veran *et al.* [180] and Introïni *et al.* [84], we decompose the fluid domain in two subdomains: one close to the rough wall, Ω_w , and one that represents the center of the pores, Ω_s . Therefore, we have $\Omega_\gamma = \Omega_w \cup \Omega_s$ and the two subdomains are separated by the surface Γ_{ws} , as illustrated in Fig 3.2. To derive an *effective* boundary condition applying to Γ_{ws} , Achdou *et al.* used a technique based on a two-scale asymptotic expansion [5]. This method is also used in the works of Barrenechea *et al.* [17], Bassion and Gerard-Varet [18], and Mikelić and Devigne [111]. Veran *et al.* and Introïni *et al.* used a different method based on the resolution of a local boundary problem in the small representative domain Ω_{w_i} , also using ideas similar to those of porous media homogenization approaches. Here, we present briefly the main ideas of this last approach with a particular focus on the tensor formalism for the slip length. More detailed developments are described in [180, 84].

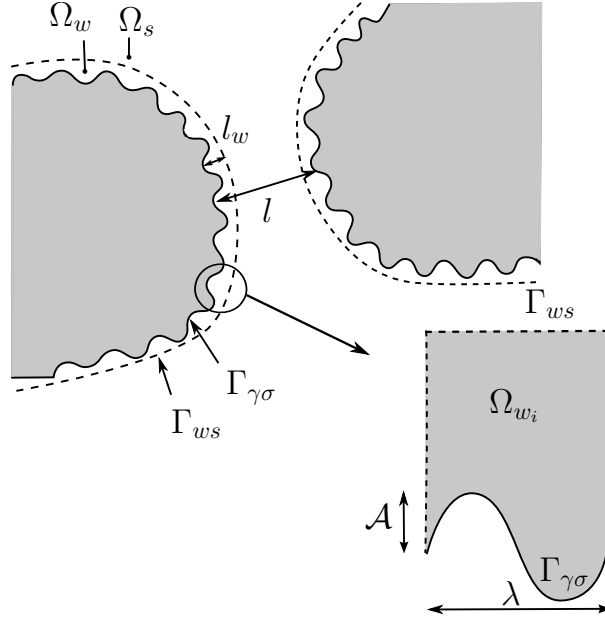


Figure 3.2 – Schematics of the multi-domain decomposition. Γ_{ws} and Ω_s refer to the effective surface and domain, respectively. Ω_w is the subdomain that contains the rough wall and Ω_{w_i} is the local domain over a rough element. l_w is the characteristic distance from the rough pattern to the effective surface and l is the characteristic length scale of the pore. \mathcal{A} and λ are the amplitude and wavelength of the roughness.

The main assumptions of the effective boundary condition are as follows:

- The impact of the roughness on the flow is localized to a viscous boundary layer above the roughness. This is correct when the Reynolds number is sufficiently low or in the fully turbulent regime if the roughness is smaller than the viscous sublayer [165].
- The interface Γ_{ws} is placed sufficiently far above the roughness, so that the pressure and velocity fluctuations due to the roughness vanishes on Γ_{ws} .
- The roughness is much smaller than the pores, $l_w \ll l$. This means that the fields in the sub-domain Ω_w vary on the length scale l_w , whereas the fields in the bulk domain Ω_s vary on a much larger length scale, l . The wavelength, λ , of the roughnesses is much smaller than the radius of curvature of the smoothed interface $1/\kappa$, so that the closure problem can be solved once for a flat surface and mapped onto the curved surface.
- The subdomain Ω_w can be represented locally by a periodic structure made of cells denoted Ω_{w_i} , as shown in Fig 3.2.

The first step of the method consists in building an approximate solution of the flow close to the rough wall, in the subdomain Ω_w . Following ideas of *mapping* used in porous media sciences and homogenization techniques for the estimation of spatial or temporal deviations from averaged quantities, (p_w, \mathbf{u}_w) is mapped linearly to the tangential components of the shear stress vector on Γ_{ws} as

$$p_w(\mathbf{x}) = \mu_\gamma \mathbf{a}(\mathbf{x}) \cdot \left[\mathbf{n} \cdot \left(\nabla \mathbf{u}_s + (\nabla \mathbf{u}_s)^T \right) \cdot (\mathbf{I} - \mathbf{nn}) \Big|_{\Gamma_{ws}} \right] \text{ in } \Omega_{w_i}, \quad (3.6)$$

$$\mathbf{u}_w(\mathbf{x}) = \mathbf{A}(\mathbf{x}) \cdot \left[\mathbf{n} \cdot \left(\nabla \mathbf{u}_s + (\nabla \mathbf{u}_s)^T \right) \cdot (\mathbf{I} - \mathbf{nn}) \Big|_{\Gamma_{ws}} \right] \text{ in } \Omega_{w_i}, \quad (3.7)$$

where (\mathbf{a}, \mathbf{A}) are solutions of a mathematical problem that is solved over the representative cell Ω_{w_i} . The normal vector \mathbf{n} on Γ_{ws} is uniform and oriented from the domain Ω_w to the domain Ω_s . In these equations, we consider that the couple (p_w, \mathbf{u}_w) is mapped to the tangential components, $\mathbf{n} \cdot \left(\nabla \mathbf{u}_s + (\nabla \mathbf{u}_s)^T \right) \cdot (\mathbf{I} - \mathbf{nn})$ of the shear stress vector $\mathbf{n} \cdot \left(\nabla \mathbf{u}_s + (\nabla \mathbf{u}_s)^T \right)$ on Γ_{ws} , assuming that the normal component of the velocity can be neglected under the conditions stated above. We also consider that variations of $\mathbf{n} \cdot \left(\nabla \mathbf{u}_s + (\nabla \mathbf{u}_s)^T \right) \cdot (\mathbf{I} - \mathbf{nn})$ on Γ_{ws} occur on a lengthscale that is much larger than the wavelength of the roughness, λ . This is because the creeping flow in Ω_w implies that variations induced by the roughnesses rapidly attenuate away from the wall (see [92] for analytical solution showing an exponential decrease). The shear stress vector is therefore treated as approximately constant over each unit-cell and the point on Γ_{w_i} at which it is evaluated for the mappings Eqs 3.6 and 4.53 is not fundamentally important. As an example, we could map the velocities and pressures at point \mathbf{x} to the shear stress vector evaluated at point \mathbf{x}' , defined so that $\mathbf{x} - \mathbf{x}'$ and \mathbf{n} are collinear. We could also use the surface average of the stress vector evaluated at the nearest point on Γ_{ws} . In Eqs 3.6, 4.53 and in the remainder of this work, we use the generic notation $\mathbf{n} \cdot \left(\nabla \mathbf{u}_s + (\nabla \mathbf{u}_s)^T \right) \cdot (\mathbf{I} - \mathbf{nn}) \Big|_{\Gamma_{ws}}$ with the idea that locally, in each unit-cell, the stress vector can be treated as constant so that the mapping can be done to any point in Ω_w and any point on Γ_{ws} .

The corresponding local problem reads

$$\nabla \cdot \mathbf{A} = 0 \text{ in } \Omega_{w_i}, \quad (3.8a)$$

$$0 = -\nabla \mathbf{a} + \nabla^2 \mathbf{A} \text{ in } \Omega_{w_i}, \quad (3.8b)$$

$$\mathbf{A} = 0 \text{ on } \Gamma_{\gamma\sigma}, \quad (3.8c)$$

$$-\mathbf{an} + \mathbf{n} \cdot \left(\nabla \mathbf{A} + (\nabla \mathbf{A})^T \right) = \mathbf{I} - \mathbf{nn} \text{ on } \Gamma_{ws}, \quad (3.8d)$$

$$\mathbf{a}(\mathbf{r}) = \mathbf{a}(\mathbf{r} + \lambda \mathbf{e}_i) \quad i = 1, m-1, \quad (3.8e)$$

$$\mathbf{A}(\mathbf{r}) = \mathbf{A}(\mathbf{r} + \lambda \mathbf{e}_i) \quad i = 1, m-1, \quad (3.8f)$$

where λ is the wavelength and \mathbf{e}_i are the two orthonormal unit vectors for directions tangential to the surface Γ_{ws} . Here, the transpose of the third-order tensor $(\nabla \mathbf{A})^T$ is defined as $\left[(\nabla \mathbf{A})^T \right]_{ijk} = \partial_j A_{ik}$ with $i, j, k \in \llbracket 1, m \rrbracket$ ($m = 2, 3$ in our calculations). Recalling the mapping of \mathbf{u}_w , Eq. 4.53, we can write at any point on Γ_{ws}

$$\mathbf{u}_w = \mathbf{A}|_{\Gamma_{ws}} \cdot \left[\mathbf{n} \cdot \left(\nabla \mathbf{u}_s + (\nabla \mathbf{u}_s)^T \right) \cdot (\mathbf{I} - \mathbf{nn}) \Big|_{\Gamma_{ws}} \right]. \quad (3.9)$$

As discussed before, for Γ_{ws} placed sufficiently far away from the rough wall, $\mathbf{A}|_{\Gamma_{ws}}$ is approximately constant in the tangential directions and may be computed as the surface average of the field \mathbf{A} over the interface Γ_{ws} of the periodic unit-cell.

Using the continuity of the velocities, $\mathbf{u}_s = \mathbf{u}_w$ on the interface Γ_{ws} , we then have the form of a generalized Navier condition, where $\mathbf{M} = \mathbf{A}|_{\Gamma_{ws}}$ is a second-order tensor that can be interpreted in terms of slip coefficients along the directions tangential to the interface,

$$\mathbf{u}_w = \mathbf{M} \cdot \left[\mathbf{n} \cdot \left(\nabla \mathbf{u}_s + (\nabla \mathbf{u}_s)^T \right) \cdot (\mathbf{I} - \mathbf{nn}) \Big|_{\Gamma_{ws}} \right] \text{ on } \Gamma_{ws}. \quad (3.10)$$

This parameter is also referred to as the mobility tensor in the work of Kamrin et al. [92].

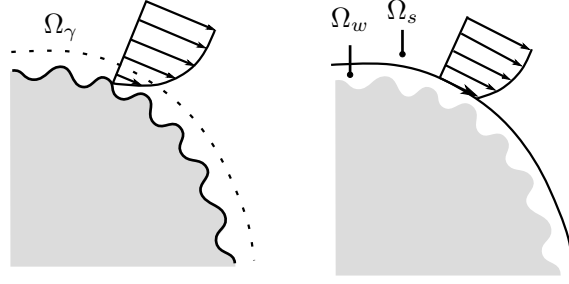


Figure 3.3 – Schematics of the rough domain Ω_γ , on the left-hand side, and the effective domain Ω_s , on the right-hand side.

The flow problem in Ω_s finally reads

$$\nabla \cdot \mathbf{u}_s = 0 \text{ in } \Omega_s, \quad (3.11a)$$

$$\rho_s \left(\frac{\partial \mathbf{u}_s}{\partial t} + \mathbf{u}_s \cdot \nabla \mathbf{u}_s \right) = -\nabla p_s + \nabla \cdot \left[\mu_\gamma \left(\nabla \mathbf{u}_s + (\nabla \mathbf{u}_s)^T \right) \right] + \rho_s \mathbf{g}, \quad (3.11b)$$

$$\mathbf{u}_s = \mathbf{M} \cdot \left[\mathbf{n} \cdot \left(\nabla \mathbf{u}_s + (\nabla \mathbf{u}_s)^T \right) \cdot (\mathbf{I} - \mathbf{nn}) \right] \text{ on } \Gamma_{ws}. \quad (3.11c)$$

Fig 3.3 shows the different domains and the change in boundary condition. We remark that the accuracy of the linear relation Eq. 3.11c between the velocity in the vicinity of the wall and the shear stress vector on Γ_{ws} will strongly depend on the type of flow. The solution is accurate for a Couette flow, but only roughly approximates the quadratic profile of a Poiseuille flow within Ω_w . In general, this implies that the error increases with the distance to the rough surface and that we must have $l_w \ll l$ in order to minimize the part of the flow that is linearly approximated. This aspect is further detailed in the computations section 3.5.2.

Finally, the position of Γ_{ws} can also be modified *a posteriori*, as first discussed by Veran et al. in [180]. Consistent with the first-order closure in Eqs 3.8, we write the first-order Taylor series expansion

$$\mathbf{u}_s(\mathbf{x}_2) = \mathbf{u}_s(\mathbf{x}_1) + (\mathbf{x}_2 - \mathbf{x}_1) \cdot \left(\nabla \mathbf{u}_s + (\nabla \mathbf{u}_s)^T \right) \Big|_{\mathbf{x}_1} + \mathcal{O}(\|\mathbf{x}_2 - \mathbf{x}_1\|^2), \quad (3.12)$$

with $\mathbf{x}_1 - \mathbf{x}_2$ the displacement of the interface and \mathbf{x}_1 the reference position corresponding to Eq 3.11c. If we move the interface in the normal direction, $\mathbf{x}_1 - \mathbf{x}_2 = \mathbf{n} \Delta x$, and if we consider that \mathbf{u}_s remains tangential, we can write

$$\mathbf{u}_s(\mathbf{x}_2) \simeq \mathbf{u}_s(\mathbf{x}_1) - (\Delta x \mathbf{I}) \cdot \left[\mathbf{n} \cdot \left(\nabla \mathbf{u}_s + (\nabla \mathbf{u}_s)^T \right) \Big|_{\mathbf{x}_1} \cdot (\mathbf{I} - \mathbf{nn}) \right]. \quad (3.13)$$

Injecting $\mathbf{u}_s(\mathbf{x}_1)$ from Eq 3.11c into Eq 3.13 yields

$$\mathbf{u}_s(\mathbf{x}_2) \simeq (\mathbf{M} - \Delta x \mathbf{I}) \cdot \left[\mathbf{n} \cdot \left(\nabla \mathbf{u}_s + (\nabla \mathbf{u}_s)^T \right) \cdot (\mathbf{I} - \mathbf{nn}) \right]. \quad (3.14)$$

This step, which is described in detail in [180] or [84], can impact the accuracy of the Navier-slip boundary condition (see also [180] or [84]), as we will demonstrate for a specific example later on. It is particularly useful in two-dimensional cases or isotropic configurations in order to derive an equivalent *effective no-slip* condition, which is obtained by choosing Δx so that $\mathbf{M} - \Delta x \mathbf{I} = 0$ in Eq. 3.14 (\mathbf{M} is a scalar in 2D). This specific position of the effective boundary is interesting, mostly for its simplicity of implementation in a computational framework. However, we emphasize that such a position does not exist in three-dimensional cases if the roughness is anisotropic. If this is the case, the slip lengths are different in all directions and a tensorial form of the Navier-condition is necessary.

3.4 Upscaling at the Darcy-scale via volume averaging

Now that we have derived an effective smooth condition that replaces the rough wall, we can further upscale the system of equations, Eqs 3.11, to obtain a homogenized system at the Darcy-scale. We use the method of volume averaging that has been utilized before to study this problem in the viscous and inertial regimes. In this approach, the partial differential equations at the micro-scale are averaged in space and approximate solutions for the velocity and pressure perturbations are determined using scaling arguments. When applied to Stokes equations, this process yields Darcy's law with a permeability tensor that can be calculated from the numerical resolution of a closure problem. Quasi-linearized Navier-Stokes equations can be treated in a similar manner, leading to an additional drag and a generalized Darcy-Forchheimer law [188] (generalized in the sense that anisotropy is included and that inertial terms are not necessarily quadratic). The development closely follows the early work of Whitaker [186] and the more recent work of Lasseux *et al.* [102] for the homogenization of a low-pressure gas phase in porous media with a similar slip condition on the walls, although tensorial in our case.

3.4.1 Notations

For a tensor ψ_i , where i is the phase, we define the superficial average of ψ_i at point \mathbf{x} as

$$\langle \psi_i \rangle (\mathbf{x}) = \frac{1}{|\mathcal{V}|} \int_{\mathcal{V}_i(\mathbf{x})} \psi_i(\mathbf{r}) \, d\mathbf{r}, \quad (3.15)$$

where $\mathcal{V}_i(\mathbf{x})$ (i can be s , γ or w for each corresponding domain) is the averaging volume centered at \mathbf{x} and $\mathcal{V}_i(\mathbf{x}) = \mathcal{V}(\mathbf{x}) \cap \Omega_i$. The intrinsic average is defined as

$$\langle \psi_i \rangle^i = \frac{1}{|\mathcal{V}_i|} \int_{\mathcal{V}_i} \psi_i \, d\mathbf{r}, \quad (3.16)$$

so that the two definitions are related by

$$\langle \psi_i \rangle = \phi_i \langle \psi_i \rangle^i, \quad (3.17)$$

where the volume fraction of the domain Ω_i , ϕ_i , is defined as

$$\phi_i = \frac{|\mathcal{V}_i|}{|\mathcal{V}|}. \quad (3.18)$$

We use the perturbation decomposition (see [185, 64])

$$\psi_i = \langle \psi_i \rangle^i + \tilde{\psi}_i, \quad (3.19)$$

where the deviation $\tilde{\psi}_i$ varies on a length scale l and the intrinsic average $\langle \psi_i \rangle^i$ varies on a length scale L , such that $l \ll r_0 \ll L$. We further require that (see e.g. [189])

$$\langle \tilde{\psi}_i \rangle \simeq 0. \quad (3.20)$$

3.4.2 Temporal averaging

For sufficiently high Reynolds numbers, when the flow becomes fully unsteady, a macroscopic formulation of momentum transport generally requires both spatial and temporal averaging. In theory, the order in which

these operators are applied is unimportant. The process should lead to the exact same results, whether the equations are first averaged in space or time. In practice, however, the combination of approximations that are used during upscaling often depends on the averaging order (see [47, 120] for further details). Here, we start by averaging the pore-scale equations in time.

When unsteady flow develops, we use a time averaging operator for the field $\phi(\mathbf{x}, t)$ defined as

$$\bar{\phi}(\mathbf{x}, t) = \frac{1}{\Delta T} \int_{t-\Delta T/2}^{t+\Delta T/2} \phi(\mathbf{x}, \tau) d\tau, \quad (3.21)$$

where ΔT is the integration interval. We also use a standard average plus perturbation decomposition as

$$\phi = \bar{\phi} + \phi'. \quad (3.22)$$

With these, we can average Eqs 3.11 in time and obtain Reynolds stresses in the equations, a detailed analysis of this operation is given in [47]. In this study, we primarily concentrate on regimes for which the time fluctuations are of low amplitude. Therefore, we neglect terms involving the product $\mathbf{u}'\mathbf{u}'$. In the fully turbulent regime, further theoretical developments should account for transient effects at the macro-scale. One way to deal with this issue could be an approach similar to that in [163], where the system is first averaged in time using a standard closure for the Reynolds stress to model the turbulence at the micro-scale, before averaging the model in space.

With our approximations, the time-averaged mathematical problem is then

$$\nabla \cdot \bar{\mathbf{u}}_s = 0 \text{ in } \Omega_s, \quad (3.23a)$$

$$\rho_\gamma \left(\frac{\partial \bar{\mathbf{u}}_s}{\partial t} + \bar{\mathbf{u}}_s \cdot \nabla \bar{\mathbf{u}}_s \right) = -\nabla \bar{p}_s + \mu_\gamma \nabla^2 \bar{\mathbf{u}}_s + \rho_\gamma \mathbf{g} \text{ in } \Omega_s, \quad (3.23b)$$

$$\bar{\mathbf{u}}_s = \mathbf{M} \cdot \left[\mathbf{n} \cdot \left(\nabla \bar{\mathbf{u}}_s + (\nabla \bar{\mathbf{u}}_s)^T \right) \cdot (\mathbf{I} - \mathbf{nn}) \right] \text{ on } \Gamma_{ws}. \quad (3.23c)$$

For simplicity, we remove the overline notation in the remainder of the paper, with the pressure and velocity fields implicitly understood as averaged in time.

3.4.3 Spatial averaging

In this section, the system of equations Eqs 3.23 is upscaled using the method of volume averaging. Since the method is similar to the original work of Whitaker [186] leading to Darcy's law (see also [139, 138, 137]), the details of the developments are in Appendix A.1. The Darcy-scale mass and momentum balance equations read

$$\nabla \cdot \langle \mathbf{u}_s \rangle = 0, \quad (3.24)$$

$$\langle \mathbf{u}_s \rangle = -\frac{\mathbf{K}_s^*}{\mu_\gamma} \cdot (\nabla \langle p_s \rangle^s - \rho_\gamma \mathbf{g}), \quad (3.25)$$

where \mathbf{K}_s^* is the apparent permeability [51], which is computed from the resolution of a closure problem. This equation is obtained using an approximate form of the pressure and velocity perturbations, \bar{p}_s and $\bar{\mathbf{u}}_s$, which are mapped linearly to $\langle \mathbf{u}_s \rangle^s$ as

$$\bar{\mathbf{u}}_s = \mathbf{B}_s \cdot \langle \mathbf{u}_s \rangle^s, \quad (3.26)$$

$$\bar{p}_s = \mu_\gamma \mathbf{b}_s \cdot \langle \mathbf{u}_s \rangle^s, \quad (3.27)$$

where $(\mathbf{b}_s, \mathbf{B}_s)$ are closure/mapping variables. \mathbf{K}_s^* can be computed from \mathbf{b}_s and \mathbf{B}_s as

$$\mathbf{K}_s^{*-1} \phi_s = -\frac{1}{|\mathcal{V}_s|} \int_{\mathcal{V} \cap \Gamma_{ws}} \mathbf{n} \cdot \left[-\mathbf{b}_s \mathbf{I} + \left(\nabla \mathbf{B}_s + (\nabla \mathbf{B}_s)^T \right) \right] d\mathbf{r}. \quad (3.28)$$

For a viscous incompressible flow, it is well established that the flow at the macro-scale is described by Darcy's law. The presence of inertial effects at the micro-scale, as is the case in this study, yields an additional drag and a deviation from the classical Darcy's law. A correction, usually termed the Forchheimer correction [188], can be used to approximate the additional drag. The form of this correction has been widely studied in the literature, both numerically and experimentally. It is now known that different regimes can be distinguished for increasing Reynolds numbers [58, 97, 158], even though the transition and the form of the corrections most likely depend on the porous structure [100]. To recover a generalized form of the Darcy-Forchheimer equation, we decompose the tensor \mathbf{K}_s^* as

$$\mathbf{K}_s^* = \mathbf{K}_s \cdot (\mathbf{I} + \mathbf{F}_s)^{-1}, \quad (3.29)$$

where \mathbf{K}_s is the intrinsic permeability of the effective domain and the second part, \mathbf{F}_s , is the inertial correction. We then obtain

$$\langle \mathbf{u}_s \rangle = -\frac{\mathbf{K}_s}{\mu_\gamma} \cdot (\nabla \langle p_s \rangle^s - \rho_\gamma \mathbf{g}) - \mathbf{F}_s \cdot \langle \mathbf{u}_s \rangle. \quad (3.30)$$

Here, we emphasize that the permeability \mathbf{K}_s^* corresponds to the permeability of the effective smooth domain, Ω_s , not to the *initial domain*, Ω_γ . To recover the exact velocity field in Ω_γ and the corresponding permeability, consider the following expression of the velocity field,

$$\mathbf{u}_\gamma = \chi_w \mathbf{u}_w + \chi_s \mathbf{u}_s, \quad (3.31)$$

where χ_w and χ_s are phase indicator functions of the domains Ω_w and Ω_s respectively, so that we have

$$\langle \mathbf{u}_\gamma \rangle = \phi_w \langle \mathbf{u}_w \rangle^w + \phi_s \langle \mathbf{u}_s \rangle^s. \quad (3.32)$$

We can simplify this expression using the fact that the domain Ω_w is a relatively small subdomain close to the no-slip wall, $\Gamma_{\gamma\sigma}$. Therefore, we have $\phi_w \ll \phi_s$ and consider that $\langle \mathbf{u}_w \rangle^w \ll \langle \mathbf{u}_s \rangle^s$, so that

$$\langle \mathbf{u}_\gamma \rangle \simeq \phi_s \langle \mathbf{u}_s \rangle^s. \quad (3.33)$$

For the pressure, we assume that there is a small perturbation of the pressure within Ω_s so that

$$\langle p_\gamma \rangle^\gamma \simeq \langle p_s \rangle^s. \quad (3.34)$$

With these, we can write

$$\langle \mathbf{u}_\gamma \rangle = -\frac{\mathbf{K}_s}{\mu_\gamma} \cdot (\nabla \langle p_\gamma \rangle^\gamma - \rho_\gamma \mathbf{g}) - \mathbf{F}_s \cdot \langle \mathbf{u}_\gamma \rangle. \quad (3.35)$$

The impact of these approximations is illustrated and discussed in the results of the next Section.

3.5 Results

In this section, we compare our methodology to direct numerical simulations in various geometries of rough porous media. Our primary objective is to answer the following questions:

- Is our method efficient for a wide range of Reynolds number?
- How does the apparent permeability of the porous medium depend on the Reynolds number?
- What is the impact of different classes of roughness on the permeability?

In order to validate the method, we first focus on a creeping flow in a two-dimensional channel with rough walls. We discuss the impact of the roughness and of the position of the slip condition on the results, a study that is reminiscent of the analysis by Veran *et al.* in [180]. We then go on to investigate the case of an inertial flow in a 2D array of cylinders with sinusoidal roughness, assessing the impact of the roughness on the permeability for Stokes and inertial flows. The methodology is finally applied to an element of structured packing with different classes of roughness and a tensorial slip.

3.5.1 Methods

Boundary conditions Here, we describe the different boundary conditions used for applications. We have the rough, Ω_γ , and effective, Ω_s , domains. We also introduce the smooth domain Ω_{smooth} , which is similar to Ω_γ , but with smooth walls $\Gamma_{\gamma\sigma}^{\text{smooth}}$ positioned at the averaged position of the roughnesses. Fig. 3.4 shows these three configurations.

A no-slip condition applies to the boundaries $\Gamma_{\gamma\sigma}$ and $\Gamma_{\gamma\sigma}^{\text{smooth}}$

$$\mathbf{u}_\gamma = 0, \quad (3.36)$$

while the effective condition Eq. 3.10 applies at the smooth wall Γ_{ws}

$$\mathbf{u}_s = \mathbf{M} \cdot \left[\mathbf{n} \cdot \left(\nabla \mathbf{u}_s + (\nabla \mathbf{u}_s)^T \right) \cdot (\mathbf{I} - \mathbf{nn}) \right] \quad \text{on } \Gamma_{ws}. \quad (3.37)$$

Recall that Γ_{ws} can be placed arbitrarily using the Taylor series approximation with the conditions detailed in Section 3.3.2.

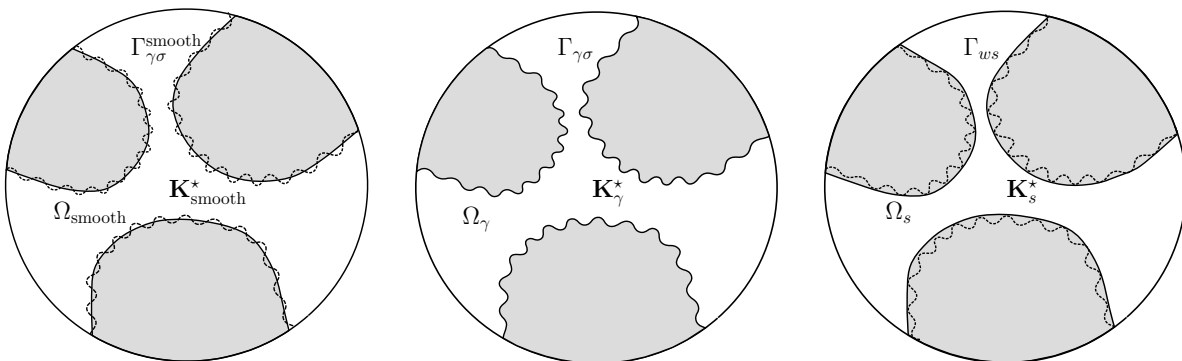


Figure 3.4 – Schematics of the different domains considered for comparison. $\mathbf{K}_{\text{smooth}}^*$, \mathbf{K}_γ^* and \mathbf{K}_s^* are, respectively, the permeability in the smooth, rough and effective domains.

General algorithm We summarize here the methodology used for the different geometries considered in this Section. Our goal is to compare results obtained with the upscaling methods with those of direct numerical simulations. The different steps are as follows:

1. Direct numerical simulations in the domains Ω_γ and Ω_{smooth} .
2. Upscaling approach:
 - (a) Definition of a representative element for the roughness, Ω_{w_i} .
 - (b) Determination of the effective condition via the resolution of a local boundary value problem over Ω_{w_i} .
 - (c) Computation of the velocity field \mathbf{u}_s in Ω_s .
 - (d) Resolution of the closure problem for the determination of \mathbf{K}_s^* .
3. Comparison of the permeabilities \mathbf{K}_γ^* and $\mathbf{K}_{\text{smooth}}^*$ computed from point 1 to \mathbf{K}_s^* computed from point 2.

Numerical schemes Two different methods are applied for the resolution of the closure problems. For the creeping flow in the two-dimensional rough channel, the boundary value problem Eqs 3.8 and the closure problem Eqs A.24 (in Appendix A.1) are solved using standard finite element methods. Stokes equations are discretized using Lagrange quadratic elements for the velocity and linear elements for the pressure (P2/P1). A stabilization term is also added in the equations to fix the constant part of the pressure. We use the generic solver FreeFem++ [74], which provides a flexible environment where the grid and the rough geometry can be easily modified.

More demanding simulations in the inertial regimes, for both the two-dimensional array of cylinders and the three-dimensional structured packings, are performed using the standard finite volume methods in OpenFoam[®]. The closure problem Eqs A.24 was implemented using the solver simpleFoam (SIMPLE algorithm, [128]) with the tensorial Navier condition derived from the slip boundary conditions (named *slip* in OpenFoam[®], see [56] for more detail).

As required for the resolution of the closure problem, the velocity field is determined using direct numerical simulations of the flow via the solver icoFoam (PISO algorithm, [85]), with a volume source term and periodic boundary conditions. All calculations were performed using the HPC resources of CALMIP supercomputing center with 160 cores for the most demanding simulations. The CPU time (number of cores \times computing time) required up to 10^5 h for all calculations.

Assessing the accuracy of the three-dimensional direct numerical simulations Three-dimensional direct numerical simulations are carried out from the creeping flow until the onset of unsteady flow. To estimate the accuracy of our solutions on a fixed grid, we use an approach similar to that described by Jin *et al.* in [88], who introduced the following quantity Δ ,

$$\Delta = \frac{g_p - g_s}{g_p}, \quad (3.38)$$

where g_p and g_s are two ways of defining the pressure gradient. g_p corresponds to the global pressure gradient across the simulated geometry, whereas g_s is determined by integrating the local dissipation rate over the fluid domain,

$$g_s = \frac{\mu_\gamma}{2|\mathcal{V}_s| \|\langle \mathbf{u}_s \rangle^s\|} \int_{\mathcal{V}_s} \nabla \mathbf{u}_s : \nabla \mathbf{u}_s \, d\mathbf{r}. \quad (3.39)$$

Note that the same definition also holds for the domains Ω_γ and Ω_{smooth} , and the corresponding averaging volumes \mathcal{V}_γ and $\mathcal{V}_{\text{smooth}}$.

In theory, $\Delta = 0$. However, if the grid size does not resolve the smallest scales of the flow, the global dissipation rate is undervalued and $\Delta > 0$. Therefore, the accuracy of the calculations can be evaluated by calculating Δ and, following studies in [88], we consider that the calculations are accurate when Δ is below 10% (see [88] for further detail).

Definition of the REV and boundary conditions A precise definition of the REV and whether or not it should consist of one or several periodic unit-cells for turbulent flows is a delicate issue. For instance, the idea that the porous medium filters the longest lengths scales of the turbulence has been widely used for simulations in structured packings [141, 151, 163]. Few results of large scale simulations are available in the literature (see [121, 125]) and most of the simulations are limited to steady state. For arrays of squares, Jin *et al.* in [88] have recently shown that the porous structure does indeed impose a cut-off in the characteristic length scales of the flow. They further study the spatial correlations of the velocity field while changing the number of unit-cells included in the REV, showing that the largest possible structures of the flow are about the size of the pores, even for large values of the porosity. This suggests that calculations over a single unit-cell with periodic boundary conditions recover most of the flow features for a broad range of porosities. This question of the size of the REV is addressed further by the results presented in [7] about the flow stability and Hopf bifurcation in arrays of cylinders. Their results indicate that the transition to unsteady flow is sensitive to the number of unit cells included in the REV for porosities larger than $\sim 50\%$ ($> 55\%$ in Fig. 10 in [7], arrays of squares). These two studies seem to indicate that:

1. for values of the porosity less than 50%, a single unit-cell with periodic conditions captures both the stability and the structure of the flow,
2. for larger values of the porosity, a single unit-cell captures most of the features of the flow but may fail to accurately describe its stability and the transition to unsteady flow.

In this Section, we will study a variety of porous media including ones with porosities larger than 50%. In all cases, we chose to limit our computations to a single unit-cell with periodic boundary conditions to minimize the computational cost. This is because our primary objective is not to study stability and transitions, but the ability of our models to recover the spatial structure of the flow.

Definition of the Reynolds number To analyze the effect of inertial flow, we define here a set of dimensionless Reynolds numbers. The difficulty in doing so is mostly the choice of the characteristic length scale. In isotropic porous media, a common choice is the square root, \sqrt{K} , of the intrinsic permeability, K , so that

$$Re_k = \frac{\rho_\gamma \|\langle \mathbf{u}_\gamma \rangle\| \sqrt{K}}{\mu_\gamma}. \quad (3.40)$$

This length scale has several advantages over the average pore-size l . First, when the variance of the pore-size distribution is large and the porous medium consists of large voids and small pore-throats, defining a unique length scale that characterizes the flow at large Reynolds number is difficult. \sqrt{K} is an evaluation of such a unique length scale, but one that characterizes the flow at small Reynolds number and is directly connected to distribution of viscous dissipation inside the porous structure [190]. Second, it has been shown that this definition of the Reynolds number captures more accurately the transition to the inertial regime [100, 11].

For comparison with the literature in chemical engineering, we also define the following Reynolds number

$$Re_h = \frac{\rho_\gamma \|\langle \mathbf{u}_\gamma \rangle\| h}{\mu_\gamma}, \quad (3.41)$$

where h is a geometrical length scale. We will use $h = d$ with d the diameter of the cylinder in the case of the rough cylinder and $h = H$ for the structured packings.

3.5.2 Case 1: Application to a channel with sinusoidal walls

The methodology is first applied to a creeping flow within a two-dimensional channel with sinusoidal walls. In a two-dimensional configuration, the effective boundary condition, Eq. 3.10, reads

$$u_s \mathbf{e}_x = M_{xx} \frac{\partial u_s}{\partial y} \mathbf{e}_x, \quad (3.42)$$

where M_{xx} is the Navier coefficient (or equivalently the slip length). In order to assess the effect of the distance of the effective surface to the rough wall on the accuracy of the method, we apply the methodology for multiple positions (A to G in Fig 3.5). The effective condition corresponding to each position is derived from Eq. 3.42 using the Taylor series Eq. 3.14. Position B corresponds to the effective *no-slip* position, i.e. the displacement of the interface that leads to $M_{xx} - \Delta x = 0$. The permeability K_s , normalized to the exact permeability K_γ of the rough channel, is given in Fig 3.5 along with the different positions considered. It is shown that displacing the effective boundary closer to the rough wall improves the accuracy, and that the effective no-slip condition (line B) is the most accurate configuration, as previously discussed in [180].

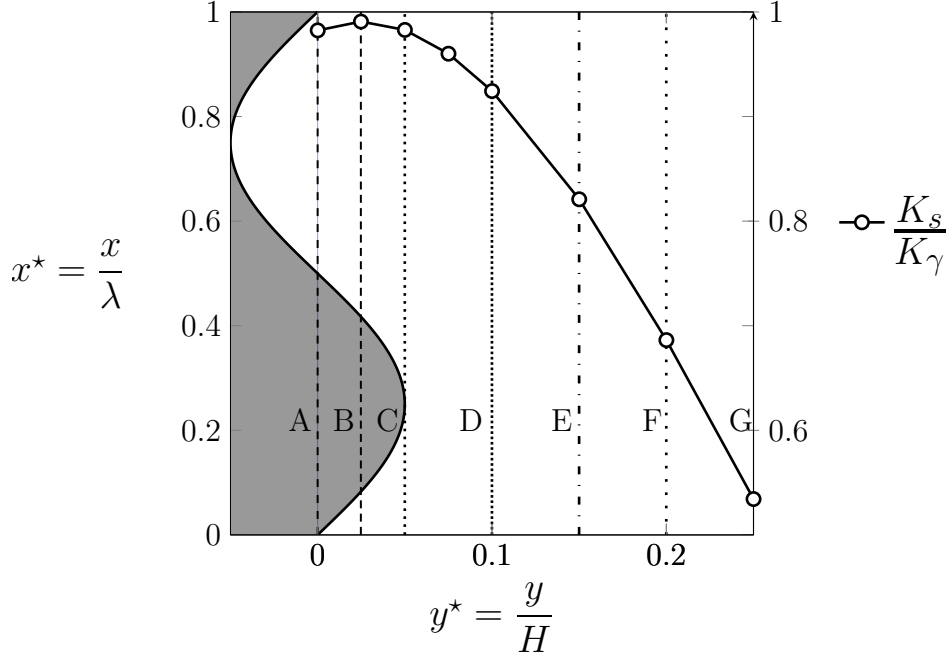


Figure 3.5 – Permeability K_s of the effective domain non-dimensionalized with the permeability K_γ from the exact geometry, as a function of the distance y from the effective surface to the sinusoidal wall, normalized with H , the height of the channel. The effective surface is positioned from A ($y^* = 0$) to G ($y^* = 0.25$). Accurate results are obtained for the equivalent “no-slip” position (line B). Line A corresponds to the average of the sinusoid, $\Gamma_{\gamma\sigma}^{\text{smooth}}$.

We then fix the position of effective boundary at the no-slip position and vary the amplitude and wavelength of the sinusoid. The effective and exact permeabilities, normalized to the intrinsic permeability of a Poiseuille flow, $K = \frac{H^2}{12}$, are presented in Fig 3.6. We observe several limit cases. First, when the amplitude tends to zero, we recover the permeability of the flat case. Second, when the wavelength tends to zero, we recover the permeability of an equivalent flat surface positioned on top of the sinusoid. Third, when the wavelength is much larger than the height of the channel H , two different situations are observed. If both sinusoids are in phase (blue curve in Fig 3.6), we have $k_\gamma \rightarrow 1$, whereas if there is a phase shift of $\frac{\pi}{2}$ (red curve in Fig 3.6) another limit is attained, $k_{\gamma\text{-shift}} < 1$. This is because, for a fixed value of the amplitude, this geometry generates a bottleneck effect with flow focusing and defocusing even in the limit of large wavelengths. The effective condition accurately captures the large variations in the permeability (about 25% to 50%) induced by the roughness, except in the specific case of the asymmetry between both boundaries. In this case, there is a strong coupling between the pore flow and the boundaries and the approximations needed for the derivation of the slip boundary condition, in particular the constraint $\frac{l_w}{l} \ll 1$, are not valid.

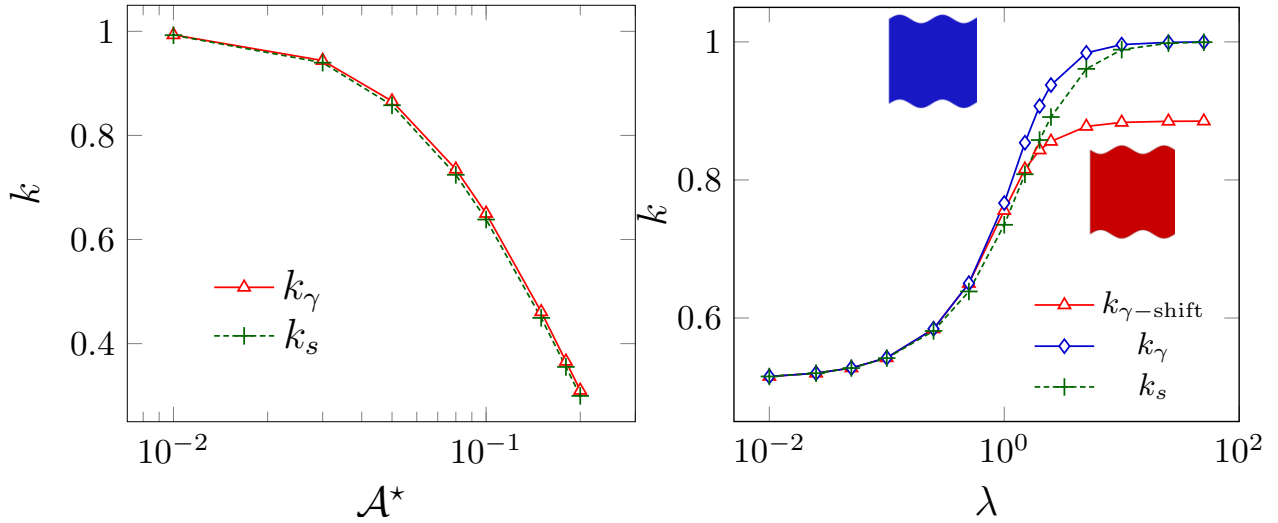


Figure 3.6 – Plots of the dimensionless permeabilities with the effective slip, $k_s = \frac{K_s}{K}$, and with the rough boundary, $k_\gamma = \frac{K_\gamma}{K}$. $K = \frac{H^2}{12}$ is the permeability of a Poiseuille flow in the smooth channel. On the left-hand side, permeabilities are functions of the amplitude of the roughnesses \mathcal{A}^* for a fixed value of the wavelength, $\lambda^* = 0.5$. On the right-hand side, permeabilities are functions of the wavelength λ^* for a fixed value of the amplitude, $\mathcal{A}^* = 0.1$.

3.5.3 Case 2: Application to an array of rough cylinders

We now apply the effective boundary approach to a two-dimensional array of rough cylinders, as shown in Fig 3.7, both in the Stokes and inertial regimes. In order to minimize the error induced by the effective surface theory, the boundary Γ_{ws} is placed at the no-slip position. Example 2D meshes used for the effective and rough domains are given in Appendix A.2.

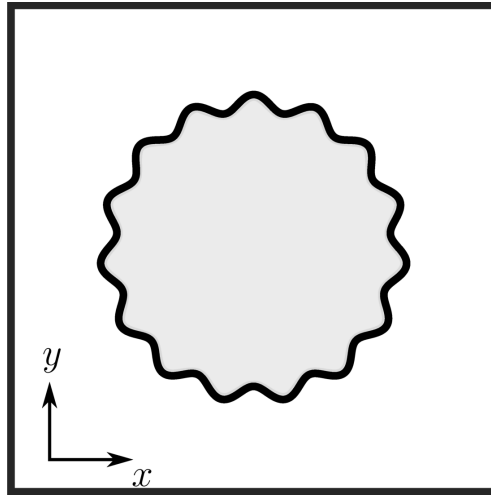


Figure 3.7 – Illustration of a unit-cell for a 2D array of rough cylinders.

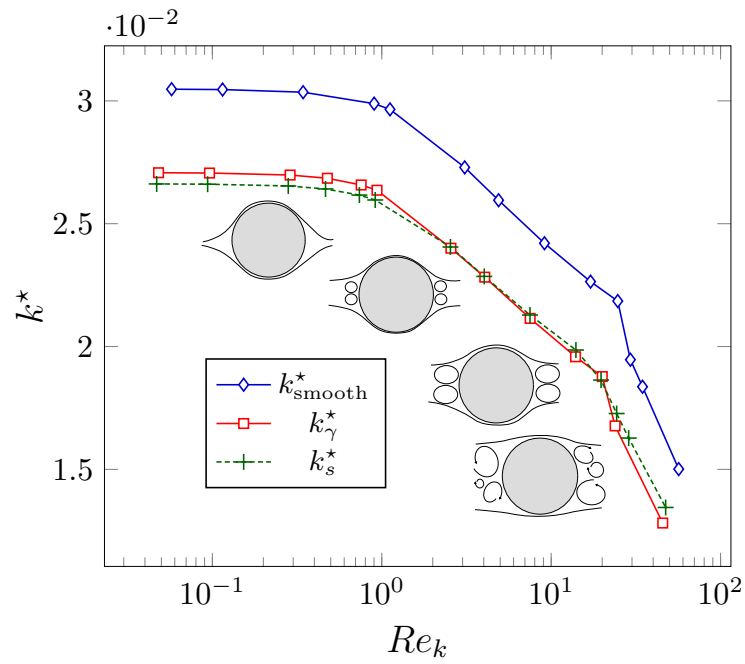


Figure 3.8 – Dimensionless apparent permeability k^* along the x -axis as a function of the Reynolds number for the effective condition $k_s^* = \frac{K_s^*}{d^2}$, the rough $k_\gamma^* = \frac{K_\gamma^*}{d^2}$ and smooth $k_{smooth}^* = \frac{K_{smooth}^*}{d^2}$ cylinders.

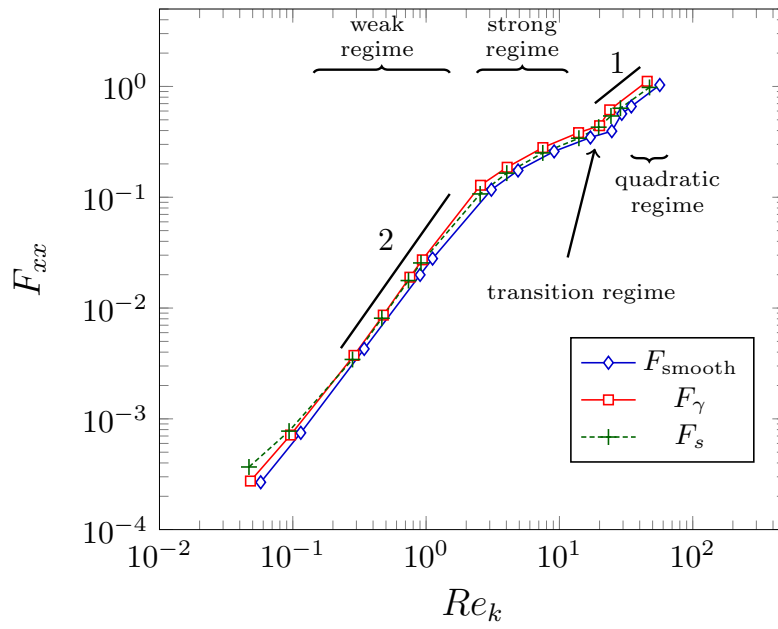


Figure 3.9 – Correction coefficient F_{xx} as a function of the Reynolds number for the effective, rough, and smooth domains.

Flow regimes

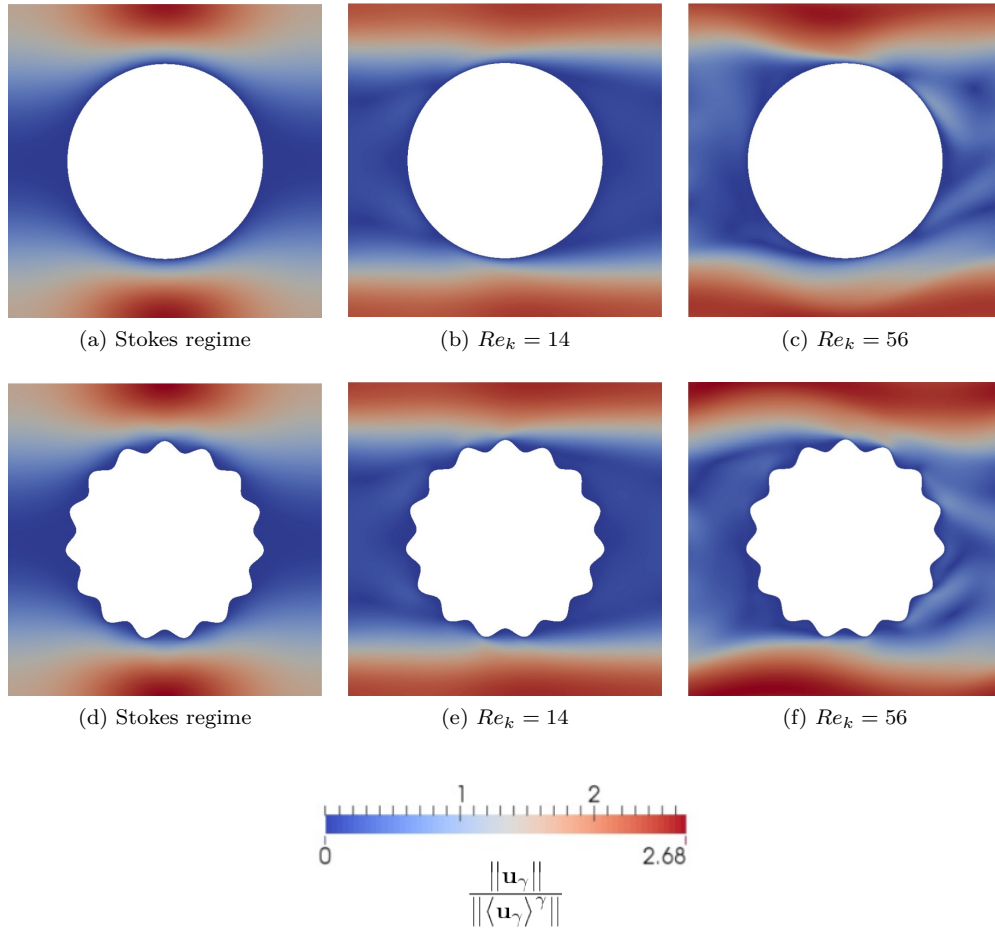


Figure 3.10 – Norm of the velocity fields in the domains Ω_s (top) and Ω_γ (bottom).

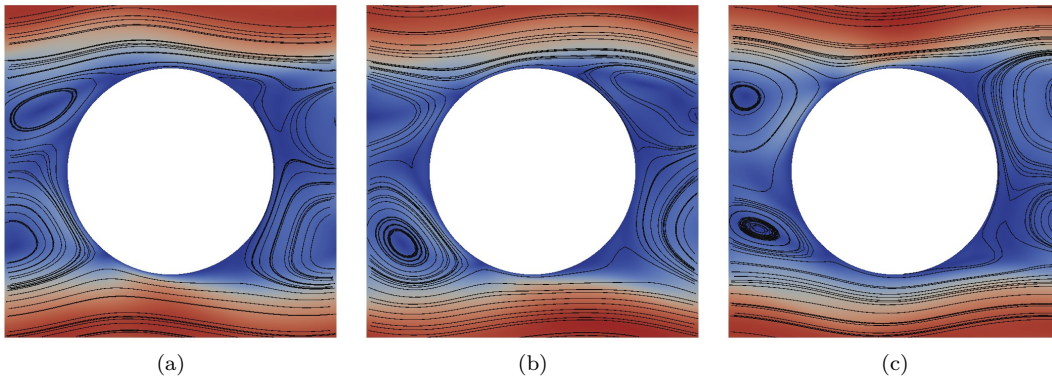


Figure 3.11 – Velocity streamlines in the domains Ω_s for $Re_k = 56$ at three different times. The oscillation motion of the vortices is seen from left to right.

Results are presented in Figs. 3.8 and 3.9 for a cylinder of diameter $d = 0.6H$ ($\phi_\gamma \approx 0.72$), where H is the

unit-cell width. As discussed previously in [100], the transition between the Darcean and the fully turbulent regime is complex and strongly depends on the geometry of the porous structure. Here, we identify five different regimes as follows.

- For $Re_k \lesssim 0.3$ ($Re_d \lesssim 1.7$), the flow is Darcean and the apparent permeability is constant (velocity field in Fig 4.9).
- For $0.3 < Re_k < 2$ ($1.7 < Re_d < 11.5$), we observe a weakly inertial regime where F scales in Re_k^2 . This regime has been widely referenced in the literature [58, 97].
- For $3 < Re_k < 20$ ($17 < Re_d < 114$), a strongly inertial regime develops (velocity field in Fig 4.6), which is characterized by a slowdown in the growth of F , see [100].
- For $Re_k \simeq 25$ ($Re_d \simeq 172$), there is a step increase in the correction F that reflects the transition from steady to unsteady flow. A plot of the volume averaged velocity $\langle \mathbf{u}_s \rangle$ without time-averaging is given in Fig 3.12 and velocity fields at different times are presented in Fig 3.11, highlighting the cyclic behavior of two large vortices. This transition is described in detail by Koch and Ladd in [93] for a similar two-dimensional geometry where they show that the pressure drag exhibits a sudden increase.
- For large Reynolds numbers, $Re_k > 50$ ($Re_d > 285$), the flow is completely unsteady (velocity field in Figs 4.6 and 3.10f). For the few points that we computed, we observe that F scales linearly with Re_k and the pressure drag, $-\int_{\Gamma_{\gamma\sigma}} \mathbf{n} \cdot (p_\gamma \mathbf{I}) d\mathbf{r}$, dominates over the viscous drag. To further understand the unsteady regime and the impact of temporal fluctuations on the results, additional computations for larger values of the Reynolds number are needed. Such simulations should also be performed in three-dimensional configurations since two-dimensional computations usually fail to recover important features of turbulent flows.

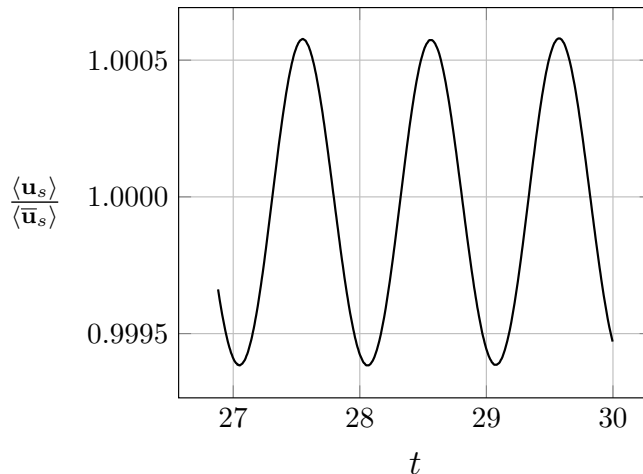


Figure 3.12 – Volume averaged velocity $\langle \mathbf{u}_s \rangle$ as a function of time for $Re_k = 29$ ($Re_d = 168$).

Independently from the slip condition, we emphasize several important results from these direct numerical simulations. First, although we observe a decrease in the slope of F in the strongly inertial regime ($3 < Re_k < 20$), we did not recover a scaling where the correction F is linear with Re_k . This was already observed for simple arrays of cylinders in [100], and they also found that the introduction of disorder favors the emergence of a quadratic regime. Second, we observe that the standard Forchheimer correction, where

the drag scales with Re_k^2 (F is linear with Re_k), seems to be valid for the onset of the unsteady regime when Re_k is just above 50. This may suggest that the Darcy-Forchheimer formulation actually corresponds to a time-averaged macro-scale equation, although further analysis and simulations at larger Reynolds numbers are necessary. This slow transition from the Darcy to the Forchheimer regime is in contrast with some previous works in the literature ([58, 97]) where the transition regime is neglected and the drag rapidly becomes quadratic. These effects have been considered negligible for practical applications in previous works (see [96, 39]). However, our results on this simple unit cell show that the drag is not quadratic for a significant range of Reynolds numbers (about a decade). As previously mentioned, the introduction of disorder in arrays of squares favors the emergence of a quadratic regime [100], which may explain why Forchheimer corrections can be used with good accuracy for disordered media over a broad range of Reynolds number (see discussion in [95, 35]). This emphasizes the importance of the pore space topology on these results, which should be revisited for more complex and disordered three-dimensional structures.

Impact of the slip condition For the slip condition, we see that the effective approach accurately captures the impact of the roughness on the permeability for $Re_k \lesssim 40$. For larger Reynolds number, however, the roughness generates additional inertial effects and viscous dissipation that are not captured by the effective condition; a difference that is expected to be further amplified for larger Reynolds numbers for various reasons. First, the effective boundary condition, as presented in this paper, uses a creeping flow approximation within the boundary layer and is therefore limited to moderate Reynolds numbers. In addition, unless the roughness is so small as to be included in the viscous sublayer, the flow perturbations induced by the wall in the turbulent regime will propagate to the center of the pores, a phenomenon lying outside the domain of validity of the model. Finally, the closure problem is quasi-stationary, which is only true for $Re_k < 25$. Beyond this point, the velocity field \mathbf{u}_s is time-averaged for the resolution of the closure problem and further theoretical developments are required to accurately capture the effects of fluctuations in time. For instance, macro-scale equations involving time convolutions have been used previously to capture high-frequency temporal fluctuations of the average fields (see discussion in [43] regarding dispersion effects).

To evaluate the effect of the ratio $\frac{l_w}{l}$, we further study the impact of the porosity, and therefore the size of the pores, on the accuracy of the slip boundary condition for a viscous flow. Results are plotted in Fig 3.13. Consistent with the case of the sinusoidal wall, we see that the error increases as the porosity decreases (i.e. $\frac{l_w}{l}$ increases).

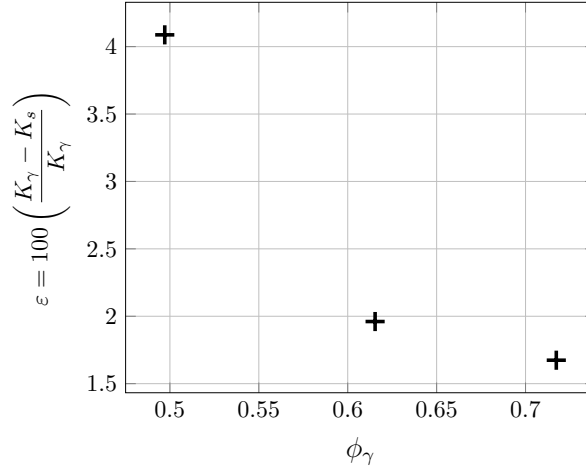


Figure 3.13 – Error between exact and effective intrinsic permeabilities for three porosity levels. Cylinder diameters from left to right: $d/H = 0.8$, ($l_w/l = 0.0250$) $d/H = 0.7$, ($l_w/l = 0.0167$), and $d/H = 0.6$ ($l_w/l = 0.0125$).

3.5.4 Case 3: Application to structured packings

We now consider a geometry representative of structured packings used in separation processes. The flow of the gas phase in such packings is the focus of a number of studies in the literature (see [141, 151, 163, 125]), using primarily computational fluid dynamics. Recently, Soulaire and Quintard in [163] proposed a detailed analysis of the upscaling procedure for momentum transport and derived a generalized Darcy-Forchheimer law at the macro-scale for the gas phase that can be used, theoretically, for relatively high Reynolds numbers. They showed that the permeability tensor, \mathbf{K}^* , has a null row and column describing the absence of flow in the direction orthogonal to the corrugated sheets. They also found that the amplitude of the non-diagonal terms is negligible compared to diagonal ones and that the diagonal terms on \mathbf{K}^* are identical. This was also assumed in earlier works by Mahr and Mewes in [113] and Raynal and Royon-Lebeaud in [141]. The tensor \mathbf{K}^* is therefore written as

$$\mathbf{K}^* = K^* \begin{pmatrix} 1 & 0 & 0 \\ 0 & 1 & 0 \\ 0 & 0 & 0 \end{pmatrix}, \quad (3.43)$$

with the z-axis normal to the corrugated sheets. This form of the tensor \mathbf{K}^* , however, is only valid for specific symmetries of the local structure. The surface roughness, either generated by a traveling train of waves at the liquid-gas interface [10, 178] or engineered as a textured corrugated sheet, may break symmetries of the unit-cell. We therefore consider a more general form of the tensor as

$$\mathbf{K}^* = \begin{pmatrix} K_{xx}^* & K_{yx}^* & 0 \\ K_{xy}^* & K_{yy}^* & 0 \\ 0 & 0 & 0 \end{pmatrix}. \quad (3.44)$$

In this Section, we explore the impact of three different orientations and profiles of rough patterns on the coefficients of \mathbf{K}^* (see Fig. 3.14).

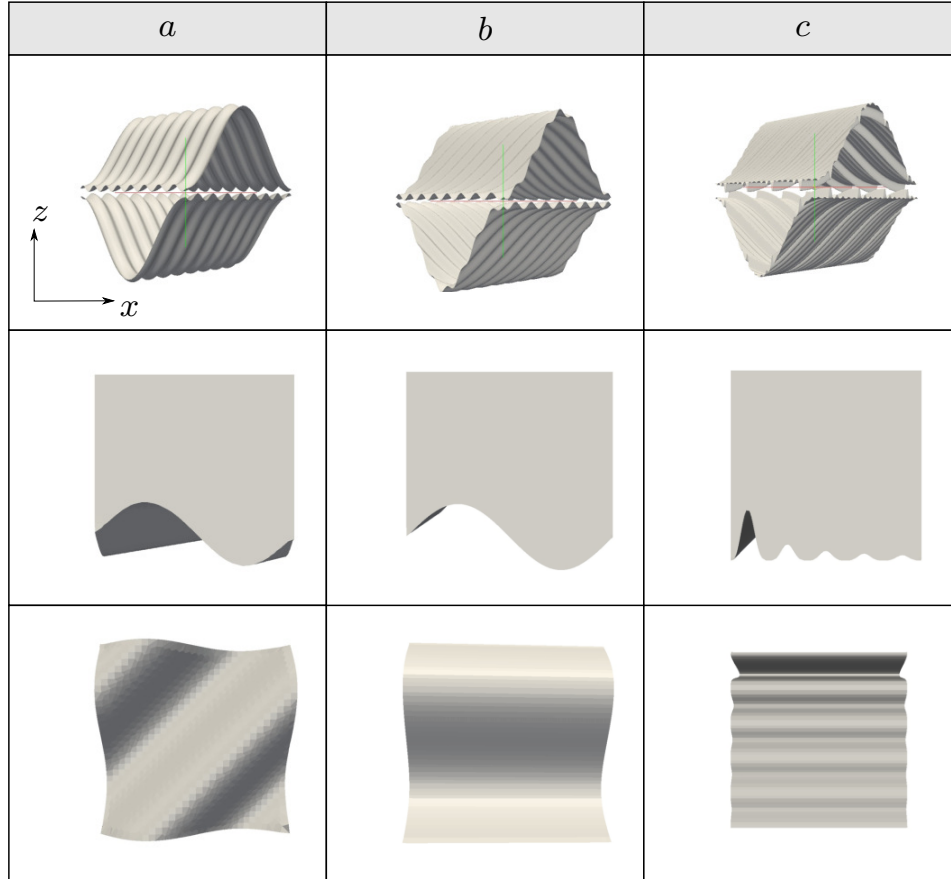


Figure 3.14 – Geometries considered in the simulations. The first line shows the unit-cells of structured packings, while the second and third lines are the rough elements Ω_{w_i} on the surface. Roughness types *a* and *b* correspond to typical wall-textures that can be engineered on the surface. Roughness *c* represents a traveling train of soliton waves along the column axis.

The geometries are now three-dimensional, so that we need the full slip tensor \mathbf{M} of the Navier condition

$$\mathbf{u}_s = \mathbf{M} \cdot \left[\mathbf{n} \cdot \left(\nabla \mathbf{u}_s + (\nabla \mathbf{u}_s)^T \right) \cdot (\mathbf{I} - \mathbf{nn}) \right]. \quad (3.45)$$

In order to limit the error introduced by the linear approximation, the effective surface is positioned on the top of the roughness for all the cases treated in this Section. The geometry *a* describes a wall texture that can be found in structured packings [118] to control the liquid phase dispersion. The rough pattern *b* is identical to the profile *a*, but rotated 45° to study the impact of an inclined pattern on the isotropy of the permeability tensor. The geometry *c* represents a train of soliton waves propagating on the surface of a thin liquid film along the axis of the column.

Mesh $\sim 120^3$ cells			Accuracy		
$\nabla \langle p_\gamma \rangle^\gamma$	Re_k	Re_H	g_p	g_s	Δ
5	18	220	5	4.99	0.18
10	34	402	10	9.93	0.62
15	46	541	15	14.82	1.19
20	48	574	20	19.71	1.47
30	58	693	30	29.43	1.89
50	79	940	50	47.37	5.22
100	118	1401	100	91.28	8.72

Table 3.1 – Numerical accuracy of the results for the unit-cell a .

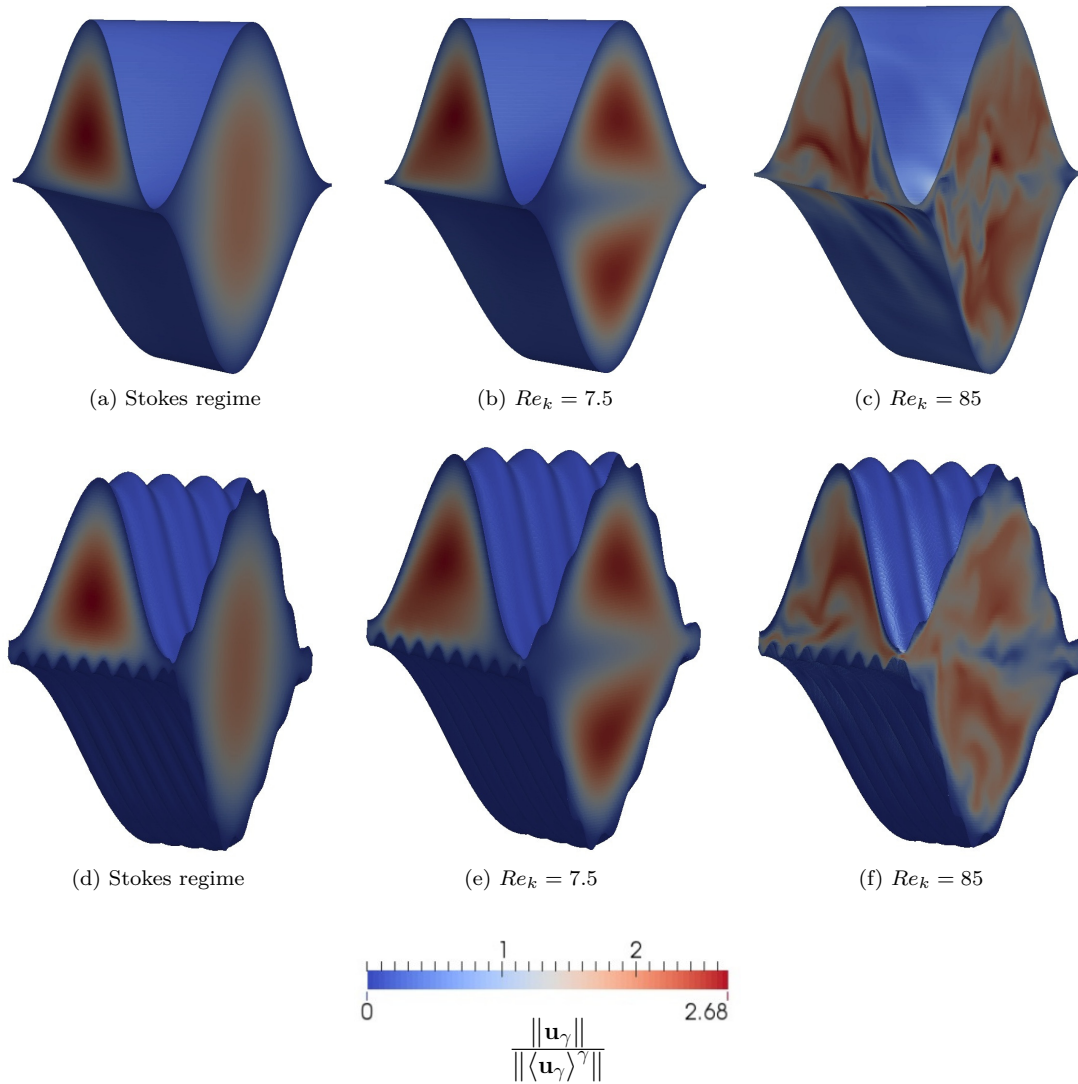


Figure 3.15 – Norm of the velocity fields in the domains Ω_s (top) and Ω_γ (bottom).

Flow regimes Direct numerical computations are performed in all cases (see Fig. 3.15) with the quality of the numerics evaluated as described in Section 3.5.1 (see Table 3.1 for the unit-cell a) and the mesh of

the geometry a in Appendix A.2. Results are presented in Fig 3.16 for the permeability and Fig 3.17 for the Forchheimer term. Similarly to the rough cylinder, different regimes can be identified depending on the Reynolds number. We recover weak and strong inertial regimes, with a scaling of F in Re_k^2 in the weak regime ($0.8 < Re_k < 4$). The transition to unsteady flow occurs for $Re_k \sim 40$ leading to a significant loss in permeability, both in the smooth and rough domains. Consistent with the two-dimensional observations for the rough cylinders, the effective domain method accurately captures the pressure drop, until the transition for $Re_k \sim 40$ ($Re_H \sim 500$). As discussed previously, this regime cannot be captured by the effective boundary condition developed in this paper. This is particularly true for the geometry c , which generates an important reduction of permeability, even in the Stokes regime, and yields strong inertial effects. These effects are shown in Fig 3.17, where we observe a correction in the effective domain that is similar to the smooth case, further suggesting that the slip boundary does not recover the perturbations of the flow generated at the small scale by the rough wall and propagating to the center of the pores.

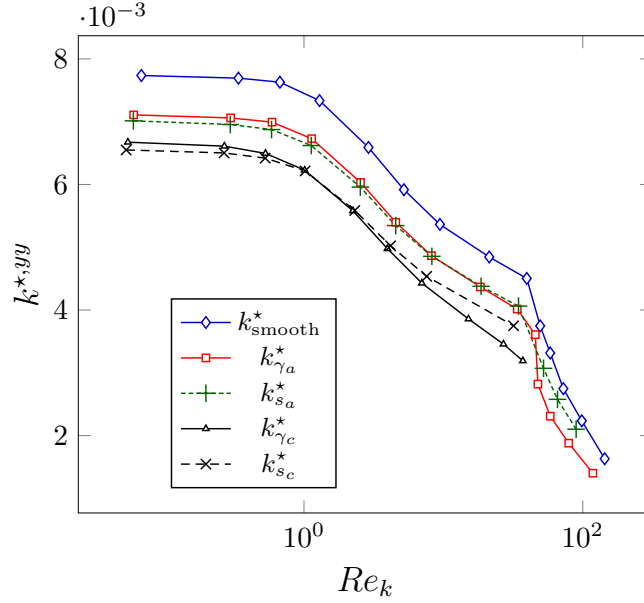


Figure 3.16 – Dimensionless permeability $k^{*,yy}$ along the y -axis for the geometries a and c as a function of the Reynolds number. The exact permeabilities of the smooth $k_{smooth}^* = \frac{K_{smooth}^*}{H^2}$ and rough $k_{\gamma}^* = \frac{K_{\gamma}^*}{H^2}$ domains are compared to the permeability $k_s^* = \frac{K_s^*}{H^2}$ obtained with the tensorial slip condition.

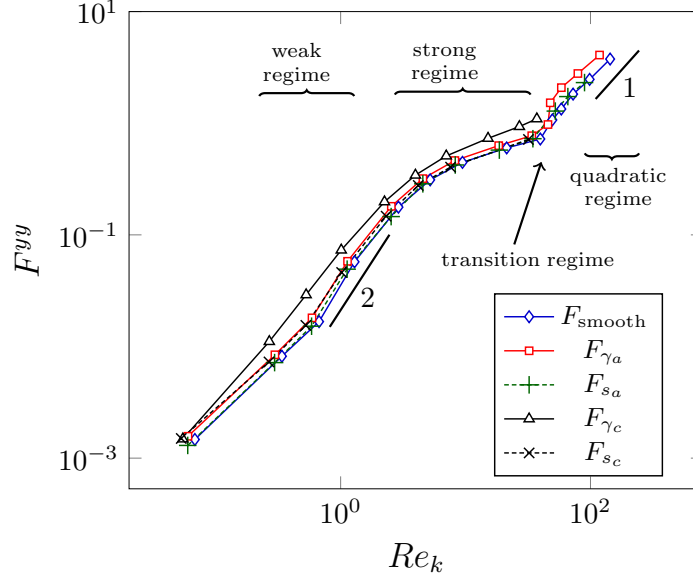


Figure 3.17 – Correction coefficient along the y -axis F^{yy} for the geometries a and c as a function of the Reynolds number. The exact corrections of the smooth F_{smooth} and rough F_{γ} domains are compared to the correction F_s obtained with the tensorial slip condition.

Impact of the slip condition We now compare the exact permeabilities for the smooth and rough geometries, $\mathbf{K}_{\text{smooth}}^*$ and \mathbf{K}_{γ}^* , to the permeability resulting from the up-scaling analysis \mathbf{K}_s^* . Results of the simulations in a large range of Reynolds numbers are presented in Fig 3.16 for the permeability coefficients $K_{s_a}^*$ and $K_{s_c}^*$ along the axis of the column, y , non-dimensionalized with the characteristic length $H = 0.01$. For the geometry a , the slip coefficients of the effective tensor \mathbf{M} are identical along the x and y axis, $M_{xx} = M_{yy} = 7.9 \times 10^{-5} m$. The consequence of this symmetry in the slip tensor is a symmetry in the intrinsic permeability tensor \mathbf{K}_{s_a} , with $K_{s_a}^{xx} = K_{s_a}^{yy}$. The coefficients $K_{s_a}^{xx} = K_{s_a}^{yy} \simeq 7.1 \times 10^{-7} m^2$ are of the same order of magnitude as those in [163]. In agreement with [163], the non-diagonal terms are negligible compared to diagonal ones, which indicates that this specific structure of packings does not generate anisotropic effects. For the geometry b , we have $M_{xx} > M_{yy}$, with $M_{xx} = 1.2 \times 10^{-4} m$ and $M_{yy} = 7.5 \times 10^{-5} m$, leading to different permeability coefficients along x and y , with $K_{s_b}^{xx} \simeq 7.1 \times 10^{-7} m^2$ and $K_{s_b}^{yy} = 6.9 \times 10^{-7} m^2$. For the geometry c , the tensor \mathbf{M} also exhibits different diagonal coefficients, $M_{xx} = 8.1 \times 10^{-5} m$ and $M_{yy} = 1.8 \times 10^{-5}$, which lead to $K_{s_c}^{xx} \simeq 7.1 \times 10^{-7} m^2$ and $K_{s_c}^{yy} = 6.5 \times 10^{-7} m^2$ in the permeability tensor \mathbf{K}_{s_c} . For the geometry b , comparison between the exact and effective permeabilities are shown in Fig 3.18 for the stationary regime. We find that the roughnesses a and b reduce the permeability of about 12%, while the roughness c induces a change of about 18%. These results concur with the experimental data of Tsai in [173], who compared the dry pressure drop for a packing with and without roughness at the surface. For the geometry b , the effective domain method recovers the anisotropy with a lower permeability in the x -direction than in the y -direction in Fig 3.18.

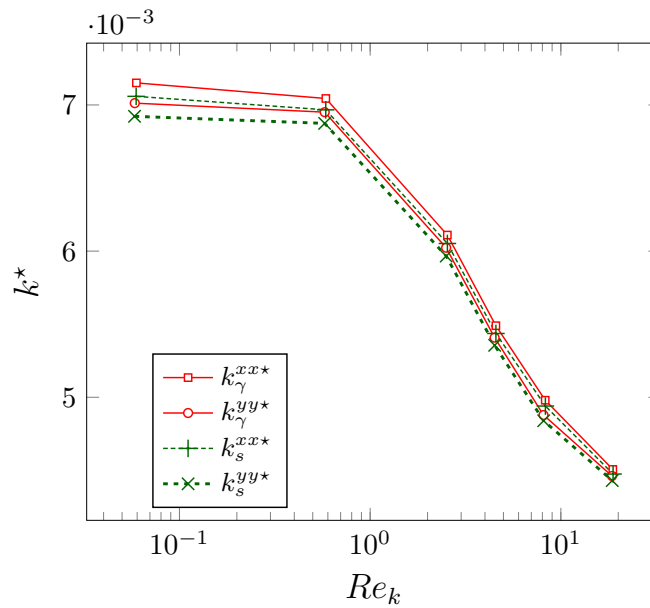


Figure 3.18 – Dimensionless permeability k^* coefficients in the x and y directions as functions of the Reynolds number for the geometry b . Results show good agreement between the exact and effective permeabilities with the anisotropy $k_s^{xx^*} > k_s^{yy^*}$.

The primary reason for using the effective boundary condition, rather than the no-slip condition on the rough surface, was to make computations tractable. To evaluate the gain, we show a mesh convergence plot for simulations in the Stokes regime for the soliton case (geometry c) in Fig 3.19. We see that we obtain a similar accuracy for both calculations only for a much finer mesh in the case of the rough surface. This is because the rough structure is composed of sharp soliton waves and we need a fine mesh to capture the flow over these structures. The consequences are twofold. First, obtaining a good quality mesh is much more difficult in the rough surface than in the smooth case. Second, the simulation times are longer for the rough case. For instance, the finest simulation (last point on Fig 3.19) represents over 500h of CPU time with the rough surface, whereas the equivalent simulation in the effective domain only represents about 120h of CPU time.

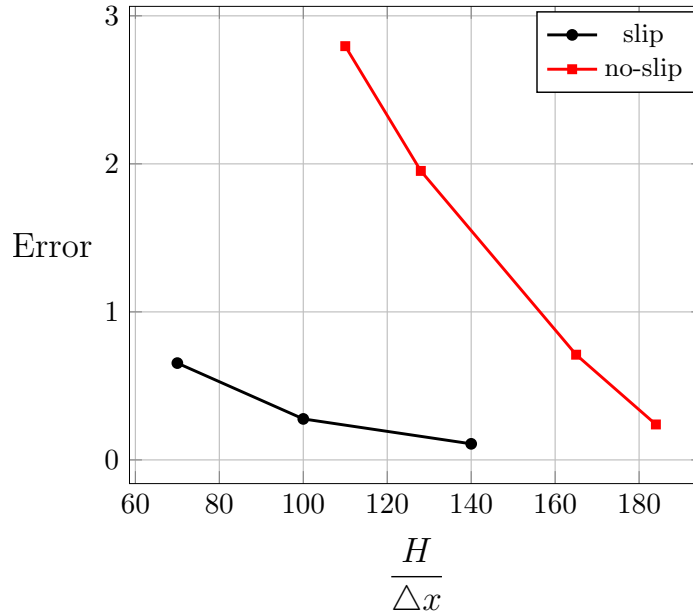


Figure 3.19 – Plot of the error as a function of the average number of mesh elements per direction, $\frac{H}{\Delta x}$. The error is defined $100 \left(\left\| \frac{\langle u_x \rangle - \langle u_x \rangle|_R}{\langle u_x \rangle|_R} \right\| \right)$ where $\langle u_x \rangle|_R$ is a reference average velocity obtained with an extremely fine mesh, $\frac{H}{\Delta x} = 180$ for the smooth surface and $\frac{H}{\Delta x} = 285$ for the rough surface.

3.6 Conclusion

The aim of this work was to contribute to the development of models for the characterization of flow in columns equipped with structured packings. We provide a generic two-step methodology for the estimation of macro-scale properties in porous media with rough surfaces. The rough surface is first replaced by an effective smooth one with a slip boundary condition, which considerably simplifies computations in large domains. In three-dimensional configurations, the slip condition has a tensorial form that can capture surface anisotropy. Secondly, the micro-scale flow problem is upscaled at the Darcy-scale to obtain a generalized Darcy-Forchheimer formulation.

In applying our approach to a variety of geometries, we identified a number of fundamental aspects of flow in porous media with rough surfaces:

- even a small roughness can induce a significant decrease in permeability, suggesting that those complex surfaces, often treated as smooth ones, should be considered carefully in a multi-scale analysis.
- in the smooth, slip and rough cases, we have studied the evolution of the apparent permeability as a function of the Reynolds number. We show that several different regimes can be identified. These results suggest that the standard quadratic Darcy-Forchheimer formulation may be valid only for relatively large Reynolds numbers when the flow is fully unsteady. Computations of the flow for larger values of the Reynolds numbers are necessary to further understand this regime, along with the impact of temporal fluctuations on the permeability.
- the effective boundary condition accurately describes the permeability at the macro-scale for the Stokes and inertial flow regimes, but fails when unsteady flow develops. This is because, in this last regime, the impact of the roughness is not localized to the vicinity of the wall but propagates to the center of the pores. For large amplitudes of the roughness, our approach is therefore limited to relatively small

Reynolds number. Further developments are needed to accurately model the flow characteristics at high Reynolds numbers.

Acknowledgements

This work was granted access to the HPC resources of CALMIP supercomputing center under the allocation 2015-[P1547].

Part II

Multiphase modeling

In this second part of the manuscript, the analysis is extended to *multiphase* modeling approaches. The monophasic approach developed in Chapter 3 is indeed restricted to moderate flow rates. Although it allows to bypass the modeling of the liquid phase, the method of the effective condition assumes that the thickness of the liquid film remains constant or is negligible compared to the pore size, which is not true for high flow rates. This second part is therefore dedicated to multiphase approaches. Two singular features can be identified about the gas-liquid flow in columns equipped with structured packings.

1. For high flow rates (loading regime), the flow is characterized by a strong interfacial shear-stress which generates macroscale effects such as liquid retention and drastic changes in pressure drop. These effects favor the transport of the chemical species between the two phases and lead ultimately to the flooding of the column.
2. The distribution of the liquid phase is strongly affected by the anisotropy of the structure, and therefore differs significantly from flows in more classical porous media.

The analysis of these two points is decomposed for a better clarity, as they treat on two different aspects of the flow process. The first point is treated in Chapters 4 and 5, while the last point is discussed in Chapter 6. The two modeling approaches are however fully compatible and are both required in the modeling of the gas-liquid flow in the distillation process. The complete model including the results from the two parts is provided in Appendix C.

Chapter 4

Two-phase flow in highly permeable media: models with cross terms

Contents

4.1	Introduction	63
4.2	Two-phase flow model at macroscale: step by step method	64
4.2.1	Step 1: Mathematical problem at pore-scale	64
4.2.2	Step 2: volume averaging	65
4.2.3	Step 3: Problem on the deviations	66
4.2.4	Step 4: Approximation of the perturbations	71
4.2.5	Step 5: Closure at macroscale	71
	Paper: Modeling two-phase flow of immiscible fluids in porous media: Buckley-Leverett theory with explicit coupling terms	75
4.3	Introduction	76
4.4	Methods	77
4.4.1	Models and assumptions	77
4.4.2	Buckley-Leverett theory	79
4.4.3	Boundary, initial conditions and fluids	83
4.4.4	Closures for the effective parameters	83
4.5	Results	85
4.5.1	Case 1: Drainage: water/air flow in a particle bed	85
4.5.2	Case 2: Imbibition: air/water flow in highly permeable media	89
4.5.3	Case 3: Imbibition: oil/water flow in low permeability media	92
4.6	Conclusion	94

4.1 Introduction

As explained in Chapter 1, a column equipped with structured packings is a porous medium of high permeability, up to around 10^{-6} m^2 . In this sense, the distillation process can be placed in the class of two-phase flows in highly permeable media, encountered in other industrial processes such as packed beds or heat exchangers, or in some natural porous media, including canopy, urban canyons, etc. It differs from many other two-phase flows in media of lower permeabilities, such as those most often considered in petroleum engineering or hydrology, or in micro or nano devices such as fuel cells. These two families of porous media involve physical phenomena of different nature. In low permeable media, one can for instance assume the wetting phase to fill entirely the smallest pores, due to locally strong capillary effects. The consequence is a segregated repartition of the two phases within the medium, with small pores occupied by the wetting phase and large pores occupied by the non-wetting phase. Conversely, in highly permeable media, one observes that the two phases often occupy each pore. The two configurations - immiscible phases in low vs high permeable media - are schematically illustrated in Fig. 4.1. The question of the phases repartition is important as the fluid/fluid interface plays a central role in many processes, and especially in chemical processes. In the first case (a), the area of the fluid/fluid interface is low compared to the area of the fluid/solid interface, while in the second case (b), the order of magnitude of the two interfaces are likely to be comparable. These areas control in particular the momentum exchanges in the system, and therefore constitute a key issue when considering the modeling of the momentum transport.

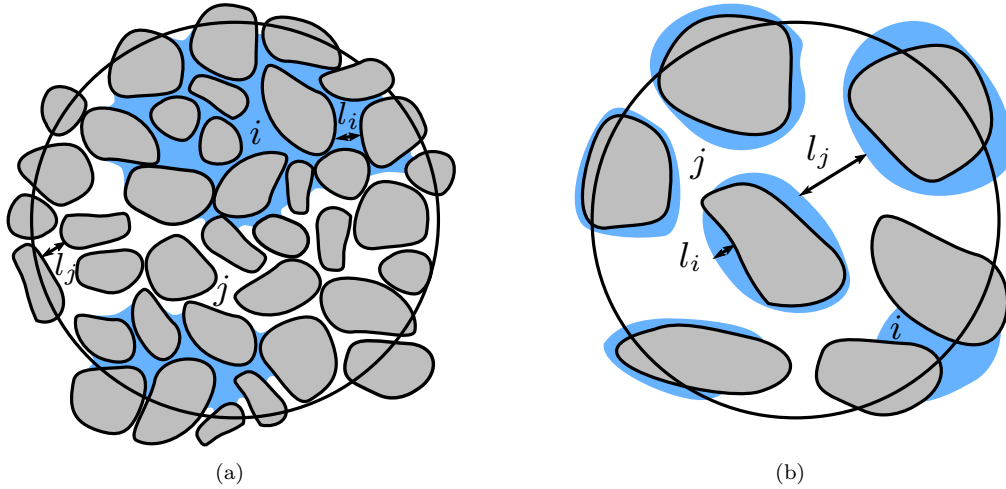


Figure 4.1 – Two-phase flow within porous media - a) low permeability b) high permeability

The preponderance of some effects compared to others for a two-phase system is quantified using the Reynolds Re , Capillary Ca and Bond Bo numbers. We recall that they read (for i , and respectively for j)

$$Re_i = \frac{\rho_i \|\langle \mathbf{u}_i \rangle^i\| l_i}{\mu_i}, \quad Ca_i = \frac{\mu_i \|\langle \mathbf{u}_i \rangle^i\|}{\gamma}, \quad Bo_i = \frac{(\rho_i - \rho_j) g l_i^2}{\gamma}, \quad (4.1)$$

where γ is the surface tension of the couple of fluid i, j . Flows in highly permeable media, inevitably, are more prone to exhibit high Bond, Capillary, and Reynolds numbers. This is due to the large pore-scale and to higher values of the averaged velocities. This is the case in the distillation process, where the liquid flows

as a thin film, wetting the entire surface of the structure and forming meniscus only at the contact points between two corrugated sheets [9]. As mentioned in the introduction, the Reynolds number of the vapor phase can be as high as $Re_g = 20000$ for the highest flow rates and be up to $Re_l = 200$ for the liquid phase. Estimations of the upper bounds for the Bond and Capillary numbers for the liquid phase are about $Bo_w \sim 50$ and $Ca_w \sim 2 \times 10^{-3}$, which is high for two-phase flows in porous media. The problem is, however, that it goes against a common assumption used in the modeling of immiscible fluids in porous media, which is to hypothesize predominant capillary effects at the pore-scale. Indeed, models generally used in the literature rely on the assumption of a quasi-static fluid-fluid interface, which does not necessarily mean that the system is steady but that the evolution of the interface is slow. Also, this means that the interface curvature is essentially determined by the difference of the fluid pressures. This situation translates macroscopically into the notion of a macroscale capillary pressure

$$P_c = \langle p_j \rangle^j - \langle p_i \rangle^i = 2\gamma \langle H \rangle_{ij}, \quad (4.2)$$

that states that the average of the curvature H of the interface Γ_{ij} , $\langle H \rangle_{ij}$, is controlled by the difference of the averaged pressures ($\langle \cdot \rangle_{ij}$ refers to the surface average on Γ_{ij} , see Eq. 2.12).

Knowing these issues, how can two-phase flows in highly permeable media be characterized? Starting from the mathematical problem at the local scale, we propose to discuss the volume averaging method for two-phase flows in porous media. The method presented here was introduced initially by Whitaker [187] (1986) for creeping flows, and was further developed later by Torres [53] (1987) and Lasseux et al. [103] (1996), [101] (2008, inertial flows). Some of the steps of the developments are somehow classical and are not developed in details here, but can be found in the works referred above. Although the analysis relies on strong assumptions for the flow at pore-scale (quasi-staticity, strong capillary effects, etc), that are not verified in our case, it is interesting to discuss on the consequences of these assumptions, and to what extent they are required to establish a closure. These developments will indeed serve as a basis for the development of our model for more dynamic flows in the next chapter.

At the end of this chapter, we continue the reflection with an analysis of the momentum exchange between two immiscible fluid phases in porous media. This exchange is characterized by the macroscopic cross-terms that appear in the momentum balance at macroscale. It can be of primary importance for two-phase flows in highly permeable media, and especially for gas-liquid flows in columns equipped with structured packings. This analysis is presented in a paper that was published in *Physical Review Fluids*.

4.2 Two-phase flow model at macroscale: step by step method

4.2.1 Step 1: Mathematical problem at pore-scale

A system of two immiscible fluid phases i and j in a domain Ω is considered. The wetting phase is assumed to wet perfectly the medium, i.e., triple line effects are not considered. This assumption is verified in the distillation process, but it is known that triple line effects are encountered in other separation processes in structured packings ([174] for instance, using an aqueous amine solution). Assuming constant densities and viscosities, the mass and momentum conservation equations at the pore-scale respectively read

$$\nabla \cdot \mathbf{u}_\alpha = 0 \quad \text{in } \Omega_\alpha, \quad \alpha = i, j, \quad (4.3a)$$

and

$$\rho_\alpha \left(\frac{\partial \mathbf{u}_\alpha}{\partial t} + \mathbf{u}_\alpha \cdot \nabla \mathbf{u}_\alpha \right) = -\nabla p_\alpha + \nabla \cdot \left[\mu_\alpha \left(\nabla \mathbf{u}_\alpha + (\nabla \mathbf{u}_\alpha)^T \right) \right] + \rho_\alpha \mathbf{g} \quad \text{in } \Omega_\alpha, \quad \alpha = i, j. \quad (4.3b)$$

This system of conservation equations is completed by boundary conditions, including no-slip conditions at the walls

$$\mathbf{u}_\alpha = 0 \text{ at } \Gamma_{\alpha\sigma} \quad \alpha = i, j, \quad (4.3c)$$

where σ refers to the solid structure. The continuity of velocities at the interface Γ_{ij}

$$\mathbf{u}_i = \mathbf{u}_j \text{ at } \Gamma_{ij}, \quad (4.3d)$$

is also verified, as well as the balance of the stress jump at Γ_{ij}

$$-p_i \mathbf{n}_{ij} + \mu_i \mathbf{n}_{ij} \cdot \left[\nabla \mathbf{u}_i + (\nabla \mathbf{u}_i)^T \right] = -p_j \mathbf{n}_{ij} + \mu_j \mathbf{n}_{ij} \cdot \left[\nabla \mathbf{u}_j + (\nabla \mathbf{u}_j)^T \right] + 2\gamma H \mathbf{n}_{ij} \text{ at } \Gamma_{ij}, \quad (4.3e)$$

where γ is the surface tension and H is the local curvature of the interface. Finally, assuming that there is no phase change, the velocity of the interface Γ_{ij} verifies

$$\mathbf{n}_{ij} \cdot \mathbf{w}_{ij} = \mathbf{n}_{ij} \cdot \mathbf{u}_i = \mathbf{n}_{ij} \cdot \mathbf{u}_j \text{ at } \Gamma_{ij}. \quad (4.4)$$

This relationship is however not true if one considers the exchange of chemical species in the distillation process [66].

4.2.2 Step 2: volume averaging

The volume averaging of the mass conservation equation Eq. 4.3a for phases i and j leads to

$$\nabla \cdot \langle \mathbf{u}_\alpha \rangle + \frac{1}{V_\alpha} \int_{\Gamma_{\alpha\sigma} \cup \Gamma_{ij}} \mathbf{n}_\alpha \cdot \mathbf{u}_\alpha d\Gamma = 0 \quad \alpha = i, j, \quad (4.5)$$

where the notation \mathbf{n}_α denotes the normal vector to the interfaces with the phase α . This relation simplifies in

$$\nabla \cdot \langle \mathbf{u}_\alpha \rangle + \frac{1}{V_\alpha} \int_{\Gamma_{ij}} \mathbf{n}_\alpha \cdot \mathbf{u}_\alpha d\Gamma = 0 \quad \alpha = i, j, \quad (4.6)$$

when one considers the no-slip condition $\mathbf{u}_\alpha = 0$ at $\Gamma_{\alpha\sigma}$. It is now relevant to introduce the velocity \mathbf{w}_{ij} of the interface Γ_{ij}

$$\nabla \cdot \langle \mathbf{u}_\alpha \rangle + \frac{1}{V_\alpha} \int_{\Gamma_{ij}} \mathbf{n}_\alpha \cdot (\mathbf{u}_\alpha - \mathbf{w}_{ij}) d\Gamma + \frac{1}{V_\alpha} \int_{\Gamma_{ij}} \mathbf{n}_\alpha \cdot \mathbf{w}_{ij} d\Gamma = 0 \quad \alpha = i, j. \quad (4.7)$$

Using the relation Eq. 2.19, $\varepsilon \frac{\partial S_\alpha}{\partial t} = \frac{1}{V_\alpha} \int_{\Gamma_{ij}} \mathbf{n}_\alpha \cdot \mathbf{w}_{ij} d\Gamma$, introduced in Chapter 2, it comes

$$\varepsilon \frac{\partial S_\alpha}{\partial t} + \nabla \cdot \langle \mathbf{u}_\alpha \rangle + \frac{1}{V_\alpha} \int_{\Gamma_{ij}} \mathbf{n}_\alpha \cdot (\mathbf{u}_\alpha - \mathbf{w}_{ij}) d\Gamma = 0 \quad \alpha = i, j. \quad (4.8)$$

This relation involves an integral term in $\mathbf{n}_\alpha \cdot (\mathbf{u}_\alpha - \mathbf{w}_{ij})$, which might be of importance if the interfacial mass transfer is strong. In case of immiscible fluid phases, it reduces to zero based on the relation Eq. 4.4. It therefore comes

$$\varepsilon \frac{\partial S_\alpha}{\partial t} + \nabla \cdot \langle \mathbf{u}_\alpha \rangle = 0 \quad \alpha = i, j. \quad (4.9)$$

This relation characterizes the evolution of the fluid saturation S_α within the medium at large scale. This is a *closed* relation, in the sense that it contains only averaged quantities.

The macroscale momentum relation Eq. 4.3b requires a more complex treatment. By averaging and using the theorems of volume averaging, we first establish the intrinsic average of the momentum equations of the phases i and j

$$\begin{aligned} \rho_\alpha \frac{\partial \langle \mathbf{u}_\alpha \rangle^\alpha}{\partial t} + \rho_\alpha \nabla \cdot \langle \mathbf{u}_\alpha \mathbf{u}_\alpha \rangle^\alpha &= -\nabla \langle p_\alpha \rangle^\alpha + \rho_\alpha \mathbf{g} + \mu_\alpha \nabla^2 \langle \mathbf{u}_\alpha \rangle^\alpha + \\ \frac{1}{V_\alpha} \int_{\Gamma_{\alpha\sigma} \cup \Gamma_{ij}} \mathbf{n}_\alpha \cdot \left[-p_\alpha \mathbf{I} + \mu_\alpha \left(\nabla \mathbf{u}_\alpha + (\nabla \mathbf{u}_\alpha)^T \right) \right] d\Gamma, \quad \alpha &= i, j. \end{aligned} \quad (4.10)$$

Using the theorems of volume averaging and the decomposition in average plus deviation, the intrinsic average momentum balance for phases i and j becomes after simplification

$$\begin{aligned} \rho_\alpha \frac{\partial \langle \mathbf{u}_\alpha \rangle^\alpha}{\partial t} + \rho_\alpha \langle \mathbf{u}_\alpha \rangle^\alpha \cdot \nabla \langle \mathbf{u}_\alpha \rangle^\alpha + \rho_\alpha \varepsilon_\alpha^{-1} \nabla \cdot \langle \tilde{\mathbf{u}}_\alpha \tilde{\mathbf{u}}_\alpha \rangle &= -\nabla \langle p_\alpha \rangle^\alpha + \rho_\alpha \mathbf{g} + \\ \frac{1}{V_\alpha} \int_{\Gamma_{\alpha\sigma} \cup \Gamma_{ij}} \mathbf{n}_\alpha \cdot \left[-\tilde{p}_\alpha \mathbf{I} + \mu_\alpha \left(\nabla \tilde{\mathbf{u}}_\alpha + (\nabla \tilde{\mathbf{u}}_\alpha)^T \right) \right] d\Gamma - \mu_\alpha \varepsilon_\alpha^{-1} \left(\nabla^2 \langle \mathbf{u}_\alpha \rangle^\alpha + \nabla \varepsilon_\alpha \cdot \nabla \langle \mathbf{u}_\alpha \rangle^\alpha \right), \quad \alpha &= i, j. \end{aligned} \quad (4.11)$$

The terms in this relation can be identified as follows

- the two first terms correspond respectively to a macroscopic acceleration and to a macroscopic convection.
- the term $\rho_\alpha \varepsilon_\alpha^{-1} \nabla \cdot \langle \tilde{\mathbf{u}}_\alpha \tilde{\mathbf{u}}_\alpha \rangle$ contains information from the local scale and is referred as a dispersion term.
- the term $-\nabla \langle p_\alpha \rangle^\alpha + \rho_\alpha \mathbf{g}$ is the pressure drop in the flow.
- the integral term is often referred to as a *surface filter*, and corresponds to the pressure and viscous stress at the interfaces.
- the terms involving gradients of the averaged velocity, on the right hand side, are known as the Brinkman terms. They are often considered negligible far from the boundary conditions, where the averaged velocity is nearly uniform.

This momentum balance is said as *unclosed*, as it mixes terms varying at the pore-scale, \tilde{p}_α , $\tilde{\mathbf{u}}_\alpha$, and averaged quantities varying at a much larger scale $\langle p_\alpha \rangle^\alpha$, $\langle \mathbf{u}_\alpha \rangle^\alpha$. It will be seen later that some of these terms are negligible compared to others, and can be removed. Now, the step is to *close* the system, which is achieved by constructing approximations of the deviation terms \tilde{p}_α and $\tilde{\mathbf{u}}_\alpha$, thus relating the micro and the macro scales.

4.2.3 Step 3: Problem on the deviations

Mass and momentum balances The boundary value problems on the perturbations is in particular established by subtracting the averaged system from the system at the microscale. Subtracting the averaged

mass balance Eq. 4.8 from the mass balance at the local scale Eq. 4.3a leads to

$$\nabla \cdot \tilde{\mathbf{u}}_\alpha = 0 \quad \text{in } \Omega_\alpha, \quad \alpha = i, j, \quad (4.12)$$

if one assumes that

$$\varepsilon \frac{\partial S_\alpha}{\partial t} \ll \nabla \cdot \tilde{\mathbf{u}}_\alpha, \quad \alpha = i, j, \quad (4.13)$$

This condition holds if the characteristic time for the variations of S_α , t_α^* , is such that

$$t_\alpha^* \gg \frac{l_\alpha}{\|\langle \mathbf{u}_\alpha \rangle^\alpha\|}, \quad \alpha = i, j, \quad (4.14)$$

where $\nabla \cdot \tilde{\mathbf{u}}_\alpha \sim \frac{\|\langle \mathbf{u}_\alpha \rangle^\alpha\|}{l_\alpha}$. Using the relation $\varepsilon \frac{\partial S_\alpha}{\partial t} = \frac{1}{V_\alpha} \int_{\Gamma_{ij}} \mathbf{n}_\alpha \cdot \mathbf{w}_{ij} d\Gamma$, the constraint also reads

$$\left\| \mathbf{n}_\alpha \cdot \langle \mathbf{w}_{ij} \rangle_{ij} \right\| \ll \|\langle \mathbf{u}_\alpha \rangle^\alpha\|, \quad \alpha = i, j, \quad (4.15)$$

if one estimates the interfacial area per unit volume $\frac{\Gamma_{ij}}{V_\alpha}$ to be on the order of $\frac{1}{l_\alpha}$. This estimation constrains the interface Γ_{ij} to be quasi-static compared to the flow process. It is well-known, however, that such a condition is not verified in case of rapid pore-scale displacements events, also referred to as Haines jumps [55, 12] (or snap-off, ganglion dynamics). Experimental and numerical analysis were proposed recently [55, 12], showing that the Haines jumps correspond to successive reconfigurations of the system. In between these reconfigurations, though, the interface can be considered as quasi-static compared to the fluid flow. In the distillation process in normal operating conditions (apart from flooding), there are no such Haines jumps or snap-off, but the propagation of a train of soliton-like waves at the surface of the film also raises questions regarding the hypothesis of quasi-staticity.

Similarly, the momentum conservation equation is obtained by subtracting the averaged momentum balance Eq. 4.11 from the momentum balance at pore-scale Eq. 4.3b. After simplifications based on the orders of magnitude of the different terms [101], it reduces to

$$\rho_\alpha \mathbf{u}_\alpha \cdot \nabla \tilde{\mathbf{u}}_\alpha = -\nabla \tilde{p}_\alpha + \mu_\alpha \nabla^2 \tilde{\mathbf{u}}_\alpha - \frac{1}{V_\alpha} \int_{\Gamma_{\alpha\sigma} \cup \Gamma_{ij}} \mathbf{n}_\alpha \cdot \left(-\tilde{p}_\alpha \mathbf{I} + \mu_\alpha \left(\nabla \tilde{\mathbf{u}}_\alpha + (\nabla \tilde{\mathbf{u}}_\alpha)^T \right) \right) d\Gamma \quad \text{in } \Omega_\alpha, \quad \alpha = i, j. \quad (4.16)$$

In this relation, the acceleration term $\rho_\alpha \frac{\partial \tilde{\mathbf{u}}_\alpha}{\partial t}$ is especially neglected if the process is observed at times much larger than the time corresponding to the viscous relaxation of the flow

$$t_\alpha^* \gg \frac{\rho_\alpha l_\alpha^2}{\mu_\alpha}, \quad \alpha = i, j. \quad (4.17)$$

This concerns for instance the relaxation of any perturbations close to the boundary conditions or the relaxation of an initial state of the flow. The system must therefore be observed after a certain amount of time. This condition is not necessarily verified in case of time-dependent boundary conditions, or when one considers intrinsically unsteady flows (for instance train of bubbles). It is however required for the establishment of the closure as it allows to obtain a steady-state problem at the pore-scale for the perturbations.

Together with the time-scale constraint Eq. 4.14, the system must be considered at a time t^* such that

$$t^* \gg \max \left[\max_{\alpha=i,j} \left(\frac{\rho_\alpha l_\alpha^2}{\mu_\alpha} \right), \max_{\alpha=l,g} \left(\frac{l_\alpha}{\|\langle \mathbf{u}_\alpha \rangle^\alpha\|} \right) \right]. \quad (4.18)$$

Boundary conditions By decomposing the boundary conditions Eqs 4.3c to 4.3e using an average plus perturbation decomposition, it comes respectively

$$\tilde{\mathbf{u}}_\alpha = -\langle \mathbf{u}_\alpha \rangle^\alpha \text{ at } \Gamma_{\alpha\sigma} \quad \alpha = i, j, \quad (4.19)$$

$$\tilde{\mathbf{u}}_i = \tilde{\mathbf{u}}_j + \langle \mathbf{u}_j \rangle^j - \langle \mathbf{u}_i \rangle^i \text{ at } \Gamma_{ij}, \quad (4.20)$$

$$\mathbf{n}_{ij} (\tilde{p}_j - \tilde{p}_i) + \mathbf{n}_{ij} \left(\langle p_j \rangle^j - \langle p_i \rangle^i \right) = \mu_j \mathbf{n}_{ij} \cdot \left(\nabla \tilde{\mathbf{u}}_j + (\nabla \tilde{\mathbf{u}}_j)^T \right) - \mu_i \mathbf{n}_{ij} \cdot \left(\nabla \tilde{\mathbf{u}}_i + (\nabla \tilde{\mathbf{u}}_i)^T \right) + 2\gamma H \mathbf{n}_{ij} \text{ at } \Gamma_{ij}, \quad (4.21)$$

where the macroscale velocity gradients are neglected as they vary at a much larger scale than the gradients of the velocity perturbations. At this stage, to be able to totally understand the issues involved in the derivation of closure relationships, it is interesting to focus on the continuity of the constraints at the interface Γ_{ij} , Eq. 4.21. To highlight the different forces that contribute to the deformation of the interface, we consider the effects of the averaged pressure fields at all points $\mathbf{x} + \mathbf{y}$ in the REV on the stress-jump. This variation is estimated via a Taylor series approximation, so that the pressure field p_i reads for instance

$$p_i|_{\mathbf{x}+\mathbf{y}_i} = \left[\langle p_i \rangle^i \Big|_{\mathbf{x}} + \mathbf{y}_i \cdot \nabla \langle p_i \rangle^i \Big|_{\mathbf{x}} + \mathcal{O}(\mathbf{y}_i^2) \right] + \tilde{p}_i|_{\mathbf{x}+\mathbf{y}_i},$$

where \mathbf{y}_i indicates the position in the phase i from the centroid of the averaging volume \mathbf{x} . Considering only the first order development, the stress-jump can be rewritten as follows

$$\begin{aligned} & \mathbf{n}_{ij} \left(\langle p_j \rangle^j \Big|_{\mathbf{x}} - \langle p_i \rangle^i \Big|_{\mathbf{x}} \right) + \underbrace{\mathbf{n}_{ij} \mathbf{y} \cdot \left[\left(\nabla \langle p_j \rangle^j \Big|_{\mathbf{x}} - \rho_j \mathbf{g} \right) - \left(\nabla \langle p_i \rangle^i \Big|_{\mathbf{x}} - \rho_i \mathbf{g} \right) \right]}_{\text{dynamic pressure}} + \underbrace{\mathbf{n}_{ij} \mathbf{y} \cdot (\rho_j - \rho_i) \mathbf{g}}_{\text{hydrostatic pressure}} \\ & = -\mathbf{n}_{ij} (\tilde{p}_j - \tilde{p}_i) + \mu_j \mathbf{n}_{ij} \cdot \left(\nabla \tilde{\mathbf{u}}_j + (\nabla \tilde{\mathbf{u}}_j)^T \right) - \mu_i \mathbf{n}_{ij} \cdot \left(\nabla \tilde{\mathbf{u}}_i + (\nabla \tilde{\mathbf{u}}_i)^T \right) + 2\gamma H \mathbf{n}_{ij} \text{ at } \Gamma_{ij}, \end{aligned} \quad (4.22)$$

where the hydrostatic pressure terms were voluntarily considered separately. The different contributions can be listed as

- the difference of the averaged pressures $\langle p_j \rangle^j \Big|_{\mathbf{x}} - \langle p_i \rangle^i \Big|_{\mathbf{x}}$,
- dynamic contributions, related to the term $\mathbf{n}_{ij} \mathbf{y} \cdot \left[\left(\nabla \langle p_j \rangle^j \Big|_{\mathbf{x}} - \rho_j \mathbf{g} \right) - \left(\nabla \langle p_i \rangle^i \Big|_{\mathbf{x}} - \rho_i \mathbf{g} \right) \right]$ and to the variations of the pressure deviations $\mathbf{n}_{ij} (\tilde{p}_j - \tilde{p}_i)$,
- a gravity effect $\mathbf{n}_{ij} \mathbf{y} \cdot (\rho_j - \rho_i) \mathbf{g}$ due the density contrast,
- viscous effects, characterized by the terms $\mu_j \mathbf{n}_{ij} \cdot \left(\nabla \tilde{\mathbf{u}}_j + (\nabla \tilde{\mathbf{u}}_j)^T \right)$ and $\mu_i \mathbf{n}_{ij} \cdot \left(\nabla \tilde{\mathbf{u}}_i + (\nabla \tilde{\mathbf{u}}_i)^T \right)$.

It is seen here that the fluid-fluid interface is submitted to deformations arising from various phenomena, and at different scales. Stricto sensu, the closure of the two-phase system should account for these different contributions. To further analyze the relative importance of the different terms, it is therefore suggested to consider the surface average of the stress jump on the interface Γ_{ij} , $\langle \cdot \rangle_{ij}(\mathbf{x})$. This allows to introduce the averaged surface curvature $\langle H \rangle_{ij}$, following the idea from the work of Whitaker [187]. By considering the projection on the normal \mathbf{n}_{ij} , it comes

$$\begin{aligned} & \left\langle \left(\langle p_j \rangle^j \Big|_{\mathbf{x}} - \langle p_i \rangle^i \Big|_{\mathbf{x}} \right) \right\rangle_{ij} + \left\langle \mathbf{y} \cdot \left[\left(\nabla \langle p_j \rangle^j \Big|_{\mathbf{x}} - \rho_j \mathbf{g} \right) - \left(\nabla \langle p_i \rangle^i \Big|_{\mathbf{x}} - \rho_i \mathbf{g} \right) \right] \right\rangle_{ij} + \langle \mathbf{y} \cdot (\rho_j - \rho_i) \mathbf{g} \rangle_{ij} \\ & = \left\langle -(\tilde{p}_j - \tilde{p}_i) + \mu_j \mathbf{n}_{ij} \cdot \left(\nabla \tilde{\mathbf{u}}_j + (\nabla \tilde{\mathbf{u}}_j)^T \right) - \mu_i \mathbf{n}_{ij} \cdot \left(\nabla \tilde{\mathbf{u}}_i + (\nabla \tilde{\mathbf{u}}_i)^T \right) \right\rangle_{ij} + 2\gamma \langle H \rangle_{ij} \text{ at } \Gamma_{ij}, \end{aligned} \quad (4.23)$$

Using the fact that the terms $\langle p_\alpha \rangle^\alpha|_{\mathbf{x}}$, $\nabla \langle p_\alpha \rangle^\alpha|_{\mathbf{x}}$ and $\rho_\alpha \mathbf{g}$ are constant along the surface average and can be extracted from the integral, it comes

$$\begin{aligned} & \left(\langle p_j \rangle^j|_{\mathbf{x}} - \langle p_i \rangle^i|_{\mathbf{x}} \right) + \langle \mathbf{y} \rangle_{ij} \cdot \left[\left(\nabla \langle p_j \rangle^j|_{\mathbf{x}} - \rho_j \mathbf{g} \right) - \left(\nabla \langle p_i \rangle^i|_{\mathbf{x}} - \rho_i \mathbf{g} \right) \right] + (\rho_j - \rho_i) \langle \mathbf{y} \rangle_{ij} \cdot \mathbf{g} \\ & = \left\langle -\mathbf{n}_{ij} (\tilde{p}_j - \tilde{p}_i) + \mu_j \mathbf{n}_{ij} \cdot \left(\nabla \tilde{\mathbf{u}}_j + (\nabla \tilde{\mathbf{u}}_j)^T \right) - \mu_i \mathbf{n}_{ij} \cdot \left(\nabla \tilde{\mathbf{u}}_i + (\nabla \tilde{\mathbf{u}}_i)^T \right) \right\rangle_{ij} + 2\gamma \langle H \rangle_{ij} \text{ at } \Gamma_{ij}, \end{aligned} \quad (4.24)$$

where $\langle \mathbf{y} \rangle_{ij}$ is the averaged position of the interface Γ_{ij} . An estimation of the pressure deviations \tilde{p}_i and \tilde{p}_j can then be roughly made using the momentum balance on the perturbations, Eq. 4.16,

$$\tilde{p}_\alpha \sim \mathcal{O} \left(\mu_\alpha l_\alpha \|\nabla^2 \tilde{\mathbf{u}}_\alpha\| + \rho_\alpha l_\alpha \|\mathbf{u}_\alpha \cdot \nabla \tilde{\mathbf{u}}_\alpha\| \right), \quad \alpha = i, j. \quad (4.25)$$

Using this estimation, one can also non-dimensionalize Eq. 4.24 with the capillary pressure $2\gamma \langle H \rangle_{ij}$ in order to identify relevant dimensionless numbers. It yields

$$\begin{aligned} & \frac{\left(\langle p_j \rangle^j|_{\mathbf{x}} - \langle p_i \rangle^i|_{\mathbf{x}} \right)}{2\gamma \langle H \rangle_{ij}} + \frac{\langle \mathbf{y} \rangle_{ij} \cdot \left[\left(\nabla \langle p_j \rangle^j|_{\mathbf{x}} - \rho_j \mathbf{g} \right) - \left(\nabla \langle p_i \rangle^i|_{\mathbf{x}} - \rho_i \mathbf{g} \right) \right]}{2\gamma \langle H \rangle} + \frac{\langle \mathbf{y} \rangle_{ij} \cdot (\rho_j - \rho_i) \mathbf{g}}{2\gamma \langle H \rangle_{ij}} \\ & \sim \frac{\max_{\alpha=i,j} \mathcal{O} \left(\mu_\alpha \langle \|\nabla \tilde{\mathbf{u}}_\alpha\| \rangle_{ij} \right)}{2\gamma \langle H \rangle_{ij}} + \frac{\max_{\alpha=i,j} \mathcal{O} \left(\rho_\alpha l_\alpha \|\mathbf{u}_\alpha \cdot \nabla \tilde{\mathbf{u}}_\alpha\| \right)}{2\gamma \langle H \rangle_{ij}} + 1 \text{ at } \Gamma_{ij}, \end{aligned} \quad (4.26)$$

or, by introducing different dimensionless numbers,

$$\frac{\left(\langle p_j \rangle^j|_{\mathbf{x}} - \langle p_i \rangle^i|_{\mathbf{x}} \right)}{2\gamma \langle H \rangle_{ij}} + Bo_d + Bo \sim Ca_\alpha \frac{1}{l_\alpha \langle H \rangle_{ij}} + Ca_\alpha Re_\alpha \frac{1}{l_\alpha \langle H \rangle_{ij}} + 1 \text{ at } \Gamma_{ij}. \quad (4.27)$$

The dimensionless numbers read as follows

- a Bond number $Bo = \frac{(\rho_j - \rho_i) \|\langle \mathbf{y} \rangle_{ij} \cdot \mathbf{g}\|}{2\gamma \langle H \rangle_{ij}} \sim \frac{(\rho_j - \rho_i) gl}{2\gamma \langle H \rangle_{ij}}$, when one estimates the averaged position of the interface to be on the order of the pore lengthscale $\langle \mathbf{y} \rangle_{ij} \sim l$. The Bond number is likely to be small in case of a small pore-scale l , i.e. in low permeability media, and if the averaged curvature of the interface $\langle H \rangle_{ij}$ is large. This constitutes a drastic assumption for two-phase flows in highly permeable porous media, where conversely l is quite large, and which are more prone to generate films, i.e. a moderate curvature $\langle H \rangle_{ij}$ of the interface. In structured packings, it will more likely be true in dense packings (more than $500m^2/m^3$), where the number of contact points between the sheets is high, which favors the development of meniscus.
- a dynamic Bond number $Bo_d = \frac{\langle \mathbf{y} \rangle_{ij} \cdot \left[\left(\nabla \langle p_j \rangle^j|_{\mathbf{x}} - \rho_j \mathbf{g} \right) - \left(\nabla \langle p_i \rangle^i|_{\mathbf{x}} - \rho_i \mathbf{g} \right) \right]}{2\gamma \langle H \rangle_{ij}} \sim \frac{l \left\| \left(\nabla \langle p_j \rangle^j|_{\mathbf{x}} - \rho_j \mathbf{g} \right) - \left(\nabla \langle p_i \rangle^i|_{\mathbf{x}} - \rho_i \mathbf{g} \right) \right\|}{2\gamma \langle H \rangle_{ij}}$. The dynamic Bond number is zero in the limit of a quasi-static interface, $\nabla \langle p_\alpha \rangle^\alpha|_{\mathbf{x}} = \rho_\alpha \mathbf{g}$, but can affect the interface if $\nabla \langle p_\alpha \rangle^\alpha|_{\mathbf{x}} \neq \rho_\alpha \mathbf{g}$. This is typically the case in chemical reactors, where the gas phase is often forced co or counter-currently to the liquid phase, leading to a strong pressure gradient.
- a Capillary number, when one expresses $\frac{\max_{\alpha=i,j} \mathcal{O} \left(\mu_\alpha \langle \|\nabla \tilde{\mathbf{u}}_\alpha\| \rangle_{ij} \right)}{2\gamma \langle H \rangle_{ij}} \sim \frac{\mu_\alpha \|\langle \mathbf{u}_\alpha \rangle^\alpha\|}{2\gamma} \frac{1}{l_\alpha \langle H \rangle_{ij}} \sim Ca_\alpha \frac{1}{l_\alpha \langle H \rangle_{ij}}$, $\alpha = i, j$. This term is negligible at low Capillary numbers and if $\langle H \rangle_{ij}$ is large, which is more prone to occur in low permeable media.
- a Reynolds number, when one expresses $\frac{\max_{\alpha=i,j} \mathcal{O} \left(\rho_\alpha l_\alpha \|\mathbf{u}_\alpha \cdot \nabla \tilde{\mathbf{u}}_\alpha\| \right)}{2\gamma \langle H \rangle_{ij}} \sim \frac{\mu_\alpha \|\langle \mathbf{u}_\alpha \rangle^\alpha\|}{2\gamma} \frac{\rho_\alpha l_\alpha \|\langle \mathbf{u}_\alpha \rangle^\alpha\|}{\mu_\alpha} \frac{1}{l_\alpha \langle H \rangle_{ij}} = Ca_\alpha Re_\alpha \frac{1}{l_\alpha \langle H \rangle_{ij}}$, $\alpha =$

i, j . A low Reynolds number is therefore required to keep this term low.

In the limit when these dimensionless numbers remain low, the relation Eq. 4.26 reduces to

$$\frac{\langle p_j \rangle^j \Big|_{\mathbf{x}} - \langle p_i \rangle^i \Big|_{\mathbf{x}}}{2\gamma \langle H \rangle_{ij}} \sim 1. \quad (4.28)$$

This is also the definition of the *macroscale capillary pressure* evocated earlier

$$\langle p_j \rangle^j - \langle p_i \rangle^i = 2\gamma \langle H \rangle_{ij}. \quad (4.29)$$

This relation means that the difference of the averaged pressures $\langle p_j \rangle^j - \langle p_i \rangle^i$ controls the interface curvature. It relies on the conditions developed above, including low Bond (static and dynamic) and Capillary numbers. Keeping in mind the assumptions leading to the quasi-stationary interface, one can insert the relation Eq. 4.29 within the stress jump Eq. 4.21 for the perturbations. It yields

$$0 = -\mathbf{n}_{ij} (\tilde{p}_j - \tilde{p}_i) + \mu_j \mathbf{n}_{ij} \cdot \left(\nabla \tilde{\mathbf{u}}_j + (\nabla \tilde{\mathbf{u}}_j)^T \right) - \mu_i \mathbf{n}_{ij} \cdot \left(\nabla \tilde{\mathbf{u}}_i + (\nabla \tilde{\mathbf{u}}_i)^T \right) + 2\gamma \tilde{H} \mathbf{n}_{ij} \text{ at } \Gamma_{ij}, \quad (4.30)$$

where \tilde{H} is the local deviation $H - \langle H \rangle_{ij}$. One can see that the stress-jump at Γ_{ij} still involve the term $2\gamma \tilde{H} \mathbf{n}_{ij}$. Strictly speaking, this term should be considered as a source term for the mapping of the perturbations. It is however considered negligible at the closure scale [187, 53, 101], under the assumption that the mean curvature $\langle H \rangle_{ij}$ undergoes negligible variations within the averaging volume

$$\tilde{H} \ll \langle H \rangle_{ij}. \quad (4.31)$$

Therefore, under the conditions discussed thus far, one obtains a new mathematical problem on the perturbations \tilde{p}_α and $\tilde{\mathbf{u}}_\alpha$. It is also assumed that one can exhibit a representative elementary volume for the perturbations, so that periodic conditions can be assumed. The boundary value problem reads

$$\nabla \cdot \tilde{\mathbf{u}}_\alpha = 0 \quad \text{in } \Omega_\alpha, \quad \alpha = i, j, \quad (4.32a)$$

$$\rho_\alpha \mathbf{u}_\alpha \cdot \nabla \tilde{\mathbf{u}}_\alpha = -\nabla \tilde{p}_\alpha + \mu_\alpha \nabla^2 \tilde{\mathbf{u}}_\alpha - \frac{1}{V_\alpha} \int_{\Gamma_{\alpha\sigma} \cup \Gamma_{ij}} \mathbf{n}_\alpha \cdot \left[-\tilde{p}_\alpha \mathbf{I} + \mu_\alpha \left(\nabla \tilde{\mathbf{u}}_\alpha + (\nabla \tilde{\mathbf{u}}_\alpha)^T \right) \right] d\Gamma \quad \text{in } \Omega_\alpha, \quad \alpha = i, j, \quad (4.32b)$$

$$\tilde{\mathbf{u}}_\alpha = -\langle \mathbf{u}_\alpha \rangle^\alpha \text{ at } \Gamma_{\alpha\sigma}, \quad \alpha = i, j, \quad (4.32c)$$

$$\tilde{\mathbf{u}}_i = \tilde{\mathbf{u}}_j - \left(\langle \mathbf{u}_i \rangle^i - \langle \mathbf{u}_j \rangle^j \right) \text{ at } \Gamma_{ij}, \quad (4.32d)$$

$$0 = -\mathbf{n}_{ij} (\tilde{p}_j - \tilde{p}_i) + \mu_j \mathbf{n}_{ij} \cdot \left[\nabla \tilde{\mathbf{u}}_j + (\nabla \tilde{\mathbf{u}}_j)^T \right] - \mu_i \mathbf{n}_{ij} \cdot \left[\nabla \tilde{\mathbf{u}}_i + (\nabla \tilde{\mathbf{u}}_i)^T \right] \text{ at } \Gamma_{ij}. \quad (4.32e)$$

with periodicity conditions for the perturbations in a representative unit-cell of the system

$$\tilde{\mathbf{u}}_\alpha(\mathbf{r}) = \tilde{\mathbf{u}}_\alpha(\mathbf{r} + \mathbf{l}_k), \quad \alpha = i, j, \quad k = 1, 2, 3, \quad (4.32f)$$

$$\tilde{p}_\alpha(\mathbf{r}) = \tilde{p}_\alpha(\mathbf{r} + \mathbf{l}_k), \quad \alpha = i, j, \quad k = 1, 2, 3. \quad (4.32g)$$

At this stage of the procedure, it has been established

1. *unclosed* mass and momentum macroscale balances for the two phases, Eq. 4.8 and Eq. 4.11 respectively, in Section 4.2.2.

2. the boundary value problem that is verified at local scale by the perturbations, Eq 4.32, if one considers a quasi-static process and low Capillary, Bond and Reynolds numbers at the pore-scale.

Based on this mathematical problem, the next step consists in proposing closure relationships for the perturbations.

4.2.4 Step 4: Approximation of the perturbations

Closure problems The mathematical problem on the perturbations Eq 4.32 involves two “source terms”, $\langle \mathbf{u}_i \rangle^i$ and $\langle \mathbf{u}_j \rangle^j$. The representation of the perturbations is therefore seen as a linear combination of the two source terms, and reads respectively for the couples $(\tilde{p}_i, \tilde{\mathbf{u}}_i)$ and $(\tilde{p}_j, \tilde{\mathbf{u}}_j)$

$$\tilde{\mathbf{u}}_i = \mathbf{A}_{ii} \cdot \langle \mathbf{u}_i \rangle^i + \mathbf{A}_{ij} \cdot \langle \mathbf{u}_j \rangle^j, \quad (4.33a)$$

$$\tilde{p}_i = \mu_i \left[\mathbf{a}_{ii} \cdot \langle \mathbf{u}_i \rangle^i + \mathbf{a}_{ij} \cdot \langle \mathbf{u}_j \rangle^j \right], \quad (4.33b)$$

and

$$\tilde{\mathbf{u}}_j = \mathbf{A}_{ji} \cdot \langle \mathbf{u}_i \rangle^i + \mathbf{A}_{jj} \cdot \langle \mathbf{u}_j \rangle^j, \quad (4.34a)$$

$$\tilde{p}_j = \mu_j \left[\mathbf{a}_{ji} \cdot \langle \mathbf{u}_i \rangle^i + \mathbf{a}_{jj} \cdot \langle \mathbf{u}_j \rangle^j \right], \quad (4.34b)$$

where the couples $(\mathbf{a}_{ii}, \mathbf{A}_{ii})$ and $(\mathbf{a}_{ij}, \mathbf{A}_{ij})$ are the closure variables for $(\tilde{p}_i, \tilde{\mathbf{u}}_i)$ and $(\mathbf{a}_{jj}, \mathbf{A}_{jj})$ and $(\mathbf{a}_{ji}, \mathbf{A}_{ji})$ the closure variables for $(\tilde{p}_j, \tilde{\mathbf{u}}_j)$ respectively. To achieve that result, we adopt the approximation that the equations are homogeneous with respect to the averaged velocities $\langle \mathbf{u}_i \rangle^i$ and $\langle \mathbf{u}_j \rangle^j$. This is only an approximation since in principle the mapping variables should also depend on the averaged velocities. These representations can be inserted in the boundary value problem for the perturbations, Eqs 4.32. One obtains two boundary values problems respectively on, the couples $(\mathbf{a}_{ii}, \mathbf{A}_{ii})$ and $(\mathbf{a}_{ij}, \mathbf{A}_{ij})$, and the couples $(\mathbf{a}_{jj}, \mathbf{A}_{jj})$ and $(\mathbf{a}_{ji}, \mathbf{A}_{ji})$. These two problems are given in the Appendix B.1. These closure problems still involve the velocities \mathbf{u}_i and \mathbf{u}_j of the flow at pore-scale, from the inertial term $\rho_\alpha \mathbf{u}_\alpha \cdot \nabla \tilde{\mathbf{u}}_\alpha$ in Eq. 4.32b. In the limit of a creeping flow, this term vanishes to zero. When this terms is non-zero, however, the resolution of the closure problems requires to solve initially the flow at pore-scale in order to obtain \mathbf{u}_i and \mathbf{u}_j in the representative unit-cell of the system. In the same spirit, the resolution of the closure problem in Chapter 3 required to resolve the flow at the microscale beforehand to get the velocity field. The resolution of these closure problems has not been published yet in the literature.

4.2.5 Step 5: Closure at macroscale

Given the representations of the perturbations Eqs 4.33 and 4.34, it is now possible to close the momentum balance that results from the volume averaging method Eq. 4.11. Prior to that, the relation is reassessed as some of the terms become negligible due to the constraints introduced throughout the developments. We recall that the unclosed macroscale momentum balance reads

$$\begin{aligned} & \rho_\alpha \frac{\partial \langle \mathbf{u}_\alpha \rangle^\alpha}{\partial t} + \rho_\alpha \langle \mathbf{u}_\alpha \rangle^\alpha \cdot \nabla \langle \mathbf{u}_\alpha \rangle^\alpha + \rho_\alpha \varepsilon_\alpha^{-1} \nabla \cdot \langle \tilde{\mathbf{u}}_\alpha \tilde{\mathbf{u}}_\alpha \rangle = -\nabla \langle p_\alpha \rangle^\alpha + \rho_\alpha \mathbf{g} + \\ & \frac{1}{V_\alpha} \int_{\Gamma_{\alpha\sigma} \cup \Gamma_{ij}} \mathbf{n}_\alpha \cdot \left[-\tilde{p}_\alpha \mathbf{I} + \mu_\alpha (\nabla \tilde{\mathbf{u}}_\alpha + \nabla \tilde{\mathbf{u}}_\alpha^T) \right] d\Gamma - \mu_\alpha \varepsilon_\alpha^{-1} (\nabla^2 \langle \mathbf{u}_\alpha \rangle^\alpha + \nabla \varepsilon_\alpha \cdot \nabla \langle \mathbf{u}_\alpha \rangle^\alpha), \quad \alpha = i, j. \end{aligned} \quad (4.35)$$

The terms $\mu_\alpha \varepsilon_\alpha^{-1} \nabla^2 \langle \mathbf{u}_\alpha \rangle$ and $\mu_\alpha \varepsilon_\alpha^{-1} \nabla \varepsilon_\alpha \cdot \nabla \langle \mathbf{u}_\alpha \rangle^\alpha$, referred to as the Brinkman terms, are generally considered negligible, as they consist in large scale variations. They can be of importance close to the boundary conditions, where the gradients of saturation or averaged velocities are stronger. In columns equipped with structured packings, the boundary conditions may play a significant role at the side of the column or at the transition between packs, and it might be required to keep these terms. In the bulk of the column, however, the Brinkman terms can be safely neglected. Also, under the time-scale constraint Eq. 4.18 that guarantees that the process is quasi-static, the acceleration term $\rho_\alpha \frac{\partial \langle \mathbf{u}_\alpha \rangle^\alpha}{\partial t}$ becomes negligible. Finally, the issue is on the terms $\rho_\alpha \langle \mathbf{u}_\alpha \rangle^\alpha \cdot \nabla \langle \mathbf{u}_\alpha \rangle^\alpha$ and $\rho_\alpha \varepsilon_\alpha^{-1} \nabla \cdot \langle \tilde{\mathbf{u}}_\alpha \tilde{\mathbf{u}}_\alpha \rangle$. By estimating their order of magnitude as

$$\rho_\alpha \langle \mathbf{u}_\alpha \rangle^\alpha \cdot \nabla \langle \mathbf{u}_\alpha \rangle^\alpha, \rho_\alpha \varepsilon_\alpha^{-1} \nabla \cdot \langle \tilde{\mathbf{u}}_\alpha \tilde{\mathbf{u}}_\alpha \rangle = \mathcal{O} \left(\frac{\rho_\alpha \|\langle \mathbf{u}_\alpha \rangle^\alpha\|^2}{L} \right), \quad (4.36)$$

and estimating roughly the magnitude of the integral term via the interfacial viscous shear stress, one gets that the ratio of the macroscopic inertial terms to the integral terms is

$$\frac{\rho_\alpha \|\langle \mathbf{u}_\alpha \rangle^\alpha\|^2 / L}{\mu_\alpha \|\langle \mathbf{u}_\alpha \rangle^\alpha\| / l_\alpha^2} = \frac{\rho_\alpha \|\langle \mathbf{u}_\alpha \rangle^\alpha\| l_\alpha}{\mu_\alpha} \frac{l_\alpha}{L}. \quad (4.37)$$

The macroscopic inertial terms are therefore negligible if

$$Re_\alpha \frac{l_\alpha}{L} \ll 1. \quad (4.38)$$

This condition is generally very reasonable in porous media, where the Reynolds numbers are limited. One can also argue that for high Reynolds flows, the porous medium will destroy coherent structures larger than the size of the pores [88]. However, for the gas-liquid flow within structured packings, which is of high porosity level and where the gas phase is turbulent, this is an open question. Considering the highest air flow rate that is considered in the experiments of Suess and Spiegel [167] (3 m/s), and estimating the characteristic lengthscale of the gas phase in the column as $l_a \sim \sqrt{K_0} \sim 8.36e-4 \text{ m}$ from the permeability of the packing considered in Chapter 3, one obtains

$$L = 13.9 \times 10^{-2} \text{ m}, \quad (4.39)$$

to obtain $Re_\alpha \frac{l_a}{L} = 1$. According to this estimation, one therefore has to consider a very large representative volume in order to neglect the macroscopic inertial terms in the momentum balance. However, following the work of Jin et al. [88], we think that macroscopic eddies cannot propagate in such structures in the turbulent regime. Following, also, the assumption made in the previous chapter of localized inertial effects, we consider that the macroscopic terms in the momentum balance are negligible. Further simulation works over sufficiently large volumes are here required to address more precisely this question and to determine whether there is macroscopic turbulent eddies in structured packings.

Following the simplifications, the momentum balance at the continuum scale for the phases i and j therefore reduces to

$$0 = -\nabla \langle p_\alpha \rangle^\alpha + \rho_\alpha \mathbf{g} + \frac{1}{V_\alpha} \int_{\Gamma_{\alpha\sigma} \cup \Gamma_{ij}} \mathbf{n}_\alpha \cdot [-\tilde{p}_\alpha \mathbf{I} + \mu_\alpha (\nabla \tilde{\mathbf{u}}_\alpha + \nabla \tilde{\mathbf{u}}_\alpha^T)] d\Gamma, \quad \alpha = i, j. \quad (4.40)$$

Inserting the closure relations Eqs 4.33 and 4.34, it comes respectively for the phase i

$$\begin{aligned}
0 &= -\left(\nabla \langle p_i \rangle^i - \rho_i \mathbf{g}\right) \\
&+ \mu_i \left\{ \frac{1}{V_i} \int_{\Gamma_{i\sigma} \cup \Gamma_{ij}} \mathbf{n}_i \cdot \left[-\mathbf{a}_{ii} \mathbf{I} + \left(\nabla \mathbf{A}_{ii} + \nabla \mathbf{A}_{ii}^T \right) \right] d\Gamma \right\} \cdot \langle \mathbf{u}_i \rangle^i \\
&+ \mu_i \left\{ \frac{1}{V_i} \int_{\Gamma_{i\sigma} \cup \Gamma_{ij}} \mathbf{n}_i \cdot \left[-\mathbf{a}_{ij} \mathbf{I} + \left(\nabla \mathbf{A}_{ij} + \nabla \mathbf{A}_{ij}^T \right) \right] d\Gamma \right\} \cdot \langle \mathbf{u}_j \rangle^j,
\end{aligned} \tag{4.41}$$

and for the phase j

$$\begin{aligned}
0 &= -\left(\nabla \langle p_j \rangle^j - \rho_j \mathbf{g}\right) \\
&+ \mu_j \left\{ \frac{1}{V_j} \int_{\Gamma_{j\sigma} \cup \Gamma_{ij}} \mathbf{n}_j \cdot \left[-\mathbf{a}_{jj} \mathbf{I} + \left(\nabla \mathbf{A}_{jj} + \nabla \mathbf{A}_{jj}^T \right) \right] d\Gamma \right\} \cdot \langle \mathbf{u}_j \rangle^j \\
&+ \mu_j \left\{ \frac{1}{V_j} \int_{\Gamma_{j\sigma} \cup \Gamma_{ij}} \mathbf{n}_j \cdot \left[-\mathbf{a}_{ji} \mathbf{I} + \left(\nabla \mathbf{A}_{ji} + \nabla \mathbf{A}_{ji}^T \right) \right] d\Gamma \right\} \cdot \langle \mathbf{u}_i \rangle^i.
\end{aligned} \tag{4.42}$$

The integral terms represent the transfer of information from the micro to the macroscale and can be identified as effective parameters. Lasseux et al. [101] suggest here to decompose the viscous and the inertial contributions in the integrals. This is actually identical to the method used in Chapter 3 for the derivation of the generalized Darcy's law in the inertial regime (introduction of an inertial correction). The effective parameters are defined as follows

$$\begin{aligned}
0 &= -\left(\nabla \langle p_i \rangle^i - \rho_i \mathbf{g}\right) \\
&+ \mu_i \left\{ \underbrace{\frac{1}{V_i} \int_{\Gamma_{i\sigma} \cup \Gamma_{ij}} \mathbf{n}_i \cdot \left[-\mathbf{a}_{ii} \mathbf{I} + \left(\nabla \mathbf{A}_{ii} + \nabla \mathbf{A}_{ii}^T \right) \right] d\Gamma}_{-\mathbf{K}_{ii}^{-1} \cdot (\mathbf{I} + \mathbf{F}_{ii}) \varepsilon_i} \right\} \cdot \langle \mathbf{u}_i \rangle^i \\
&+ \mu_i \left\{ \underbrace{\frac{1}{V_i} \int_{\Gamma_{i\sigma} \cup \Gamma_{ij}} \mathbf{n}_i \cdot \left[-\mathbf{a}_{ij} \mathbf{I} + \left(\nabla \mathbf{A}_{ij} + \nabla \mathbf{A}_{ij}^T \right) \right] d\Gamma}_{\mathbf{K}_{ii}^{-1} \cdot (\mathbf{K}_{ij} - \mathbf{F}_{ij}) \varepsilon_j} \right\} \cdot \langle \mathbf{u}_j \rangle^j,
\end{aligned} \tag{4.43}$$

and

$$\begin{aligned}
0 &= - \left(\nabla \langle p_j \rangle^j - \rho_j \mathbf{g} \right) \\
&+ \mu_j \left\{ \underbrace{\frac{1}{V_j} \int_{\Gamma_{j\sigma} \cup \Gamma_{ij}} \mathbf{n}_j \cdot \left[-\mathbf{a}_{jj} \mathbf{I} + \left(\nabla \mathbf{A}_{jj} + \nabla \mathbf{A}_{jj}^T \right) \right] d\Gamma}_{-\mathbf{K}_{jj}^{-1} \cdot (\mathbf{I} + \mathbf{F}_{jj}) \varepsilon_j} \right\} \cdot \langle \mathbf{u}_j \rangle^j \\
&+ \mu_j \left\{ \underbrace{\frac{1}{V_j} \int_{\Gamma_{j\sigma} \cup \Gamma_{ij}} \mathbf{n}_j \cdot \left[-\mathbf{a}_{ji} \mathbf{I} + \left(\nabla \mathbf{A}_{ji} + \nabla \mathbf{A}_{ji}^T \right) \right] d\Gamma}_{\mathbf{K}_{jj}^{-1} \cdot (\mathbf{K}_{ji} - \mathbf{F}_{ji}) \varepsilon_i} \right\} \langle \mathbf{u}_i \rangle^i.
\end{aligned} \tag{4.44}$$

Based on the resolution of the closure problems, one can determine the effective terms by computing the surface integrals. Another formulation of the closure problems, via a change of variables, also allows to compute the effective terms as volume integrals. Here,

- \mathbf{K}_{ii} and \mathbf{K}_{jj} are the intrinsic permeability tensors
- \mathbf{K}_{ij} and \mathbf{K}_{ji} are the viscous drag tensors
- \mathbf{F}_{ii} and \mathbf{F}_{jj} are the inertial correction tensors
- \mathbf{F}_{ij} and \mathbf{F}_{ji} are the inertial drag tensors

The system at the continuum scale can be rewritten under the form of Darcy-like laws, which read

$$\varepsilon \frac{\partial S_i}{\partial t} + \nabla \cdot \langle \mathbf{u}_i \rangle = 0, \tag{4.45a}$$

$$\langle \mathbf{u}_i \rangle = -\frac{\mathbf{K}_{ii}}{\mu_i} \cdot (\nabla P_i - \rho_i \mathbf{g}) - \mathbf{F}_{ii} \cdot \langle \mathbf{u}_i \rangle + (\mathbf{K}_{ij} - \mathbf{F}_{ij}) \cdot \langle \mathbf{u}_j \rangle, \tag{4.45b}$$

and

$$\varepsilon \frac{\partial S_j}{\partial t} + \nabla \cdot \langle \mathbf{u}_j \rangle = 0, \tag{4.46a}$$

$$\langle \mathbf{u}_j \rangle = -\frac{\mathbf{K}_{jj}}{\mu_j} \cdot (\nabla P_j - \rho_j \mathbf{g}) - \mathbf{F}_{jj} \cdot \langle \mathbf{u}_j \rangle + (\mathbf{K}_{ji} - \mathbf{F}_{ji}) \cdot \langle \mathbf{u}_i \rangle. \tag{4.46b}$$

We propose now to study the structure of the model with *cross-terms* Eqs 4.45 and 4.46 in the viscous regime (\mathbf{F} terms equal to zero), and more generally the impact of the viscous coupling on the flow at steady-state and on the fluid fronts. The methodology is based on the Buckley-Leverett theory, which is extended to the model with cross-terms. This method allows to obtain a semi-analytical solution of the flow for the model with and without cross-terms, and therefore to analyze the impact of the momentum exchange. The impact of the permeability, the viscosity ratio, and the relative importance of the gravity effects are investigated and discussed on classical configurations encountered in porous media. The theoretical solutions are compared to experimental data, validating the importance of cross-terms, especially in highly permeable media.

Modeling two-phase flow of immiscible fluids in porous media: Buckley-Leverett theory with explicit coupling terms

Sylvain Pasquier, Michel Quintard and Yohan Davit

*Institut de Mécanique des Fluides de Toulouse (IMFT) - Université de Toulouse, CNRS-INPT-UPS, Toulouse
France*

Published 12 October 2017

Abstract

Continuum models that describe two-phase flow of immiscible fluids in porous media often treat momentum exchange between the two phases by simply generalizing the single-phase Darcy's law and introducing saturation-dependent permeabilities. Here, we study models of creeping flows that include an explicit coupling between both phases via the addition of cross-terms in the generalized Darcy's law. Using an extension of the Buckley-Leverett theory, we analyze the impact of these cross-terms on saturation profiles and pressure drops for different couples of fluids and closure relations of the effective parameters. We show that these cross-terms in the macroscale models may significantly impact the flow compared to results obtained with the generalized Darcy's laws without cross-terms. Analytical solutions, validated against experimental data, suggest that the effect of this coupling on the dynamics of saturation fronts and the steady state profiles is very sensitive to gravitational effects, the ratio of viscosity between the two phases and the permeability. Our results indicate that effects of momentum exchange on two-phase flow may increase with the permeability of the porous medium, when the influence of the fluid/fluid interface becomes similar to that of the solid/fluids interface.

4.3 Introduction

Modeling two-phase flows of immiscible fluids in porous media is important in many scientific and industrial areas, including petroleum engineering and hydrogeology [98, 20], chemical engineering, and nuclear safety [57, 33]. The classical mathematical descriptions of momentum transport at the continuum-scale are simple extensions of Darcy’s law for single-phase flow. The most widespread model corresponds to the generalized Darcy’s laws [119], where the relative influence of one phase on the other one is captured by a relative permeability, which is usually treated as a function of the saturations [77]. In most of these representations, the coupling between the two phases is done by simply correcting effective parameters of models initially developed for single-phase flow.

While generalized Darcy’s laws models are being currently used in engineering practice, research of the last decades has led to more elaborate models capable of dealing with complex and dynamic pore-scale physics [187, 16, 90, 135, 73, 143, 76, 64, 112, 38]. Among these models, there has been recently a renewed interest for those that include an explicit coupling for the description of mass and momentum exchanges between the phases [33, 36]. Cross-terms that couple the equations for momentum transport of each phase can be obtained theoretically, either by considering the case of the annular viscous two-phase flow in tubes, for which a simple analytical solution analogous to that of Poiseuille can be derived [149, 91], or from upscaling techniques such as the method of volume averaging ([187], more detail in Section 4.4.1) or homogenization theory [16].

How important are these cross-terms? We anticipate that this will strongly depend upon the contact area between the two fluid phases, which in turn is controlled by effects such as the capillary action, wettability or the structure of the porous medium. If the area of the fluid/fluid interface is comparable to the area of fluid/solid interfaces, the coupling terms may be important, whereas if the area of the fluid/solid interface is much larger than that of the fluid/fluid interface, exchanges may be minimal. The hypothesis that we explore in this paper is that the size of the pores can control the influence of the fluid/fluid and fluids/solid interfaces, and therefore exchanges between the two phases. In particular, our idea is that there is a positive correlation between the size of the pores and the effects of the cross-terms on momentum transport. This hypothesis is based on a variety of results from the literature that we detail below.

On the one hand, studies such as [192] show that coupling effects are relatively small for water (wetting) and mercury (non-wetting) flowing through packed sand (permeability of about $34 \times 10^{-12} \text{m}^2$). Zarcone and Lenormand hypothesize that the wetting and non-wetting phases flow through different pore networks, most likely because of capillarity, and therefore minimize the interfacial area between the two fluid. The consequence is that solid/fluid interactions dominate over fluid/fluid interactions. While this is a controversial hypothesis (see e.g. [148, 149, 91, 26, 24]), there is also circumstantial evidence that coupling effects are small in low permeability media. For instance, these terms are always neglected in reservoir modeling of water–oil flow through rocks with relatively low permeabilities—typically, permeabilities of the rocks are about 10^{-12}m^2 or less in petroleum engineering.

On the other hand, studies such as [41, 90, 91, 150] indicate that a strong friction between the two phases can occur when the interface area and the permeability are large. Such a strong interaction between phases has also been observed in many chemical engineering or nuclear engineering applications involving regular packed beds or structured packings with large permeabilities (permeabilities of about 10^{-8} to 10^{-6}m^2). For instance models of co- and counter-current flows in trickle beds or structured packings often consist of conservations laws corrected with additional *friction terms* [81] describing phase interactions. This is also the case for boiling water-steam flows in nuclear debris bed, for which various heuristic models have been developed [108, 155, 177, 176]. Experiments for such systems show that many observations *cannot be reproduced* by the

classical models without cross-terms [176, 33, 36].

In this paper, our goal is to analyze the relative importance of coupling terms in continuum-scale models of two-phase flows in porous media. To do so,

- we first develop a generic model for two-phase flow of immiscible fluids in porous media with an explicit exchange of momentum between both phases (Section 4.4.1).
- we then use the Buckley-Leverett theory (Section 4.4.2), that is extended to account for the cross-terms, to calculate the saturation profiles and their dynamics in a one-dimensional setting (Section 4.5). Considering simulations and experimental data from the literature on imbibition (Section 4.5) and drainage (Section 4.5) for water-air and water-oil, we evaluate the relative influence of the cross-terms and their physical relevance depending on the system considered.

4.4 Methods

Here, we first present a continuum model to describe two-phase flow of immiscible fluids in porous media. We then go on to provide a brief description of the Buckley-leverett theory (Section 4.4.2), the configurations studied (Section 4.4.3), along with a list of the different closure relations used (Section 4.4.4).

4.4.1 Models and assumptions

4.4.1.1 Model with cross-terms

Continuum models for the creeping flow of two immiscible fluids, phases i and j , involving cross-terms for momentum exchanges were initially postulated by Raats and Klute in [140] and Baveye and Sposito in [19], often following arguments based on the concepts of irreversible thermodynamics [90, 72, 116]. Using the volume averaging theory, Whitaker in [187] derived a model with closure problems for the effective parameters. In this work, we will use these expressions from volume averaging as a basis to construct our model. Similar coupled laws were also derived by Auriault in [16] using the method of homogenization and by Marle in [116] using concepts of irreversible thermodynamics.

The mass conservation equation for phases i and j reads

$$\varepsilon \frac{\partial}{\partial t} \begin{pmatrix} S_i \\ S_j \end{pmatrix} + \nabla \cdot \begin{pmatrix} \mathbf{U}_i \\ \mathbf{U}_j \end{pmatrix} = \begin{pmatrix} 0 \\ 0 \end{pmatrix}, \quad (4.47)$$

with \mathbf{U}_i and \mathbf{U}_j the superficial velocities and ε the porosity of the porous medium. For simplicity, we do not take into account residual saturations, which could be easily treated by changing the saturation variables to the reduced saturations, $S_i^* = \frac{S_i - S_i^{\min}}{S_i^{\max} - S_i^{\min}}$ and $S_j^* = \frac{S_j - S_j^{\min}}{S_j^{\max} - S_j^{\min}}$.

The momentum transport equations read [187]

$$\mathbf{U}_i = -\frac{\mathbf{K}_{ii}}{\mu_i} \cdot (\nabla P_i - \rho_i \mathbf{g}) + \mathbf{K}_{ij} \cdot \mathbf{U}_j, \quad (4.48a)$$

$$\mathbf{U}_j = -\frac{\mathbf{K}_{jj}}{\mu_j} \cdot (\nabla P_j - \rho_j \mathbf{g}) + \mathbf{K}_{ji} \cdot \mathbf{U}_i, \quad (4.48b)$$

where ∇P_i and ∇P_j are the pressure gradients, ρ_i (ρ_j) and μ_i (μ_j) the density and viscosity of phase i (j respectively) and \mathbf{g} is the gravitational acceleration. \mathbf{K}_{ii} and \mathbf{K}_{jj} are second-order permeability tensors and \mathbf{K}_{ij} and \mathbf{K}_{ji} are second-order viscous coupling tensors. Eqs 4.48a and 4.48b are the equations that differ from

the generalized Darcy's law in that we have cross-terms $\mathbf{K}_{ij} \cdot \mathbf{U}_j$ and $\mathbf{K}_{ji} \cdot \mathbf{U}_i$ describing momentum exchange between both phases. Lasseux et al. recently showed that this model can be further extended to account for inertial effects by including additional drag terms [101], but we limit our analysis to creeping flow in this paper. In fact, in such cases, the velocity dependant terms are not compatible with the Buckley-Leverett theory.

The derivation of these models requires several important assumptions. One of these is that the interface between the immiscible fluids remains locally quasi-static, i.e., that the flow at the pore-scale relaxes quickly compared to characteristic timescales of the macroscale process. Another important assumption is that the Capillary and Bond numbers, which respectively compare the viscous and gravity effects to surface tension, are much smaller than unity. Alternative models have been proposed to account for dynamic effects (see for example [87, 4] for the use of pseudo-functions, [132, 76, 112] for other forms of laws accounting for dynamic effects induced by heterogeneities, multi-zones, or [152] for the use of the theory of irreversible thermodynamics). However, it is probable that less restrictive assumptions in the upscaling may still yield equations similar to Eqs 4.48a and 4.48b for momentum transport, with the same effective parameters but capturing additional physical effects. Further, the expression in Eqs 4.48 is used, in a variety of different forms, in engineering applications, where it is successful in describing many different systems [162]. We therefore base our model on the system of equations 4.47, 4.48a and 4.48b, with simplifications that are described in the next Section.

4.4.1.2 Simplifications

The objective of this paper is to emphasize the contribution of the additional terms compared to the behavior of the classical model. Many different initial boundary value problems could be used as test cases. However, we will limit our investigation to one-dimensional situations commonly encountered in the laboratory experiments that have been used to study flows and measure transport parameters in such systems. Simplifications that correspond to these most common situations are as follows:

- *Isotropy*: for simplicity, we consider that the tensorial permeabilities \mathbf{K}_{ii} and \mathbf{K}_{jj} can be written as

$$\mathbf{K}_{ii} = K_0 k_{r_i} \mathbf{I}, \quad \mathbf{K}_{jj} = K_0 k_{r_j} \mathbf{I}, \quad (4.49)$$

where \mathbf{I} is the identity tensor, K_0 is the intrinsic permeability of the medium and k_{r_i} and k_{r_j} are the relative permeabilities of phases i and j respectively. This form is based on the assumptions that the porous structure is isotropic and that there is no anisotropy generated by the two-phase flow itself [134]. Similarly, we write

$$\mathbf{K}_{ij} = K_{ij} \mathbf{I}, \quad \mathbf{K}_{ji} = K_{ji} \mathbf{I}.$$

- *Dimensions*: we limit our analysis to a one-dimensional system.
- *Consistency of the relative permeabilities*: we assume that

$$k_{r_i}(S_i = 1) = 1, \quad k_{r_j}(S_i = 1) = 0, \quad (4.50)$$

$$k_{r_i}(S_i = 0) = 0, \quad k_{r_j}(S_i = 0) = 1, \quad (4.51)$$

$$K_{ji}(S_i = 1) = 0, \quad K_{ij}(S_j = 1) = 0, \quad (4.52)$$

which are necessary assumptions to obtain Darcy's law in the limit of single-phase flow.

- *Local pressure equilibrium*: assuming that capillary effects are negligible at macroscale, we write $P_i = P_j \equiv P$ and $\frac{\partial P_i}{\partial x} = \frac{\partial P_j}{\partial x} \equiv \frac{\partial P}{\partial x}$. This assumption holds for flows within highly permeable media, where viscous and inertial effects dominate over the capillary pressures. This will be correct for pores much larger than the capillary length. For air-water flow at standard temperature and pressure, an order of magnitude estimation is therefore that the pores are significantly larger than the millimeter, i.e., that the permeability is larger than about 10^{-9} m^2 . This is consistent with the fact that, as discussed in introduction, the coupling terms are likely to play a more significant role for highly permeable media.

4.4.1.3 Mass balance

With these assumptions, the mass balance equations now read

$$\varepsilon \begin{pmatrix} \frac{\partial S_i}{\partial t} \\ \frac{\partial S_j}{\partial t} \end{pmatrix} + \begin{pmatrix} \frac{\partial U_i}{\partial x} \\ \frac{\partial U_j}{\partial x} \end{pmatrix} = \begin{pmatrix} 0 \\ 0 \end{pmatrix}. \quad (4.53)$$

4.4.1.4 Momentum balance with cross-terms

Momentum balance equations with cross-terms can be written as

$$U_i = -\frac{K_{ii}}{\mu_i} \left(\frac{\partial P}{\partial x} - \rho_i g \right) + K_{ij} U_j, \quad (4.54)$$

$$U_j = -\frac{K_{jj}}{\mu_j} \left(\frac{\partial P}{\partial x} - \rho_j g \right) + K_{ji} U_i, \quad (4.55)$$

with gravity colinear and oriented with the basis vector \mathbf{e}_x , so that $\mathbf{g} \cdot \mathbf{e}_x = g$.

An alternative formulation, initially derived by Lasseux et al. [103], can be obtained by combining Eqs 4.54 and 4.55

$$\begin{pmatrix} U_i \\ U_j \end{pmatrix} + \mathcal{K}^* \begin{pmatrix} \frac{\partial P}{\partial x} - \rho_i g \\ \frac{\partial P}{\partial x} - \rho_j g \end{pmatrix} = 0. \quad (4.56)$$

The matrix \mathcal{K}^* is symmetric and reads

$$\mathcal{K}^* = \begin{pmatrix} K_{ii}^*/\mu_i & K_{ij}^*/\mu_j \\ K_{ji}^*/\mu_i & K_{jj}^*/\mu_j \end{pmatrix} = \frac{1}{1 - K_{ij}K_{ji}} \begin{pmatrix} K_{ii}/\mu_i & K_{jj}K_{ij}/\mu_j \\ K_{ii}K_{ji}/\mu_i & K_{jj}/\mu_j \end{pmatrix}. \quad (4.57)$$

4.4.1.5 Momentum balance without cross-terms (generalized Darcy's laws)

Momentum balance equations without cross-terms are simply obtained by setting $K_{ij} = 0$ and $K_{ji} = 0$ in the previous model, so that we have

$$U_i = -\frac{K_{ii}}{\mu_i} \left(\frac{\partial P}{\partial x} - \rho_i g \right), \quad (4.58)$$

$$U_j = -\frac{K_{jj}}{\mu_j} \left(\frac{\partial P}{\partial x} - \rho_j g \right). \quad (4.59)$$

4.4.2 Buckley-Leverett theory

With these simplifications, equations can be grouped together into a single non-linear hyperbolic equation suitable for an analysis based on the Buckley-Leverett theory.

4.4.2.1 Formulation

The Buckley-Leverett theory [31] has been widely used in the literature to analyze the structure of two-phase flows through both homogeneous and heterogeneous media [31, 67, 22, 89, 32, 50]. It is also used as a reference to validate numerical solvers [105, 171, 3, 79] and to evaluate their accuracy in capturing shocks. Here, we consider a one-dimensional domain, with the initial condition $S_j = 1$ and phase i injected at constant flow rate $U_i(0, t)$ for $t > 0$. The Buckley-Leverett problem characterizes the propagation of the fluid front in the domain and can be obtained by combining Eqs 4.53, 4.54 and 4.55. Introducing the total velocity $U = U_i + U_j$, one obtains the velocity of phase i as

$$U_i = \frac{m_i + K_{ij}m_j}{m_i + m_j + K_{ji}m_i + K_{ij}m_j}U + \frac{m_i m_j}{m_i + m_j + K_{ji}m_i + K_{ij}m_j}(\rho_i - \rho_j)g, \quad (4.60)$$

where $m_i = K_{ii}/\mu_i$ and $m_j = K_{jj}/\mu_j$ are the mobility parameters. This yields

$$\varepsilon \frac{\partial S_i}{\partial t} + \frac{\partial \mathcal{F}_i}{\partial x} = 0, \quad (4.61a)$$

$$S_i(x, 0) = 0, \quad (S_j(x, 0) = 1), \quad (4.61b)$$

$$U_i(0, t) = \mathcal{F}_i[S_i(0, t)] = U, \quad t > 0, \quad (4.61c)$$

where $\mathcal{F}_i(S_i)$ is the flux function (also called fractional flow in the Buckley-Leverett theory) that reads

$$\mathcal{F}_i(S_i) = U_i = \frac{m_i}{m_i + m_j}U \left(f_1 + \frac{\mu_i}{\mu_j} \mathcal{N}_g k_{r_j}(S_i) f_2 \right). \quad (4.62)$$

Here, $\mathcal{N}_g = \frac{K_0(\rho_i - \rho_j)g}{U\mu_i}$ is the *gravity number*, $k_{r_j}(S_i)$ is the relative permeability for the phase j and f_1 and f_2 are functions that characterize the impact of the coupling coefficients K_{ij} and K_{ji} in the momentum balance equations,

$$f_1 = \frac{1 + K_{ij} \frac{m_j}{m_i}}{1 + \frac{K_{ji}m_i + K_{ij}m_j}{m_i + m_j}}, \quad f_2 = \frac{1}{1 + \frac{K_{ji}m_i + K_{ij}m_j}{m_i + m_j}}. \quad (4.63)$$

4.4.2.2 Unique solution for the conservation law

Eq. 4.61a is a scalar one-dimensional conservation law, whose solutions might involve discontinuities. Solving this problem is meaningful only in a weak sense, allowing for discontinuous functions to be solutions. Further, obtaining a unique and physically realistic result requires additional admissibility and entropic conditions. Those are well discussed in the literature [31, 131, 48, 89, 144] and a little summary of methods for constructing solutions is provided here.

We present in Fig. 4.2 the two configurations encountered in this study. In the former case, the inlet condition, $\mathcal{F}_i(S_L) = U = U_i(0, t)$ admits $S_L = 1$ as unique solution (indices L and R for left and right). The solution $S_i(x, t)$ of the Riemann problem admits two shocks between S_L and S_2 , and between S_1 and S_R , and a rarefaction wave between S_1 and S_2 . The *unique* solution $S_i(x, t)$, shown in Fig. 4.2b, reads

$$S_i(x, t) = \begin{cases} S_L, & \text{for } x < \hat{\mathcal{F}}'_i(S_1)t, \\ S_i(x, t) = \left(\hat{\mathcal{F}}'_i\right)^{-1}\left(\frac{x}{t}\right), & \text{for } \hat{\mathcal{F}}'_i(S_2) < \frac{x}{t} < \hat{\mathcal{F}}'_i(S_1), \\ S_R, & \text{for } x > \hat{\mathcal{F}}'_i(S_2)t, \end{cases} \quad (4.64)$$

The solution $S_i(x, t)$ of the two-phase system is determined by considering the Riemann problem that is associated with Eqs. 4.61. It reads

$$\varepsilon \frac{\partial S_i}{\partial t} + \frac{\partial \mathcal{F}_i}{\partial x} = 0, \quad (4.65a)$$

$$S_L = S_i(0, t), \quad (4.65b)$$

$$S_R = S_i(x, 0), \quad (4.65c)$$

with $S_L > S_R$. The inlet value S_L is not known *a priori*, but verifies the equation of the inlet flow rate, $\mathcal{F}_i(S_L) = U(0, t) = U_i(0, t)$ (Eq. 4.61c). Given the conditions presented in Section 4.4.1.2, $S_L = 1$ is always solution of this equation, but other values can also be solutions when gravity effects dominate over viscous effects ($\mathcal{N}_g > 1$) [131].

The *unique* admissible solution of the system Eqs 4.65 is determined by constructing the concave hull [131, 48], $\hat{\mathcal{F}}_i$, which is defined on the interval $[S_R, S_L]$ as

$$\hat{\mathcal{F}}_i = \inf_{h \in \mathcal{C}o} (h), \quad (4.66)$$

with $\mathcal{C}o$ the ensemble of concave functions such that, $h \in \mathcal{C}o$ is equivalent to

$$h(S_i) > \mathcal{F}_i(S_i), \quad \forall S_i \in [S_R, S_L]. \quad (4.67)$$

By construction, we obtain a number of intermediate points $\{S_k\}_0^{n+1}$ such that $S_R < S_1 < S_k < S_n < S_L$, with $k \in [0, n]$ and where the $n+1$ points correspond to the intersection points between $\hat{\mathcal{F}}_i$ and \mathcal{F}_i [131]. On each of the interval $[S_k, S_{k+1}]$, $\hat{\mathcal{F}}_i$ either coincides with \mathcal{F}_i or connects linearly $\hat{\mathcal{F}}_i(S_k)$ to $\hat{\mathcal{F}}_i(S_{k+1})$. In the former case, the solution between S_k and S_{k+1} consists in a rarefaction wave, while in the second case the solution is a shock that propagates with the speed

$$\hat{\mathcal{F}}_i'(S_{k+1}) = \frac{\mathcal{F}_i(S_{k+1}) - \mathcal{F}_i(S_k)}{S_{k+1} - S_k}, \quad k \in [0, n]. \quad (4.68)$$

This relation is the Rankine-Hugoniot condition. The solution must also verify the Oleinik entropy constraint, that reads

$$\frac{\mathcal{F}_i(S_i) - \mathcal{F}_i(S_{k+1})}{S_i - S_{k+1}} \geq \hat{\mathcal{F}}_i'(S_{k+1}) \geq \frac{\mathcal{F}_i(S_i) - \mathcal{F}_i(S_k)}{S_i - S_k}, \quad \forall S \in [S_k, S_{k+1}]. \quad (4.69)$$

The characteristic curves of the system in the $x - t$ plane verify

$$\frac{dx}{dt} = \hat{\mathcal{F}}_i'(S_i), \quad \forall S_i \in [S_R, S_L], \quad (4.70)$$

leading the following equations for the characteristic curves (see Fig. 1c)

$$x = \hat{\mathcal{F}}_i'(S_i)t + r, \quad \forall S_i \in [S_R, S_L], \quad (4.71)$$

where r parametrizes the position of x at $t = 0$.

If the inlet condition Eq. 4.61c admits more than one solution (as illustrated in Fig. 4.2, bottom), which is encountered when gravity effects dominate viscous effects, we select the minimum of the solutions of Eq. 4.61c, $\mathcal{F}_i(S_i) = U(0, t) = U_i(0, t)$, which corresponds to a positive shock speed. In the case illustrated in Fig. 4.2e),

this corresponds to a unique shock between S_L and S_R given by the Rankine-Hugoniot condition

$$\hat{\mathcal{F}}'_i(S_L) = \frac{\mathcal{F}_i(S_L) - \mathcal{F}_i(S_R)}{S_L - S_R}. \quad (4.72)$$

Other possible solutions have a shock with a negative propagation velocity, a case that has been previously studied in [144]. The main difference between the case in [144] and the configurations here are the boundary and initial conditions. In the case in [144], a fraction of the medium is initially fully saturated with one phase and the rest fully saturated with the other phase. Therefore the values of the saturations are known everywhere, yielding fronts propagating in opposite directions. In our case, the porous medium is initially saturated only with one phase and we impose a velocity U at the inlet, which is the case corresponding to the experimental data that we use. Given these boundary and initial conditions, we consider that shocks cannot propagate contrary to the inlet velocity and that the only physically realistic solution $S_i(x, t)$ admits one unique shock between S_R and S_L (see the illustration in Fig. 4.2), which is expressed as

$$S_i(x, t) = S_L, \quad \text{for } x < \hat{\mathcal{F}}'_i(S_L) t. \quad (4.73)$$

As we will see later on, comparison of results obtained with this choice are in very good agreement with experimental data, confirming that this is the correct case for the experimental data considered in this paper.

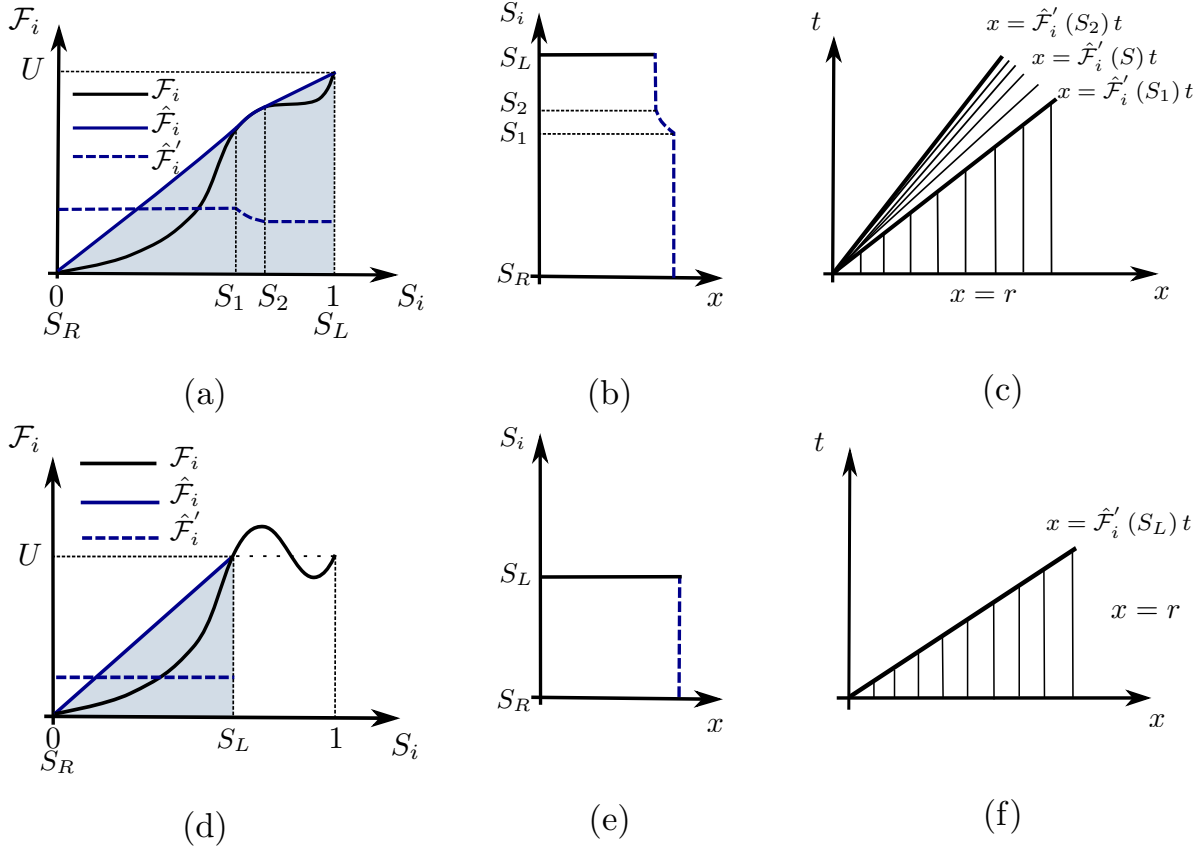


Figure 4.2 – Construction of the saturation fronts. a) and d) Plots of the flux function \mathcal{F}_i , the concave hull $\hat{\mathcal{F}}_i$ and its derivative $\hat{\mathcal{F}}'_i$. b) and e) The corresponding profile of the front S_i along x . c) and f) Characteristic curves of the system in the $x - t$ plane. The first line corresponds to $\mathcal{F}_i(S_i) = U$ having a unique solution. The second line corresponds to $\mathcal{F}_i(S_i) = U$ having multiple solutions.

4.4.3 Boundary, initial conditions and fluids

We consider two boundary value problems corresponding to two classical configurations encountered in porous media. The first configuration corresponds to the experiments of Chikhi et al. in [33], which is an air/water system in a particle bed, a configuration known to emphasize the impact of the coupling terms as discussed in [36]. It corresponds to a drainage process, since the non-wetting phase (air) is displacing the wetting phase (water) out of the column. The second configuration describes an imbibition process, where a wetting phase is introduced into a porous medium initially filled with a non-wetting phase. This problem corresponds to the standard use of the Buckley-Leverett theory, for application to oil recovery using water. The two configurations are illustrated in Fig. 4.3. The fluid properties—density and the viscosity—of air, water and oil are given in Tab. 4.1.

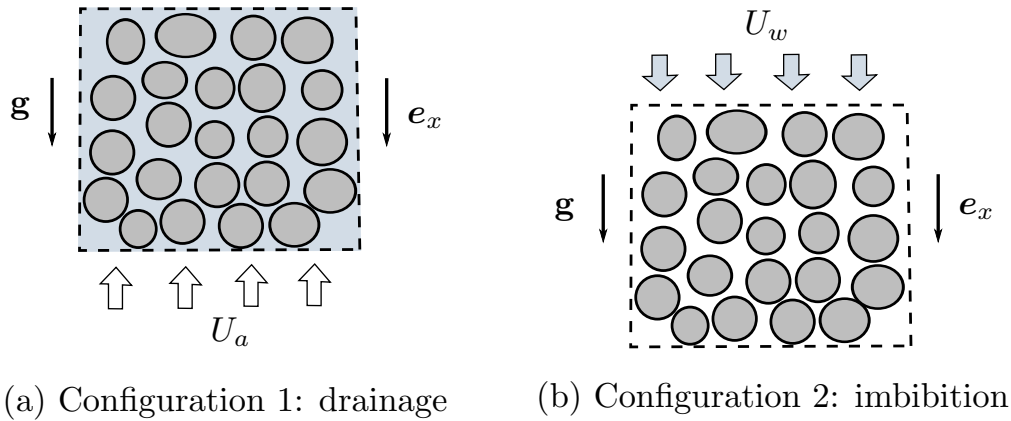


Figure 4.3 – Illustrations of the two configurations considered.

	density ρ (kg/m^3)	viscosity μ ($Pa.s$)
air	1	1.8×10^{-5}
water	10^3	10^{-3}
oil	8×10^2	10^{-1}

Table 4.1 – Fluid properties

4.4.4 Closures for the effective parameters

We consider two classes of closures for the effective parameters: one obtained from the literature in Clavier et al. [36] (constructed from experimental data [33]) and one based on the analytical solution of an annular two-phase viscous flow within a capillary tube. These closures are also compared to the one obtained by Rothman in [150], Zarcone and Lenormand in [192] and Kalaydjian in [91] in Section 4.5.

4.4.4.1 Configuration 1: closure from [36], based on experimental data

The first closure relations used in this paper have been recently obtained [36] from the experimental database presented in [33] (CALIDE experiment). The experiments, which focus on water-air flow in a column filled with coarse particles, were part of a large work studying water-steam flows in debris bed in the context of a severe accident in a nuclear reactor. Air and water are injected from below, with controlled flow rate, in a vertical column initially saturated with water until a steady-state is obtained (sketch in Fig. 4.2b). The phase saturations were then measured using capacitance probes and the pressure drop was obtained via a differential measure of the pressure. These experiments offer a very valuable database of saturations and pressure drops over a wide range of flow rates. From these data, the authors also derive closures for the effective parameters of the model Section 4.4.1. The term K_{ww} of the water phase is assumed to be

$$K_{ww} = K_0 S_w^3, \quad (4.74a)$$

which also corresponds to a Brooks and Corey correlation. The effective parameters K_{aa} and K_{wa} are then derived from the experimental data as

$$K_{aa} = K_0 (1 - S_w)^4, \quad (4.74b)$$

$$K_{wa} = \beta \frac{\mu_a}{\mu_w} \frac{S_w^2}{(1 - S_w)}, \quad (4.74c)$$

where β is a factor that weights the amplitude of the cross-term and which is directly related to the particle size. The term K_{aw} is finally determined using the relation between the non-diagonal coefficients in Eq. 4.57

$$K_{aw} = \frac{\mu_w}{\mu_a} \frac{K_{aa} K_{wa}}{K_{ww}} = \beta \frac{(1 - S_w)^3}{S_w}. \quad (4.74d)$$

4.4.4.2 Configuration 2: analytical solution of the annular viscous flow

The second closure relations are derived from the analytical solution of an annular two-phase viscous flow i, j within a capillary tube [78, 34] (see Fig. 4.4 for an illustration)

$$K_{ii} = S_i^2 - 2S_i(1 - S_i) - 2(1 - S_i)^2 \ln(1 - S_i) - 4r_\mu \frac{[S_i + (1 - S_i) \ln(1 - S_i)]^2}{1 - 2r_\mu \ln(1 - S_i)}, \quad (4.75a)$$

$$K_{jj} = (1 - S_i)^2 - 2r_\mu(1 - S_i)^2 \ln(1 - S_i) - 4r_\mu \frac{(1 - S_i)^2 [S_i + (1 - S_i) \ln(1 - S_i)]^2}{S_i^2 - 2S_i(1 - S_i) - 2(1 - S_i)^2 \ln(1 - S_i)}, \quad (4.75b)$$

$$K_{ij} = 2r_\mu \frac{S_i + (1 - S_i) \ln(1 - S_i)}{1 - 2r_\mu \ln(1 - S_i)}, \quad (4.75c)$$

$$K_{ji} = 2(1 - S_i) \frac{S_i + (1 - S_i) \ln(1 - S_i)}{S_i^2 - 2S_i(1 - S_i) - 2(1 - S_i)^2 \ln(1 - S_i)}, \quad (4.75d)$$

where i is the wetting phase and j is the non-wetting phase, and where $r_\mu = \frac{\mu_j}{\mu_i}$ is the viscosity ratio. Clavier [34] suggest simplified expressions in the limit where $r_\mu \ll 1$,

$$K_{ii}^{\text{approx}} = K_0 S_i^3, \quad K_{jj}^{\text{approx}} = K_0 (1 - S_i)^2, \quad (4.76a)$$

$$K_{ji}^{\text{approx}} = \frac{1 - S_i}{S_i}, \quad K_{ij}^{\text{approx}} = r_\mu \frac{S_i^2}{1 - S_i}. \quad (4.76b)$$

K_{ii}^{approx} and K_{jj}^{approx} correspond here to the Brooks and Corey correlations [29] that are used extensively in the literature for two-phase flows in porous media. We see in Fig. 4.5 that the simplified expressions approximate very well the exact solution for the air-water system when $r_\mu \ll 1$ ($r_\mu = 0.018$).

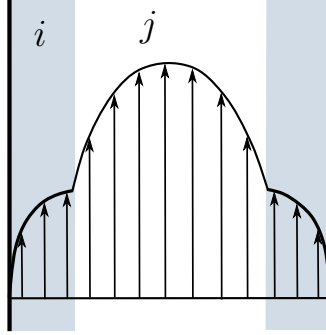


Figure 4.4 – Velocity field in a cross-section of a capillary tube illustrating the annular two-phase viscous flow.

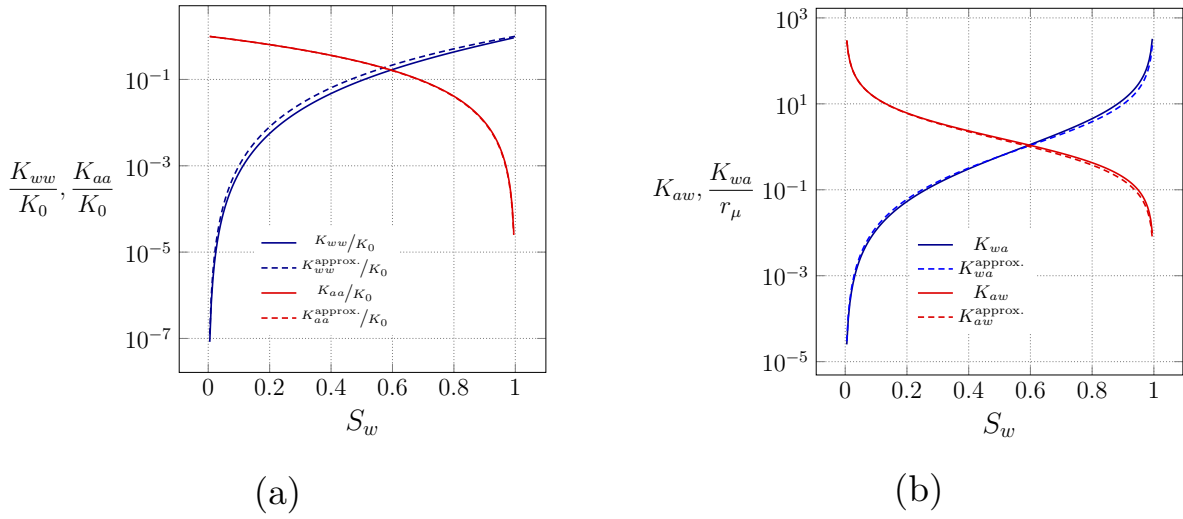


Figure 4.5 – Comparison of exact (K_{ww}/K_0 , K_{aa}/K_0 , K_{wa} , K_{aw} , from Eqs 4.75) and approximated ($K_{ww}^{\text{approx}}/K_0$, $K_{aa}^{\text{approx}}/K_0$, K_{wa}^{approx} , K_{aw}^{approx} , from Eqs 4.76) effective properties for the two-phase annular flow, with a) intrinsic permeabilities and b) cross-terms.

4.5 Results

4.5.1 Case 1: Drainage: water/air flow in a particle bed

We first proceed to the computation of the boundary value problem presented in Fig. 4.2a, which is the case of drainage of a water column with air. The analysis is based on the experimental closures presented in section 4.4.4.1. Results at steady-state are presented for both models and experimental data in Fig. 4.6. First, we see that the model with cross-terms provides a much more accurate representation of the pressure drop and

the liquid saturation for $1/\mathcal{N}_g \lesssim 0.01$. In particular, it captures correctly the variation of the pressure drop that is due to the momentum transfer from the air to the water, when the model without cross-terms can only balance $\frac{\partial P}{\partial x}$ with $\rho_w g$ for any flow rate. The dimensionless pressure drop $\frac{1}{\rho_w g} \frac{\partial P}{\partial x}$ is indeed computed at steady-state from Eq. 4.54 as

$$\frac{1}{\rho_w g} \frac{\partial P}{\partial x} = 1 + \frac{\mu_w U_a K_{wa} K_{ww}^{-1}}{\rho_w g}. \quad (4.77)$$

Consistent with experiment of Tutu et al. in [176], these results confirm that the generalized Darcy's law fails to recover the flow properties for such systems. As discussed previously, our hypothesis is that the high permeability of the medium favors momentum transfers between the two phases. For $1/\mathcal{N}_g \sim 0.01$ ($Re_d \sim 30$), even the model with cross-terms deviates from experimental results, an effect which is likely due to inertial effects [33, 36] that start to become significant as the flow rate is increased.

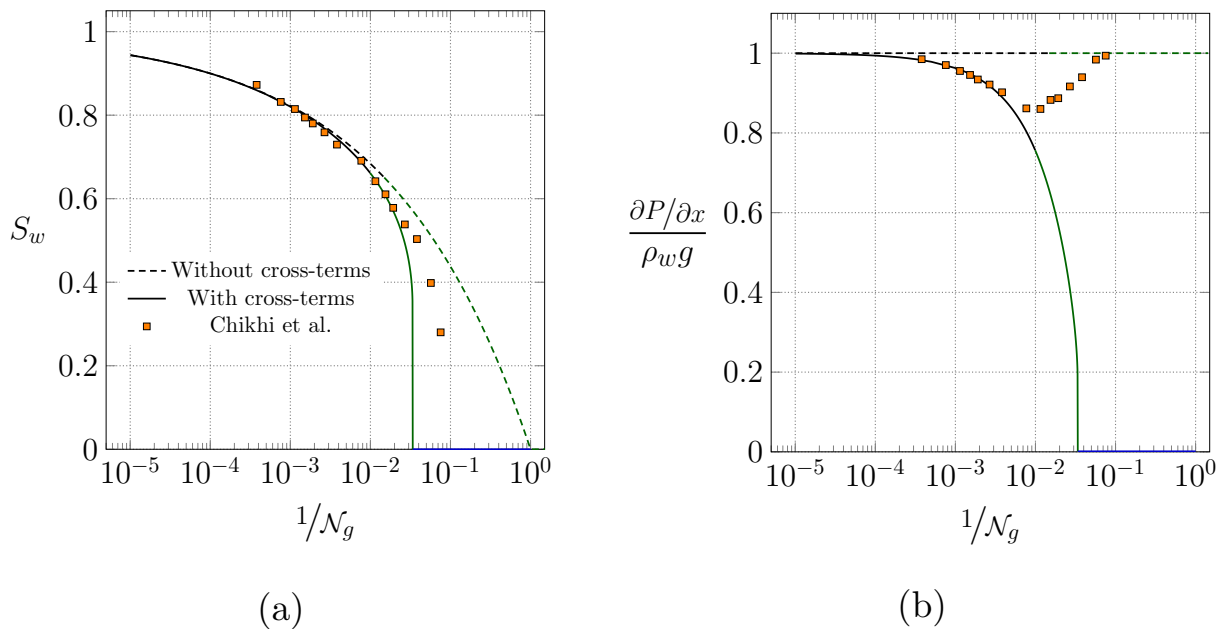


Figure 4.6 – Comparison of steady-state profiles with (solid lines) and without (dashed lines) cross-terms to experimental data from [33, 36] with a) the water saturation and b) dimensionless pressure gradient as a function of $1/\mathcal{N}_g$. The colors distinguish different regimes of \mathcal{N}_g , with a shock (black), a rarefaction wave (blue) or both (green), see Fig. 4.7.

We show in Fig. 4.6, using different colors, that the nature of the propagation front can change depending on \mathcal{N}_g . The propagation fronts of water, S_w , are presented for each of the different regimes in Fig. 4.7 in the presence and absence of cross-terms. The construction of the shocks is outlined only for the model including cross-terms. This is the front S_a (air phase) that is computed using the Buckley-Leverett theory, since we consider the injection of the air in the column (drainage). However, for consistency with other cases in the paper, we always consider the profile of the wetting phase in the transient regime (S_w here). Fig. 4.7a, 4.7b correspond to a gravity-dominated regime (high gravity number, $1/\mathcal{N}_g = 2 \times 10^{-3}$) where air propagates as a single front and where the impact of the cross-terms is moderate. For lower values of \mathcal{N}_g , Fig. 4.7c, 4.7d ($1/\mathcal{N}_g = 2 \times 10^{-2}$), the model with cross-terms yields a rarefaction wave. For $1/\mathcal{N}_g = 4 \times 10^{-2}$, in Fig. 4.7e, 4.7f, the two models generate very different front profiles, with a single rarefaction wave for the

model with cross-terms. At steady-state, however, this range of gravity numbers is not necessarily relevant as it corresponds to flow rates for which inertial effects are expected to be significant.

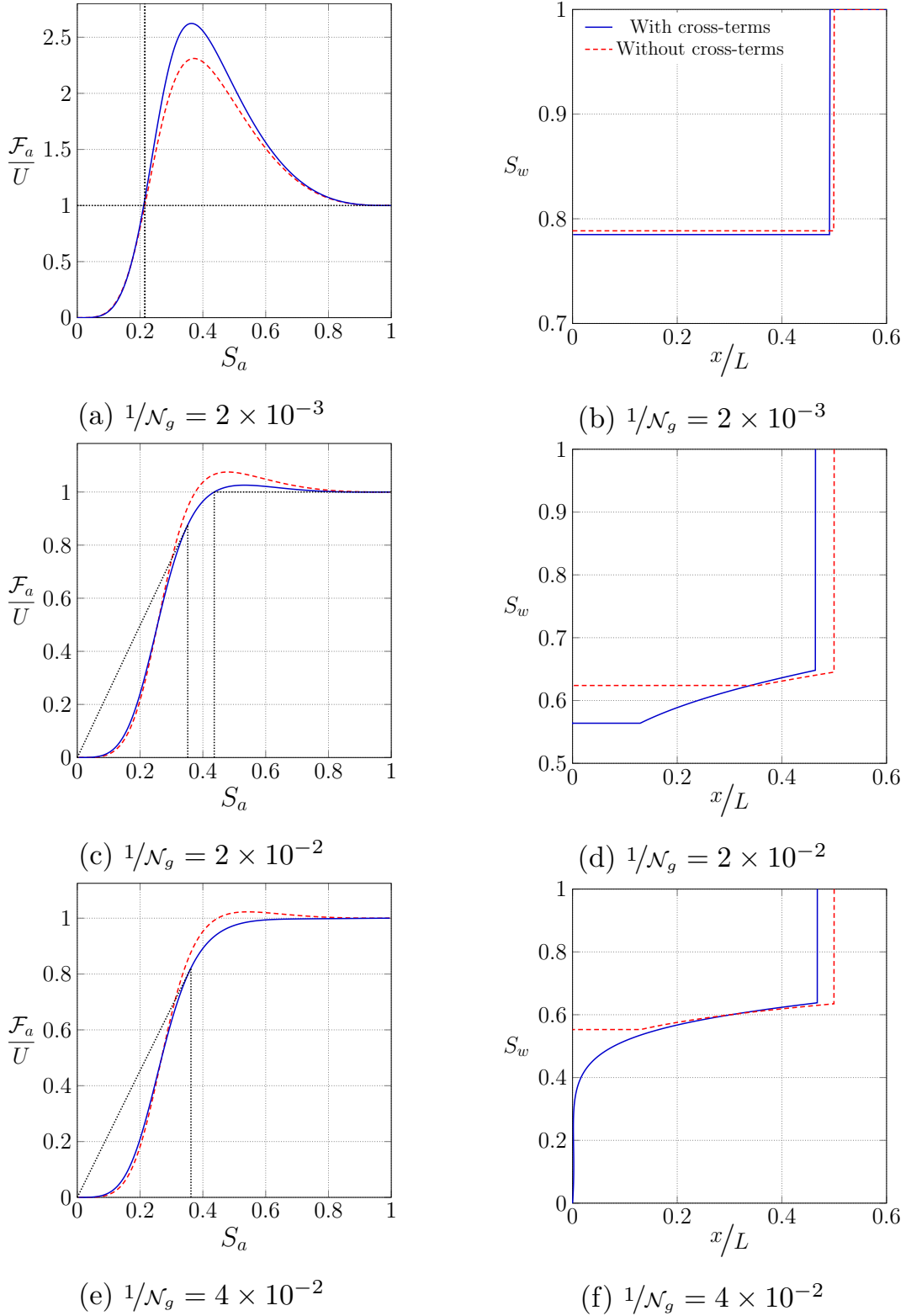


Figure 4.7 – Profiles of the water saturation S_w with (solid lines) and without (dashed lines) cross-terms for different gravity numbers \mathcal{N}_g (right) and the corresponding flux functions \mathcal{F}_w non-dimensionalized by the total velocity U (left). The profiles are given at the time corresponding to the front reaching half of the domain, i.e. $t = \frac{0.5L}{\hat{\mathcal{F}}'_w(S_w|_{\text{front}})}$, using the model without cross-terms, with L the domain length and $\hat{\mathcal{F}}'_w(S_w|_{\text{front}})$ the water front speed (see Eq. 4.68).

4.5.2 Case 2: Imbibition: air/water flow in highly permeable media

Here, we proceed to the computation of the boundary value problem presented in Fig. 4.3a, with water injected within a medium initially saturated with air. The gas phase is initially at rest while water is injected at a constant flow rate and we vary the inlet flow rate from very low inlet velocities (high gravity number \mathcal{N}_g) to relatively high inlet velocities (low \mathcal{N}_g). We adopt the simplified annular viscous flow closures for the effective parameters (see Section 4.4.4.2).

We first analyze the flow properties at steady state. Fig. 4.8 shows the profiles of water saturation, S_w , as a function of the dimensionless pressure gradient $\frac{1}{\rho_a g} \frac{\partial P}{\partial x}$ and the gravity number \mathcal{N}_g . As observed in the case of drainage, the generalized Darcy's law without cross-terms leads to a pressure drop that is balanced by $\rho_a g$ regardless of the flow rate. The model with cross-terms, on the other hand, generates significant variations of the pressure drop, from $\frac{\partial P}{\partial x} = \rho_a g$ at high \mathcal{N}_g (low flow rates), to $\frac{\partial P}{\partial x} = \rho_w g$ at low \mathcal{N}_g (high flow rates). Overall, the effect of the cross-terms is also to *retain water* within the medium at moderate gravity number ($1/\mathcal{N}_g \gtrsim 0.5$), which corresponds to flow rates where water invades almost entirely the medium. For higher gravity numbers ($1/\mathcal{N}_g \lesssim 0.5$), the impact of the cross-terms upon the saturation is limited, suggesting that cross-terms are of little importance for large values of \mathcal{N}_g .

This result only applies to the one-dimensional Buckley-Leverett configuration with co-current flow presented here. There are other situations where cross-terms may be important even in the limit of large values of \mathcal{N}_g . For instance, in structured packings used for separation processes, a thin liquid film is strongly sheared by a counter-current gas phase and often displays surface instabilities. The fact that both phases flow counter-currently ($K_{wa} U_a \neq 0$) combined with the development of instabilities (larger values of K_{wa}) may greatly increase the impact of cross terms, potentially leading to strong liquid retention [167]. Our results then suggest that the quantitative analysis of the retention phenomena requires an accurate estimation of the coupling terms, something often overlooked in the literature.

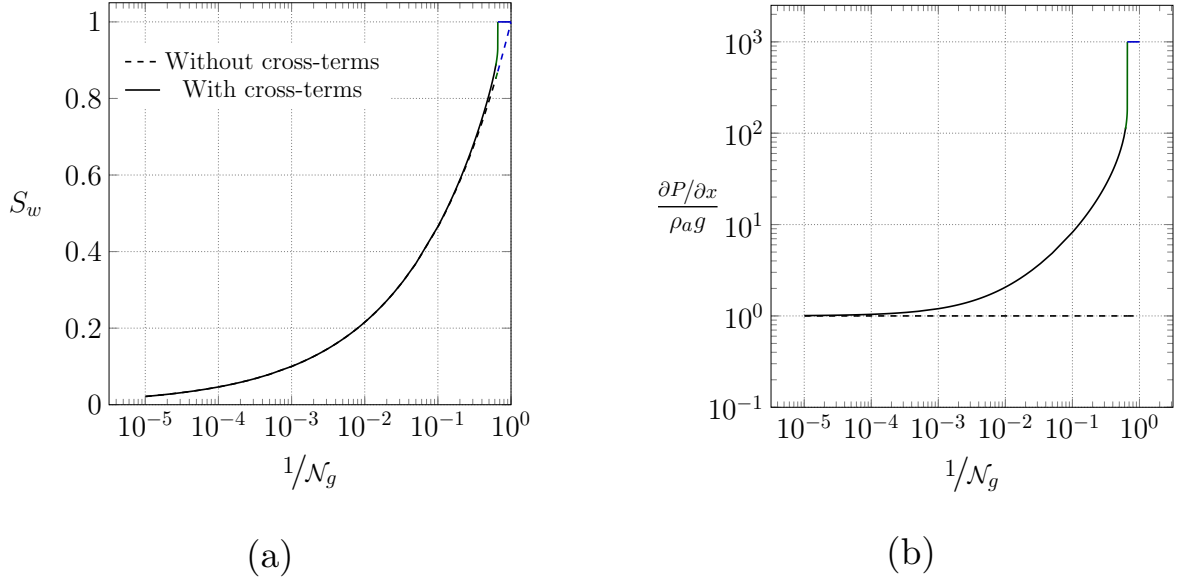


Figure 4.8 – Comparison of steady-state profiles with and without cross-terms as a function of $1/\mathcal{N}_g$ with a) the water saturation and b) dimensionless pressure gradient. The colors distinguish different regimes of \mathcal{N}_g , with a shock (black), a rarefaction wave (blue) or both (green), see Fig. 4.9.

In Fig. 4.8, we see that the nature of the fronts in the dynamic regime can change depending on the intensity of the flow rate with different colors indicating different regimes. This is detailed in Fig. 4.9 in the presence and absence of cross-terms for different values of \mathcal{N}_g . The water profile is plotted at a given time for each case, along with the corresponding flux functions \mathcal{F}_w depending on the water saturation S_w . As before, the construction of the shocks is outlined only for the model including cross-terms, along with a sketch of the characteristic curves in the $x - t$ plane. Fig. 4.9 shows that there is an increasing effect of the cross-terms with $1/\mathcal{N}_g$, on both the dynamics and steady-state. In Figs 4.9a, 4.9b, we see that for $1/\mathcal{N}_g$ small ($1/\mathcal{N}_g = 10^{-1}$), the regime is dominated by gravity and the water phase propagates as a single front. In this regime cross-terms weakly impact the dynamics of the flow and the steady-state (Fig. 4.8). For lower gravity numbers ($1/\mathcal{N}_g \gtrsim 0.5$), as plotted in Fig. 4.9c to Fig. 4.9h, the cross-terms significantly impact the profiles of the fronts. The propagation of the saturation front is slowed down because of the transfer of momentum from water to the air. Further, the model with cross-terms yields a rarefaction wave for $1/\mathcal{N}_g = 0.65$ and $1/\mathcal{N}_g = 0.83$ (Fig. 4.9c, 4.9d and 4.9e, 4.9f respectively), while the model without cross-terms leads to a single front for a wider range of \mathcal{N}_g . Finally, in Fig. 4.9g and 4.9h, which correspond to $1/\mathcal{N}_g = 1.1$, the model with cross-terms yields a single shock that propagates through the entire medium, while the model without cross-terms recovers the traditional Buckley-Leverett solution.

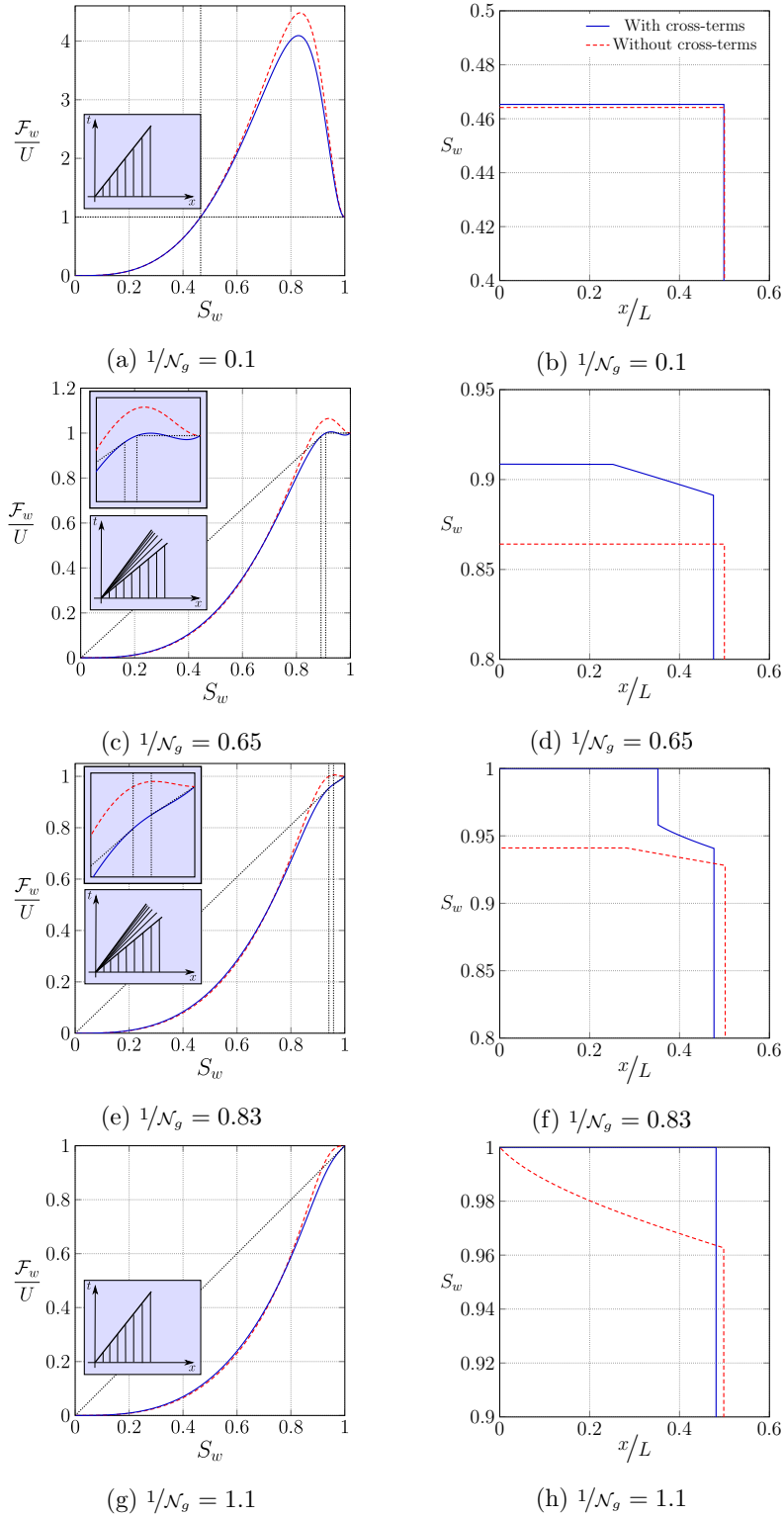


Figure 4.9 – Profiles of the water saturation S_w for different gravity numbers \mathcal{N}_g (right) and the corresponding flux functions \mathcal{F}_w non-dimensionalized by the total velocity U (left). The profiles are given at the time corresponding to the front reaching half of the domain, i.e. $t = \frac{0.5L}{\hat{\mathcal{F}}'_w(S_w|_{\text{front}})}$, using the model without cross-terms, with L the domain length and $\hat{\mathcal{F}}'_w(S_w|_{\text{front}})$ the water front speed (see Eq. 4.68). The dashed lines correspond to the model without cross-terms and the solid lines to the model with cross-terms. Insets highlight the construction of the shocks for the case with cross-terms, with indications on the position of the shocks and plots of the characteristic curves in the $x - t$ plane.

4.5.3 Case 3: Imbibition: oil/water flow in low permeability media

We now consider the constant injection of water in a porous medium of low permeability initially saturated with oil, which is a case of importance in petroleum engineering. As discussed in the introduction, we expect the fluid/solid interface to play a much important role in this case, especially when fluid phases flow in distinct pore networks and momentum exchange between the two fluid phases is negligible. Can we include this effect in the formulation with the cross-term coefficients, K_{wo} and K_{ow} ?

In order to do so, we hypothesize that the separation into different flow paths and the relative influence of fluids/solid and fluid/fluid interfaces can be represented by a scalar coefficient $\beta \in [0, 1]$, weighting the cross-terms

$$K_{wo}(\beta) = \beta K_{wo}, \quad K_{ow}(\beta) = \beta K_{ow}. \quad (4.78)$$

Here, $K_{wo}(\beta)$ and $K_{ow}(\beta)$ are cross-terms from the annular viscous closures that are simply weighted by β . As before, the K coefficients are based on the analytical solution of the annular two-phase flow Eq. 4.75. However, we do not use the simplified expressions ($\frac{\mu_j}{\mu_i} \ll 1$), since $\frac{\mu_o}{\mu_w} = 100$ in the case of oil and water.

We compare in Fig. 4.10 the profiles of $K_{ji}^*/K_0 = 1/r_\mu K_{ij}^*/K_0$ as functions of S_i for different values of β to experimental measurements from [192, 91]. Kalaydjian showed experimentally and analytically, using multiple couples of fluids, that the maximum value of the dimensionless cross-terms $K_{ji}^*/K_0 = 1/r_\mu K_{ij}^*/K_0$ obtained for capillary tubes with square section is ~ 0.2 . Zarcone and Lenormand [192] performed measurements of the cross-terms for mercury and water flows in a sand pack. They found that the magnitude of the cross-terms is much less important in their case than in experiments using capillary tubes with square section. They measured that the dimensionless cross-terms are at most $\sim 4 \times 10^{-3}$, which is well below ~ 0.2 . As discussed in the introduction, their primary hypothesis is that this weaker influence stems from the smaller interfacial area between the two-phases.

These experimental results are plotted in Fig. 4.10, along with our weighted representation of the coupling terms. Importantly, we see that changing the value of β allows us to recover both results for the sand and capillaries. For the sand we have $\beta \sim 0.1$, which confirms that the momentum exchange is smaller in low permeability media than in capillaries. Numerical results from Rothman in [150], consisting of a two-phase flow calculations in a pore-network of large permeability, are also plotted for comparison. This case is intermediate between the sand pack and the capillaries, with a maximum value of the cross-terms, ~ 0.17 , that is slightly below the one obtained for capillaries. These results are captured by using a weighting value $\beta \sim 0.96$. We conclude that only one scalar coefficient captures the trend of the coupling coefficients for different media. However, a lot of work remains to be done to derive proper constitutive relations for each effective parameter and each case. This means that a better understanding of the the link between the pore-scale physics and the macroscale behavior is needed, maybe through pore-scale simulations of the two-phase flows and new experimental designs.

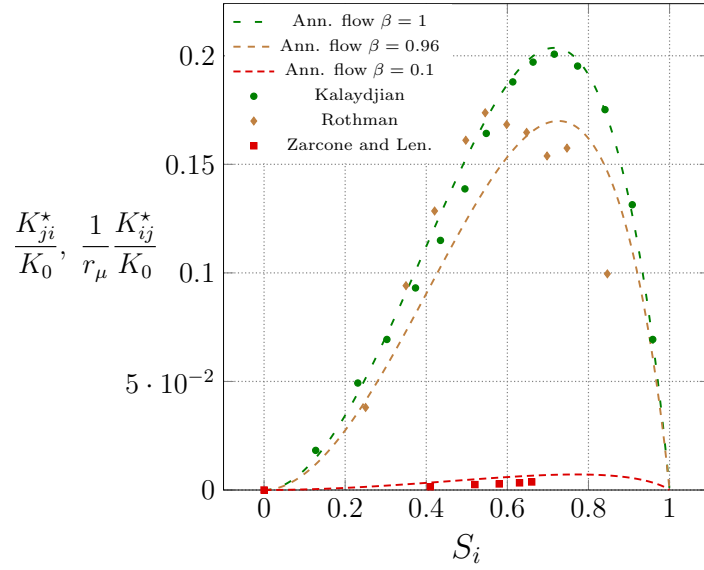


Figure 4.10 – Comparison of non-dimensionalized cross-terms for multiple weighting factors β (dashed lines, see Eq. 4.78) to experimental results from [192], [91] and numerical results from [150]. K_{ij}^*/K_0 and $K_{ji}^*/(K_0 r_\mu)$ are plotted as functions of the saturation S_i .

Based on these observations, we simulate the injection of water in a low permeability medium ($K_0 = 10^{-11} \text{m}^2$) initially filled with oil. The influence of the cross-terms on the flow properties (multiple values of β) is presented in Fig. 4.11 at *steady state* as a function of the gravity number. The pressure drop and the quantity of oil that is recovered are highly affected by the value of β , especially for moderate values of \mathcal{N}_g ($1/\mathcal{N}_g \gtrsim 0.01$). This is confirmed in the dynamic regime for $1/\mathcal{N}_g = 0.1$, in Fig. 4.12, where the profiles are considerably modified by the value of β . For $\beta \ll 1$, the profile consists in a single gravity shock with a moderate displacement of the oil, whereas for $\beta = 1$, water displaces the oil phase entirely. This result for $\beta = 1$ is unrealistic and seems to indicate that the capillary tube solution overestimates the coupling effects in low permeability media. This is also consistent with the experimental results from Zarcone and Lenormand, whose measurements correspond to $\beta \sim 0.1$. We therefore hypothesize that the permeability of the porous structure is key in evaluating the impact of the cross-terms, as it controls the relative influence of the fluid/solid and fluid/fluid interfaces. For low permeability media, the fluid/solid interface may dominate momentum transport, possibly due to a separation of flow paths for the two fluids, which may limit momentum exchanges. In contrast, highly permeable media may yield a relatively smaller influence of the fluid/solid interface and favor film, bubble or annular flows that generate more exchanges.

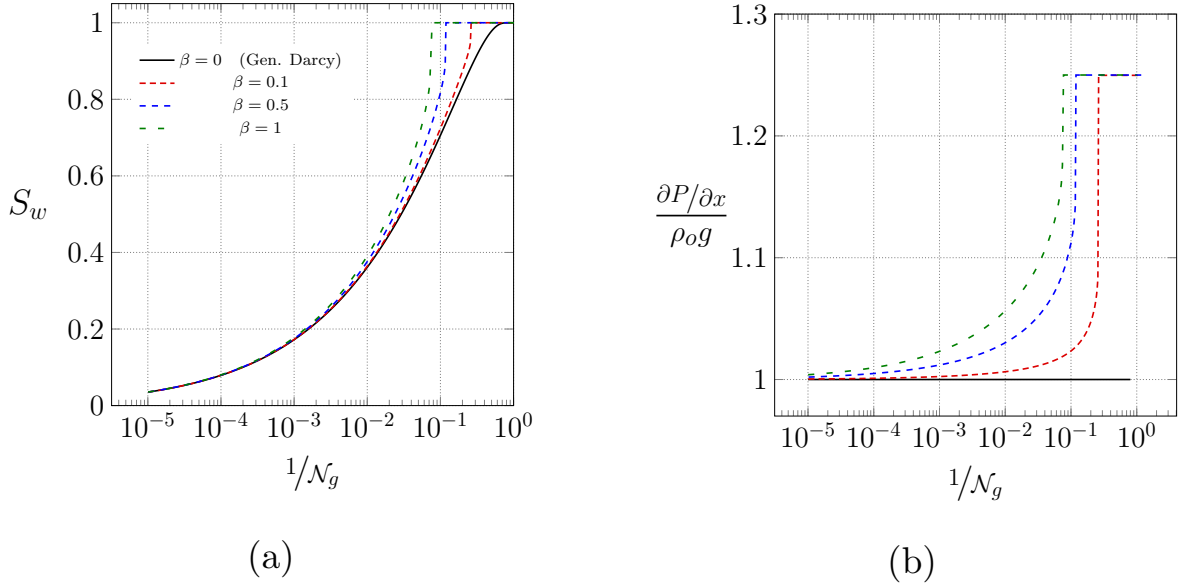


Figure 4.11 – Comparison of steady-state profiles for different values of the coefficient β with a) the water saturation and b) dimensionless pressure gradient at steady-state as a function of $1/\mathcal{N}_g$.

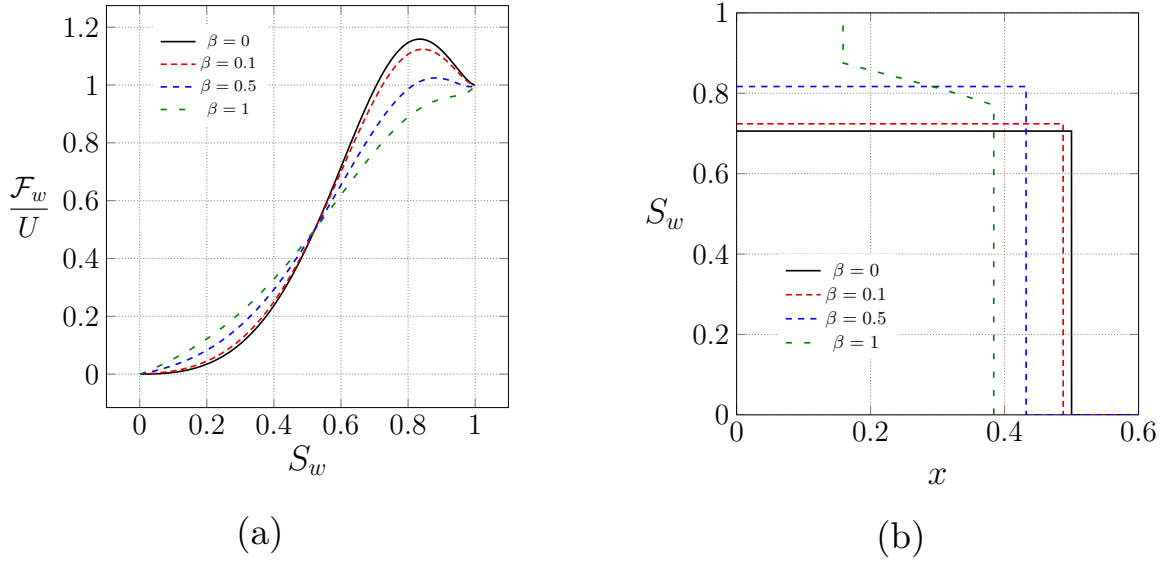


Figure 4.12 – Comparison of dynamic profiles for different values of the coefficient β with a) the flux functions \mathcal{F}_w non-dimensionalized with the total velocity U at $1/\mathcal{N}_g = 0.1$ and b) the corresponding profiles of water saturation S_w at a given time.

4.6 Conclusion

In this paper, we study the influence of momentum coupling effects for two-phase creeping flows of immiscible fluids in porous media. Our analysis is based on the Buckley-Leverett theory in a one-dimensional setting,

which is extended to account for cross-terms in the models. We consider two boundary value problems corresponding to two classical configurations encountered in porous media applications (drainage and imbibition). We study different couples of fluids, different closure relations for the effective parameters and compare our results to experimental data.

Our main result is that the cross-terms can significantly affect the flux functions, the dynamics of saturation fronts and the steady states, in ways that are confirmed experimentally and therefore physically realistic. This is important because these cross-terms are generally assumed to be negligible in the momentum balance. Our hypothesis is that, for the low permeability media considered in many studies, the fluid/solid interface dominates momentum transport, therefore limiting the influence of fluid/fluid exchanges. Depending on the wettability, capillary action and pore size distribution, low permeability media also favor the appearance of preferential flow paths for the phases and therefore further limit momentum exchange by reducing the fluid/fluid interfacial area. In contrast, highly permeable media may yield large fluid-fluid interfaces relatively to the fluid/solid ones, therefore maximizing exchanges. This is particularly obvious when comparing the experimental results from the literature to our theoretical results.

To get one step further in the description of such systems, we need experiments that measure simultaneously the flow at pore-scale and at macroscale for a broad range of permeabilities. Further, we need to go beyond the creeping flow limit that proved to be limiting in describing experiments from [33]. Similar models, including additional drag terms accounting for inertial effects can be used for this purpose [101]. The analysis of such models may be of importance in many applications involving flows at high Reynolds numbers, for instance in chemical exchangers or debris beds.

Chapter 5

Extension to the inertial regime and application to structured packings

Contents

Paper: Momentum exchange drives immiscible two-phase flows within highly permeable porous media	98
5.1 Introduction	99
5.2 The fundamental physics of two-phase flow in porous media	100
5.2.1 Mathematical system at the pore-scale	100
5.2.2 Flow regimes: low vs high permeability	100
5.3 Continuum-scale models for two-phase flows	102
5.3.1 Empirical models for highly permeable porous media	102
5.3.2 Semi-heuristic model for highly permeable porous media	103
5.3.3 Simplified one-dimensional model	107
5.4 Semi-analytical and numerical methods	108
5.4.1 Buckley-Leverett theory	108
5.4.2 Finite-volume solver	109
5.5 Results	111
5.5.1 Case 1: creeping flows	111
5.5.2 Case 2: co-current flows within particle beds	113
5.5.3 Case 3: counter-current flows within structured packings	119
5.6 Conclusion	128

Macroscale models with additional *cross-terms* were shown to be efficient for the characterization of two-phase flows with a non-negligible interaction in porous media. This interaction was shown to be directly correlated with the permeability of the medium, as high permeability media favor a large interfacial area between the two phases. The study was so far restricted to moderate flow rates and the viscous macroscale model was considered. It was especially showed that the results deviate from the experimental data of Chikhi et al. [33] as the gas flow rate increases. In this chapter, the discussion is therefore extended to high Reynolds two-phase flows, as this is the case in the distillation process. The discussion is presented in a draft of paper that is in preparation for publication.

Starting from the upscaling method developed in the literature and detailed in the last chapter, we propose a generic formulation of mass and momentum transport of immiscible gas/liquid flows in highly permeable porous media at the continuum scale. This modeling strategy is compared to the ones used in the literature for two-phase flows in such media (chemical engineering, nuclear safety). We then go on to numerical simulations of the model for multiple configurations including the gas-liquid flow in columns equipped with structured packings. In this case, a set of correlations is derived for the effective parameters of the model based on experimental data from the literature [167, 182].

Momentum exchange drives immiscible two-phase flows within highly permeable media

Sylvain Pasquier, Michel Quintard and Yohan Davit

Institut de Mécanique des Fluides de Toulouse (IMFT) - Université de Toulouse, CNRS-INPT-UPS, Toulouse France

Abstract

Multiphase flows in porous media are important in many natural and industrial processes, such as transport mechanisms in the vadose zone, CO₂ sequestration in saline aquifers, oil recovery in petroleum applications. The traditional picture for such flows is one at low Reynolds number where the distribution and flow of the different phases is controlled by interfacial energies of fluid/fluid and fluid/solid interfaces, with a major influence of wettability and capillarity. While this is accurate for flows in relatively low permeability porous media, highly permeable porous structures –such as those found in trickle bed reactors, fuel bundles in nuclear cores or distillation columns used in chemical engineering applications– challenge the relevance of this representation. In those, the relative importance of interfacial energies may be reduced, with much larger inertial effects and exchanges of momentum between fluid phases. Here, we ask the question of whether the continuum models used for flows in low permeability porous media, such as generalized Darcy’s laws, are inadequate for highly permeable porous structures. To answer this question, we first propose an alternative representation for mass and momentum transport of two-phase immiscible flow at the continuum-scale, which is based on a multiscale analysis starting from the flow problem at the pore-scale. This representation contains additional drag and cross terms, accounting respectively for inertial effects and exchanges between fluid phases. We then go on to evaluate the influence of these terms using experimental data on co- and counter-current flows from recent water/air experimental data. Our results show that this representation is much more accurate and that the additional terms capture important physical aspects of the flow, that the generalized Darcy’s law fails to describe.

5.1 Introduction

Two-phase flows of immiscible fluids in porous media play an essential role in many processes, such as transport mechanisms in the vadose zone, CO₂ sequestration in saline aquifers, oil recovery in petroleum applications, or heat transfers in nuclear cores. Such flows are complex, primarily because they combine the multiscale nature inherent to porous structures with a variety of fluid mechanics phenomena, including viscous and inertial effects, wettability, capillarity and gravity. To further add to this complexity, the relative importance of each phenomenon, which is often characterized by dimensionless numbers, may vary over several orders of magnitude –depending on the fluid properties, the flow conditions, the type of porous material, the geometry and topology of the structure– yielding extremely different flow regimes.

Modeling such flows is challenging, both at the pore- and continuum-scale. The numerical cost of pore-scale approaches is often prohibitive. Continuum-scale models are broadly used in engineering practice because they are simpler and less computationally intensive than pore-scale models. However, such models have been derived for relatively low permeability porous media, for instance for rocks in petroleum engineering (about 10^{-12} m² or less). This raises the question of whether these models apply to systems involving far greater permeabilities, for instance packed beds or structured packings used in chemical engineering applications (about 10^{-8} to 10^{-6} m²). The ratio of characteristic lengthscales between low and high permeability media is indeed about 10^3 and the dimensionless numbers –Reynolds (Re), Bond (Bo) and Weber (We) numbers– that depend on a characteristic lengthscale will be affected in the same proportion. Physically, this means that the flow regimes may be completely different, hence suggesting that standard models of porous media sciences may not apply to transport in highly permeable structures.

To further evaluate the limitations of standard approaches and whether these can be extended to large permeabilities, we first review two-phase flow models in low permeability porous media. The traditional picture for two-phase flow modeling at the continuum scale is to consider low Reynolds numbers where the interfacial energies of fluid/fluid and fluid/solid interfaces control the flow fields, with a major influence of wettability and capillarity. The early modeling approach, still widely used in engineering practice, is for instance the one of Muskat [119], which is a direct extension of the monophasic Darcy’s law for two fluid phases. The relative influence of one phase on the other one is captured by a relative permeability, which is usually treated as a function of the saturations [77]. This means that coupling between phases are treated implicitly only via a reduction of the apparent permeability. Such an approach relies implicitly on important assumptions at the pore-scale, including quasi-stationarity of the flow, whereby the pressure and velocity fields relax quickly at the pore-scale compared to the characteristic timescales of the macroscale process. Other important assumptions are that $Re \ll 1$, $Bo \ll 1$, $We \ll 1$ and the Capillary number is sufficiently small, $Ca \ll 1$ meaning predominant interfacial and viscous effects at the pore-scale. These assumptions can be used to obtain closed macroscale forms at the continuum-scale [187, 16, 91, 149, 103].

Can these models deal with large permeabilities? The most important clue comes from experimental data in engineering applications, suggesting that the generalized Darcy’s law is not be adapted to such cases. One striking configuration is counter-current flows in phase separation processes in industrial columns, where the liquid flows in the direction of gravity and gas flows counter-currently. Experimental observations [167, 182] have shown that gas flow can induce strong variations of the liquid retention and of the pressure drop. This is, in essence, a strong coupling effect where the velocity in one phase is directly influencing the velocity in the other phase, a phenomenon that cannot be described with an implicit coupling and standard expressions of the relative permeability. To model such effects, engineers have introduced cross terms that couple explicitly the velocities, allowing for momentum exchanges between both phases. These have been used in chemical engineering ([167, 83, 82]) and nuclear safety applications [108, 177, 176, 155]. Comparison with experimental

data [33, 35, 176] have shown that these cross-terms are essential to systems with high permeabilities .

Do these empirical formulations solve the problem of modeling mass and momentum transport in highly permeable porous structures? They are certainly an important element and provide a good basis on which to build. However, we need to develop more generic formulations and to understand better the link between the fundamental physics at the pore-scale (detailed in Section 5.2) and the continuum-scale models. Here, our goal is to propose a generic formulation of mass and momentum transport of immiscible gas/liquid flows in highly permeable porous media (detailed in Section 5.3), along with elements of understanding for linking the pore- and continuum-scale. To do so, our strategy consists in a semi-heuristic approach, whereby we mix results obtained from experiments with theoretical approaches. In particular, we will use spatial averaging consideration, with an approach close to the volume averaging theory, which also provides a good basis on which to build and understand the links between the different scales. Using semi-analytical and numerical methods (Section 5.4), we will then study two different cases based on experimental data from the literature [36, 182] to assess the relevance and accuracy of our model.

5.2 The fundamental physics of two-phase flow in porous media

Here, we start by discussing several fundamental aspects of two-phase flows in porous media, starting with the mathematical description of mass and momentum transport.

5.2.1 Mathematical system at the pore-scale

We consider a system of two immiscible and Newtonian fluids, i (domain Ω_i) and j (domain Ω_j), in a domain Ω containing a solid structure denoted σ . Assuming constant densities and viscosities, the boundary value problem describing the flow at the pore-scale is

$$\nabla \cdot \mathbf{u}_\alpha = 0 \quad \text{in } \Omega_\alpha, \quad \alpha = i, j, \quad (5.1a)$$

$$\rho_\alpha \left(\frac{\partial \mathbf{u}_\alpha}{\partial t} + \mathbf{u}_\alpha \cdot \nabla \mathbf{u}_\alpha \right) = -\nabla p_\alpha + \nabla \cdot \left[\mu_\alpha \left(\nabla \mathbf{u}_\alpha + (\nabla \mathbf{u}_\alpha)^T \right) \right] + \rho_\alpha \mathbf{g} \quad \text{in } \Omega_\alpha, \quad \alpha = i, j. \quad (5.1b)$$

$$\mathbf{u}_\alpha = 0 \quad \text{at } \Gamma_{\alpha\sigma} \quad \alpha = i, j, \quad (5.1c)$$

$$\mathbf{u}_i = \mathbf{u}_j \quad \text{at } \Gamma_{ij}, \quad (5.1d)$$

$$-p_i \mathbf{n}_{ij} + \mu_i \mathbf{n}_{ij} \cdot \left(\nabla \mathbf{u}_i + (\nabla \mathbf{u}_i)^T \right) = -p_j \mathbf{n}_{ij} + \mu_j \mathbf{n}_{ij} \cdot \left(\nabla \mathbf{u}_j + (\nabla \mathbf{u}_j)^T \right) + 2\gamma H \mathbf{n}_{ij} \quad \text{at } \Gamma_{ij}, \quad (5.1e)$$

where γ is the surface tension for the couple of fluids i and j and H is the local curvature of the interface Γ_{ij} .

5.2.2 Flow regimes: low vs high permeability

So far, we have only given an intuitive definition of high and low permeabilities. How can we define these concepts more precisely? The first element of answer is that there is no consensus on that and different ways to define the concepts. A central idea common to all the definitions is that the permeability is expressed in squared meters, so that $\sqrt{K_0}$ can be used as characteristic lengthscale for the medium. From there, focusing for simplicity on a liquid (wetting)/gas (non-wetting system), we could define a highly permeable structure

as one in which the capillary length of the wetting phase is much smaller than the size of the pores,

$$l_c = \sqrt{\frac{\gamma}{(\rho_l - \rho_g)g}} \ll \sqrt{K_0}, \quad (5.2)$$

with g the gravitational acceleration and γ the surface tension between phases l and g . This essentially means that gravitational effects dominate over capillary ones. The high permeability case will tend to generate configurations with films, as represented in Fig. 5.1b, whereas the low permeability may lead to a distribution in segregated domains with distinct flow paths [106, 150] as in Fig. 5.1a. In terms of contact area, the fluid/fluid interfacial area, which is important for momentum exchanges between phases, will also strongly depend upon the configuration. In the film case, we have $\mathcal{A}_{lg} \sim \mathcal{A}_{l\sigma}$ with \mathcal{A}_{lg} the area between l and g and $\mathcal{A}_{l\sigma}$ the liquid/solid area. On the other hand, in the other configuration, we have $\mathcal{A}_{lg} \ll \mathcal{A}_{l\sigma}$. This suggests that $\mathcal{A}_{l\sigma}$ may control the flow in cases with low permeability whereas \mathcal{A}_{lg} (exchanges between phases) will be much important for high permeabilities.

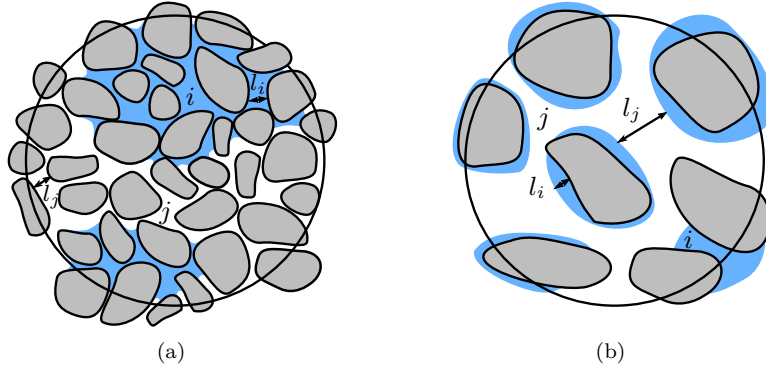


Figure 5.1 – Illustration of two-phase flows in a) low and b) high permeability media.

One problem with this definition, however, is that it does not take into account the wettability of the solid, which may be fundamentally important in determining the phases configuration. This idea of defining high permeability systems depending on the importance of surface tension can be made slightly more general by considering both l_c and a *spreading coefficient* [68, 45] of the wetting phase defined by

$$S_p = \gamma_{\sigma g} - (\gamma_{\sigma l} + \gamma_{lg}), \quad (5.3)$$

for a liquid/gas couple of fluids (σ refers to the solid). When $S_p > 0$, the liquid wets the surface completely while when $S_p < 0$, partial wetting occurs. Therefore, we would define a high permeability medium as one for which $l_c \ll \sqrt{K_0}$ and $S_p > 0$.

Other important effects such as viscosity and inertia, which potentially drastically modify the phases distribution and the flow characteristics, can also be considered. For instance, inertial effects can strongly modify the interfacial area \mathcal{A}_{lg} with surface instabilities, ripples at the surface of the wetting phase, or dispersed droplets in the non-wetting phase. To go beyond this issue, another much more general point of view is to define the concepts of low/high permeabilities based on the relative importance of all the different fluid mechanics phenomena occurring in the flow through the porous material. This can be measured by dimensionless numbers that directly depend on the permeability, such as the Reynolds number,

$$Re_i = \frac{\rho_i U_i \sqrt{K_0}}{\mu_i}, \quad (5.4)$$

with U_i a reference velocity, the Bond number,

$$Bo_i = \frac{(\rho_i - \rho_j) g K_0}{\gamma}, \quad (5.5)$$

and the Weber number,

$$We_i = \frac{\rho_i U_i^2 \sqrt{K_0}}{\gamma}. \quad (5.6)$$

It is fundamental here that all these dimensionless numbers are monotonically increasing with K_0 . Therefore we can define high permeability system as any system for which either Re_i , Bo_i or We_i is much larger than one.

5.3 Continuum-scale models for two-phase flows

5.3.1 Empirical models for highly permeable porous media

The first class of models that we consider, although they are *a priori* inadequate for our case, is based on the assumption that the flow is locally dominated by capillarity, meaning that the Bond and Capillary numbers are such that Bo , $Ca \ll 1$. Under this assumption, the fluid-fluid interface is assumed to be quasi-static and the difference of the pressures at the continuum scale reduces to

$$P_j - P_i = 2\gamma \langle H \rangle_{ij}, \quad (5.7)$$

where $\langle H \rangle_{ij}$ is the averaged curvature over a REV. We adopt here the notation P_j for the intrinsic averaged pressure of a phase j , which holds for the remaining of this paper. The Reynolds numbers Re of the two phases are also assumed to be low so that the fluids flow as creeping flows. Under these assumptions, a large range of models introduce the following sort of relationships for the macroscale capillary pressure

$$P_j - P_i = p_c(S_i, \dots), \quad (5.8)$$

with p_c referred as the capillary pressure relationship. Models include the saturation S_i and can involve other macroscale dependencies. The wettability of the solid structure (triple lines) can for instance be accounted partially through non-linear dependencies of the capillary pressure. These assumptions also lead to the heuristic system of mass and momentum equations at the macroscale

$$\varepsilon \frac{\partial S_\alpha}{\partial t} + \nabla \cdot \mathbf{U}_\alpha = 0, \quad \alpha = i, j, \quad (5.9a)$$

$$\mathbf{U}_\alpha = -\frac{\mathbf{K}_{\alpha\alpha}}{\mu_\alpha} \cdot (\nabla P_\alpha - \rho_\alpha \mathbf{g}), \quad \alpha = i, j, \quad (5.9b)$$

where the tensor $\mathbf{K}_{\alpha\alpha} = k_{r_\alpha}(S_\alpha, \dots) \mathbf{K}_0$ involves the so-called relative permeability k_{r_α} and \mathbf{K}_0 is the monophasic permeability. \mathbf{U}_α is the filtration velocity, which is the notation adopted in this paper for such velocity.

Several models were derived for two-phase flows in highly permeable media, relying primarily on heuristic and empirical basis.

$$\mathbf{K}_{\alpha\alpha} = \mathbf{K}_0 k_{r_\alpha}. \quad (5.10)$$

For instance, models used for the simulation of debris bed reflooding in case of severe accident in nuclear safety consist in one-dimensional generalizations of Ergun's equations to two-phase flows [108, 177, 155, 57].

The momentum balance in these models sometimes involve a friction term \mathcal{F}_{ij} to account for the interfacial effects of friction,

$$-(\nabla P_\alpha - \rho_\alpha \mathbf{g}) = \underbrace{\frac{\mu_\alpha}{K_0 k_{r_\alpha}} \mathbf{U}_\alpha}_{\text{Linear drag}} + \underbrace{\frac{\rho_\alpha}{\eta \eta_\alpha} \|\mathbf{U}_\alpha\| \mathbf{U}_\alpha}_{\text{Quadratic drag}} \pm \underbrace{\frac{\mathcal{F}_{ij}}{\varepsilon S_\alpha}}_{\text{Fluid/fluid friction}}, \quad \alpha = i, j. \quad (5.11)$$

This model involves coefficients known as the passability η and relative passability η_α , which are generally non-linear functions of the saturation. The friction term \mathcal{F}_{ij} is written as a quadratic function of the relative velocity in Schulenberg et al. [155]. Similar forms have also been used in petroleum engineering for the description of high flow rates flows in fractures or near wellbores [52, 110, 59, 60], and in chemical engineering where interfacial forces (solid/fluid and fluid/fluid) are modeled via friction terms and where the momentum balance takes the form of an extended Navier-Stokes equation [15, 82, 62, 130, 99]

$$\rho_\alpha \left(\frac{\partial \mathbf{U}_\alpha}{\partial t} + \mathbf{U}_\alpha \cdot \nabla \mathbf{U}_\alpha \right) = -(\nabla P_\alpha - \rho_\alpha \mathbf{g}) + \underbrace{\mathcal{F}_{\alpha\sigma}}_{\text{Solid/fluid friction}} \pm \underbrace{\mathcal{F}_{ij}}_{\text{Fluid/fluid friction}}, \quad \alpha = i, j. \quad (5.12)$$

The left hand side in Eq. 5.12 corresponds to macroscopic accumulation and advection terms that are usually not adapted to porous media formulations because the porous medium destroys coherent structures that are larger than the size of the pores [88]. The volumic friction terms fluid/solid $\mathcal{F}_{\alpha\sigma}$ and fluid/fluid \mathcal{F}_{ij} correspond to exchanges of momentum at the interfaces $\Gamma_{\alpha\sigma}$ and Γ_{ij} respectively. They are generally written as

$$\mathcal{F}_{\alpha\sigma} = \beta_1 \mathbf{U}_\alpha + \beta_2 \|\mathbf{U}_\alpha\| \mathbf{U}_\alpha, \quad \mathcal{F}_{ij} = \beta_3 \mathbf{U}_{ij}^r + \beta_4 \|\mathbf{U}_{ij}^r\| \mathbf{U}_{ij}^r, \quad \alpha = i, j, \quad (5.13)$$

where \mathbf{U}_{ij}^r is the relative velocity, $\mathbf{U}_{ij}^r = \mathbf{U}_i - \mathbf{U}_j$, and the β terms some functions of the saturation.

5.3.2 Semi-heuristic model for highly permeable porous media

In this Section, we derive a semi-heuristic formulation of mass and momentum for highly permeable media. To do so, we discuss the possibility of deriving a theoretical set of mass and momentum equations at the continuum scale based on the volume averaging method [186, 189, 188, 101]. We consider the two limit cases of low and high permeability media, where the Reynolds, Capillary and Weber numbers are likely to be low in the first case and high in the latter case.

The question of momentum transfer between two-phases in porous media has already been studied theoretically. The most simple example of this is the Poiseuille flow in an annular capillary tube for which these cross-terms appear naturally [91, 149]. The problem has also been studied using upscaling techniques, also showing the existence of these momentum exchanges through explicit cross-terms [71, 116, 46, 187, 90, 148]. Considering, respectively, a creeping and steady laminar two-phase flow, Whitaker [189, 186] and Lasseux et al. [103, 101] developed macroscale models using the volume averaging method. Let us consider the averaged momentum balance that results from the volume averaging procedure [101],

$$0 = -\nabla P_\alpha + \rho_\alpha \mathbf{g} + \frac{1}{V_\alpha} \int_{\Gamma_{\alpha\sigma} \cup \Gamma_{ij}} \mathbf{n}_\alpha \cdot [-\tilde{p}_\alpha \mathbf{I} + \mu_\alpha (\nabla \tilde{\mathbf{u}}_\alpha + \nabla \tilde{\mathbf{u}}_\alpha^T)] d\Gamma, \quad \alpha = i, j, \quad (5.14)$$

where the pressure and velocity fields are decomposed in average-plus-perturbation using the decomposition of Gray [63]. One recognizes the pressure gradient terms and a surface integral that characterizes the pressure and viscous forces at the fluid/solid and fluid/fluid interfaces. The volume averaging method consists

in building closure relationships between the microscale and the macroscale variables, i.e. build explicit relationships for the perturbation terms \tilde{p}_α and $\tilde{\mathbf{u}}_\alpha$. Considering the macroscopic terms involved in the evolution of the perturbations variables \tilde{p}_α and $\tilde{\mathbf{u}}_\alpha$, the closure relationships write under the form

$$\tilde{\mathbf{u}}_\alpha = \varepsilon_\alpha^{-1} \mathbf{A}_{\alpha\alpha} \cdot \mathbf{U}_\alpha + \varepsilon_\kappa^{-1} \mathbf{A}_{\alpha\kappa} \cdot \mathbf{U}_\kappa + \frac{\mathbf{B}_\alpha}{\mu_\alpha} \left[(P_j - P_i) - 2\gamma \langle H \rangle_{ij} \right] + \dots, \quad \alpha, \kappa = i, j, \quad \alpha \neq \kappa, \quad (5.15a)$$

$$\tilde{p}_\alpha = \mu_\alpha \left[\varepsilon_\alpha^{-1} \mathbf{a}_{\alpha\alpha} \cdot \mathbf{U}_\alpha + \varepsilon_\kappa^{-1} \mathbf{a}_{\alpha\kappa} \cdot \mathbf{U}_\kappa \right] + \frac{\mathbf{b}_\alpha}{\mu_\alpha} \left[(P_j - P_i) - 2\gamma \langle H \rangle_{ij} \right] + \dots, \quad \alpha, \kappa = i, j, \quad \alpha \neq \kappa, \quad (5.15b)$$

where the macroscopic variables involved are the intrinsic velocities of the two phases, $\varepsilon_i^{-1} \mathbf{U}_i$ and $\varepsilon_j^{-1} \mathbf{U}_j$, the difference of the averaged pressures, $P_j - P_i$, the surface average of the curvature of the interface Γ_{ij} , $\langle H \rangle_{ij}$, and, strictly speaking, potential other terms characterizing time-dependant effects. These two relationships consist in linear combinations of these macroscopic terms through a number of mapping variables, or closure variables ($\mathbf{A}_{\alpha\alpha}$, $\mathbf{A}_{\alpha\kappa}$, ...). We will now consider two limit cases where these relationships can be simplified.

5.3.2.1 Upscaling: the case of low Re , Ca and We numbers

Let us consider the boundary condition for the momentum at the interface Γ_{ij} , Eq. 5.1e, after decomposition in averaged-plus-perturbations

$$\mathbf{n}_{ij} (\tilde{p}_j - \tilde{p}_i) + \mathbf{n}_{ij} (P_j - P_i) = \mu_j \mathbf{n}_{ij} \cdot \left(\nabla \tilde{\mathbf{u}}_j + (\nabla \tilde{\mathbf{u}}_j)^T \right) - \mu_i \mathbf{n}_{ij} \cdot \left(\nabla \tilde{\mathbf{u}}_i + (\nabla \tilde{\mathbf{u}}_i)^T \right) + 2\gamma H \mathbf{n}_{ij} \text{ at } \Gamma_{ij}. \quad (5.16)$$

The macroscale viscous shear-stress was neglected in the balance as it is much smaller than the other terms. If one estimates the pressure and viscous stresses as

$$\tilde{p}_\alpha = \mathcal{O}(\rho_\alpha U_\alpha^2), \quad \mu_\alpha \nabla \tilde{\mathbf{u}}_\alpha = \mathcal{O}\left(\frac{\mu_\alpha U_\alpha}{l_\alpha}\right), \quad \alpha = i, j, \quad (5.17)$$

where l_α and U_α are characteristic lengthscale and velocity, one gets that the capillary pressure $2\gamma H$ is predominant under the conditions

$$\frac{\mu_\alpha U_\alpha / l_\alpha}{2\gamma H} = \frac{Ca_\alpha}{2l_\alpha H} \ll 1, \quad \frac{\rho_\alpha U_\alpha^2}{2\gamma H} = \frac{We_\alpha}{2l_\alpha H} \ll 1, \quad \alpha = i, j. \quad (5.18)$$

Under these conditions, the relation Eq. 5.16 therefore reduces to

$$P_j - P_i = 2\gamma H, \quad (5.19)$$

which says that the curvature of the interface is controlled by the difference of the averaged pressures. One can further obtain the macroscale capillary pressure

$$P_j - P_i = 2\gamma \langle H \rangle_{ij}, \quad (5.20)$$

by considering that the pressure deviations, \tilde{H} , remain small in this case. This relation also allows to write Eq. 5.16 under the form

$$\mathbf{n}_{ij} (\tilde{p}_j - \tilde{p}_i) = \mu_j \mathbf{n}_{ij} \cdot \left(\nabla \tilde{\mathbf{u}}_j + \nabla \tilde{\mathbf{u}}_j^T \right) - \mu_i \mathbf{n}_{ij} \cdot \left(\nabla \tilde{\mathbf{u}}_i + \nabla \tilde{\mathbf{u}}_i^T \right) \text{ at } \Gamma_{ij}. \quad (5.21)$$

This relation characterizes the exchange of momentum for the perturbations and does not involve any terms from the macroscale anymore. One can therefore rewrite the closure relationships for $\tilde{\mathbf{u}}_\alpha$ and \tilde{p}_α which

considerably simplify under the definition of the macroscale capillary pressure

$$\tilde{\mathbf{u}}_\alpha = \varepsilon_\alpha^{-1} \mathbf{A}_{\alpha\alpha} \cdot \mathbf{U}_\alpha + \varepsilon_\kappa^{-1} \mathbf{A}_{\alpha\kappa} \cdot \mathbf{U}_\kappa, \quad \alpha, \kappa = i, j, \quad \alpha \neq \kappa, \quad (5.22a)$$

$$\tilde{p}_\alpha = \mu_\alpha [\varepsilon_\alpha^{-1} \mathbf{a}_{\alpha\alpha} \cdot \mathbf{U}_\alpha + \varepsilon_\kappa^{-1} \mathbf{a}_{\alpha\kappa} \cdot \mathbf{U}_\kappa], \quad \alpha, \kappa = i, j, \quad \alpha \neq \kappa. \quad (5.22b)$$

These closure relationships are the one derived in Whitaker [189, 186] and Lasseux et al. [103, 101]. They are derived here under the conditions given in Eq. 5.18. Based on these closures, the momentum balance Eq. 5.14 can be rewritten under the form

$$\begin{aligned} 0 = & -(\nabla P_\alpha - \rho_\alpha \mathbf{g}) \\ & + \mu_\alpha \left\{ \underbrace{\frac{\varepsilon_\alpha^{-1}}{V_\alpha} \int_{\Gamma_{\alpha\sigma} \cup \Gamma_{ij}} \mathbf{n}_\alpha \cdot \left[-\mathbf{a}_{\alpha\alpha} \mathbf{I} + \left(\nabla \mathbf{A}_{\alpha\alpha} + (\nabla \mathbf{A}_{\alpha\alpha})^T \right) \right] d\Gamma}_1 \right\} \cdot \mathbf{U}_\alpha \\ & + \mu_\alpha \left\{ \underbrace{\frac{\varepsilon_\alpha^{-1}}{V_\alpha} \int_{\Gamma_{\alpha\sigma} \cup \Gamma_{ij}} \mathbf{n}_\alpha \cdot \left[-\mathbf{a}_{\alpha\kappa} \mathbf{I} + \left(\nabla \mathbf{A}_{\alpha\kappa} + (\nabla \mathbf{A}_{\alpha\kappa})^T \right) \right] d\Gamma}_2 \right\} \cdot \mathbf{U}_\kappa. \end{aligned} \quad (5.23)$$

$$\alpha, \kappa = i, j, \quad \alpha \neq \kappa.$$

The mapping variables are further solutions of a boundary value problem at the microscale, the so-called closure problem, under the strict condition of a laminar stationary flow and of a quasi-static process.

Besides, the integral terms can be interpreted in terms of effective functions \mathbf{K} and \mathbf{F} , where the \mathbf{K} functions refer to viscous contributions and the \mathbf{F} functions to inertial contributions (velocity dependant terms)

$$0 = -(\nabla P_\alpha - \rho_\alpha \mathbf{g}) - \mu_\alpha \underbrace{\mathbf{K}_{\alpha\alpha}^{-1} \cdot (\mathbf{I} + \mathbf{F}_{\alpha\alpha})}_1 \cdot \mathbf{U}_\alpha + \mu_\alpha \underbrace{\mathbf{K}_{\alpha\alpha}^{-1} \cdot (\mathbf{K}_{\alpha\kappa} - \mathbf{F}_{\alpha\kappa})}_2 \cdot \mathbf{U}_\kappa, \quad \alpha, \kappa = i, j, \quad \alpha \neq \kappa. \quad (5.24)$$

\mathbf{K}_{ii} and \mathbf{K}_{jj} are referred as the permeability tensors and \mathbf{K}_{ij} and \mathbf{K}_{ji} as the viscous *cross* tensors, while \mathbf{F}_{ii} and \mathbf{F}_{jj} are inertial correction tensors and \mathbf{F}_{ij} and \mathbf{F}_{ji} are inertial *cross* tensors. The momentum balance is generally written under the form of a Darcy-like law. Together with the mass balance at the macroscale, the complete model finally reads

$$\varepsilon \frac{\partial S_\alpha}{\partial t} + \nabla \cdot \mathbf{U}_\alpha = 0, \quad \alpha = i, j, \quad (5.25)$$

$$\mathbf{U}_\alpha = -\frac{\mathbf{K}_{\alpha\alpha}}{\mu_\alpha} \cdot (\nabla P_\alpha - \rho_\alpha \mathbf{g}) - \mathbf{F}_{\alpha\alpha} \cdot \mathbf{U}_\alpha + (\mathbf{K}_{\alpha\kappa} - \mathbf{F}_{\alpha\kappa}) \cdot \mathbf{U}_\kappa, \quad \alpha, \kappa = i, j, \quad \alpha \neq \kappa. \quad (5.26)$$

5.3.2.2 Upscaling: the case of large Re and We numbers

As pointed out earlier, highly permeable media are more prone to verify high Reynolds and Weber numbers, i.e. predominant inertial effects compared to viscous and capillary effects. One can actually show that the structure of the momentum balance Eq. 5.26 might still hold under these conditions. Indeed, using the

estimations of the pressure and velocity perturbations from Eq. 5.17, one sees that the pressure term is predominant over the viscous and capillary terms in Eq. 5.16 in case of high Reynolds and Weber numbers

$$\frac{\rho_\alpha U_\alpha^2}{\mu_\alpha U_\alpha / l_\alpha} = Re_\alpha \gg 1, \quad \frac{\rho_\alpha U_\alpha^2}{2\gamma H} = \frac{We_\alpha}{2l_\alpha H} \gg 1. \quad (5.27)$$

This condition shows that the difference of pressure between the two phases is small in case of highly permeable media. It leads to consider one unique pressure in the system

$$P = P_i = P_j, \quad (5.28)$$

which is an assumption usually made in chemical engineering [83] (for instance structured packings). Under this condition of low capillary effects and considering one unique pressure, the relation Eq. 5.16 reduces again to

$$\mathbf{n}_{ij} (\tilde{p}_j - \tilde{p}_i) = \mu_j \mathbf{n}_{ij} \cdot (\nabla \tilde{\mathbf{u}}_j + \nabla \tilde{\mathbf{u}}_j^T) - \mu_i \mathbf{n}_{ij} \cdot (\nabla \tilde{\mathbf{u}}_i + \nabla \tilde{\mathbf{u}}_i^T) \text{ at } \Gamma_{ij}. \quad (5.29)$$

From that point, one can follow the same strategy than in the case of low Capillary and Weber numbers to build closure relationships for the pressure and velocity perturbations, Eq. 5.22. Following this reasoning, the macroscale momentum balance Eq. 5.26 therefore holds for the present conditions. It should be noted, however, that in the case of high Reynolds numbers, the hypothesis of a quasi-static interface at the pore-scale cannot be verified. One has to keep the time-dependant terms in the boundary value problems for the perturbations (see [101]), leading to a distinct closure problem at the end (time dependant term in the momentum balance). We emphasize, therefore, that further theoretical developments are required in the case of highly permeable media to develop rigorous closure problems. The present approach in case of high Reynolds and Weber numbers is therefore semi-heuristic, but it proves that the momentum balance Eq. 5.26 still hold in this configuration.

5.3.2.3 Heuristic versus semi-heuristic approaches: what are the differences?

A few differences can be highlighted between the momentum balance widely used in chemical engineering Eq. 5.12 and the one that results from the volume averaging method Eq. 5.26. This difference is mainly on the treatment of the integral term in Eq. 5.23 on the interfaces $\Gamma_{i\sigma}$, $\Gamma_{j\sigma}$ and Γ_{ij} . Indeed, if one looks at the momentum balance Eq. 5.23, it is seen that the integral terms for one fluid applies on the *two* interfaces, $\Gamma_{\alpha\sigma}$ and Γ_{ij} (respectively $\Gamma_{j\sigma}$ and Γ_{ij}). In other words, the integrals on the various interfaces affect *all* effective properties. The friction forces $\mathcal{F}_{i\sigma}$ and \mathcal{F}_{ij} as in Eq. 5.12, conversely, correspond to a transfer of momentum at $\Gamma_{i\sigma}$ and Γ_{ij} respectively [82]. By rewriting the momentum balance Eq. 5.23 in terms of two friction forces

onto $\Gamma_{\alpha\sigma}$ and Γ_{ij} , it comes

$$\begin{aligned}
0 &= -(\nabla P_\alpha - \rho_\alpha \mathbf{g}) + \\
&\underbrace{\frac{\mu_\alpha}{V} \int_{\Gamma_{\alpha\sigma}} \left(\mathbf{n}_{\alpha\sigma} \cdot \left[-\mathbf{a}_{\alpha\alpha} \mathbf{I} + \left(\nabla \mathbf{A}_{\alpha\alpha} + (\nabla \mathbf{A}_{\alpha\alpha})^T \right) \right] \cdot \mathbf{U}_\alpha + \mathbf{n}_{\alpha\sigma} \cdot \left[-\mathbf{a}_{\alpha\kappa} \mathbf{I} + \left(\nabla \mathbf{A}_{\alpha\kappa} + (\nabla \mathbf{A}_{\alpha\kappa})^T \right) \right] \cdot \mathbf{U}_\kappa \right) d\Gamma}_{\mathcal{F}_{\alpha\sigma}} + \\
&\underbrace{\frac{\mu_\alpha}{V} \int_{\Gamma_{ij}} \left(\mathbf{n}_{\alpha\kappa} \cdot \left[-\mathbf{a}_{\alpha\alpha} \mathbf{I} + \left(\nabla \mathbf{A}_{\alpha\alpha} + (\nabla \mathbf{A}_{\alpha\alpha})^T \right) \right] \cdot \mathbf{U}_\alpha + \mathbf{n}_{\alpha\sigma} \cdot \left[-\mathbf{a}_{\alpha\kappa} \mathbf{I} + \left(\nabla \mathbf{A}_{\alpha\kappa} + (\nabla \mathbf{A}_{\alpha\kappa})^T \right) \right] \cdot \mathbf{U}_\kappa \right) d\Gamma}_{\mathcal{F}_{ij}}, \\
\alpha &= i, j, \quad \alpha \neq \kappa.
\end{aligned} \tag{5.30}$$

One sees in this momentum balance that the volumic forces $\mathcal{F}_{i\sigma}$ and $\mathcal{F}_{j\sigma}$ at the fluid/solid interfaces depend explicitly on the two averaged velocities \mathbf{U}_i and \mathbf{U}_j . This is in contradiction with the closures usually used in chemical engineering, where the fluid/solid friction forces involve the averaged velocity of the fluid phase only (see Eq. 5.13). Further, the friction forces in Eq. 5.30 do not constrain any scalings in terms of velocities or saturation at the continuum scale, while a quadratic scaling is often involved for the drag terms.

The structure of Eq. 5.30 therefore questions the momentum balance usually used in engineering practice. The computation of the closure problems on $(\mathbf{a}_{\alpha\alpha}, \mathbf{A}_{\alpha\alpha})$ and $(\mathbf{a}_{\alpha\kappa}, \mathbf{A}_{\alpha\kappa})$, see [103, 101], for a laminar two-phase flow, would also allow to provide further information to enhance the comparison.

5.3.3 Simplified one-dimensional model

In this section, we simplify the semi-heuristic model that results from the volume averaging method for two-phase flows in highly permeable media. We indeed consider a one-dimensional configuration and also presents an other expression of the momentum balance used later for the numerical resolution.

Mass balance With these assumptions, the mass balance equations now read

$$\varepsilon \begin{pmatrix} \frac{\partial S_i}{\partial t} \\ \frac{\partial S_j}{\partial t} \end{pmatrix} + \begin{pmatrix} \frac{\partial U_i}{\partial x} \\ \frac{\partial U_j}{\partial x} \end{pmatrix} = \begin{pmatrix} 0 \\ 0 \end{pmatrix}. \tag{5.31}$$

Momentum balance with cross-terms Momentum balance equations with cross-terms read

$$U_i = -\frac{K_{ii}}{\mu_i} \left(\frac{\partial P}{\partial x} - \rho_i g \right) - F_{ii} U_i + (K_{ij} - F_{ij}) U_j, \tag{5.32a}$$

$$U_j = -\frac{K_{jj}}{\mu_j} \left(\frac{\partial P}{\partial x} - \rho_j g \right) - F_{jj} U_j + (K_{ji} - F_{ji}) U_i, \tag{5.32b}$$

with gravity colinear with \mathbf{e}_x . The inertial terms F reduce to zero for creeping flows and it reads

$$U_i = -\frac{K_{ii}}{\mu_i} \left(\frac{\partial P}{\partial x} - \rho_i g \right) + K_{ij} U_j, \tag{5.33a}$$

$$U_j = -\frac{K_{jj}}{\mu_j} \left(\frac{\partial P}{\partial x} - \rho_j g \right) + K_{ji} U_i. \tag{5.33b}$$

Eq. 5.32 can also be written under the form of Eq. 5.33 by recombining some terms. One gets $K_{ii}^{\text{app}} = K_{ii}/1+F_{ii}$ and $K_{jj}^{\text{app}} = K_{jj}/1+F_{jj}$ as apparent permeabilities and $K_{ij}^{\text{app}} = K_{ij}-F_{ij}/1+F_{ii}$ and $K_{ji}^{\text{app}} = K_{ji}-F_{ji}/1+F_{ii}$ as apparent cross-terms.

Lasseux et al. [103] further showed that an alternative form can be obtained by combining Eqs 5.33

$$\begin{pmatrix} U_i \\ U_j \end{pmatrix} + \mathcal{K}^* \begin{pmatrix} \frac{\partial P}{\partial x} - \rho_i g \\ \frac{\partial P}{\partial x} - \rho_j g \end{pmatrix} = 0, \quad (5.34)$$

where the symmetric matrix \mathcal{K}^* reads

$$\mathcal{K}^* = \begin{pmatrix} K_{ii}^*/\mu_i & K_{ij}^*/\mu_j \\ K_{ji}^*/\mu_i & K_{jj}^*/\mu_j \end{pmatrix} = \frac{1}{1 - K_{ij}K_{ji}} \begin{pmatrix} K_{ii}/\mu_i & K_{jj}K_{ij}/\mu_j \\ K_{ii}K_{ji}/\mu_i & K_{jj}/\mu_j \end{pmatrix}. \quad (5.35)$$

Further, we consider that the tensorial permeabilities \mathbf{K}_{ii} and \mathbf{K}_{jj} can be written as

$$\mathbf{K}_{ii} = K_0 k_{r_i} \mathbf{I}, \quad \mathbf{K}_{jj} = K_0 k_{r_j} \mathbf{I}, \quad (5.36)$$

where \mathbf{I} is the identity tensor, K_0 is the intrinsic permeability of the medium and k_{r_i} and k_{r_j} are the relative permeabilities of phases i and j respectively. This form is based on the assumptions that the porous structure is isotropic and that there is no anisotropy generated by the two-phase flow itself [134]. Similarly, we write

$$\mathbf{K}_{ij} = K_{ij} \mathbf{I}, \quad \mathbf{K}_{ji} = K_{ji} \mathbf{I},$$

$$\mathbf{F}_{ii} = F_{ii} \mathbf{I}, \quad \mathbf{F}_{jj} = F_{jj} \mathbf{I},$$

$$\mathbf{F}_{ij} = F_{ij} \mathbf{I}, \quad \mathbf{F}_{ji} = F_{ji} \mathbf{I}.$$

For consistency of the model at $S_\alpha = 0$ and $S_\alpha = 1$, we also consider that

$$k_{r_i}(S_i = 1) = 1, \quad k_{r_j}(S_i = 1) = 0, \quad (5.37)$$

$$k_{r_i}(S_i = 0) = 0, \quad k_{r_j}(S_i = 0) = 1, \quad (5.38)$$

$$K_{ji}(S_i = 1) = 0, \quad K_{ij}(S_j = 1) = 0, \quad (5.39)$$

which are necessary assumptions to obtain Darcy's law in the limit of single-phase flow.

5.4 Semi-analytical and numerical methods

Two methods are used to solve the system Eqs 5.31 and 5.32. One is an extension of the Buckley-Leverett theory, leading to a semi-analytical solution of the fluid fronts (for the viscous regime, Eq. 5.33). The other is a finite-volume resolution based on the ImpES method [156]. The semi-analytical solution, strictly speaking, can also be used to solve Eqs 5.32, but only in the strict limit of coefficients F being functions of the saturations only (which are most likely velocity dependent by construction).

5.4.1 Buckley-Leverett theory

The Buckley-Leverett theory [31] has been widely used in the literature to analyze the structure of two-phase flows through both homogeneous and heterogeneous media [31, 67, 22, 89, 32, 50]. It is also used as a reference

to validate numerical solvers [105, 171, 3, 79] and to evaluate their accuracy in capturing shocks.

A one-dimensional domain is considered, with an initial condition $S_j = 1$ and phase i injected at constant flow rate $U_i(0, t)$ for $t > 0$. The Buckley-Leverett problem characterizes the propagation of the fluid front in the domain. By recombining the mass and momentum laws Eqs 5.31 and 5.33, it yields

$$\varepsilon \frac{\partial S_i}{\partial t} + \frac{\partial \mathcal{F}_i}{\partial x} = 0, \quad (5.40a)$$

$$S_i(x, 0) = 0, \quad (S_j(x, 0) = 1), \quad (5.40b)$$

$$U_i(0, t) = \mathcal{F}_i[S_i(0, t)] = U, \quad t > 0, \quad (5.40c)$$

where Eq. 5.40a is a scalar one-dimensional conservation law. $\mathcal{F}_i(S_i)$ is the flux function (also called fractional flow in the Buckley-Leverett theory) that reads

$$\mathcal{F}_i(S_i) = U_i = \frac{m_i}{m_i + m_j} U \left(f_1 + \frac{\mu_i}{\mu_j} \mathcal{N}_g k_{r_j}(S_i) f_2 \right). \quad (5.41)$$

Here, $\mathcal{N}_g = \frac{K_0(\rho_i - \rho_j)g}{U\mu_i}$ is the *gravity number*; $m_i = \frac{K_{ii}}{\mu_i}$ and $m_j = \frac{K_{jj}}{\mu_j}$ are the mobility parameters; and $k_{r_j}(S_i)$ is the relative permeability for the phase j . The velocity U is the total velocity defined by $U = U_i + U_j$. f_1 and f_2 are functions that characterize the impact of the coupling coefficients K_{ij} and K_{ji} in the momentum balance equations. These can be expressed as

$$f_1 = \frac{1 + K_{ij} \frac{m_j}{m_i}}{1 + \frac{K_{ji}m_i + K_{ij}m_j}{m_i + m_j}}, \quad f_2 = \frac{1}{1 + \frac{K_{ji}m_i + K_{ij}m_j}{m_i + m_j}}. \quad (5.42)$$

The solution of the two-phase flow system is determined by solving the Riemann problem that is associated to Eq. 5.40, based on entropic considerations to identify the shocks in the solution. The entropic conditions and a number of examples of practical application can be found in [127].

5.4.2 Finite-volume solver

Eqs 5.31 and 5.32 form a pressure-saturation system whose resolution has been discussed extensively in the literature. The ImPES method [156], as *Implicit Pressure Explicit Saturation*, consists in a sequential resolution of an equation on the saturation and an equation on the pressure. The solver is based on the open-source toolbox *porousMultiphaseFoam* developed by Horgue et al. [79] in OpenFoam for a system of generalized Darcy's laws. Using the relation Eq. 5.35 to write the momentum balance Eq. 5.32 under the form of Eq. 5.34, the following notations are introduced for the K^* coefficients

$$M_{ii} = \frac{K_{ii}^*}{\mu_i}, \quad M_{jj} = \frac{K_{jj}^*}{\mu_j}, \quad M_{ij} = \frac{K_{ij}^*}{\mu_j}, \quad M_{ji} = \frac{K_{ji}^*}{\mu_i}, \quad (5.43a)$$

$$L_{ii} = \frac{\rho_i K_{ii}^*}{\mu_i}, \quad L_{jj} = \frac{\rho_j K_{jj}^*}{\mu_j}, \quad L_{ij} = \frac{\rho_j K_{ij}^*}{\mu_j}, \quad L_{ji} = \frac{\rho_i K_{ji}^*}{\mu_i}. \quad (5.43b)$$

This yields

$$U_i = - (M_{ii} + M_{ij}) \frac{\partial P}{\partial x} + (L_{ii} + L_{ij}) g, \quad (5.44a)$$

$$U_j = - (M_{jj} + M_{ji}) \frac{\partial P}{\partial x} + (L_{jj} + L_{ji}) g. \quad (5.44b)$$

From this expression, we briefly detail next the steps of the algorithm.

1. Computation of the time step. We consider the Courant number Co_α for the phase α ,

$$Co_\alpha = \max_{\text{cells}} \left(0.5 \frac{\sum_{\text{faces}} |\phi_\alpha|}{V_{\text{cells}}} \right) \Delta t_{\text{last}}, \quad (5.45)$$

where $\sum_{\text{faces}} \phi_\alpha = \sum_{\text{faces}} U_\alpha S_f$ is the sum of the fluxes at the neighbour faces to the considered cell. The new time-step is then computed as

$$\Delta t = \Delta t_{\text{last}} \min [\min (c_{\Delta t}, 1 + 0.1c_{\Delta t}), 1.2], \quad (5.46)$$

where

$$c_{\Delta t} = \frac{Co_{\text{fixed}}}{\max (Co_\alpha)}, \quad \alpha = g, l_1, l_2, \quad (5.47)$$

and where Co_{fixed} is a fixed Courant number chosen initially to ensure the stability of the simulation ($Co_{\text{fixed}} < 1$).

2. From the saturation field $S_i(t_n)$ and velocity field $U_i(t_n)$ at a given time t_n , the mass conservation equation

$$\varepsilon \frac{\partial S_i}{\partial t} + \frac{\partial U_i}{\partial x} = 0, \quad (5.48)$$

is solved explicetly to get the saturation field $S_i(t_{n+1})$.

3. M and L coefficients Eqs 5.43 are updated from $S_i(t_{n+1})$ and $U_i(t_n)$.
4. By summing the mass conservation equations given in Eq. 5.31, and introducing the momentum conservation equations Eqs 5.44, we get the following equation on the pressure

$$\frac{\partial}{\partial x} \left[(M_{jj} + M_{ji} + M_{ij} + M_{ii}) \frac{\partial P}{\partial x} \right] = \frac{\partial}{\partial x} [(L_{jj} + L_{ji} + L_{ij} + L_{ii}) g], \quad (5.49)$$

that is solved implicetly to get the pressure field $P(t_{n+1})$.

5. From $P(t_{n+1})$ and the coefficients $M(t_{n+1})$, $L(t_{n+1})$, the velocity fields $U_i(t_{n+1})$ and $U_j(t_{n+1})$ are updated from Eqs 5.44.

Boundary conditions A zero pressure condition $P|_{\text{in}} = 0$ is imposed in the inlet, while a condition on the pressure gradient $\left. \frac{\partial P}{\partial x} \right|_{\text{out}}$ is imposed in the outlet

$$\left. \frac{\partial P}{\partial x} \right|_{\text{out}} = \frac{(L_{jj} + L_{ji}) g - U_j|_{\text{out}}}{M_{jj} + M_{ji}}. \quad (5.50)$$

This last condition (from Eq. 5.44b) allows to impose the flow rate $U_j|_{\text{out}}$. A constant flow rate $U_i|_{\text{in}}$ is also imposed in the inlet.

The solver is validated by comparing the fluid fronts obtained numerically to the theoretical solution obtained with the Buckley-Leverett theory. The test case is a case of water imbibition in a medium filled with air, which is discussed in more details in [127]. The effective parameters in Eq 5.33 are based on the analytical solution of an annular gas-liquid flow in a capillary tube. We compare in Fig. 5.2, for validation,

the numerical and theoretical solutions of the water front in the transient regime for two given flow rates. The fluid fronts are given for two values of the dimensionless term, $1/\mathcal{N}_g = \frac{U_i \mu_i}{K_0(\rho_i - \rho_j)g}$, which characterizes the fractional flow Eq. 5.41.

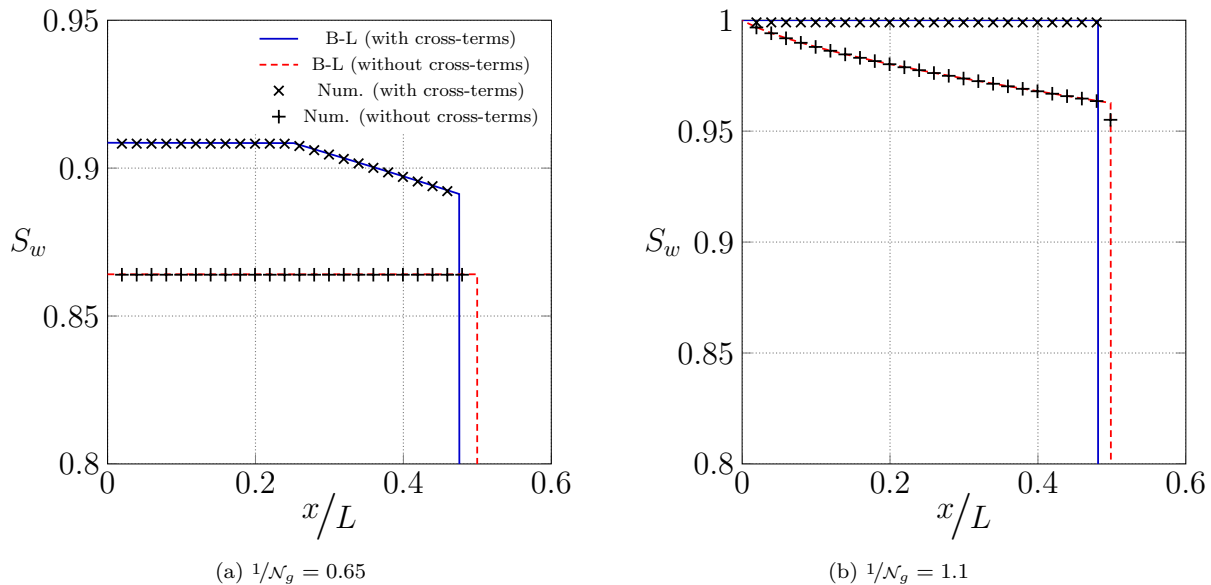


Figure 5.2 – Water front S_w in the transient regime, using the viscous model with and without cross-terms, Eq 5.33. Numerical solution (marks) is compared to the theoretical solution from the Buckley-Leverett theory (lines). Two water flow rates are considered a) $1/\mathcal{N}_g = 0.65$ and b) $1/\mathcal{N}_g = 1.1$. See [127] for further details about this case.

5.5 Results

5.5.1 Case 1: creeping flows

Since an important question in this study is on whether the permeability influences the momentum exchange between two phases in porous media, we analyze the magnitude of the cross-terms based on the few experimental measurements of these terms that were conducted in the literature. Kalaydjian set up flows in capillary tubes with square sections with multiple couples of fluids [91], Zarcone and Lenormand conducted experiments in a sand pack using water and mercury [192], and Rothman proceeded to numerical simulations (Lattice-Boltzmann) in a pore-network of large permeability [150]. These flows were low Reynolds flows and the viscous cross-terms as in Eq. 5.33 were measured. Given the different permeabilities of the media we compare, we hypothesize that the separation into different flow paths and the relative influence of fluids/solid and fluid/fluid interfaces can be represented by a scalar coefficient $\beta \in [0, 1]$, weighting the cross-terms

$$K_{ij}(\beta) = \beta K_{ij}, \quad K_{ji}(\beta) = \beta K_{ji}. \quad (5.51)$$

Further, the expressions of the cross-terms for $\beta = 1$ are assumed to be on the form of the analytical solution of the two-phase flow in an annular capillary tube [34, 78],

$$K_{ij} = 2r_\mu \frac{S_i + (1 - S_i) \log(S_i)}{1 - 2r_\mu \log(1 - S_i)}, \quad (5.52a)$$

$$K_{ji} = 2(1 - S_i) \frac{S_i + (1 - S_i) \log(S_i)}{S_i^2 - 2S_i(1 - S_i) - 2(1 - S_i)^2 \log(1 - S_i)}. \quad (5.52b)$$

The profiles of $K_{ji}^*/K_0 = 1/r_\mu K_{ij}^*/K_0$ (from K_{ji} and K_{ij} using the relation Eq. 5.35) as functions of S_i for different values of β are compared in Fig. 5.3 to the experimental and numerical results mentioned above. Kalaydjian, using capillary tubes with square section, obtained the maximum value of the dimensionless cross-terms $K_{ji}^*/K_0 = 1/r_\mu K_{ij}^*/K_0 \sim 0.2$. The maximum value and the form of the cross-coefficients as a function of the saturation proves to be identical to the result obtained analytically in a annular capillary tube. Zarcone and Lenormand found that the magnitude of the cross-terms is much less important in their case, with dimensionless cross-terms which are at most $\sim 4 \times 10^{-3}$. As discussed in the introduction, their primary hypothesis is that this weaker influence stems from the smaller interfacial area between the two-phases. The case of Rothman is intermediate between the sand pack and the capillaries, with a maximum value of the cross-terms, ~ 0.17 , that is slightly below the one obtained for capillaries. We see that changing the value of β allows to recover both results for the sand and capillaries. For the sand we have $\beta \sim 0.1$, which confirms that the momentum exchange is smaller in low permeability media than in capillaries. Further, the analytical solution of the cross-terms in a tube proves to be in accordance with the profiles of the cross-terms obtained for other types of porous media.

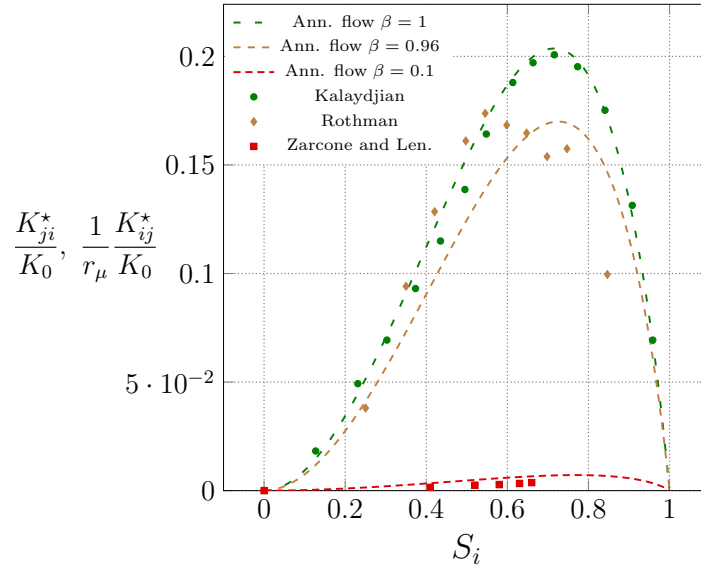


Figure 5.3 – Comparison of non-dimensionalized cross-terms for multiple weighting factors β (dashed lines, see Eq. 5.51) to experimental results from [192], [91] and numerical results from [150]. K_{ij}^*/K_0 and $K_{ji}^*/(K_0 r_\mu)$ are plotted as functions of the saturation S_i .

5.5.2 Case 2: co-current flows within particle beds

5.5.2.1 Boundary conditions

We consider now a recent experiment referred as the CALIDE facility and described in Chikhi et al. [33] and Clavier [34]. It consists in a two-phase flow (air/water) in a column filled with particles. The section of visualization is made of a Plexiglas pipe (500 mm high and 94 mm diameter), which can be filled with particles of different diameters (3.18, 6.35, 4, 8, 12.7 mm). A picture of the experiment is given in Fig. 5.4b. Air and water are supplied from the bottom of the column, which is initially filled with water, as depicted in Fig. 5.4a. This experiment was part of a large work on water-steam flows in debris bed in the context of a severe accident in a nuclear reactor. It consisted in measurements of the void-space and of the pressure drop for a large range of gas and liquid flow rates after the steady-state was obtained. The objective was especially to obtain databases for the identification of the effective parameters in the continuum models Eq 5.32. A set of data was obtained earlier by Tutu et al. [175] with a similar experiment, but there is in general a very scarce database in the literature to be used for the models.

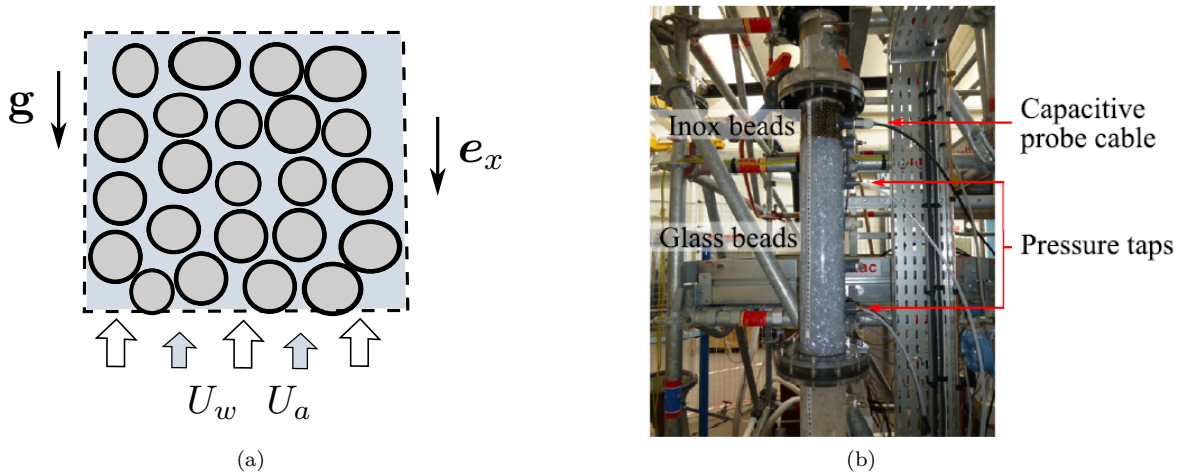


Figure 5.4 – Case 1: CALIDE facility - a) schematical representation, b) picture of the experiment.

The liquid retention and the pressure drop at steady-state are plotted in Fig. 5.5 as a function of Re_a for a diameter of particles of 4 mm. The first observation is that the liquid retention decreases with the gas flow rate (the column is emptying) but is quasi-independant of the liquid flow rate. In contrast, the pressure drop shows very different behaviors depending on the liquid and gas flow rates. At moderate liquid flow rates, for instance, the pressure drop initially decreases with the gas flow rate, which can be explained by a phenomenon of lift, as the shear-stress compensates the hydrostatic pressure drop. From a certain threshold ($Re_a \sim 1$), an inflexion is observed and is likely due to the development of significant inertial dissipation effects. Other diameters of particules are also considered in the following but for gas injection only, as the liquid flow was only considered for diameters 4 and 8 mm.

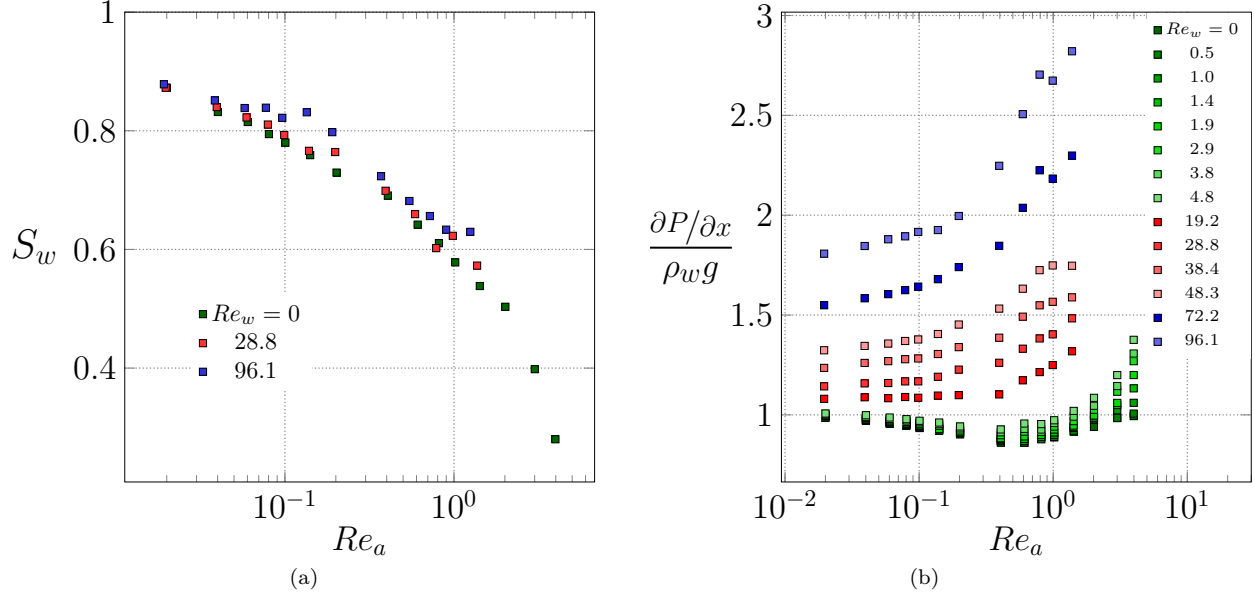


Figure 5.5 – Experimental data from Chikhi et al. [33] - a) water retention S_w and b) dimensionless pressure drop $\frac{\partial P/\partial x}{\rho_w g}$, as a function of Re_a .

5.5.2.2 Closures for the effective parameters for a co-current flow in particle bed

A set of closure relationships for the effective parameters in the momentum balance Eq. 5.32 has been recently derived in [36] based on the set of data from the experiment introduced above. The closures relationships are built based on the macroscopic dataset (pressure drop, fluid saturations, flow rates) and therefore do not rely on an information from the microscale (for instance the resolution of closure problems). The set of closures reads

$$K_{ww} = K_0 S_w^3, \quad K_{aa} = K_0 (1 - S_w)^4,$$

$$K_{wa} = \beta_1 \frac{\mu_a}{\mu_w} \frac{S_w^2}{(1 - S_w)}, \quad K_{aw} = \frac{\mu_w}{\mu_a} \frac{K_{aa} K_{wa}}{K_{ww}} = \beta_1 \frac{(1 - S_w)^3}{S_w}, \quad (5.53)$$

where β_1 is a constant that depends on the diameter of particle. The inertial parameters read

$$F_{ww} = \frac{\rho_w}{\mu_w} \frac{K}{\eta} U_w; \quad F_{wa} = f_{wa} K_{wa}, \quad (5.54)$$

$$F_{aa} = \frac{\rho_a}{\mu_a} \frac{K}{\eta} U_a; \quad F_{aw} = \beta_2 (1 - S_w)^6, \quad (5.55)$$

where η is called the passability and is commonly used in engineering practice. β_2 is a constant that depends on the diameter and f_{wa} is a fitting function of S_w which is equal to 0 for $S_w \rightarrow 1$ (low liquid and gas flow rates) and to 1 for $S_w \rightarrow 0$

$$f_{wa} = \frac{(1 - S_w)^3}{(1 - S_w)^3 + S_w^n}. \quad (5.56)$$

A few comments are worth noting about these closures. Obtaining the dependencies of the eighth unknown functions in Eqs 5.32 is a complicated task as the quantity of information extracted from the experiment

is restricted. One can derive closure relationships by making the most of some limit cases ($Re_w = 0$, low Re_w , Re_a), but a number of assumptions are still required. An example of the method of identification is proposed in the next section. Here, the most questionable closures are on the inertial cross-terms F_{wa} and F_{aw} , which, by definition, should probably be function of the velocities. They are constructed here as functions of the saturation only. In absence of more information, however, such set of closure relationships constitutes a valuable set of parameters to study the models at the macroscale.

5.5.2.3 Results

Impact of the permeability on $U_w = 0$ In accordance with the analysis made in Case 1, we analyze first the influence of the permeability (diameter of the particles 3.18, 6.35, 4, 8, 12.7 mm) on the momentum exchange between the two phases. The viscous model Eq. 5.33 is solved using the Buckley-Leverett theory for the different permeabilities. The dimensionless pressure drop and the liquid saturation are shown in Fig. 5.6 as a function of Re_a . First, it is seen that the difference of permeability clearly segregates the profiles. The pressure drop, for instance, decreases more in the highly permeable columns, which can be explained by a stronger effect of lift due to a potentially higher surface area between the two phases. It is also seen that the viscous model with cross-terms allows to capture these variations, and it is clear that the cross-terms in the momentum balance have to be employed in such a case. It is also interesting to see that the discrepancy between the model and the experimental results appears globally from $Re_a \sim 1$, which is known to be the threshold for the appearance of substantial inertial effects in porous media (see Figs 5.6a and 5.6b). This is only partially true for the smallest diameter ($d = 3.18$ mm) when one looks at the pressure drop, since the inflexion seems to occur for a smaller Re_a . This might be due to the smaller effect of the lift in this case. Further, it is also seen that the inertial effects modify drastically the profile of the saturation in the highest permeable columns ($d = 8$ and 12 mm).

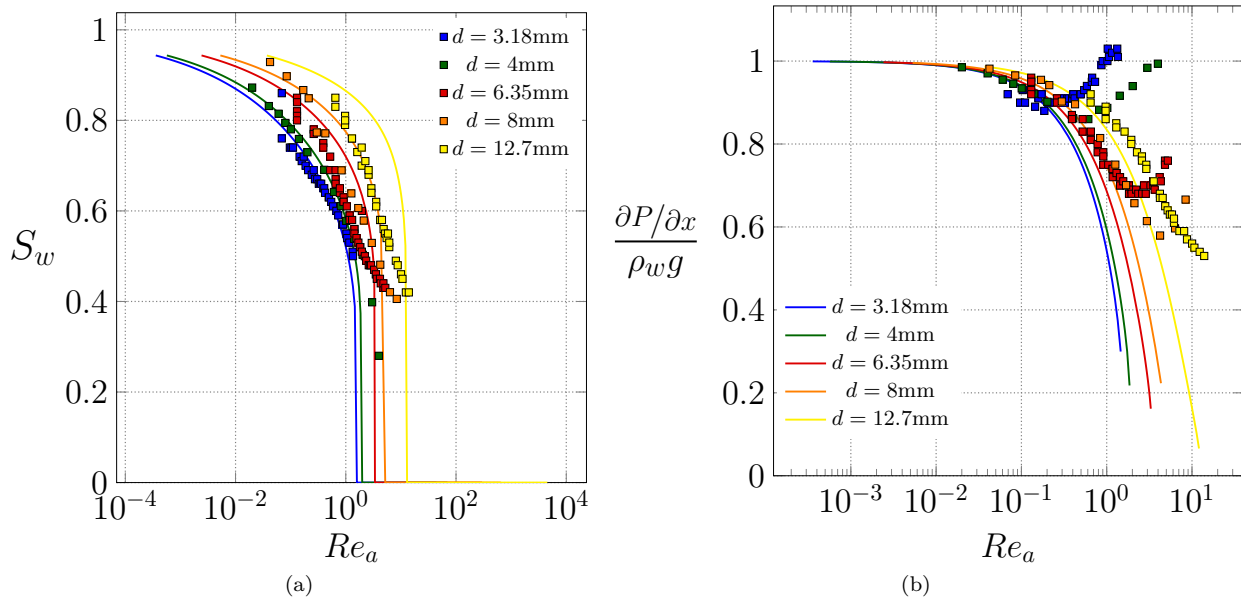


Figure 5.6 – Liquid saturation and dimensionless pressure drop for different diameters of particles, as a function of the gas flow rate at $U_w = 0$. a) and b) as a function of Re_a , a) and b) as a function of Re_k .

Co-current flow regime ($U_w \neq 0$) for $d = 4$ mm Fig 5.7 shows the results obtained in the case $d = 4$ mm when solving now the inertial model (numerically). In this case, the three model - without cross-terms, with viscous cross-terms, with inertial cross-terms - are compared. It is seen that the generalized Darcy's laws lead to a pressure drop which is balanced with the hydrostatic pressure drop $\rho_w g$. The viscous model with cross-terms, conversely, captures the decrease of the pressure drop until ($Re_a \sim 0.3$), as it was seen earlier. The inertial model allows to accurately recover the inflexion of the pressure drop and the saturation in the inertial regime. These observations mainly confirm that the macroscale structure of the momentum balance in the generalized Darcy's laws, widely employed in engineering practice, cannot be employed in such configurations. Instead, cross and inertial terms are required to model significant drag and inertial effects. This observation is further confirmed in Fig. 5.8 where the injection of the water co-currently to the gas is also considered. In this case, the motion of the water flow generates further dissipation effects and a significant increase of the pressure drop. However, the profile of the water saturation remains relatively stable despite of strong modification of the liquid flow rate. In general, it is clear that the inertial model allows to capture correctly the variations of the pressure drop with the liquid flow rate.

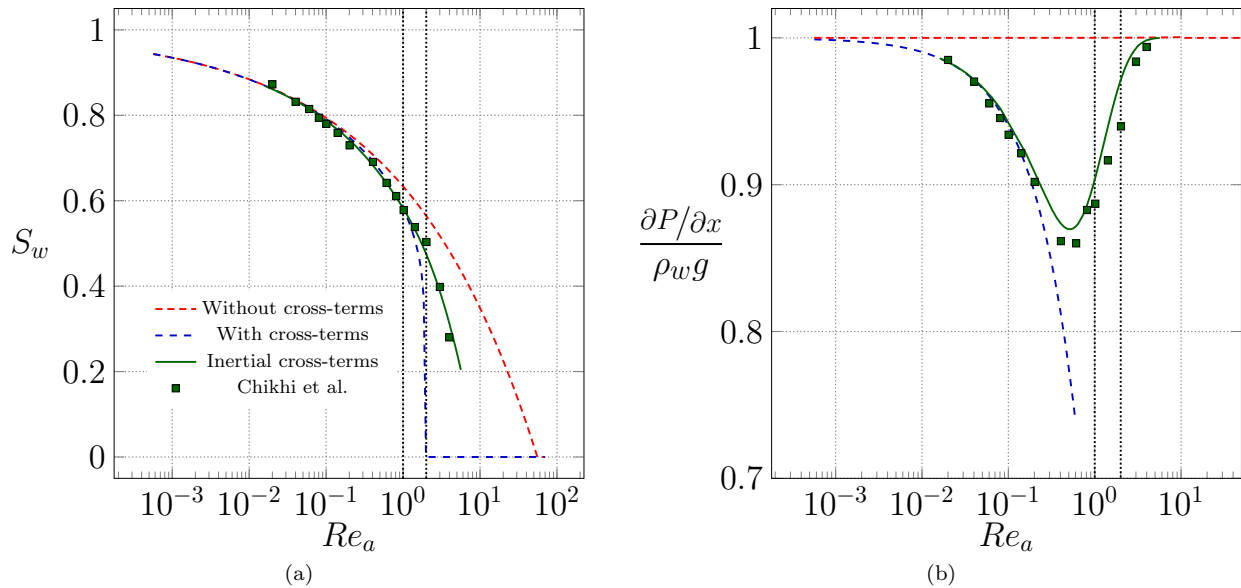


Figure 5.7 – Saturation and dimensionless pressure drop at steady state as a function of Re_a , for $U_w = 0$. The viscous model, with and without cross-terms, is compared to the inertial model. a) Saturation S_w and b) dimensionless pressure drop $\frac{\partial P / \partial x}{\rho_w g}$. The two vertical lines with dots correspond to the fronts given in Fig. 5.9.

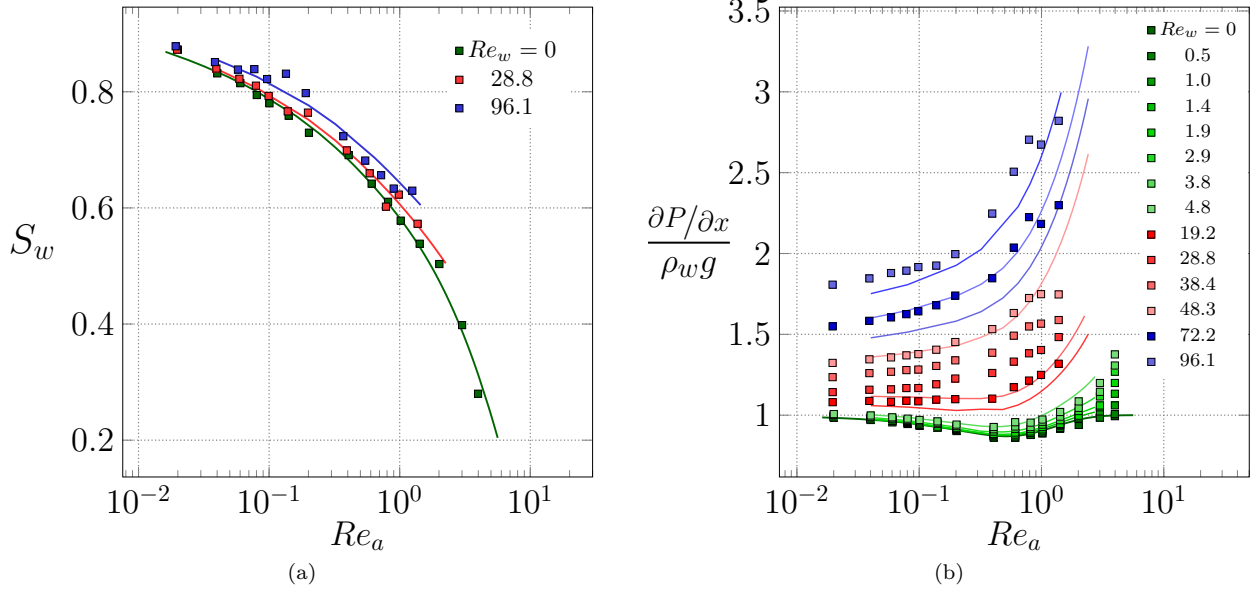


Figure 5.8 – Saturation and dimensionless pressure drop at steady state as a function of Re_a , for various water flow rates. The viscous model, with and without cross-terms, is compared to the inertial model. a) Saturation S_w and b) dimensionless pressure drop $\frac{\partial P}{\partial x} / \rho_w g$.

So far, the analysis has been limited to the steady-state regime of the system. The Buckley-Leverett solution and the numerical resolution also provide the fluid fronts in the transient regime. The influence of the cross-terms in the viscous model Eq. 5.33 on the fluid fronts was analyzed in [127], where it is shown that the macroscopic shear-stress effect tends to generate rarefaction waves in the fluid fronts. The fronts of the liquid phase are given in Fig 5.9 in the transient regime in the case $d = 4$ mm and for $U_w = 0$ and for two gas flow rates. The different models with and without cross and inertial terms are compared, in accordance with the results presented in Fig. 5.7, where the two values of Re_a are specially outlined. The first observation is that the cross and inertial terms affect significantly the fronts compared to the generalized Darcy's laws. As seen in [126], the viscous cross-terms tends to increase the size of the rarefaction wave. However, it is also observed that the inertial effects tend to favor the emergence of a plateau and to reduce the size of the rarefaction wave. This observation is further confirmed when one looks at the profiles given in Fig. 5.10, where co-injection of water is also considered. Indeed, the inertial effects in the water flow lead to a single plateau without rarefaction wave.

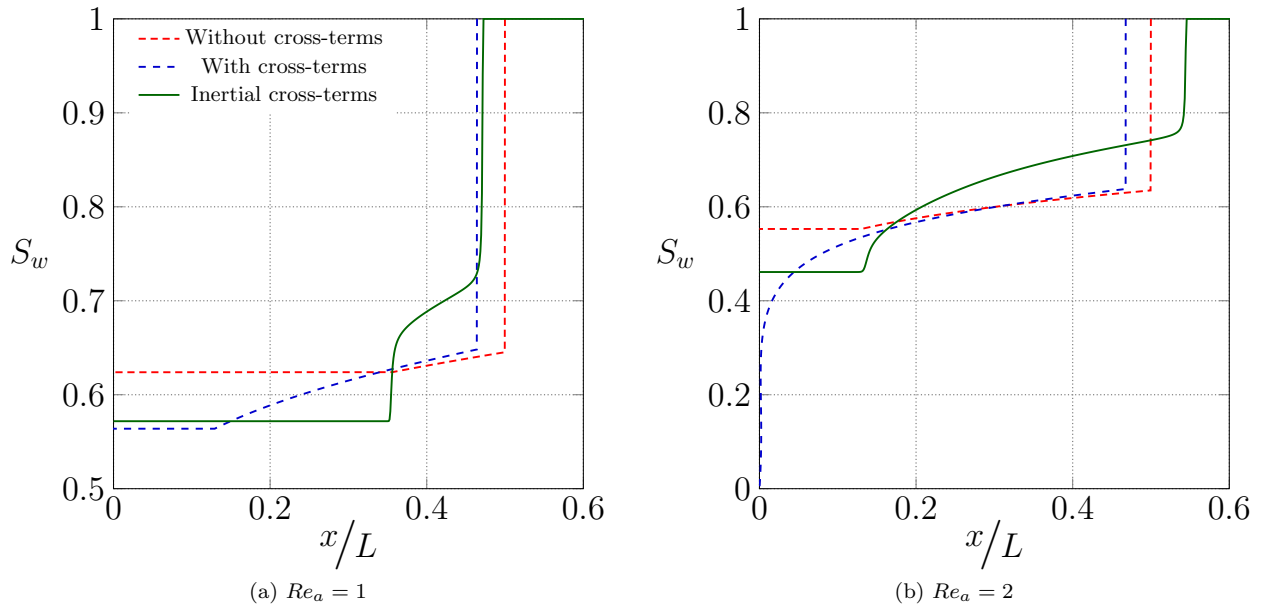


Figure 5.9 – Profiles of the water saturation S_w in the dynamic regime at two values of Re_a using the different models.

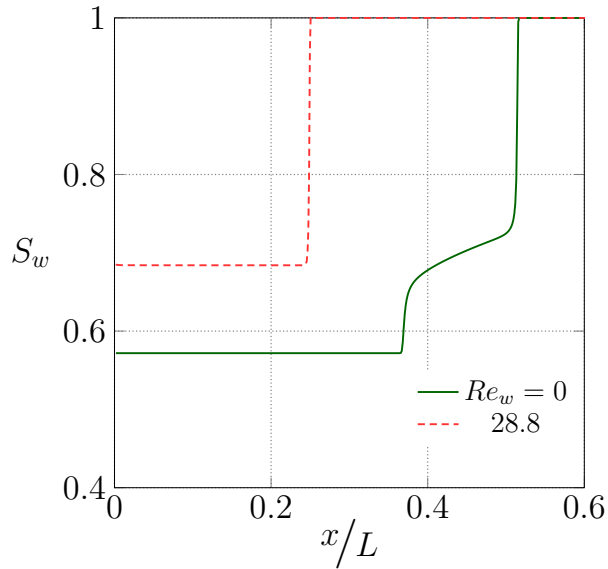


Figure 5.10 – Profiles of the water saturation S_w , using the inertial model for $Re_a = 1$ and at $Re_w = 0$ and $Re_w = 28.8$.

5.5.3 Case 3: counter-current flows within structured packings

5.5.3.1 Boundary conditions

We finally consider the case of a counter-current gas-liquid flow, as typically encountered in chemical processes. In trickle beds or columns equipped with structured packings, the gas/liquid interaction effects especially play a central role and is known to enhance the efficiency. The counter-current configuration is depicted in the sketch in Fig. 5.11. The pressure drop and of the liquid saturation from Wang [182] and Suess and Spiegel [167], for increasing gas and liquid flow rates, are given in Fig. 5.12. For sufficiently low flow rates, the liquid flows down as a thin liquid film and is moderately impacted by the gas phase (pre-loading regime), while for higher flow rates, the interfacial shear-stress retains the liquid which disperses in droplets in the gas (loading regime), leading ultimately to a regime where both the pressure drop and the liquid saturation increase sharply (flooding regime).

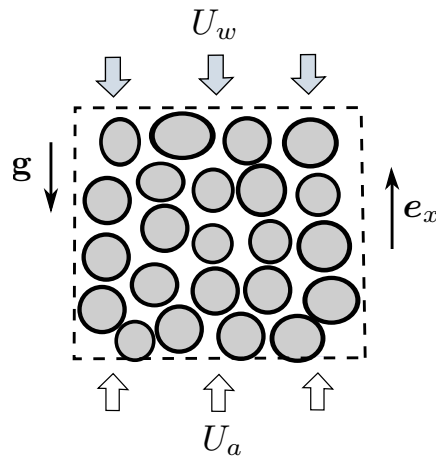


Figure 5.11 – Configuration 2: counter-current flow

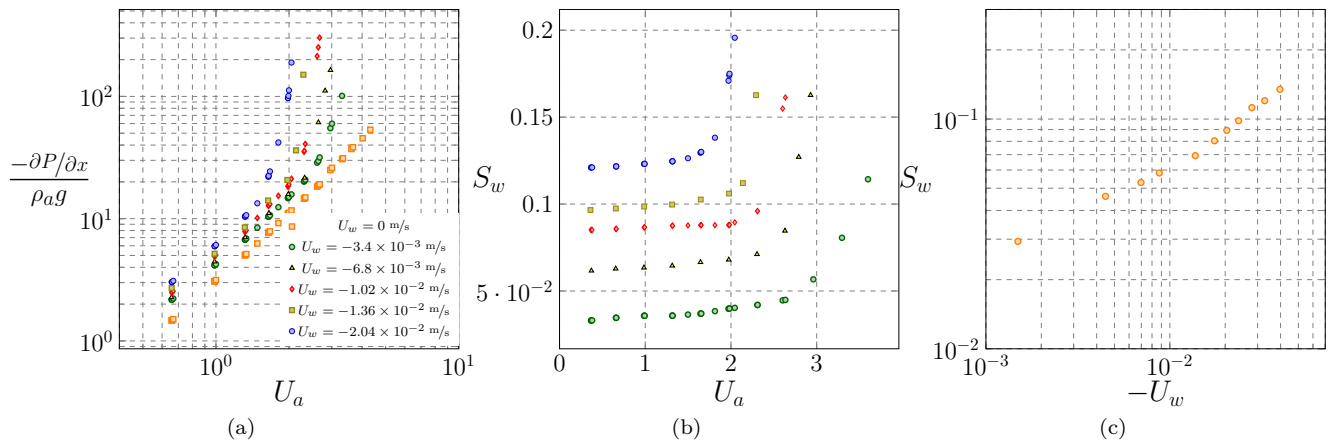


Figure 5.12 – Experimental data in columns equipped with structured packings, - a) pressure drop and b) liquid saturation, as a function of the gas flow rate U_a , from Wang [182] (2015), c) liquid saturation, as a function of the liquid flow rate U_w , at $U_a = 0$, from Suess and Spiegel [167] (1992)

5.5.3.2 Closures for the effective parameters for a counter-current flow in structured packings

So far the closure relationships of the effective coefficients were obtained based on an analytical solution (Case 1) and from the literature using experimental data (Case 2). We propose now to establish closure relationships in the case of counter-current flows. We mainly use the set of data of Wang (2015), with some results from Suess and Spiegel (1992), for a air-water flow in columns equipped with structured packings. Both studies consisted in measurements in a column equipped with a packing Sulzer Mellapack 250Y.

Determination of K_{aa} , K_{ww} and the permeability K_0 The determination of the K terms can be achieved by making the most of the experiments at low gas and liquid flow rates. The experiments conducted at zero gas flow rate case ($U_a = 0$) (see Fig. 5.12c) first allow to simplify the momentum balance Eq. 5.32 which reads

$$U_w = -\frac{K_{ww}}{\mu_w} \left(\frac{\partial P}{\partial x} - \rho_w g \right) - F_{ww} U_w \approx \frac{K_{ww}}{\mu_w} \rho_w g - F_{ww} U_w, \quad (5.57)$$

Observing that the hydrostatic pressure dominates over the pressure gradient for low gas flow rate, $\frac{\partial P}{\partial x}$ is neglected in the momentum balance. Considering that one can distinguish a viscous and an inertial regime for respectively low and high liquid flow rates, one can write in the viscous regime

$$U_w = \frac{K_{ww}}{\mu_w} \rho_w g. \quad (5.58)$$

The transition from the viscous to the inertial regime is considered to be around $U_w \sim 1 \times 10^{-2}$ m/s, as seen in Fig. 5.12c where an inflection is observed at this velocity. Based on Eq. 5.58, $K_{ww} = \frac{U_w \mu_w}{\rho_w g}$ is plotted in Fig. 5.13 and is shown to be under the form

$$K_{ww} = K_0 S_w^{2.7}. \quad (5.59)$$

One can also deduce the permeability K_0 , which is $K_0 = 2 \times 10^{-6}$ m². This value of permeability is relatively high for a geometry of structured packing, compared to value previously determined in the literature [163, 126] ($K_0 \sim 7 \times 10^{-7}$ m²). The packing Mellapack 250Y is indeed known to be a coarse packing involving a large number of holes.

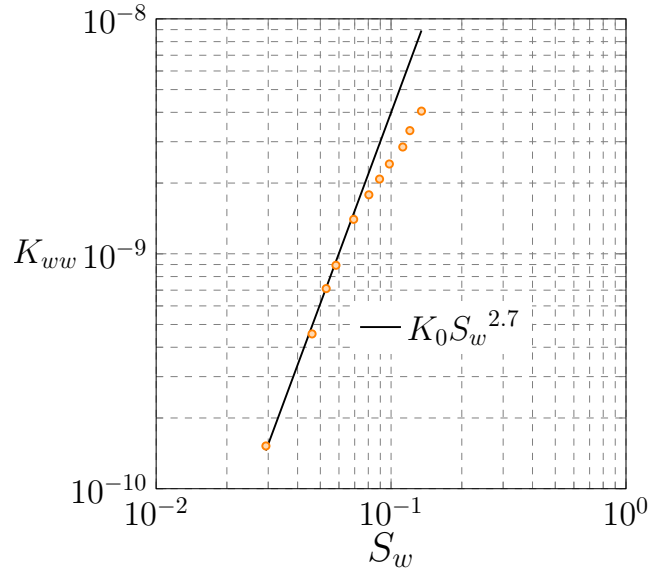


Figure 5.13 – K_{ww} as a function of S_w for $U_a = 0$. Experimental data from Suess and Spiegel [167].

Contrary to the case of the liquid flow, the viscous regime in the gas phase cannot be isolated from the inertial regime, as the lowest gas flow rate $U_a \sim 0.35 \text{ m/s}$ corresponds already to a significant value of the Reynolds number $Re_a = 32$. The coefficient K_{aa} is therefore assumed *a priori*, from the analytical solution of the liquid-gas flow in a cylinder capillary tube (also Brooks and Corey correlation [29]). It takes the form

$$K_{aa} = K_0 S_a^2. \quad (5.60)$$

Although this might look as a relatively strong assumption, the high permeability of the packing and its geometry of channels (parallel corrugated sheets) makes the comparison to the capillary tube reasonable. Further, the gas-liquid flow in columns equipped with structured packing is made of a thin liquid film and of a bulk gas flow, which is identical to the configuration considered for the analytical solution. The value obtained for K_{ww} , $K_{ww} = K_0 S_w^{2.7}$, finally, is close to the one obtained in the capillary tube, $K_{ww} = K_0 S_w^3$.

Determination of F_{aa} and F_{ww} Considering now the inertial regime in the water flow, the coefficient F_{ww} can be obtained from Eq. 5.57,

$$F_{ww} = -\frac{K_{ww} (\partial P / \partial x - \rho_w g)}{\mu_w U_w} - 1. \quad (5.61)$$

It is shown in Fig. 5.14a to scale linearly with the velocity for the highest liquid flow rates

$$F_{ww} = 30 U_w. \quad (5.62)$$

Here, the set of data is clearly too scarce to reliably conclude on the scaling of F_{ww} with the velocity. However, the linear scaling of F_{ww} that seems to be obtained with U_w corresponds to the classical quadratic correction ($F_{ww} U_w$) in the strongly inertial regime [100, 126].

Using the same method, the coefficient F_{aa} is determined based on the dry experiment ($U_w = 0$) in the

measurements of Wang. Using Eq. 5.32, F_{aa} can be expressed as

$$F_{aa} = -\frac{K_0 S_a^2 (\partial P / \partial x - \rho_a g)}{\mu_a U_a} - 1. \quad (5.63)$$

The coefficient F_{aa} is plotted in Fig. 5.14b as a function of the gas flow rate U_a . It is shown to scale with U_a as

$$F_{aa} = 2.3 U_a^{1.15}. \quad (5.64)$$

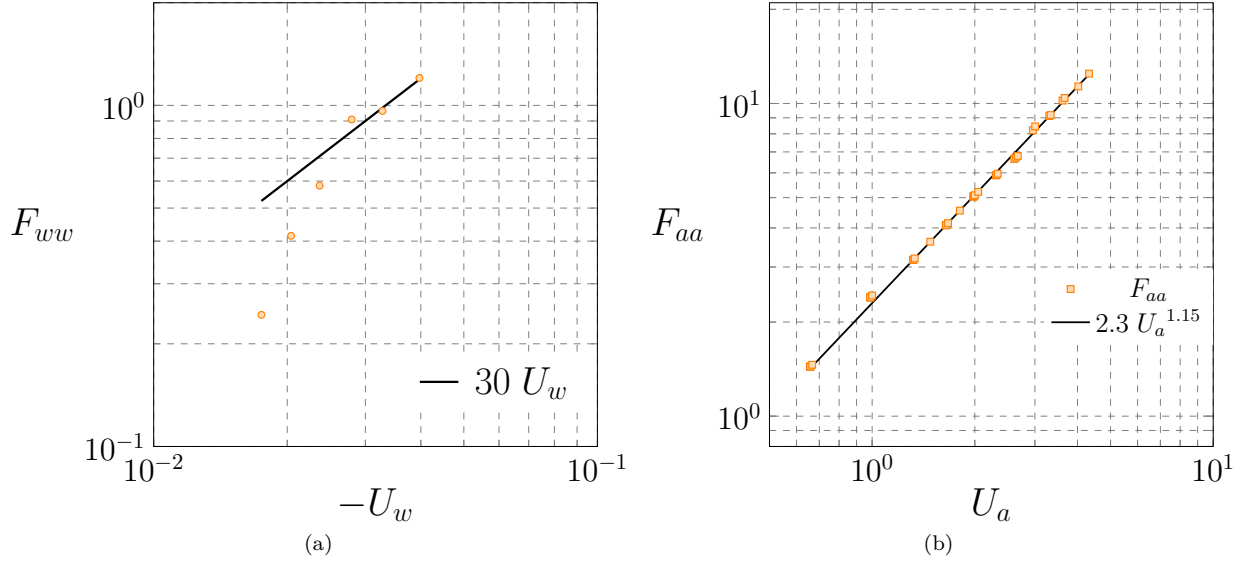


Figure 5.14 – Closure of the inertial terms F_{ww} a) and F_{aa} b) as a function of U_w and U_a respectively.

Determination of K_{aw} , K_{wa} , F_{aw} and F_{wa} We now consider the cumulative influence of the effective cross-terms K_{aw} and F_{aw} , that reads based on Eq. 5.32

$$K_{aw} - F_{aw} = U_w^{-1} \left(U_a + \frac{K_{aa}}{\mu_a} \left(\frac{\partial P}{\partial x} - \rho_a g \right) + F_{aa} U_a \right). \quad (5.65)$$

Fig. 5.15a shows the experimental values of $K_{aw} - F_{aw}$ as a function of the gas flow rate U_a . It is seen that this term also depends on the saturation and we postulate that it can be written under the form

$$K_{aw} - F_{aw} = K_{aw} [1 - f_{aw}(U_a)], \quad (5.66)$$

where f_{aw} is a function of the gas flow rate. Contrary to the closure from Clavier et al. [36], the term F_{aw} is constructed as a function of the gas velocity. The proportionality of F_{aw} with K_{aw} is inspired from Clavier et al., though, and seems relatively intuitive. In the absence of further information for the term K_{aw} and as the viscous and the internal regimes cannot be separated clearly, the expression from the analytical tube is used

$$K_{aw} = \frac{1 - S_w}{S_w}. \quad (5.67)$$

Based on this estimation, the term $-F_{aw}/K_{aw}$ is plotted in Fig. 5.15b and is shown to be indeed relatively independent of the saturation, at least for moderate flow rates. It is shown to be under the form

$$f(U_a) = -F_{aw}/K_{aw} = 10U_a^2, \quad (5.68)$$

for moderate velocities.

For higher flow rates, one clearly sees that there exists a critical gas velocity U_{crit} [62], from which both the pressure drop and the liquid retention exhibits a drastic inflection. This inflection corresponds to the gas flow rate from which the column starts to be in the flooding regime. The term $f(U_a) - 10U_a^2$ is plotted in Fig. 5.16a in order to determine the critical velocity U_{crit} for a given liquid flow rate. U_{crit} is then plotted as a function of U_w in Fig. 5.16b. Considering the two scalings, the term F_{aw} can finally be expressed under the form

$$F_{aw} = -10K_{aw}U_{\text{crit}}^2 \left[\left(\frac{U_a}{U_{\text{crit}}} \right)^2 + \left(\frac{U_a}{U_{\text{crit}}} \right)^{20} \right], \quad (5.69)$$

involving a strong scaling in U_a^{20} in the flooding regime. The two scaling in U_a^2 and U_a^{20} respectively correspond in the column to a regime of stable liquid film and to a regime involving dispersed droplets in the gas phase (flooding). The plots of Eq. 5.69 for the various values of U_{crit} are shown in Fig. 5.15b.

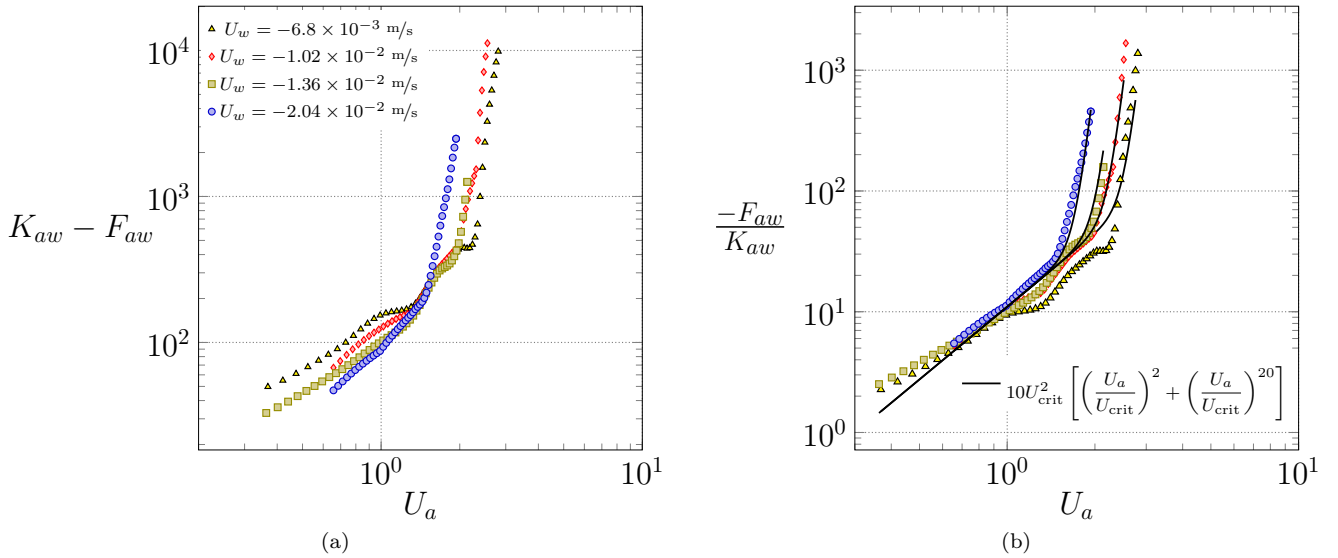


Figure 5.15 – Closures of the cross-terms K_{aw} and F_{aw} . a) $K_{aw} - F_{aw}$ and b) $-F_{aw}/K_{aw}$ as a function of U_a , see Eq. 5.70.

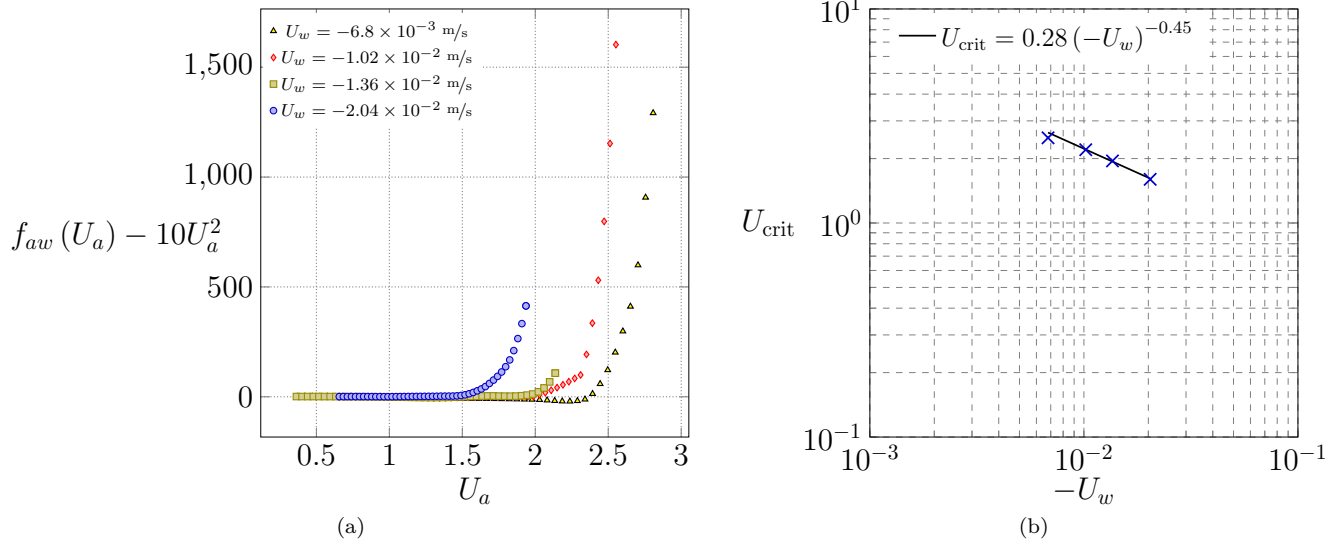


Figure 5.16 – Critical velocity $U_{crit} - K_{aw}$ - a) inflection of $-F_{aw}/K_{aw}$ characterized by the critical velocity and b) U_{crit} as a function of U_w .

The same reasoning is used for the determination of the cross-terms K_{wa} and F_{wa} . The term $K_{wa} - F_{wa}$ can be expressed from Eq. 5.32 under the form

$$K_{wa} - F_{wa} = U_a^{-1} \left(U_w + \frac{K_{ww}}{\mu_w} \left(\frac{\partial P}{\partial x} - \rho_w g \right) + F_{ww} U_w \right). \quad (5.70)$$

The experimental values of $K_{wa} - F_{wa}$ are plotted in Fig. 5.70 as a function of U_a . As previously, it is assumed that it can be written under the form

$$K_{wa} - F_{wa} = K_{wa} [1 - f_{wa}(U_a)]. \quad (5.71)$$

where f_{wa} is a function of the gas velocity only. It is found that if K_{wa} is under the form

$$K_{wa} = \frac{S_w^3}{1 - S_w}, \quad (5.72)$$

f_{wa} is independant of the saturation, as seen in Fig. 5.17b. This is only partially true as it does not work very well for the lowest liquid velocity, 6.8×10^{-3} m/s. The cumulative influence of K_{wa} and F_{wa} is actually shown to be relatively moderate as the liquid flow rate is low. Also, the expression of K_{wa} differs from the closure obtained from the analytical solution of film flow in a capillary tube $K_{wa} = \frac{S_w^2}{1 - S_w}$, but exhibits a similar form and the same limits. The term F_{wa} therefore takes the form

$$F_{wa} = -1000K_{wa}U_a^{-1}. \quad (5.73)$$

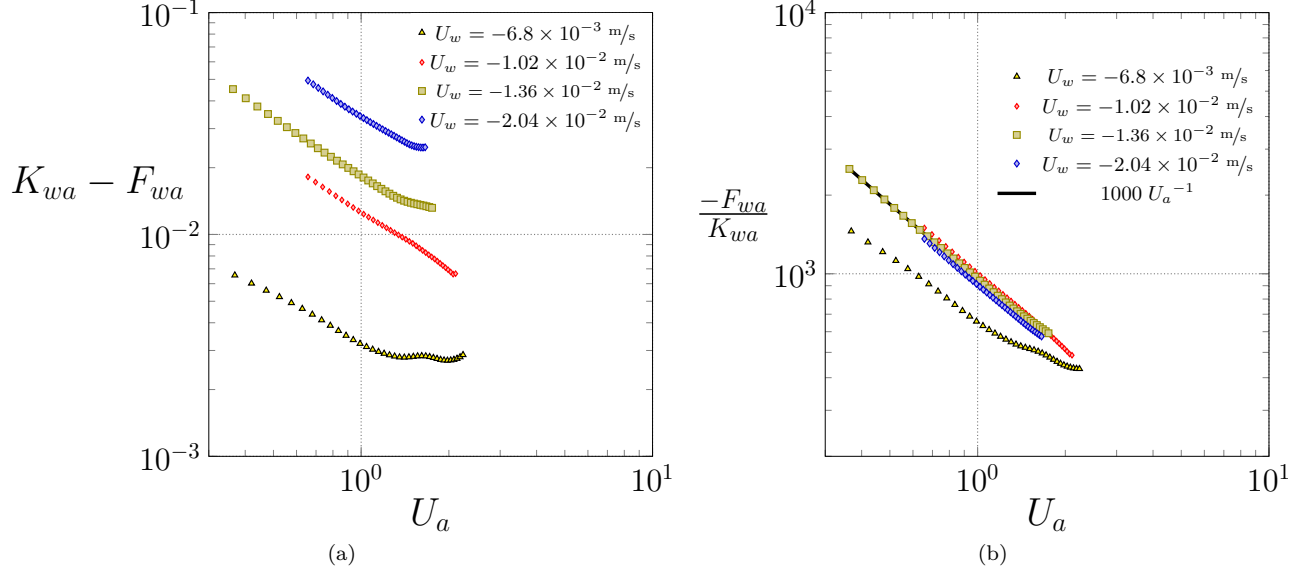


Figure 5.17 – Closures of the cross-terms K_{wa} and F_{wa} . a) $K_{wa} - F_{wa}$ and b) $-F_{wa}/K_{wa}$ as a function of U_a , see Eq. 5.70.

The closure of the eight effective parameters are rewritten in the following. The viscous terms read

$$K_{ww} = K_0 S_w^{2.7}, \quad K_{aa} = K_0 (1 - S_w)^2, \quad (5.74)$$

$$K_{wa} = \frac{\mu_a}{\mu_w} \frac{S_w^3}{(1 - S_w)}, \quad K_{aw} = \frac{(1 - S_w)}{S_w}, \quad (5.75)$$

where $K_0 = 2.0 \times 10^{-6} \text{ m}^2$. The inertial parameters read

$$F_{ww} \sim 30U_w; \quad F_{wa} = -1000K_{wa}U_a^{-1}, \quad (5.76)$$

$$F_{aa} \sim 2.3U_a^{1.15}; \quad F_{aw} = -10K_{aw}U_{\text{crit}}^2 \left[\left(\frac{U_a}{U_{\text{crit}}} \right)^2 + \left(\frac{U_a}{U_{\text{crit}}} \right)^{20} \right]. \quad (5.77)$$

One can especially notice that the inertial cross-terms F_{wa} and F_{aw} are negative in the counter-current configuration.

5.5.3.3 Results

Based on the set of closure relationships derived in the previous section, we now conduct simulations of the counter-current air-water flow for the range of flow rates considered in the experiment of Wang [182]. Water is injected from the top and streams down by gravity in the medium, while the gas phase flows counter-currently. The pressure drop and the liquid retention are shown in Fig. 5.18 as a function of the gas flow rate and for different values of the liquid flow rate. The model involving the cross and inertial terms is shown to predict accurately the flow fields from the pre-loading to the flooding regime. A discrepancy is seen for the lowest value of the liquid flow rate, which is due to the less accurate closure of the term F_{wa} in that case,

see Fig. 5.17b. The effective cross-terms are plotted in Fig. 5.19. In the flow regime that we consider, the inertial cross-terms are predominant compared to the viscous cross-terms.

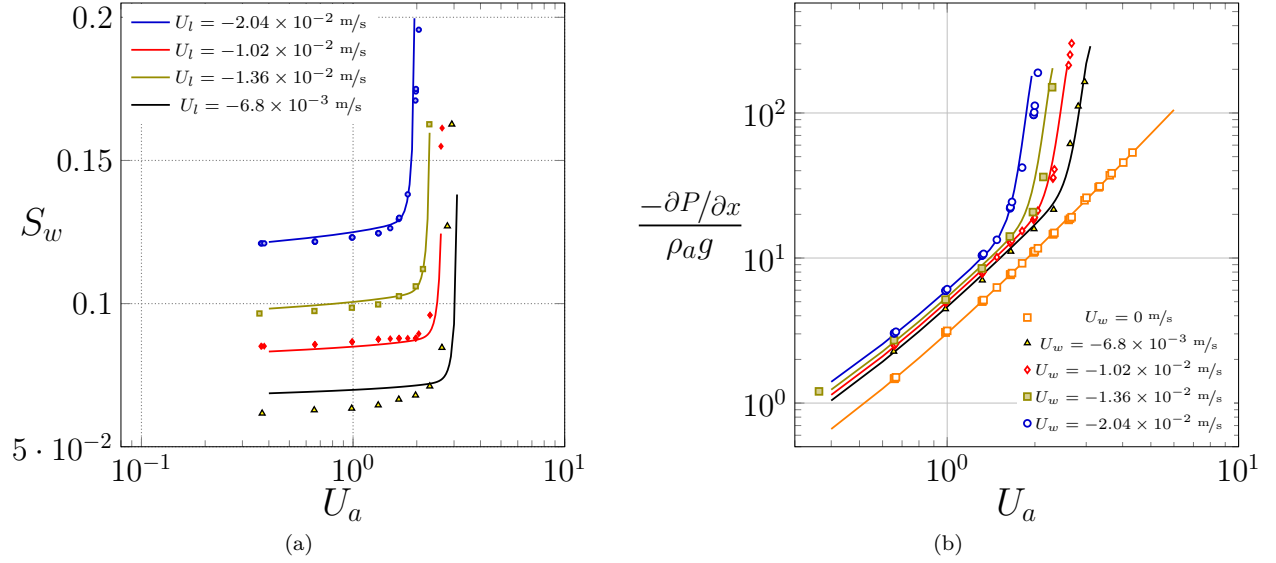


Figure 5.18 – Comparison between the experimental results from [182] and numerical results. a) Water saturation and b) dimensionless pressure gradient at steady-state as a function of U_a for three values of the liquid flow rate.

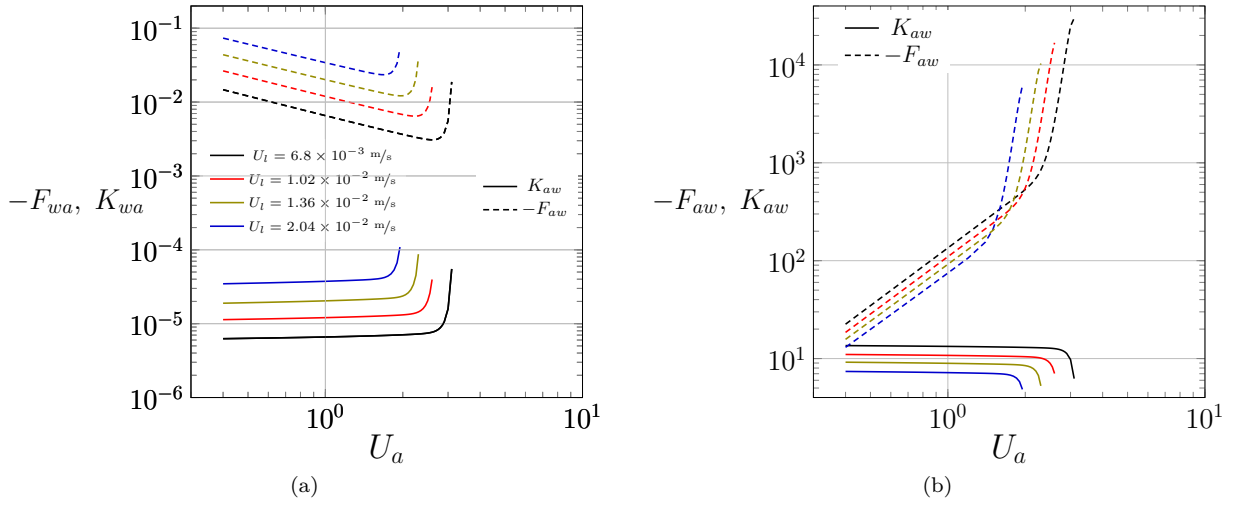


Figure 5.19 – Cross coefficients as a function of the gas flow rate U_a a) K_{wa} and F_{wa} and b) K_{aw} and F_{aw} .

To further analyze the importance of the momentum exchanges between the two phases, Eq. 5.32, we reconsider the momentum balance for the two phases under the form

$$0 = - \left(\frac{\partial P}{\partial x} + \rho a g \right) - \underbrace{\mu_a K_{aa}^{-1} (1 + F_{aa}) U_a}_1 + \underbrace{\mu_a K_{aa}^{-1} (K_{aw} - F_{aw}) U_w}_2, \quad (5.78a)$$

$$0 = - \left(\frac{\partial P}{\partial x} + \rho_w g \right) - \underbrace{\mu_w K_{ww}^{-1} (1 + F_{ww}) U_w}_3 + \underbrace{\mu_w K_{ww}^{-1} (K_{wa} - F_{wa}) U_a}_4. \quad (5.78b)$$

This form allows to express explicitly the contribution of the additional terms 2 and 4 in the momentum balance. Fig. 5.20 shows the evolution of these different terms as a function of the gas velocity U_a for $U_w = -1.02 \times 10^{-2} \text{ m/s}$. It is confirmed, first, that none of these terms is negligible for the range of Reynolds that is considered in the structured packings. Further, it is seen that the two curves intersect at a certain point, where the additional terms 2 and 4 become predominant in the momentum balances. The velocity corresponding to the intersection of the two curves is approximately U_{crit} , i.e. that it occurs at the beginning of the flooding regime where the interaction between the two phases is very strong. The ratio of the terms 2 to 1, and 4 to 3 of Eq. 5.78 are also plotted in Eq. 5.21. These ratio become higher than 1 as the additional terms become predominant.

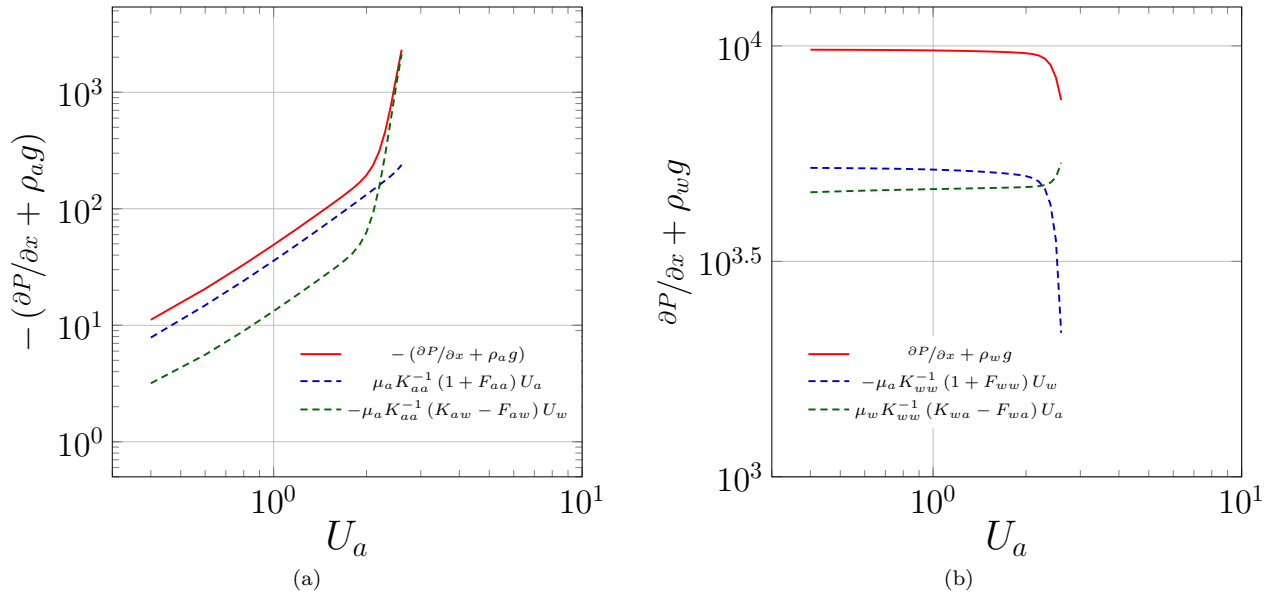


Figure 5.20 – Plot of the contributions to the momentum balance in Eq. 5.78 as a function of the gas flow rate U_a for $U_w = -1.02 \times 10^{-2} \text{ m/s}$ - a) Contributions in Eq. 5.78a and b) Contributions in Eq. 5.78b.

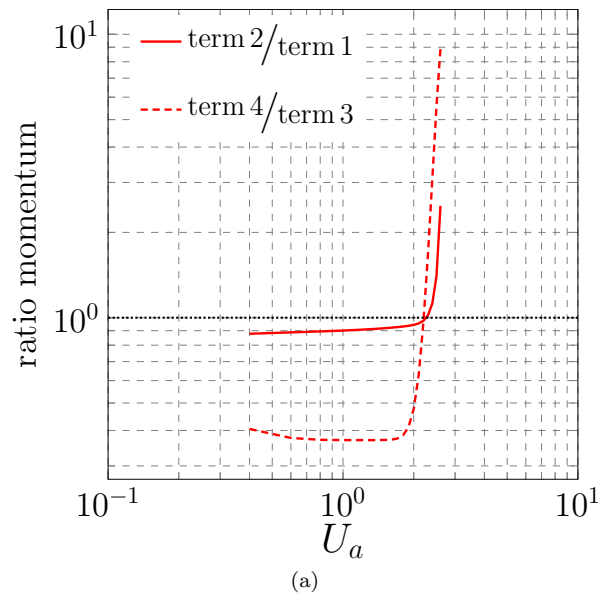


Figure 5.21 – Ratio of the contributions 2 to 1, and 4 to 3 respectively, in Eq. 5.78, as a function of the gas flow rate U_a .

5.6 Conclusion

In this work we attempted to answer the question on whether momentum exchange drives two-phase flow processes in highly permeable media. Our very first step was to identify the main features of two-phase flows in highly permeable media and to deduce a definition for such media. The main observation is that two-phase flows in low and high permeability media exhibit very distinct flow behaviors. We then restart from the mathematical system at pore-scale and discuss the volume averaging method leading potentially to closed forms at the continuum scale. We showed that the structure of the momentum balance at the continuum scale can be the same for the two extremes cases, i.e. either a system dominated by capillary effects or a system dominated by inertial effects. We deduce from this analysis a semi-heuristic modeling strategy involving cross and inertial effective parameters in the momentum balance and proceed to one-dimensional numerical resolution of the model for multiple configurations.

Our main conclusion is that these additional terms in the momentum balance are of major importance for flows in highly permeable media. The numerical simulations were conducted in cases of co- and a counter-current flows and were compared to experimental results. As expected, the momentum exchange between the two phases was first shown to be positively correlated with the permeability of the medium. The use of additional terms in the momentum balance also proved to capture properly the variations of the pressure drop and the global saturations of the phases. Above all, it is clear from this analysis that the additional cross-terms in the Darcy-like laws can be of major importance for the modeling of two-phase flows in highly permeable media.

The main limit of this approach is on the fact that in case of high Reynolds flows, the flow is intrinsically unsteady. The macroscale variables in our model at the continuum scale therefore somehow involve a time-averaging process. Some ergodicity effect could also be at play between space and time to explain that such model is able to reproduce macroscopically the system. Further developments should now be focused on

obtaining further information from the flow at pore-scale, to better characterize the effective parameters in the momentum balance and to ensure its mathematical structure.

Chapter 6

Distribution of the liquid phase

Contents

6.1	Previous approaches in the literature	131
6.1.1	Liquid “splitting”	132
6.1.2	One-phase flow in a bi-structured medium	133
6.2	Modeling strategy based on liquid splitting	134
6.2.1	Mass and momentum transport	135
6.2.2	Liquid exchange between the pseudo phases	138
6.2.3	Internal boundaries and rotation of the packs	139
6.2.4	Reduction toward a two-liquids approach	140
6.3	Numerical method	141
6.4	Results	142
6.4.1	Case 1: two pseudo-liquids in a two-pack column	142
6.4.2	Case 2: two and four liquids models between two sheets	144

As referred earlier in this study, the distribution of the liquid phase in the column is a key issue of the distillation process. Its modeling is actually a major step in the global modeling strategy. Modeling the momentum transport for the liquid phase means, on one hand, predicting the maldistributions, and, on the other hand, transporting accurately the chemical species. The structure of parallel corrugated sheets is known to affect significantly its distribution, and even little modifications of the design can have a significant impact. The contact points between two plates, for instance, are known to modify the dynamic of the liquid phase, through local reorientations of the flow. Their density between two plates was also recently shown to be linked to the mass transfer coefficient in the liquid [183]. Capturing precisely the different flow paths for given geometrical parameters is therefore crucial in the global modeling strategy of the process. So far, we characterized the macroscale momentum transport of the two-phase flow using a two-equation model: one equation for the liquid phase and one equation for the gas phase. The strong anisotropy of the structure and the way the liquid film distributes lead to consider other approaches. A number of questions are also unsolved for the liquid flow near internal boundaries, i.e., at the transition between the packs and at the external walls of the column. The medium was conceived so far as a single region with spatially constant properties. The successive rotation of the packs, the side effects, lead, as well, to consider new approaches.

In this chapter, we first describe the way the liquid phase distributes within the equipment of structured packing, based on imagery results from the literature. A strategy consisting in decomposing the liquid phase in four pseudo-phases is then proposed and discussed. Numerical experiments are conducted using this modeling strategy and the strategy consisting in splitting in only two phases [114, 162]. The two methods are compared by considering the distribution of the flow fields in multiple configurations.

Since this chapter is limited to a liquid-gas couple of fluids, we consider the notations $i = l$ and $j = g$. Also, since the notations can become excessively heavy, the intrinsic averaged pressure for the phase l is for instance denoted $P_l = \langle p_l \rangle^l$, and respectively for other phases. In the same way, the velocities which are employed are filtration velocities and denoted in the form U_l . Further, the double subscript notation in the intrinsic permeabilities is reduced to a single one, for instance K_l , to facilitate reading.

6.1 Previous approaches in the literature

While the gas phase turns to homogenize relatively well in the structure, the liquid phase appears to be much more affected by the anisotropy and by the specific structure of the packing. The gas phase was indeed shown to mix very well in the core of the pattern of packing. Conversely, the liquid phase tends to be much more guided along the grooves, and therefore to flow toward the outer part of the column. This behavior has been especially shown using tomography imagery [27, 114, 65, 181, 154]. A valuable result is for instance the one of Mahr and Mewes [114], who considered the point injection of a liquid phase from the top of two parallel corrugated sheets (MellaPack 250Y). As seen in Fig. 6.1, the liquid globally streams down within a cone delimited by $+\theta$ and $-\theta$, which are the incline angles of the corrugations along the two parallel sheets respectively. Multiple preferential paths can then be distinguished. First, one sees that a part of the liquid remains confined within the grooves, probably constrained by capillarity effects, and flows toward the external walls of the columns. An other part is guided toward a preferential direction that is between the axis of the column and the incline of the corrugations. This direction is sometimes associated to a *gravity angle* [157, 162], meaning the the liquid film flows along the steepest angle along a corrugated sheet. Due to the arrangement in parallel sheets, however, this direction is also affected by a phenomenon of local liquid retention at discrete points, as seen in Fig. 6.1. These local retentions correspond to an area around the contact points between two corrugated sheets, where capillary effects dominate and retain the liquid. The

liquid is seen to reorient at these points, meaning that a part of the liquid flowing over one sheet suddenly changes its trajectory to go toward the sheet which is adjacent.

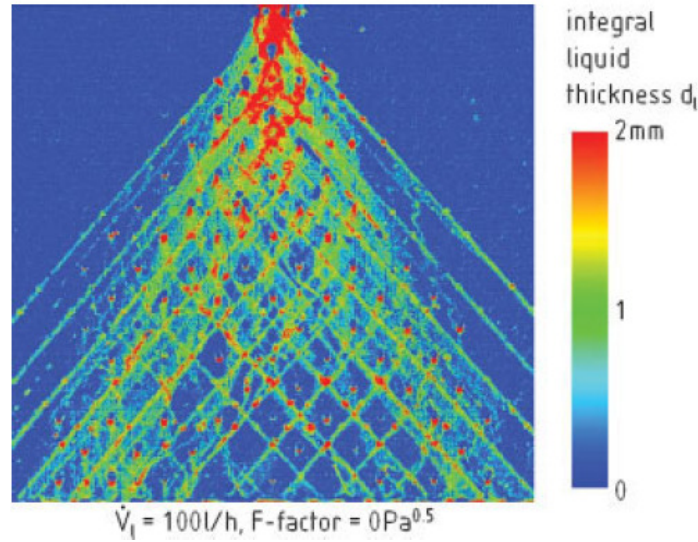


Figure 6.1 – X-ray measurements from [114] - Liquid pattern between two corrugated sheets from a point injection.

6.1.1 Liquid “splitting”

The geometry of structured packings therefore constrains drastically the flow of the liquid phase, and generates a number of different flow paths for the liquid phase. This leads to consider a specific modeling strategy for this phase at the continuum scale. Indeed, a special feature of two parallel corrugated sheets is also the symmetry with respect to the vertical axis of the column. This symmetry leads to a purely vertical flow when one considers the averaged velocity over a REV. The classical two-phase flow models used in porous media, including the generalized Darcy’s laws with or without cross-terms as presented in the previous chapters, become therefore inaccurate. One can actually impose a dispersion term in the momentum balance in order to force the liquid phase radially [61]. This method does not allow, however, to capture the preferential paths within the structures, including the reorientations at the contact points. Mahr and Mewes, based on their experimental observations, suggest to arbitrarily split the liquid phase in two interpenetrating liquid phases. The two *pseudo-liquids* are seen as two quasi-independent films, considering one film on each of two parallel sheets. The two films flow along two main directions, characterized by a steepest angle $\pm\theta^*$ with the vertical axis of the column. The configuration is depicted in Fig. 6.2. The approach also includes a liquid exchange between the two liquid films, which is supposed to occur at the contact points between two corrugated sheets. It therefore permits to recover the tendency of the liquid phase to flow radially as well as the constant redistribution at the contact points. The system of mass and momentum conservation laws is derived for a three-phase system, gas-liquid-liquid, and is based on an approach inspired from the volume averaging method. The resulting macroscale laws include second-order effective tensors in the momentum equations, which determine the direction of the phases along preferential paths. Also, the fluid/fluid and fluid/solid interfacial effects are modeled via friction terms, following the idea used in chemical engineering. A similar approach is used by Soulaire et al. [162], who introduce the concept of bi-structured medium

to characterize the structured packing [160]. Such medium exhibits a topology composed of two distinct regions, leading to two separate behaviors at the macroscale. These two regions correspond to two parallel corrugated sheets, which guide the liquid in two opposite directions. The model of Soulaire et al. relies on more theoretical basis than the one of Mahr and Mewes, especially due to the generic analysis of a fluid flow in a bi-structured medium, but the liquid splitting in structured packings is still semi-heuristic.

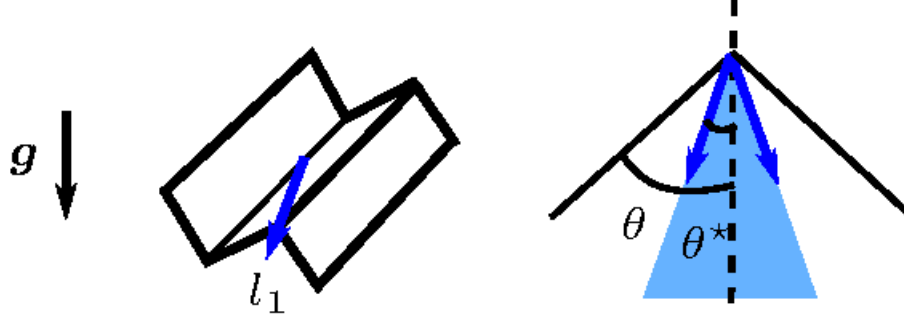


Figure 6.2 – Illustration of the strategy of liquid splitting using a two-liquids approach - left: flow direction along one corrugated sheet - right: distribution between two corrugated sheets. θ is the inclination angle of the corrugations and θ^* is referred as an effective angle [114] or as the gravity angle [157, 162].

6.1.2 One-phase flow in a bi-structured medium

As introduced above, the underlying idea of the approach is to arbitrarily split the liquid phase in quasi-independent pseudo-phases for distinct regions in the medium. Considering for instance a splitting in two pseudo-phases, the first step here would therefore consist in averaging spatially the gas-liquid-liquid mathematical system, following an initial arbitrary splitting at the microscale. However, such a procedure implies a high level of complexity in the developments, and closing the system rigorously is today out of reach. As an initial approach, to better understand the implications of a local “splitting”, Soulaire et al. [160] suggest to consider the case of a one-phase flow in a bi-structured medium. A fluid l flowing in a bi-structured porous medium is therefore arbitrarily split in two pseudo-phases l_1 and l_2 at the local scale. Using the volume averaging method, it is shown that the structure of the macroscale laws is somehow complex, involving in particular cross-terms in the momentum balance. It reads

$$\mathbf{U}_{l_1} = -\frac{\mathbf{K}_{l_1}}{\mu_l} \cdot (\nabla P_{l_1} - \rho_l \mathbf{g}) + \mathbf{K}_{l_1 l_2} \cdot \mathbf{U}_{l_2} + \mathbf{\Pi}_{l_1} (P_{l_1} - P_{l_2}), \quad (6.1a)$$

$$\mathbf{U}_{l_2} = -\frac{\mathbf{K}_{l_2}}{\mu_l} \cdot (\nabla P_{l_2} - \rho_l \mathbf{g}) + \mathbf{K}_{l_2 l_1} \cdot \mathbf{U}_{l_1} + \mathbf{\Pi}_{l_2} (P_{l_1} - P_{l_2}), \quad (6.1b)$$

where \mathbf{K}_{l_1} and \mathbf{K}_{l_2} refer to the intrinsic permeabilities and the cross-terms $\mathbf{K}_{l_1 l_2}$ and $\mathbf{\Pi}_{l_1}$ for the pseudo-phase l_1 (respectively $\mathbf{K}_{l_2 l_1}$ and $\mathbf{\Pi}_{l_2}$ for l_2) characterize an exchange of momentum between the two coexisting pseudo-liquids. Although it is limited to a one-phase flow, the approach gives some indications about the structure of the momentum laws at the continuum scale in case of “pseudo-phases”. It especially shows that,

strictly speaking, macroscale cross-terms have to be considered to characterize the exchange of momentum. Further, the mass conservation equations are shown to be

$$\varepsilon \frac{\partial S_{l_1}}{\partial t} + \nabla \cdot \mathbf{U}_{l_1} = +\dot{m}, \quad (6.2a)$$

$$\varepsilon \frac{\partial S_{l_2}}{\partial t} + \nabla \cdot \mathbf{U}_{l_2} = -\dot{m}, \quad (6.2b)$$

where the mass transfer term \dot{m} characterizes an exchange of matter between l_1 and l_2 . The closure for this term takes the form

$$\dot{m} = -\chi_{l_1} \cdot \mathbf{U}_{l_1} + \chi_{l_2} \cdot \mathbf{U}_{l_2} + h(P_{l_1} - P_{l_2}). \quad (6.3)$$

The liquid exchange is therefore controlled on one hand by the difference of the averaged pressures $P_{l_1} - P_{l_2}$, and on the other hand by velocity terms which can be associated to dynamic effects. This relation is important as it allows to better apprehend the mathematical structure of \dot{m} and the underlying physical effects at play in the exchange of matter. In this relation, the effective parameters χ_{l_1} , χ_{l_2} and h are solutions of closure problems (emerging from the volume averaging method), and potentially vary with the position of the l_1 - l_2 interface and the pore-scale velocity fields. Considering that dynamic effects play a minor role at the leading order, Soulaie et al. neglect the velocity terms and consider that the difference of the averaged pressures governs the exchange

$$\dot{m} = h(P_{l_1} - P_{l_2}). \quad (6.4)$$

It can be concluded from this initial analysis that cross-terms (Eqs 6.1) and mass exchange terms (Eq. 6.3) are likely to be present in the modeling of a gas-liquid flow with liquid splitting. It must be noted that these terms come in addition to the cross and inertial terms introduced in Chapters 4 and 5 for the liquid-gas momentum exchange.

6.2 Modeling strategy based on liquid splitting

In this part, we derive a macroscale model for the liquid/gas flow in structured packings based on splitting of the liquid phase in multiple pseudo-phases. The mass and momentum equations are derived as a semi-heuristic extension of the model derived for a one-phase flow in the previous section. It is presumed that the liquid film flowing along *one* corrugated sheet (and independently of the parallel sheet) involves two behaviors at the macroscale meaning two preferential flow paths. The domain corresponding to one sheet is therefore decomposed into two regions, corresponding to the two flow paths. The whole liquid phase between two corrugated sheets is therefore decomposed into *four* pseudo-phases, i.e. two films per corrugated sheets. This liquid splitting is illustrated in Fig. 6.3. A part of the liquid is assumed to flow within the grooves of the corrugations, as seen in the experiment Fig. 6.1, while an other part flows in a downward direction.

The system is therefore composed of a gas phase and of four pseudo-phases, referred as l_1^θ and $l_1^{\theta_{\min}}$ for the corrugated sheet 1, and l_2^θ and $l_2^{\theta_{\min}}$ for the corrugated sheet 2 (adjacent to 1). The indices θ and θ_{\min} refer to the directions of the flow of the pseudo-phases. l_1^θ and l_2^θ are the parts of the liquid which are confined within the grooves (inclined at the angle θ), while $l_1^{\theta_{\min}}$ and $l_2^{\theta_{\min}}$ are the parts of the liquid flowing downward along a minimal angle θ_{\min} . Of course, such a model brings further complexity to the global picture, however, the results in this chapter show that a minimum number of parameters is required to take full advantages of the model capabilities.

Why consider a splitting of the liquid phase in four pseudo-phases? The previous approaches involving the concept of “steepest flow” could actually “forget” a part of the liquid film flowing in the grooves. More

generally, it seems that multiple behaviors can be encountered. The experiment from Mahr and Mewes indicates that some liquid is present within a cone delimited by $\pm\theta$. The experiment developed by Soulaïne [159], consisting of a point injection of liquid from the top of two translucent corrugated sheets, seems to indicate, conversely, that the liquid flows along a steep angle. This is probably explained by high saturation values at the injection point, which tend to favor the flow in the downward direction and to increase the exchange at the contact points. These two results indicate that the flow behavior depends locally on the saturation. One can actually expect the distribution to be function of a large number of parameters, including geometrical parameters (height of the grooves, wavelength, angle of incline of the corrugations), the properties of the liquid, the flow rates, as well as potential surface roughness. Tightened corrugations tend, for instance, to reinforce the capillary effects within the grooves and therefore to constrain the liquid there. The rotation of the packs, finally, could also be included in the analysis. The successive rotations somehow constantly reinitialize the liquid film between two packs. Regardless of the conditions of injection, one can presume the liquid to go through a certain distance within a pack before a steady-state is reached. Since the height of the pack is not high (~ 20 cm), this distance might be significant and might affect the global dynamic of the flow. These few remarks motivated us to investigate on a new modeling approach to better characterize the flow of the liquid phase.

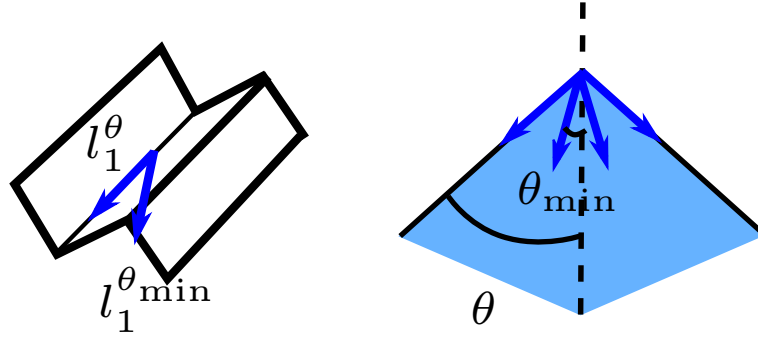


Figure 6.3 – Sketch of the liquid distribution - left: along corrugated sheet - right: distribution within two corrugated sheets, using the four-equation approach. θ is the inclination angle of the corrugations and θ^{\min} the steepest direction that the liquid can follow along one corrugated sheet.

ys

6.2.1 Mass and momentum transport

The global liquid saturation reads

$$S_l = S_{l_1^\theta} + S_{l_1^{\theta_{\min}}} + S_{l_2^\theta} + S_{l_2^{\theta_{\min}}}, \quad (6.5)$$

and the definition of saturations requires

$$S_g + S_l = 1. \quad (6.6)$$

The averaged velocity of the liquid phase reads

$$\mathbf{U}_l = \mathbf{U}_{l_1^\theta} + \mathbf{U}_{l_1^{\theta_{\min}}} + \mathbf{U}_{l_2^\theta} + \mathbf{U}_{l_2^{\theta_{\min}}}. \quad (6.7)$$

The mass conservation of the system is characterized by a set of five equations at macroscale, including liquid exchange between the pseudo-phases. It reads

$$\varepsilon \frac{\partial S_g}{\partial t} + \nabla \cdot \mathbf{U}_g = 0, \quad (6.8a)$$

$$\varepsilon \frac{\partial S_{l_1^\theta}}{\partial t} + \nabla \cdot \mathbf{U}_{l_1^\theta} = \dot{m}_1, \quad \varepsilon \frac{\partial S_{l_1^{\theta_{\min}}}}{\partial t} + \nabla \cdot \mathbf{U}_{l_1^{\theta_{\min}}} = -\dot{m}_1 + \dot{m}, \quad (6.8b)$$

$$\varepsilon \frac{\partial S_{l_2^\theta}}{\partial t} + \nabla \cdot \mathbf{U}_{l_2^\theta} = \dot{m}_2, \quad \varepsilon \frac{\partial S_{l_2^{\theta_{\min}}}}{\partial t} + \nabla \cdot \mathbf{U}_{l_2^{\theta_{\min}}} = -\dot{m}_2 - \dot{m}. \quad (6.8c)$$

\dot{m} characterizes the liquid exchange between the films 1 and 2 along the two corrugated sheets. \dot{m}_1 and \dot{m}_2 characterize the liquid exchanges *per plate*, between l_1^θ and $l_1^{\theta_{\min}}$, and l_2^θ and $l_2^{\theta_{\min}}$ respectively. The exchanges are illustrated in Fig. 6.4. Strictly speaking, one should consider an exchange of matter for each couple of pseudo-phases in the medium. We assume instead that the liquid part which is confined within the grooves of the corrugations cannot exchange with the liquid film which is on the adjacent sheet (zero exchange between l_1^θ and l_2^θ). This assumption relies on the fact that the liquid exchange occurs at the contact points, and therefore concerns the pseudo-liquids $l_1^{\theta_{\min}}$ and $l_2^{\theta_{\min}}$. This is actually true apart from the region of transition between the packs where the liquid redistributes (see Section 6.2.3) and where the exchanges are maximal.

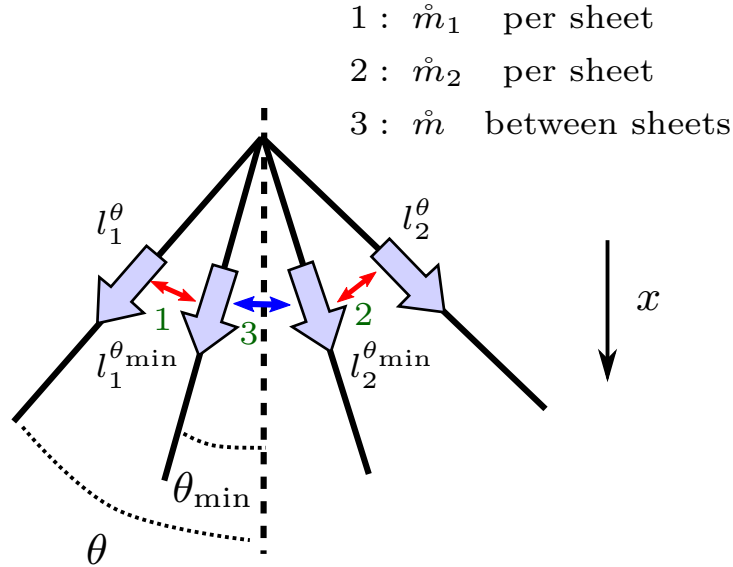


Figure 6.4 – Sketch of the liquid distribution with a splitting in four pseudo-phases

The momentum conservation laws for the system read

$$\mathbf{U}_g = -\frac{\mathbf{K}_g}{\mu_g} \cdot (\nabla P_g - \rho_g \mathbf{g}), \quad (6.9a)$$

$$\mathbf{U}_{l_1^\theta} = -\frac{\mathbf{K}_{l_1^\theta}}{\mu_l} \cdot (\nabla P_{l_1^\theta} - \rho_l \mathbf{g}), \quad \mathbf{U}_{l_1^{\theta_{\min}}} = -\frac{\mathbf{K}_{l_1^{\theta_{\min}}}}{\mu_l} \cdot (\nabla P_{l_1^{\theta_{\min}}} - \rho_l \mathbf{g}), \quad (6.9b)$$

$$\mathbf{U}_{l_2^\theta} = -\frac{\mathbf{K}_{l_2^\theta}}{\mu_l} \cdot (\nabla P_{l_2^\theta} - \rho_l \mathbf{g}), \quad \mathbf{U}_{l_2^{\theta_{\min}}} = -\frac{\mathbf{K}_{l_2^{\theta_{\min}}}}{\mu_l} \cdot (\nabla P_{l_2^{\theta_{\min}}} - \rho_l \mathbf{g}). \quad (6.9c)$$

\mathbf{K}_g is the permeability for the gas phase and $\mathbf{K}_{l_1^\theta}$, $\mathbf{K}_{l_1^{\theta_{\min}}}$, $\mathbf{K}_{l_2^\theta}$ and $\mathbf{K}_{l_2^{\theta_{\min}}}$ are the permeabilities of the four pseudo liquids respectively. Strictly speaking, the momentum balance for the pseudo-phases should include additional cross-terms characterizing momentum exchanges. In the case of the vapor-liquid flow within structured packings, however, a number of reasonable assumptions can be made. One can indeed presume that the contact surface between $l_1 = l_1^\theta \cup l_1^{\theta_{\min}}$ and $l_2 = l_2^\theta \cup l_2^{\theta_{\min}}$ is restricted to the contact points between the corrugated sheets, where the liquid forms meniscus. For high gas and liquid flow rates (in the loading regime), or in case of a dense packing, the surface of exchange is probably larger, as the liquid phase is more likely destabilized. This is however more prone to occur for absorption processes (for instance CO₂ in a MEA solution) than for the distillation of the air, where the low surface tensions favor a distribution in well separated films. Assuming a small contact surface, the momentum exchange between l_1 and l_2 plays a little role and any cross-terms similar to those in Eqs 6.1 are considered to be negligible. The momentum transfer between the gas and the liquid phase is also assumed negligible in this chapter, as the emphasis is on the distribution of the liquid phase in the structure (the gas phase is at rest). In the same spirit, we consider creeping flows and therefore neglect any inertial dissipation effects. The complete model including the inertial effects and the momentum exchange with the gas phase is given in Appendix C.

At this stage, the question is on the closure for the permeability tensors. The idea is to associate the four pseudo-phases to four films flowing along planes inclined with an angle $\pm\theta$ or $\pm\theta_{\min}$ compared to the vertical axis of the column. These planes are represented in Fig. 6.4. In the coordinate system associated to the axis of the column, the permeability tensors for the various pseudo-phases, for a pack oriented along the plane xOy , respectively read [159]

$$\mathbf{K}_{l_1^\theta} = K_0 k_{r_{l_1^\theta}} \begin{pmatrix} \cos^2\theta \sin^2\theta & \cos\theta \sin\theta & 0 \\ \cos\theta \sin\theta & \cos^2\theta \sin^2\theta & 0 \\ 0 & 0 & 0 \end{pmatrix}, \quad \mathbf{K}_{l_2^\theta} = K_0 k_{r_{l_2^\theta}} \begin{pmatrix} \cos^2\theta \sin^2\theta & -\cos\theta \sin\theta & 0 \\ -\cos\theta \sin\theta & \cos^2\theta \sin^2\theta & 0 \\ 0 & 0 & 0 \end{pmatrix}, \quad (6.10a)$$

$$\mathbf{K}_{l_1^{\theta_{\min}}} = K_0 k_{r_{l_1^{\theta_{\min}}}} \begin{pmatrix} \cos^2\theta_{\min} \sin^2\theta_{\min} & \cos\theta_{\min} \sin\theta_{\min} & 0 \\ \cos\theta_{\min} \sin\theta_{\min} & \cos^2\theta_{\min} \sin^2\theta_{\min} & 0 \\ 0 & 0 & 0 \end{pmatrix}, \quad (6.10b)$$

$$\mathbf{K}_{l_2^{\theta_{\min}}} = K_0 k_{r_{l_2^{\theta_{\min}}}} \begin{pmatrix} \cos^2\theta_{\min} \sin^2\theta_{\min} & -\cos\theta_{\min} \sin\theta_{\min} & 0 \\ -\cos\theta_{\min} \sin\theta_{\min} & \cos^2\theta_{\min} \sin^2\theta_{\min} & 0 \\ 0 & 0 & 0 \end{pmatrix}. \quad (6.10c)$$

The k_r terms are the relative permeabilities and are functions of the saturation only. Following the idea that the phases remain confined within two parallel corrugated sheets, the transverse direction is prohibited (z direction), which translates in the permeability tensors into a line and a column of zeros. The tensors Eq. 6.10 correspond to sheets oriented along the plane xOy . The permeability $\mathbf{K}_{l_1^\theta}$ of the packs oriented along the plane xOz reads for instance

$$\mathbf{K}_{l_1^\theta} = K_0 k_{r_{l_1^\theta}} \begin{pmatrix} \cos^2\theta \sin^2\theta & 0 & \cos\theta \sin\theta \\ 0 & 0 & 0 \\ \cos\theta \sin\theta & 0 & \cos^2\theta \sin^2\theta \end{pmatrix}. \quad (6.11)$$

The two orientations of sheets actually correspond to two regions of the column, which will be referred later as regions a and b (see section 6.2.3). It should be mentioned that the transverse flow through the holes is sometimes accounted for in the literature [13, 168], but it is likely to be moderate due to the small diameters of the holes, leading to significant capillary effects locally and the formation of meniscus. Nevertheless, the holes are likely to affect the relative permeabilities and the exchange between the pseudo-phases.

The permeability tensor for the gas phase, \mathbf{K}_g , is determined based on the experience acquired from the one-phase approach conducted in Chapter 3. The non-diagonal terms of the tensor were proved to be negligible compared to the diagonal terms, and these later were proved to be equal for corrugations inclined at an angle $\theta = 45^\circ$. \mathbf{K}_g therefore reads

$$\mathbf{K}_g = K_0 k_{r_g} \begin{pmatrix} 1 & 0 & 0 \\ 0 & 1 & 0 \\ 0 & 0 & 0 \end{pmatrix}, \quad (6.12)$$

for the pack oriented along the plane xOy . One can also notice that, strictly speaking, the gas phase should also be splitted in multiple pseudo-phases as it flows in the same structure. Actually, the flow of the gas phase would correspond to the case of a very strong mass exchange in the right hand side of the mass balance Eq. 6.13, due to the strong mixing between the potential pseudo-phases. In this specific case, the flow derives to a single one-phase flow in the vertical direction (see later simulations including a strong exchange between the two plates for illustration).

6.2.2 Liquid exchange between the pseudo phases

The mechanisms which control the liquid exchange \dot{m}_1 (respectively \dot{m}_2) between the two pseudo-phases l_1^θ and $l_1^{\theta_{\min}}$ (respectively l_2^θ and $l_2^{\theta_{\min}}$) are difficult to assess. Following the analysis from the monophasic analysis, the liquid exchanges \dot{m} , \dot{m}_1 and \dot{m}_2 are assumed to be controlled by a difference of pressures and to read

$$\dot{m} = h \left(P_{l_1^\theta} - P_{l_2^\theta} \right), \quad \dot{m}_1 = h_1 \left(P_{l_1^\theta} - P_{l_1^{\theta_{\min}}} \right), \quad \dot{m}_2 = h_2 \left(P_{l_2^\theta} - P_{l_2^{\theta_{\min}}} \right). \quad (6.13)$$

Strictly speaking, the liquid exchange in the monophasic case (Eq. 6.3) also involved velocity terms, meaning that some dynamic effects could also be at play. In this study, we only conduct as a first step a phenomenological analysis of the impact of the exchange, and \dot{m} , \dot{m}_1 and \dot{m}_2 are chosen as functions of the saturations of the two phases. Prior works also included the notion of macroscale capillary pressures between the gas phase and the pseudo-liquid phases to explain the liquid exchanges [162], but we do not think that such phenomena explain entirely the exchanges. We write the mass exchange terms under the form

$$\dot{m} = h \left(S_{l_1^\theta}^\alpha - S_{l_2^\theta}^\alpha \right), \quad \dot{m}_1 = h_1 \left(S_{l_1^\theta}^\alpha - S_{l_1^{\theta_{\min}}}^\alpha \right), \quad \dot{m}_2 = h_2 \left(S_{l_2^\theta}^\alpha - S_{l_2^{\theta_{\min}}}^\alpha \right), \quad (6.14)$$

which in fact correspond to the use of Corey capillary pressure relationships for the liquid-gas couple of phases, as explained in [162]. The constant α is chosen positive, such that the liquid exchange increases with the saturation and h is a constant, although rigorously it might depend on the saturation. Due to the symmetry of two parallel corrugated sheets, we also have $h_{l_1} = h_{l_2}$.

6.2.3 Internal boundaries and rotation of the packs

So far in this study, the domain has been seen as a purely periodic porous medium made of a repetitive pattern. When one considers the entire column, however, internal boundaries have to be considered. These boundaries are the external walls of the column and the region of transition between the successive packs.

At the transition between two packs, the liquid is assumed to balance equally in the new pack along two corrugated sheets 1 and 2. There is indeed no reason for a given phase to be guided along one sheet more than along the other, since the corrugations are inclined symmetrically with the vertical axis. It is therefore assumed that the pseudo-phase l_1^θ (and respectively for the others) redistributes equally in the four pseudo-phases l_1^θ , $l_1^{\theta_{\min}}$, l_2^θ and $l_2^{\theta_{\min}}$. Although the symmetrical redistribution between 1 and 2 is quite intuitive, the entrance redistribution between l_1^θ and $l_1^{\theta_{\min}}$ on one hand and l_2^θ and $l_2^{\theta_{\min}}$ on the other hand is not straightforward. One can for instance suppose that for very thin films, the liquid tends to flow initially within the grooves of the corrugated sheets (θ), and conversely for high saturations to flow downward (θ_{\min}). This discussion also concerns the entrance conditions from the injectors at the top of the columns. For the moment, we assume a balanced redistribution.

In a thin layer at the transition between two packs, the mass conservation equations therefore read

$$\varepsilon \frac{\partial S_{l_1^\theta}}{\partial t} + \nabla \cdot \mathbf{U}_{l_1^\theta} = \dot{m}_{l_1^\theta l_1^{\theta_{\min}}} + \dot{m}_{l_1^\theta l_2^\theta} + \dot{m}_{l_1^\theta l_2^{\theta_{\min}}}, \quad (6.15a)$$

$$\varepsilon \frac{\partial S_{l_1^{\theta_{\min}}}}{\partial t} + \nabla \cdot \mathbf{U}_{l_1^{\theta_{\min}}} = -\dot{m}_{l_1^\theta l_1^{\theta_{\min}}} + \dot{m}_{l_1^{\theta_{\min}} l_2^\theta} + \dot{m}_{l_1^{\theta_{\min}} l_2^{\theta_{\min}}}, \quad (6.15b)$$

$$\varepsilon \frac{\partial S_{l_2^\theta}}{\partial t} + \nabla \cdot \mathbf{U}_{l_2^\theta} = -\dot{m}_{l_1^\theta l_2^\theta} - \dot{m}_{l_1^{\theta_{\min}} l_2^\theta} + \dot{m}_{l_2^\theta l_2^{\theta_{\min}}}, \quad (6.15c)$$

$$\varepsilon \frac{\partial S_{l_2^{\theta_{\min}}}}{\partial t} + \nabla \cdot \mathbf{U}_{l_2^{\theta_{\min}}} = -\dot{m}_{l_1^\theta l_2^{\theta_{\min}}} - \dot{m}_{l_1^{\theta_{\min}} l_2^{\theta_{\min}}} - \dot{m}_{l_2^\theta l_2^{\theta_{\min}}}, \quad (6.15d)$$

where liquid exchange terms for each couple of pseudo-phases are introduced at the transition layer. These relations apply in the transition layers between the packs. A scalar function α that is 1 in the packs and 0 in the transition layer is considered to distinguish the two regions. This can be roughly illustrated through the relation

$$\dot{m} = \alpha \dot{m}_{\text{packs}} + (1 - \alpha) \dot{m}_{\text{trans}}. \quad (6.16)$$

Further, the correlations used for the exchange terms at the transition between two packs are under the same form as those introduced in Eq. 6.14, with $h_{\text{trans}} \gg h_{\text{packs}}$.

The side effects in the outer part of the column are treated in a similar way. So far, however, it is unclear whether the liquid arriving at the external wall accumulates, flows downward along the wall, or instead flows toward the internal part of the column. We introduce again a thin porous medium layer in the outer part of the column, where different physical properties can be specified. We consider in this work that the liquid is partially redirected toward the center of the column, i.e. that the liquid exchange between the pseudo-phases

is very important in this region. The coefficient h in Eq. 6.14 is therefore maximal in this region.

The successive rotation of the packs in the column, which leads to different orientations of the corrugated sheets successively, also corresponds to a variation of the spatial properties of the porous medium. The two orientations of the packs are seen as two regions, referred as a and b, and are characterized by a scalar function β , that is 0 or 1 depending on the pack orientation. The permeability tensor $\mathbf{K}_{l_1^\theta}$ (respectively for the other permeabilities) therefore reads

$$\mathbf{K}_{l_1^\theta} = \beta \mathbf{K}_{l_1^\theta}^a + (1 - \beta) \mathbf{K}_{l_1^\theta}^b, \quad (6.17)$$

where $\mathbf{K}_{l_1^\theta}^a$ corresponds to the orientation along xOy , Eq. 6.10a (left), and $\mathbf{K}_{l_1^\theta}^b$ corresponds to the orientation along xOz , Eq. 6.11.

6.2.4 Reduction toward a two-liquids approach

One can actually easily reduce the model with four pseudo-phases to a model with two pseudo-phases. In such a case, the two phases are supposed to flow along two opposite directions characterized by an effective angle $\pm\theta^*$. The configuration is illustrated in Fig. 6.5. The angle θ^* is referred as an effective angle or the gravity angle. It is defined as the steepest direction that a particle of fluid can follow along a corrugated surface in [157, 162] and it is estimated based on an analytical solution and is purely geometric.

Using this strategy, the mass balances developed in the previous sections reduce to

$$\varepsilon \frac{\partial S_{l_1}}{\partial t} + \nabla \cdot \mathbf{U}_{l_1} = \dot{m}, \quad \varepsilon \frac{\partial S_{l_2}}{\partial t} + \nabla \cdot \mathbf{U}_{l_2} = -\dot{m}, \quad (6.18)$$

where l_1 and l_2 are the two pseudo-phases and \dot{m} the liquid exchange which is supposed to occur at the contact points. The momentum balance read

$$\mathbf{U}_{l_1} = -\frac{\mathbf{K}_{l_1}}{\mu_{l_1}} \cdot (\nabla P_{l_1} - \rho_{l_1} \mathbf{g}), \quad \mathbf{U}_{l_2} = -\frac{\mathbf{K}_{l_2}}{\mu_{l_2}} \cdot (\nabla P_{l_2} - \rho_{l_2} \mathbf{g}), \quad (6.19)$$

where

$$\mathbf{K}_{l_1} = K_0 k_{r_{l_1}} \begin{pmatrix} \cos^2 \theta^* \sin^2 \theta^* & \cos \theta^* \sin \theta^* & 0 \\ \cos \theta^* \sin \theta^* & \cos^2 \theta^* \sin^2 \theta^* & 0 \\ 0 & 0 & 0 \end{pmatrix}, \quad \mathbf{K}_{l_2} = K_0 k_{r_{l_2}} \begin{pmatrix} \cos^2 \theta^* \sin^2 \theta^* & -\cos \theta^* \sin \theta^* & 0 \\ -\cos \theta^* \sin \theta^* & \cos^2 \theta^* \sin^2 \theta^* & 0 \\ 0 & 0 & 0 \end{pmatrix}, \quad (6.20)$$

for a given orientation of the packs. Similarly to previously, the exchange term is written in the form of a Corey relationship,

$$\dot{m} = h (S_{l_1}^\alpha - S_{l_2}^\alpha). \quad (6.21)$$

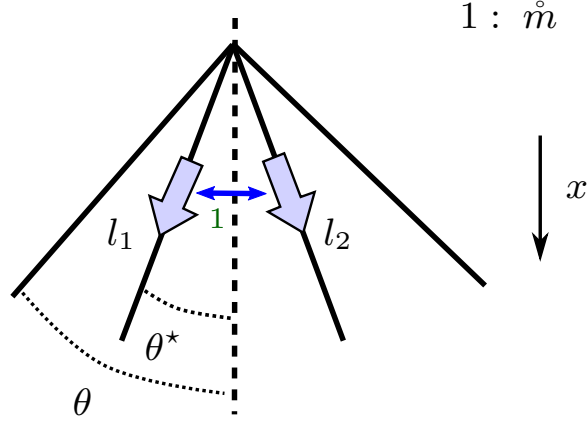


Figure 6.5 – Sketch of the liquid distribution with a splitting in two pseudo-phases

6.3 Numerical method

The simulations are conducted with the same method than in the previous chapter. The solver is edited to account for the models introduced here. It can be used to solve the model involving two or four pseudo-phases for the liquid phase. In case of four pseudo-phases, the following notations are introduced

$$M_g = \frac{\mathbf{K}_g}{\mu_g}, \quad M_{l_1^\theta} = \frac{\mathbf{K}_{l_1^\theta}}{\mu_l}, \quad M_{l_2^\theta} = \frac{\mathbf{K}_{l_2^\theta}}{\mu_l}, \quad M_{l_1^{\theta_{\min}}} = \frac{\mathbf{K}_{l_1^{\theta_{\min}}}}{\mu_l}, \quad M_{l_2^{\theta_{\min}}} = \frac{\mathbf{K}_{l_2^{\theta_{\min}}}}{\mu_l}, \quad (6.22a)$$

$$\mathbf{L}_g = \frac{\rho_g \mathbf{K}_g}{\mu_g}, \quad \mathbf{L}_{l_1^\theta} = \frac{\rho_l \mathbf{K}_{l_1^\theta}}{\mu_l}, \quad \mathbf{L}_{l_2^\theta} = \frac{\rho_l \mathbf{K}_{l_2^\theta}}{\mu_l}, \quad \mathbf{L}_{l_1^{\theta_{\min}}} = \frac{\rho_l \mathbf{K}_{l_1^{\theta_{\min}}}}{\mu_l}, \quad \mathbf{L}_{l_2^{\theta_{\min}}} = \frac{\rho_l \mathbf{K}_{l_2^{\theta_{\min}}}}{\mu_l}. \quad (6.22b)$$

This yields for the momentum balances

$$\mathbf{U}_g = -M_g \cdot \nabla P_g + \mathbf{L}_g \cdot \mathbf{g}, \quad (6.23a)$$

$$\mathbf{U}_{l_1^\theta} = -M_{l_1^\theta} \cdot \nabla P_g + \mathbf{L}_{l_1^\theta} \cdot \mathbf{g}, \quad (6.23b)$$

$$\mathbf{U}_{l_2^\theta} = -M_{l_2^\theta} \cdot \nabla P_g + \mathbf{L}_{l_2^\theta} \cdot \mathbf{g}, \quad (6.23c)$$

$$\mathbf{U}_{l_1^{\theta_{\min}}} = -M_{l_1^{\theta_{\min}}} \cdot \nabla P_g + \mathbf{L}_{l_1^{\theta_{\min}}} \cdot \mathbf{g}, \quad (6.23d)$$

$$\mathbf{U}_{l_2^{\theta_{\min}}} = -M_{l_2^{\theta_{\min}}} \cdot \nabla P_g + \mathbf{L}_{l_2^{\theta_{\min}}} \cdot \mathbf{g}. \quad (6.23e)$$

The steps of the algorithm are the same as those described in Section 5.4.2 where it concerned a couple of phases (i, j) . The main difference on the fact that we consider now two or three-dimensional configurations with tensorial effective parameters.

1. Computation of the time step using the same constraints as for two phases, detailed in Eq. 5.46.

2. From the saturation fields $S_{l_1^\theta}(t_n)$, $S_{l_1^{\theta_{\min}}}(t_n)$, $S_{l_2^\theta}(t_n)$ and $S_{l_2^{\theta_{\min}}}(t_n)$, the mass conservation equations are solved sequentially

$$\varepsilon \frac{\partial S_{l_1^\theta}}{\partial t} + \nabla \cdot \mathbf{U}_{l_1^\theta} = \dot{m}_1, \quad (6.24)$$

$$\varepsilon \frac{\partial S_{l_1^{\theta_{\min}}}}{\partial t} + \nabla \cdot \mathbf{U}_{l_1^{\theta_{\min}}} = -\dot{m}_1 + \dot{m}, \quad (6.25)$$

$$\varepsilon \frac{\partial S_{l_2^\theta}}{\partial t} + \nabla \cdot \mathbf{U}_{l_2^\theta} = \dot{m}_2 \quad (6.26)$$

$$\varepsilon \frac{\partial S_{l_2^{\theta_{\min}}}}{\partial t} + \nabla \cdot \mathbf{U}_{l_2^{\theta_{\min}}} = -\dot{m}_2 - \dot{m}, \quad (6.27)$$

in order to obtain $S_{l_1^\theta}(t_{n+1})$, $S_{l_1^{\theta_{\min}}}(t_{n+1})$, $S_{l_2^\theta}(t_{n+1})$ and $S_{l_2^{\theta_{\min}}}(t_{n+1})$ (mass balances written outside of transition regions).

3. The \mathbf{M} and \mathbf{L} coefficients Eqs 6.22 are updated from $S_\alpha(t_{n+1})$, $\alpha = l_1^\theta, l_1^{\theta_{\min}}, l_2^\theta, l_2^{\theta_{\min}}$.
4. The equation on the pressure is solved implicitly to obtain the pressure field $P_g(t_{n+1})$,

$$\nabla \cdot (\Sigma[\mathbf{M}(t_{n+1})] \cdot \nabla P_g) = \nabla \cdot (\Sigma[\mathbf{L}(t_{n+1})] \cdot \mathbf{g}), \quad (6.28)$$

5. Computation of the velocity fields from Eqs 6.23.

6.4 Results

6.4.1 Case 1: two pseudo-liquids in a two-pack column

We propose in this section to study the influence of the liquid exchange \dot{m} between two pseudo-liquids l_1 and l_2 on the distribution of the liquid in the column. The design of the corrugated sheets at the contact points, as well as their density per unit volume, is indeed presumed to play a central role on the distribution and therefore on the process efficiency. Simulations are conducted in a column constituted of two packs, with 9 injection points at the top of the column, as depicted in Fig. 6.6. The permeability of the column is $K_0 = 7 \times 10^{-7} \text{ m}^2$.

The correlations for the relative permeabilities are determined from the analytical solution of the film flow in a capillary tube, i.e. that we consider $k_{r_{l_\alpha}} = S_{l_\alpha}^3$ for the liquid phases, $\alpha = l_1^\theta, l_1^{\theta_{\min}}, l_2^\theta, l_2^{\theta_{\min}}$, and $k_{r_g} = S_g^2$ for the gas phase. The liquid exchange \dot{m} between the two films is controlled by the relation Eq. 6.21, where $\alpha = 0.5$ for the simulations below. This is the coefficient h which is varied in the simulations, from $h = 1 \times 10^{-3} \text{ s}^{-1}$ to $h = 1 \times 10^{-1} \text{ s}^{-1}$. The coefficient h_{trans} (for the side effects) is fixed at a very high value ($h_{\text{trans}} = 100 \text{ s}^{-1}$), such that the liquid distributes equally in l_1 and l_2 in the cells of the regions concerned. The effective angle θ^* is chosen equal to 45° , which is voluntarily high compared to real configurations, to better visualize the impact of the liquid exchange (the corrugation angle θ is therefore supposed high, as $\theta > \theta^*$).

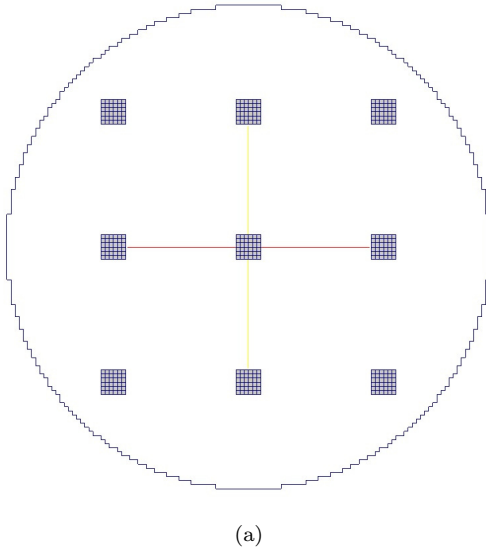


Figure 6.6 – Pictures of the domain: injection points

The distribution of the liquid phase at steady-state is shown in Fig. 6.7. It is seen that a variety of behaviors is obtained, ranging from a regime of liquid branching when the exchange is limited, to a regime of 1D homogeneous bulk flows when the exchange is maximal. These simulations show that the liquid exchange between the two films plays a central role in the global distribution of the liquid phase. In the case $h = 1 \times 10^{-1} \text{ s}^{-1}$ (large exchange), the liquid exchange modifies drastically the flow pattern, while the flow is quasi unaffected in the case $h = 1 \times 10^{-3} \text{ s}^{-1}$ (little exchange).

In packings, this flow regimes might depend on the density of the corrugated sheets, as capillary effects are more prone to retain liquid in a dense packing than in a coarse one. It also probably depend on the density of contact points between the sheets, which affects the flow pattern due to frequent local redistributions. This first analysis, overall, indicates that the model with splitting and liquid exchange is able to capture multiple flow regimes depending of the type of packing.

Further, one can observe that in the first pack the liquid is effectively confined within the corrugated sheets and cannot flow in the transverse direction. It is then redistributed equally between l_1 and l_2 at the transition layer between the two packs.

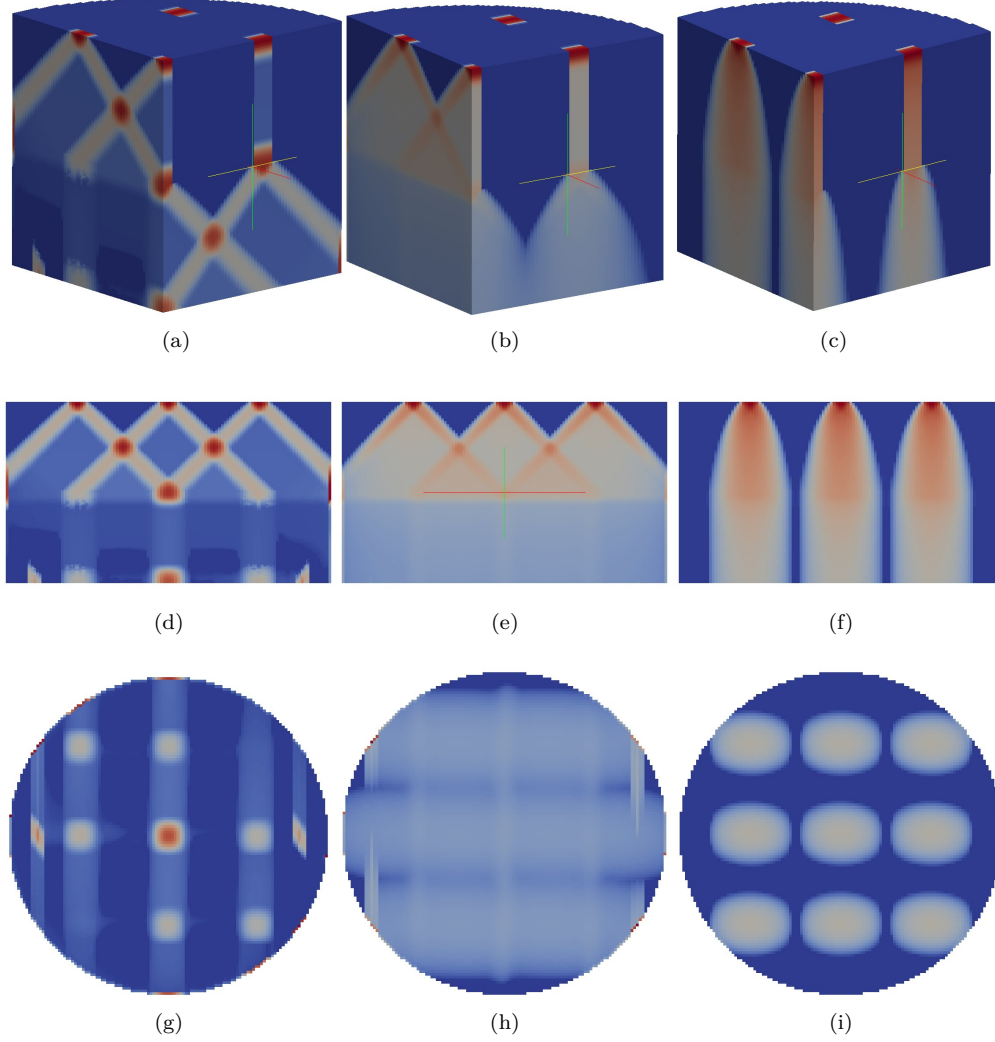


Figure 6.7 – Distribution of the liquid phase within two packs, from 9 injection points. Top line: 3D representation of a quarter of column ; middle line: sectional view ; bottom line: bottom view. From left to right: $h = 1 \times 10^{-3} \text{ s}^{-1}$, $h = 1 \times 10^{-2} \text{ s}^{-1}$, $h = 1 \times 10^{-1} \text{ s}^{-1}$ (magnitude of the liquid exchange at contact points, see Eq. 6.21).

6.4.2 Case 2: two and four liquids models between two sheets

We consider the constant injection of liquid from the top of two parallel corrugated sheets with the idea of comparing the four pseudo-phases and the two pseudo-phases approaches. Similarly to the previous case, the injection is equally balanced between the sheets 1 and 2 at the top of the two parallel sheets (co-injection of l_1 and l_2 at equal flow rates). In case of four pseudo-phases, however, it is difficult to determine the dynamic of the injection. Is the liquid initially guided along the grooves (θ), or does it directly flow downward (θ_{\min})? This issue was already raised when we introduced the question of the liquid redistribution at the transition between two packs. The dynamic is likely to be function of the flow rate (i.e. initial saturations) and of the geometry of the corrugated sheets. Here, it is considered for the most of the simulations that the liquid is initially guided along the grooves inclined at the angle θ , which is most likely to occur for small saturations. We therefore consider the injection of the pseudo-phases l_1^θ and l_2^θ only on the top of the domain, and the pseudo-phases $l_1^{\theta_{\min}}$ and $l_2^{\theta_{\min}}$ result instead of the liquid exchanges \dot{m}_1 and \dot{m}_2 respectively.

The corrugation angle is fixed at $\theta = 45^\circ$ and we consider the case corresponding to

$$\theta_{\min} = 0, \tag{6.29}$$

for the phases $l_1^{\theta_{\min}}$ and $l_2^{\theta_{\min}}$ flowing in a downward direction. This minimal angle is not necessarily equal to zero and can be chosen as the angle corresponding to the steepest direction. We considered here a limit case to better illustrate the model.

Similarly to the previous case, the effective parameters in the momentum balance are determined based on the analytical solution of an annular flow in a tube, and the correlations of the liquid exchanges are based on Eq. 6.14 with $\alpha = 0.5$.

Configuration $\dot{m} = 0$ The distribution of the pseudo-phases is given in Fig. 6.8 for a value of the liquid exchange per sheet $h_1 = h_2 = 1 \times 10^{-2} \text{ s}^{-1}$, and for $\dot{m} = 0$ ($h = 0$), i.e. without considering the liquid exchange between the two plates. This configuration therefore corresponds to the flows on two independent corrugated sheets. l_1^θ (part within the grooves) is seen in Fig 6.8a and $l_1^{\theta_{\min}}$ (flow downward) is seen in Fig. 6.8d. At this stage, we define an effective angle $\pm\theta^*$ which corresponds to the directions of the averaged velocities \mathbf{U}_{l_1} and \mathbf{U}_{l_2} of respectively $l_1 = l_1^\theta \cup l_1^{\theta_{\min}}$ and $l_2 = l_2^\theta \cup l_2^{\theta_{\min}}$ compared to the vertical axis. For the case presented in Fig. 6.8, $h_1 = h_2 = 1 \times 10^{-2} \text{ s}^{-1}$, the effective angle θ^* resulting from the exchanges \dot{m}_1 and \dot{m}_2 is for instance 23° . The variation of this effective angle θ^* with the coefficient $h_1 = h_2$ (intensity of the exchanges) is shown in Fig. 6.9. It varies from $\theta^* = 45^\circ$ in the case of a little exchange to an asymptotic value $\theta^* = 18^\circ$ when the exchange is maximal. This profile of θ^* corresponds to the very specific case where only l_1^θ is injected on the top. One could also consider other entrance conditions for comparison. In Fig. 6.9, we give further information about the distribution of the velocity field \mathbf{U}_{l_1} of $l_1^\theta \cup l_1^{\theta_{\min}}$ (by symmetry the profile for $l_2^\theta \cup l_2^{\theta_{\min}}$ is the same). This corresponds to the probability density function of the angle γ which characterizes the direction of the velocity vector \mathbf{U}_{l_1} compared to the vertical axis. The impact of h_1 on the pdf of the velocity field is especially outlined. It is seen that a quantity of liquid keeps flowing along the direction of the grooves $\gamma = 45^\circ$, except in the case of the strongest exchange where an asymptotic direction is recovered.

How can we employ this two-liquids model per corrugated sheet? From further information from the microscale, the idea would be then to close the system of macroscale equations for a given design of corrugations (height, wavelength, etc). This concern especially the exchange \dot{m}_1 (symmetrically \dot{m}_2), which can be adjusted in order to translate accurately the velocity fields from the microscale. This information from the microscale corresponds to a simulation of the film flow in a pattern of corrugated sheet with periodic conditions. Also, the behavior of the liquid flow has to be precised in order to better characterized the entrance conditions. This could for instance consist in experiments of a ponctual injection of liquid with variable flow rates.

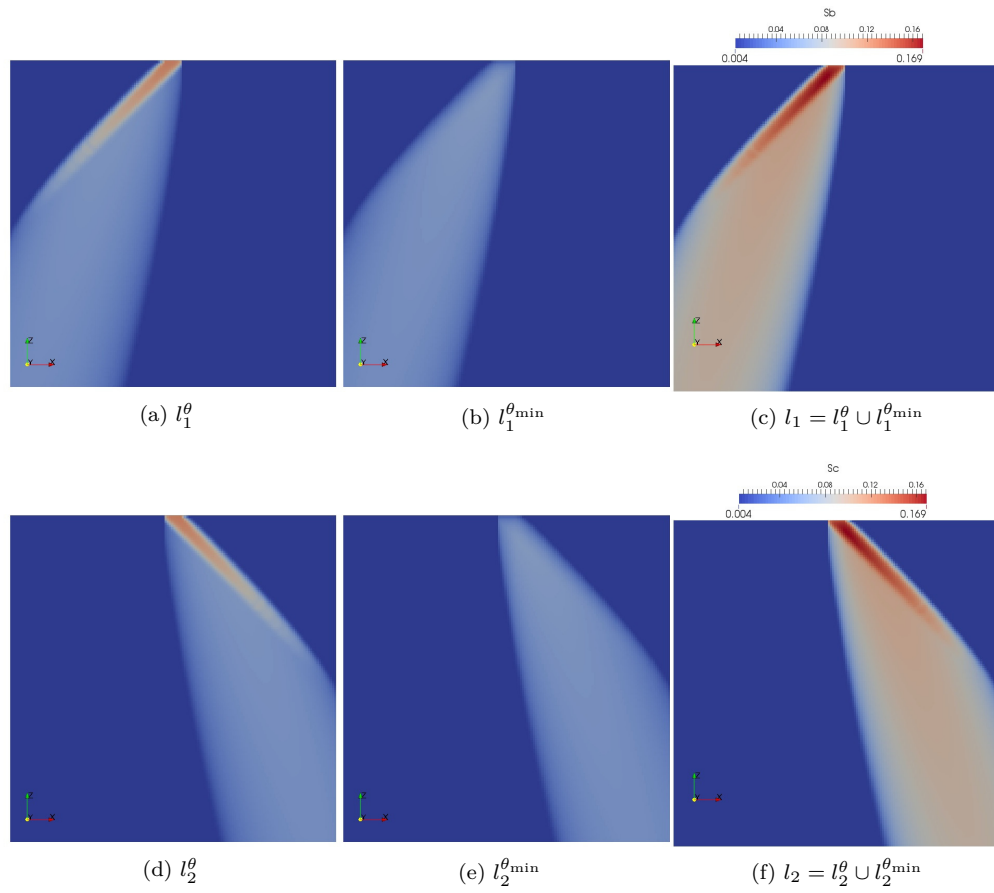


Figure 6.8 – Distribution of the pseudo phases between two corrugated sheets for $h_1 = h_2 = 1 \times 10^{-2} \text{ s}^{-1}$ and $h = 0$ (no exchange at contact points), using the four-equation model.

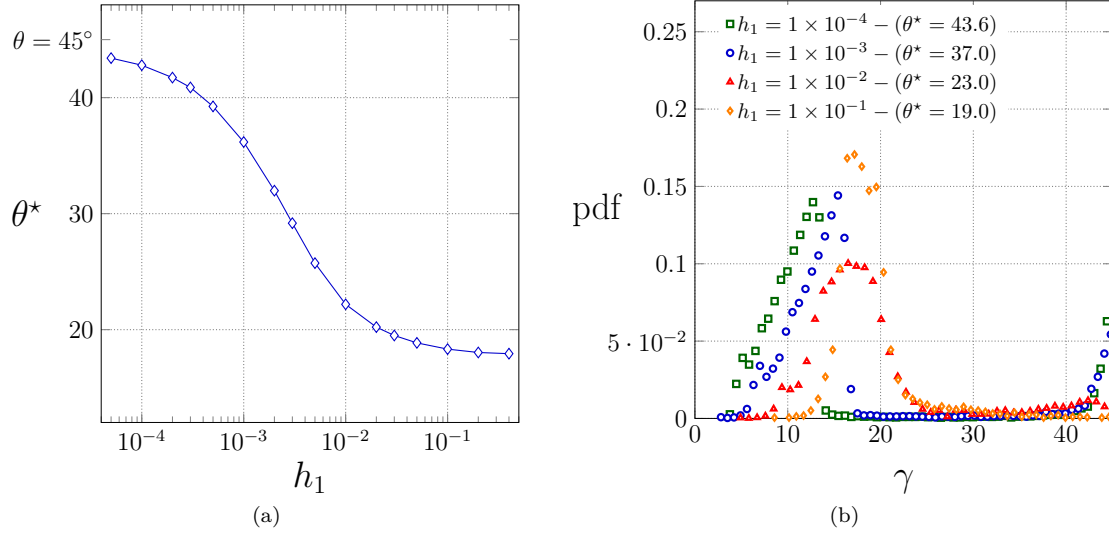


Figure 6.9 – Behavior of the liquid film $l_1 = l_1^\theta \cup l_1^{\theta_{\min}}$ for various values of exchange h_1 between l_1^θ and $l_1^{\theta_{\min}}$ ($h = 0$). a) Effective angle θ^* as a function of h_1 ; b) PDF of the direction of the velocity field \mathbf{U}_{l_1} in l_1 (angle γ compared to the vertical axis), for several values of h_1 . The case $h_1 = 1 \times 10^{-2} \text{ s}^{-1}$ is the one pictured in Fig. 6.8c.

Configuration $\dot{m} \neq 0$ We present now in Fig. 6.10 the configuration including the liquid exchange \dot{m} between the two films l_1 and l_2 , in the case $h_1 = h_2 = 1 \times 10^{-2} \text{ s}^{-1}$ ($\theta^* = 23^\circ$). Two magnitudes of exchange, $h = 1 \times 10^{-4} \text{ s}^{-1}$ and $h = 1 \times 10^{-2} \text{ s}^{-1}$ are shown. It is seen that the exchange \dot{m} between the two plates favors the homogenization of the liquid, which tends to flow as a bulk for high values of exchange, in accordance to what was observed with the two pseudo-phases model. It is also seen that the liquid goes through a certain distance before a steady-state is reached. Such a phenomenon might be observed in the columns due to the constant reorientation of the packs (whose height is about 20 cm).

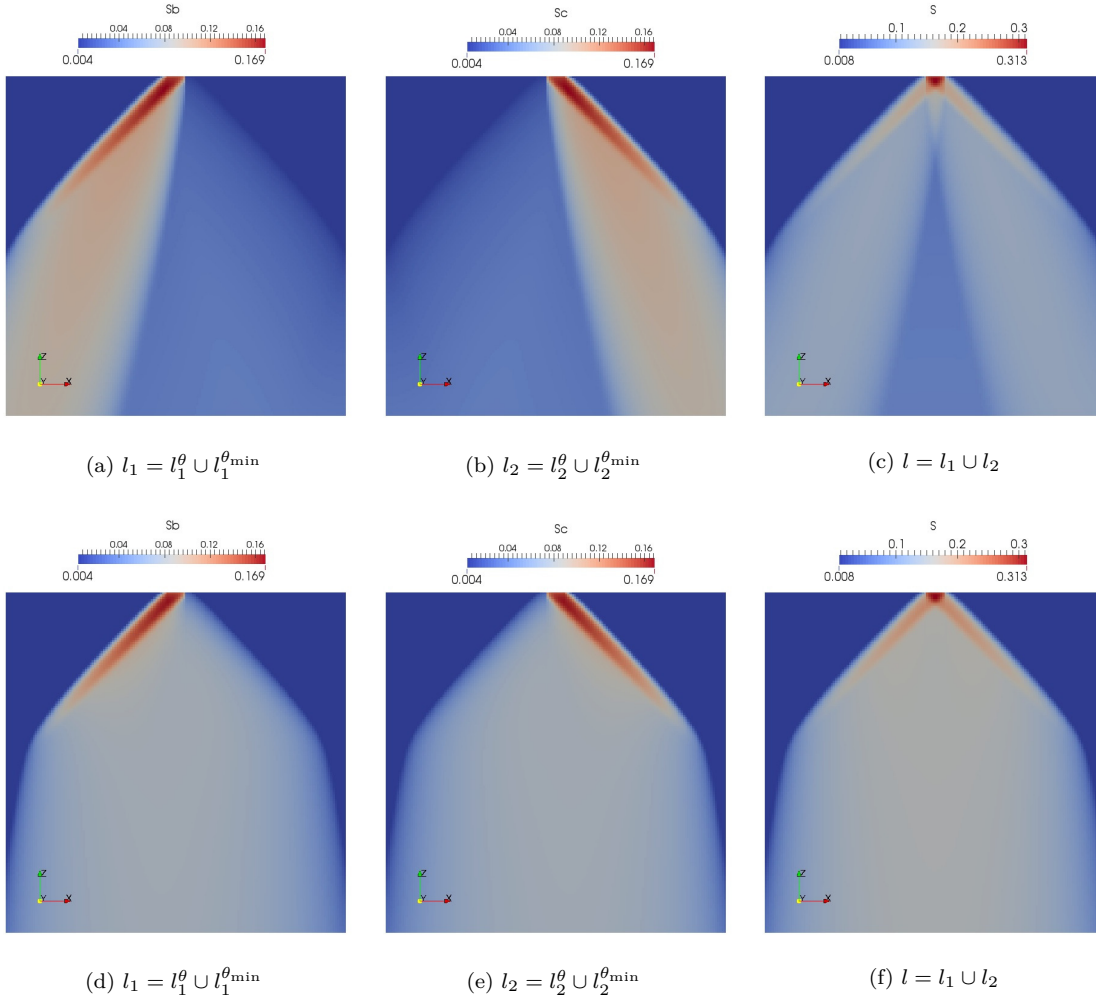


Figure 6.10 – Distribution of the liquid phase between two corrugated sheets for two values of h , using the four-equation model - Top: $h = 1 \times 10^{-4} \text{ s}^{-1}$, bottom: $h = 1 \times 10^{-2} \text{ s}^{-1}$. For all simulations: $h_{l_1} = h_{l_2} = 1 \times 10^{-2} \text{ s}^{-1}$.

Comparison of the two-liquids and four-liquids models In order to compare the two approaches involving two and four pseudo-phases, we consider on one hand a fixed effective angle $\theta^* = 23^\circ$ for the two liquids approach, and on the other hand the exchanges \dot{m}_1 and \dot{m}_2 which lead to $\theta^* = 23^\circ$ ($h_1 = h_2 = 1 \times 10^{-2} \text{ s}^{-1}$, see Fig. 6.8) for the four liquids approach. The two approaches are compared in Fig. 6.11 for the same values of h , i.e. for the same intensity of exchange between the two plates. It is seen that very distinct flow behaviors are obtained, as the two liquids approach constrain the liquid in a cone delimited by $\pm\theta^*$. The resulting effective angle θ_{eff}^* is also given in Fig. 6.12 as a function of the exchange. For high values of h , it is seen that the model with two liquids tends toward a single bulk flow that goes downward in the column ($\theta_{\text{eff}}^* \rightarrow 0$), while the four liquids model converge toward an asymptotic value. These flow behaviors are further analyzed in Fig. 6.13 based on the pdf of the direction of \mathbf{U}_{l_1} in the two cases. One sees that the two-liquid model is characterized by well segregated behaviors depending on h (quasi-vertical for high h or oriented at $\theta^* = 23^\circ$ for small h), while the four liquids approach leads to a more disperse flow pattern for the different values of h .

In the same way as said above, the complementary step of this work consists in obtaining information from the microscale in order to derive a more effective correlation for the exchange \dot{m} . This step is challenging as gas-liquid flow simulations at the scale of a contact point between two corrugated sheets cannot be implemented easily.

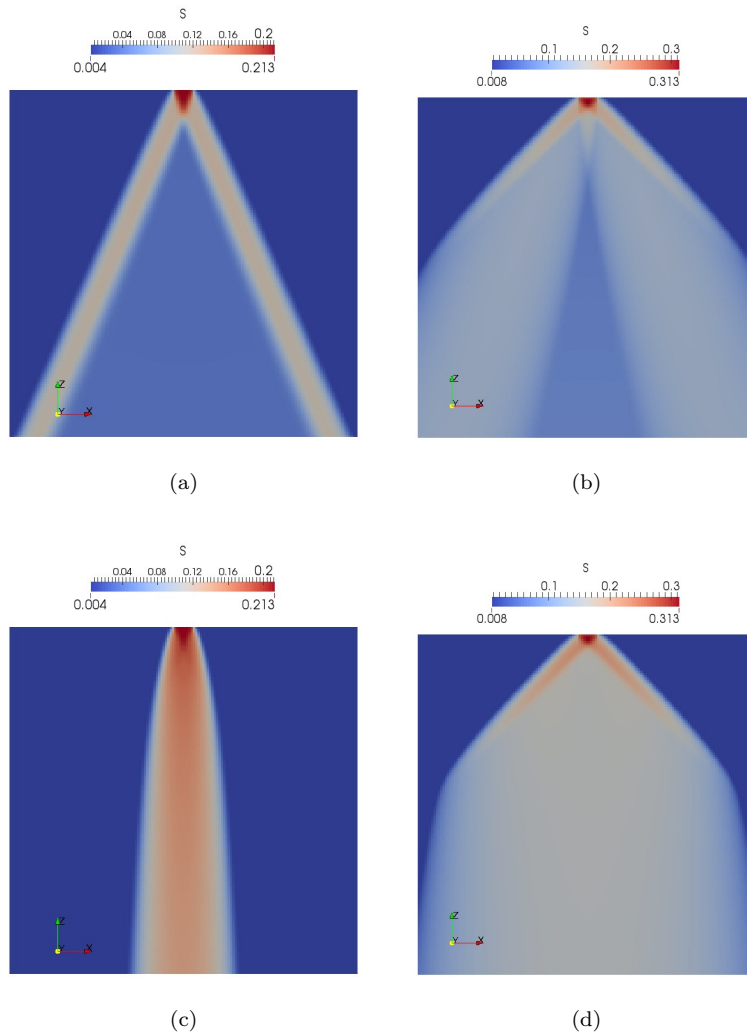


Figure 6.11 – Distribution of the liquid phase between two corrugated sheets using the two modeling approaches. Left: two-liquid approach ; right: four-liquid approach. Top: $h = 1 \times 10^{-4} \text{ s}^{-1}$, bottom: $h = 1 \times 10^{-2} \text{ s}^{-1}$. For the model with four liquids, $h_1 = h_2 = 1 \times 10^{-2} \text{ s}^{-1}$.

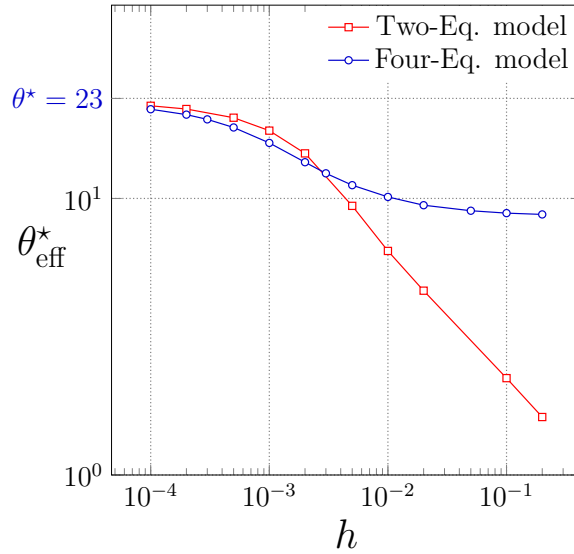


Figure 6.12 – Effective angle θ^* as a function of h using the two-equation and the four-equation model. The case $\hat{m} = 0$ is such that $\theta^* = 23^\circ$.

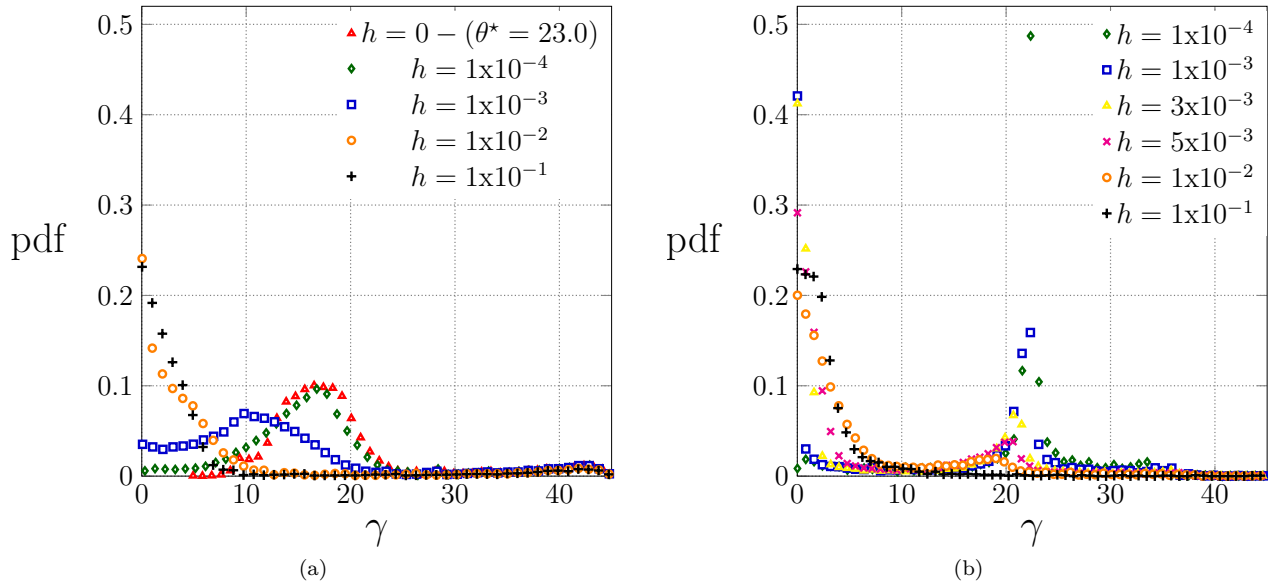


Figure 6.13 – PDF of the macroscopic directions of the velocity fields in l for different values of h (s^{-1}). a) Two pseudo-liquids model ; b) Four pseudo-liquids.

How to complete this model? The main idea of this study, overall, was to show that the models presented here provide a high level of flexibility to characterize the liquid distribution within the structure. The difficulty to directly apply it, however, arises from the absence of closure for the effective parameters in the model. This clearly deserves further studies, given the phenomenological potential of the model. The main parameters of this model are the effective angles θ and θ_{\min} and the terms characterizing the liquid

exchanges (\dot{m} terms). We think that either numerical studies of the liquid film over one corrugated sheet or experiments of a liquid injection over one sheet could provide substantial elements for the model. In case of simulations, for instance over a unit-cell with periodic conditions, the pdf of the velocity fields can be directly analyzed to identify the presence of preferential paths. The model can therefore be directly calibrated based on simulations. In the same spirit, a simple experiment could consist in analyzing the structure of the global distribution of the film along one corrugated sheet as a function of the flow rate. Information about the entrance conditions of a pack would also be accessible through experiments. One issue remains about the exchange of liquid at the contact points, since both numerical and experimental studies are today challenging. The experimental study of the flow distribution between two corrugated sheets, for multiple flow rates and for different types of packings (density, numbers of contact points), could provide relevant information as a first step, for instance by comparing to the results obtained numerically with the ones of the model.

Chapter 7

Conclusion and perspectives

The objective of this work was to improve the modeling of the distillation process in columns equipped with structured packings. Only momentum transport was considered in this work, which constitutes the primary step before further developments for the transport of the chemical species. We summarize below the main results and we indicate future orientations, either in the perspective of studying theoretical questions generic to porous media physics, or for the distillation process.

Starting from the observation that a resolution of the counter-current gas-liquid flow in packings is today out of reach, the first idea was to represent the liquid film as an effective boundary condition for the flow of the gas phase. This approach is reminiscent of the use of effective boundary conditions in porous media modeling, as soon as complex surface effects prevent the direct numerical resolution. This method is used to assess the impact of a train of soliton-like waves at the surface of the liquid film, which is seen as a surface roughness. It can further be applied to manufactured packings with surface roughnesses. The approach mainly allows to simplify the analysis to a simpler pore-scale problem than the initial problem for the two-phase system. It is however limited to the pre-loading regime, since the roughness must be included in the viscous boundary layer in order for the effective condition to hold. This encourages to work on further developments to go beyond the assumptions made here. Numerical developments are also required to better estimate the accuracy of the Navier condition on a curved interface using a finite volume method.

Given the effective condition, the macroscale system obtained using the volume averaging method consists in a generalized Darcy model (also called a generalized Darcy-Forchheimer law) which allows to predict the pressure drop based on the resolution of a closure problem at pore-scale. This method gives a rapid access to the pressure drop, but it is restricted to moderate flow rates, when the gas-liquid interaction remains limited. For higher flow rates, experimental works indicate a phenomenon of liquid retention, as well as a higher impact on the pressure drop. This led us to consider a new modeling approach where both phases are modeled and where the interaction between the liquid and the gas phase is explicitly accounted for.

In a second part, we considered more generally the question of the modeling of two-phase flows in highly permeable media. These flows are characterized by high values of the usual dimensionless numbers characterizing two-phase systems. The models employed so far in engineering practice rely globally on heuristic considerations, which constrains significantly their applicability. We started from the pore-scale problem and discussed the volume averaging method in this specific case. A model can be derived theoretically under the assumption of a quasi-static flow, meaning a system somehow governed by capillary effects. This model is interesting as it accounts explicitly for additional momentum exchange at the continuum scale. We further showed that the structure of the model still holds for the case of two-phase flows in highly permeable media, although a rigorous closure cannot be derived. This model was compared to the modeling strategies usually

used in chemical practice. It was shown to be in good agreement when comparing to experimental data, and closure relationships were specially derived for the counter-current flow in structured packings.

Finally, the impact of the anisotropy of the structure on the flow was considered. The liquid phase is specially known to be significantly affected by the structure in parallel corrugated sheets. An approach involving the separation of the liquid phase in four pseudo-liquid phases was suggested. In this approach, a part of the liquid is confined in the grooves of the corrugations (respectively oriented in two opposite directions), and an other part flows downward. This approach is shown to offer a high level of flexibility to capture the different flow paths followed by the liquid phase in the structure. The different effective parameters of the system, however, require to proceed to further numerical or experimental work at the local scale to better close the problem. The liquid exchange between the different pseudo-phases, for instance, significantly affect the structure of the flow. In this part, also, the column was not considered as a single homogenous medium, but the rotation of the packs and the effects of the internal boundaries (at the transition between packs, at the external walls) were accounted for. Further works also concern a better understanding of the mechanisms of redistribution at the external walls. These effects might be of importance for columns with small diameters.

Future research work on the modeling of the distillation columns can distinguished in multiple parts. On one hand, an extensive work is required to obtain further information from the system at the microscale. The resolution of the counter-current gas-liquid in structured packings is today out of reach, but this constitutes a final objective. As a first step, simulations of a liquid over one corrugated plate would contribute to the model derived in the Chapter 6 . One can also proceed to simulations on simplified geometries in order to better characterize the distribution of a two-phase flow in a bi-structured medium. On the other hand, one could proceed to large scale experiments in order to obtain global information on the distribution. Varying the liquid flow rate on the top of a corrugated sheet (experiment from Mahr and Mewes) would probably change considerably the liquid distribution. The combinaison of simulations and experiments of the liquid film would, undoubtedly,

Conclusion en français Ce travail s'inscrit dans la continuité de travaux antérieurs sur la modélisation des procédés de séparation en colonne à garnissage structuré. La modélisation est basée sur la méthode de la prise de moyenne volumique, qui consiste à établir un modèle par moyenne spatiale du problème aux limites du procédé à la petite échelle. Le manuscrit est divisé en plusieurs parties qui sont rappelées ci-dessous, et on discute des perspectives à la suite de ce travail.

La première méthode de modélisation a consisté en une approche monophasique, où seul l'écoulement de la phase gaz est considéré. Le modèle mis en place consiste principalement à tenir compte de la présence de rugosités de surface dans le processus de changement d'échelle. A faibles débits, la phase liquide s'écoule en effet sous la forme d'un film de faible épaisseur caractérisé par des instabilités de surface. Dans bons nombres de cas, aussi, la structure de garnissage est elle-même rugueuse. Le modèle permet d'estimer la perte de charge au sein de la colonne par le biais de la résolution d'un problème de fermeture à l'échelle d'une cellule représentative de la colonne. On a notamment montré qu'une condition effective permet de caractériser l'effet des rugosités de surface sur l'écoulement. Plus généralement, la condition effective inclue un coefficient tensoriel qui permet de caractériser un effet d'anisotropie, et peut être utilisée plus largement pour d'autres problèmes incluant des rugosités de surface. Pour ce qui est de la distillation en colonne à garnissage, la méthode est limitée aux faibles débits liquide et gaz, pour lesquels la rugosité de surface reste confinée dans une couche limite laminaire de l'écoulement. Une extension de ce travail est donc de développer une condition limite effective pour des débits plus élevés. Par ailleurs, l'implémentation numérique d'une condition limite de type Navier est vérifiée dans ce travail pour les faibles courbures. Une étude numérique est nécessaire pour valider ce type de conditions pour des courbures plus fortes.

En deuxième partie, on a considéré des approches de modélisation multiphasiques. Le travail est séparé en deux temps. D'une part (chapitres 4 et 5), on s'intéresse aux approches de modélisation permettant de caractériser les effets de cisaillement très forts pour les hauts débits. D'autre part (chapitre 6), on considère l'impact de la forte anisotropie de la structure sur les écoulements des deux phases.

Dans un premier temps, on a considéré de manière générale les écoulements diphasiques dans milieux très perméables, qui favorisent les larges surfaces d'échange entre phases. Le problème de changement d'échelle par prise de moyenne volumique est discuté. Il est vu notamment que dans le cas où les effets dynamiques sont forts, ce qui est le cas pour les écoulements en milieu très perméable, une fermeture du problème est difficile à établir. Le modèle obtenu dans l'hypothèse inverse (interface quasi-statique, faibles effets inertiels, gravitaire), même s'il est a priori limité, présente l'intérêt de caractériser explicitement l'échange de quantité de mouvement à l'interface fluide/fluide. On effectue l'analyse de cet échange de quantité de mouvement en utilisant la méthode de Buckley-Leverett (régime visqueux) et de manière numérique (régime inertiel). Dans le cas haut Reynolds, on montre notamment que le même type de fermeture ne peut être établi que dans le cas où les effets capillaires prédominent. Cette observation valide la structure du modèle dans le cas haut Reynolds, même si la présence d'effets instationnaires dans ce cas complexifie l'établissement d'un problème de fermeture. On montre par ailleurs que ce type de modèle est adapté à l'écoulement contre-courant du procédé de distillation en établissant des relations de fermeture pour les paramètres effectifs du modèle. Ces fermetures sont établies à partir de données expérimentales à grande échelle. Plusieurs travaux peuvent être envisagés à la suite de ce travail. Pour le cas stationnaire, la résolution des problèmes de fermeture à l'échelle du pore permettrait d'obtenir des indications fiables sur les dépendances des différents paramètres effectifs. A plus haut Reynolds, un travail théorique est nécessaire pour mieux caractériser le système à grande échelle, et des simulations à l'échelle du pore permettraient aussi de mieux comprendre les phénomènes en jeu (moyenne en temps, ergodicité, etc).

En dernière partie, on a considéré les effets liés à l'anisotropie de la structure. Une approche de modéli-

sation impliquant la séparation de la phase liquide en quatre “pseudo-phases” est étudiée. Cette méthode permet de représenter les chemins préférentiels suivis par un film liquide lorsqu’il est confiné entre deux plaques corruguées. On montre que cette approche offre une très grande flexibilité pour modéliser la distribution du liquide dans la structure. La fermeture des différents paramètres du système pour un type de garnissage donné, et notamment les échanges de masse entre les différentes phases, nécessite davantage d’informations sur l’écoulement à petite échelle, soit par visualisation expérimentale, soit par résolution numérique. Dans cette partie, on prend aussi en compte les effets liés à la rotation des packs sur l’écoulement et la redistribution du liquide à l’interface entre packs et aux bords extérieurs de la colonne. Une étude de la redistribution de la phase liquide aux bords extérieurs de la colonne constituerait enfin un travail intéressant, notamment pour les colonnes de faible diamètre.

Appendix A

Appendix - Chapter 3

A.1 Spatial averaging

In this section, the system of equations Eqs 3.23 is volume averaged using the definitions introduced in Section 3.4.1. We detail only the main steps of the developments, the reader is referred to the works of [102] and [186] for further details or to other works (see e.g. [139, 138, 137]).

We use the following spatial averaging theorem [80] for the permutation between volume averaging and spatial differentiation

$$\langle \nabla \psi_i \rangle = \nabla \langle \psi_i \rangle + \frac{1}{|\mathcal{V}|} \int_{\mathcal{V} \cap \Gamma} \mathbf{n} \psi_i d\mathbf{r}, \quad (\text{A.1})$$

and similar for the divergence. The porosity of the medium is also considered as constant, so that

$$\nabla \phi_s = -\frac{1}{|\mathcal{V}|} \int_{\mathcal{V} \cap \Gamma} \mathbf{n} d\mathbf{r} = 0. \quad (\text{A.2})$$

The application of the volume averaging theorem, Eq. A.1, to the continuity equation yields

$$\nabla \cdot \langle \mathbf{u}_s \rangle + \frac{1}{|\mathcal{V}|} \int_{\mathcal{V} \cap \Gamma_{ws}} \mathbf{n} \cdot \mathbf{u}_s d\mathbf{r} = 0. \quad (\text{A.3})$$

The effective condition, Eq. 3.10, implies that the velocity on the boundary Γ_{ws} is tangential, so that the integral term vanishes and the averaged continuity equations reads

$$\nabla \cdot \langle \mathbf{u}_s \rangle = 0. \quad (\text{A.4})$$

The momentum equation, Eq. 3.23b, may be written as

$$\underbrace{\rho_\gamma \left[\frac{\partial \mathbf{u}_s}{\partial t} + \nabla \cdot (\mathbf{u}_s \mathbf{u}_s) \right]}_{\text{LHS}} = \underbrace{-\nabla p_s + \nabla \cdot \left[\mu_\gamma \left(\nabla \mathbf{u}_s + (\nabla \mathbf{u}_s)^T \right) \right]}_{\text{RHS}} + \rho_\gamma \mathbf{g} \text{ in } \Omega_s, \quad (\text{A.5})$$

which is decomposed, for clarity, into a left and a right hand side, LHS and RHS respectively. Averaging the LHS leads to

$$\langle \text{LHS} \rangle = \rho_\gamma \frac{\partial \langle \mathbf{u}_s \rangle}{\partial t} + \rho_\gamma \nabla \cdot \langle \mathbf{u}_s \mathbf{u}_s \rangle + \frac{1}{|\mathcal{V}|} \int_{\mathcal{V} \cap \Gamma_{ws}} \mathbf{n} \cdot (\mathbf{u}_s \mathbf{u}_s) d\mathbf{r}. \quad (\text{A.6})$$

The slip condition on Γ_{ws} implies that $\frac{1}{|\mathcal{V}|} \int_{\mathcal{V} \cap \Gamma_{ws}} \mathbf{n} \cdot (\mathbf{u}_s \mathbf{u}_s) d\mathbf{r} = 0$. Using the relation between intrinsic and superficial averages Eq. 4.48a and the decomposition into average plus perturbation Eq. 3.19, this leads to

$$\langle \text{LHS} \rangle = \rho_\gamma \phi_s \frac{\partial \langle \mathbf{u}_s \rangle^s}{\partial t} + \rho_\gamma \nabla \cdot (\phi_s \langle \mathbf{u}_s \rangle^s \langle \mathbf{u}_s \rangle^s) + \rho_\gamma \nabla \cdot (\tilde{\mathbf{u}}_s \tilde{\mathbf{u}}_s), \quad (\text{A.7})$$

or

$$\langle \text{LHS} \rangle = \rho_\gamma \phi_s \frac{\partial \langle \mathbf{u}_s \rangle^s}{\partial t} + \rho_\gamma \phi_s \langle \mathbf{u}_s \rangle^s \cdot \nabla \langle \mathbf{u}_s \rangle^s + \rho_\gamma \nabla \cdot (\tilde{\mathbf{u}}_s \tilde{\mathbf{u}}_s), \quad (\text{A.8})$$

using the averaged mass conservation equation Eq. A.4.

Averaging the RHS of Eq. 3.23b yields

$$\begin{aligned} \langle \text{RHS} \rangle &= -\nabla \langle p_s \rangle + \mu_\gamma \nabla^2 \langle \mathbf{u}_s \rangle + \nabla \cdot \left(\frac{1}{|\mathcal{V}|} \int_{\mathcal{V} \cap \Gamma_{ws}} \mathbf{n} \mathbf{u}_s d\mathbf{r} \right) \\ &+ \frac{1}{|\mathcal{V}|} \int_{\mathcal{V} \cap \Gamma_{ws}} \mathbf{n} \cdot \left[-p_s \mathbf{I} + \mu_\gamma \left(\nabla \mathbf{u}_s + (\nabla \mathbf{u}_s)^T \right) \right] d\mathbf{r} + \rho_\gamma \mathbf{g}. \end{aligned} \quad (\text{A.9})$$

Contrary to developments for a no-slip condition, the term $\nabla \cdot \left(\frac{1}{|\mathcal{V}|} \int_{\mathcal{V} \cap \Gamma_{ws}} \mathbf{n} \mathbf{u}_s d\mathbf{r} \right)$ cannot, strictly speaking, be eliminated (this issue was also studied in the work of Lasseux in [102]). An order of magnitude estimation of this term compared to others in the equation leads to

$$\nabla \cdot \left(\frac{1}{|\mathcal{V}|} \int_{\mathcal{V} \cap \Gamma_{ws}} \mathbf{n} \mathbf{u}_s d\mathbf{r} \right) \sim O \left(\frac{\|\nabla \mathbf{u}_s\|}{L} \right) \ll \left(\frac{\|\nabla \mathbf{u}_s\|}{l} \right), \quad (\text{A.10})$$

We therefore neglect this term.

Using the spatial decomposition Eq. 3.19, we have

$$\begin{aligned} \langle \text{RHS} \rangle &= -\phi_s \nabla \langle p_s \rangle^s + \mu_\gamma \phi_s \nabla^2 \langle \mathbf{u}_s \rangle^s + \\ &\frac{1}{|\mathcal{V}|} \int_{\mathcal{V} \cap \Gamma_{ws}} \mathbf{n} \cdot \left[-\tilde{p}_s \mathbf{I} + \mu_\gamma \left(\nabla \tilde{\mathbf{u}}_s + (\nabla \tilde{\mathbf{u}}_s)^T \right) \right] d\mathbf{r} + \rho_\gamma \mathbf{g}. \end{aligned} \quad (\text{A.11})$$

Combining expressions for the LHS and RHS, we finally obtain

$$\begin{aligned} \rho_\gamma \frac{\partial \langle \mathbf{u}_s \rangle^s}{\partial t} + \rho_\gamma \langle \mathbf{u}_s \rangle^s \cdot \nabla \langle \mathbf{u}_s \rangle^s + \rho_\gamma \phi_s^{-1} \nabla \cdot (\tilde{\mathbf{u}}_s \tilde{\mathbf{u}}_s) &= -\nabla \langle p_s \rangle^s + \\ \mu_\gamma \nabla^2 \langle \mathbf{u}_s \rangle^s + \frac{1}{|\mathcal{V}_s|} \int_{\mathcal{V} \cap \Gamma_{ws}} \mathbf{n} \cdot \left[-\tilde{p}_s \mathbf{I} + \mu_\gamma \left(\nabla \tilde{\mathbf{u}}_s + (\nabla \tilde{\mathbf{u}}_s)^T \right) \right] d\mathbf{r} &+ \rho_\gamma \mathbf{g}. \end{aligned} \quad (\text{A.12})$$

As referred in [188, 163, 102], the terms in the LHS of Eq. A.12 as well as the diffusion term can be neglected compared to other terms, leading to

$$0 = -\nabla \langle p_s \rangle^s + \rho_\gamma \mathbf{g} + \frac{1}{|\mathcal{V}_s|} \int_{\mathcal{V} \cap \Gamma_{ws}} \mathbf{n} \cdot \left[-\tilde{p}_s \mathbf{I} + \mu_\gamma \left(\nabla \tilde{\mathbf{u}}_s + (\nabla \tilde{\mathbf{u}}_s)^T \right) \right] d\mathbf{r}. \quad (\text{A.13})$$

A.1.1 Mathematical problem governing the deviations

The averaged form of the continuity equation Eq. A.4 is subtracted from Eq. 3.23a to obtain

$$\nabla \cdot \tilde{\mathbf{u}}_s = 0. \quad (\text{A.14})$$

Using the same approach, we can subtract the averaged momentum equation Eq. A.12 from the pore-scale relation Eq. 3.23b. Along with the assumption of time-scale and length-scale separation, this yields

$$\begin{aligned} \rho_\gamma \left(\frac{\partial \tilde{\mathbf{u}}_s}{\partial t} + \mathbf{u}_s \cdot \nabla \tilde{\mathbf{u}}_s \right) &= -\nabla \tilde{p}_s + \mu_\gamma \nabla^2 \tilde{\mathbf{u}}_s \\ -\frac{1}{|\mathcal{V}_s|} \int_{\mathcal{V} \cap \Gamma_{ws}} \mathbf{n} \cdot \left[-\tilde{p}_s \mathbf{I} + \mu_\gamma \left(\nabla \tilde{\mathbf{u}}_s + (\nabla \tilde{\mathbf{u}}_s)^T \right) \right] d\mathbf{r}. \end{aligned} \quad (\text{A.15})$$

Using the perturbation decomposition, the Navier condition Eq. 3.10 is also written

$$\tilde{\mathbf{u}}_s + \mathbf{M} \cdot \left[\mathbf{n} \cdot \left(\nabla \tilde{\mathbf{u}}_s + (\nabla \tilde{\mathbf{u}}_s)^T \right) \cdot (\mathbf{I} - \mathbf{nn}) \right] = -\langle \mathbf{u}_s \rangle^s \quad \text{on } \Gamma_{ws}. \quad (\text{A.16})$$

As indicated in Eq. 4.77, the average of the deviations over the fluid domain is zero, [186],

$$\langle \tilde{p}_s \rangle^s = 0; \quad \langle \tilde{\mathbf{u}}_s \rangle^s = 0. \quad (\text{A.17})$$

A.1.2 Closure problem

Identifying inhomogeneous source terms in the equations above, we can now formulate an approximate form for the perturbations. In this case, the only source term is the averaged velocity $\langle \mathbf{u}_s \rangle^s$ in Eq. A.16, so that the perturbations can be mapped linearly to $\langle \mathbf{u}_s \rangle^s$ as

$$\tilde{\mathbf{u}}_s = \mathbf{B}_s \cdot \langle \mathbf{u}_s \rangle^s, \quad (\text{A.18})$$

$$\tilde{p}_s = \mu_\gamma \mathbf{b}_s \cdot \langle \mathbf{u}_s \rangle^s, \quad (\text{A.19})$$

where the closure variables ($\mathbf{b}_s, \mathbf{B}_s$) are first- and second-order tensors, respectively. By substituting Eqs A.18 and A.19 into Eqs A.14 to A.16 and assuming that Eqs A.18 and A.19 hold correct for any value of $\langle \mathbf{u}_s \rangle^s$, we obtain

$$\nabla \cdot \mathbf{B}_s = 0 \text{ in } \Omega_s, \quad (\text{A.20a})$$

$$\rho_\gamma \mathbf{u}_s \cdot \nabla \mathbf{B}_s = -\nabla \mathbf{b}_s + \nabla^2 \mathbf{B}_s - \frac{1}{|\mathcal{V}_s|} \int_{\mathcal{V} \cap \Gamma_{ws}} \mathbf{n} \cdot \left[-\mathbf{b}_s \mathbf{I} + \left(\nabla \mathbf{B}_s + (\nabla \mathbf{B}_s)^T \right) \right] d\mathbf{r},$$

$$\mathbf{B}_s + \mathbf{M} \cdot \left[\mathbf{n} \cdot \left(\nabla \mathbf{B}_s + (\nabla \mathbf{B}_s)^T \right) \cdot (\mathbf{I} - \mathbf{nn}) \right] = -\mathbf{I} \quad \text{on } \Gamma_{ws}, \quad (\text{A.20b})$$

$$\langle \mathbf{B}_s \rangle^s = 0, \quad (\text{A.20c})$$

$$\mathbf{B}_s(\mathbf{r} + \mathbf{l}_i) = \mathbf{B}_s(\mathbf{r}) \quad i = 1, 2, 3, \quad (\text{A.20d})$$

$$\mathbf{b}_s(\mathbf{r} + \mathbf{l}_i) = \mathbf{b}_s(\mathbf{r}) \quad i = 1, 2, 3, \quad (\text{A.20e})$$

where we have added the standard periodic condition for closure. This problem is integro-differential which can complicate numerical resolution. To simplify computations, we use the following change of variables (see also [189] and [163]) for \mathbf{b}_s and \mathbf{B}_s ,

$$\mathbf{B}_s^0 = (\mathbf{B}_s + \mathbf{I}) \cdot \mathbf{K}_s^* \phi_s^{-1}, \quad (\text{A.21})$$

$$\mathbf{b}_s^0 = \mathbf{b}_s \cdot \mathbf{K}_s^* \phi_s^{-1}, \quad (\text{A.22})$$

where \mathbf{K}_s^* is defined such as

$$\mathbf{K}_s^{*-1} \phi_s = -\frac{1}{|\mathcal{V}_s|} \int_{\mathcal{V} \cap \Gamma_{ws}} \mathbf{n} \cdot \left[-\mathbf{b}_s \mathbf{I} + \left(\nabla \mathbf{B}_s + (\nabla \mathbf{B}_s)^T \right) \right] d\mathbf{r}. \quad (\text{A.23})$$

Injecting Eq. A.21 and Eq. A.22 into the system of equations Eqs A.20 leads to

$$\nabla \cdot \mathbf{B}_s^0 = 0 \text{ in } \Omega_s, \quad (\text{A.24a})$$

$$\frac{\rho_\gamma}{\mu_\gamma} \mathbf{u}_s \cdot \nabla \mathbf{B}_s^0 = -\nabla \mathbf{b}_s^0 + \nabla^2 \mathbf{B}_s^0 + \mathbf{I} \text{ in } \Omega_s, \quad (\text{A.24b})$$

$$\mathbf{B}_s^0 + \mathbf{M} \cdot \mathbf{n} \cdot \left(\nabla \mathbf{B}_s^0 + (\nabla \mathbf{B}_s^0)^T \right) \cdot (\mathbf{I} - \mathbf{nn}) = 0 \text{ on } \Gamma_{ws}, \quad (\text{A.24c})$$

$$\langle \mathbf{B}_s^0 \rangle^s = \mathbf{K}_s^* \phi_s^{-1}, \quad (\text{A.24d})$$

$$\mathbf{B}_s^0(\mathbf{r} + \mathbf{l}_i) = \mathbf{B}_s^0(\mathbf{r}) \quad i = 1, 2 \quad (\text{A.24e})$$

$$\mathbf{b}_s^0(\mathbf{r} + \mathbf{l}_i) = \mathbf{b}_s^0(\mathbf{r}) \quad i = 1, 2. \quad (\text{A.24f})$$

This is a Navier-Stokes problem with the effective condition Eq. A.24c that can be solved using standard numerical methods. The components of the tensor \mathbf{K}_s^* are obtained by considering a source term along the different directions of space in the closure problem. Similarly to the work in [163], the problem still involves the micro-scale velocity field \mathbf{u}_s that solves the set Eqs 3.23 in the slip domain Ω_s .

A.2 Visualisation of the grids

We show in Fig A.1 the grids of the exact and effective domains Ω_γ and Ω_s , both for the 2D cylinder and the geometry a of structured packings.

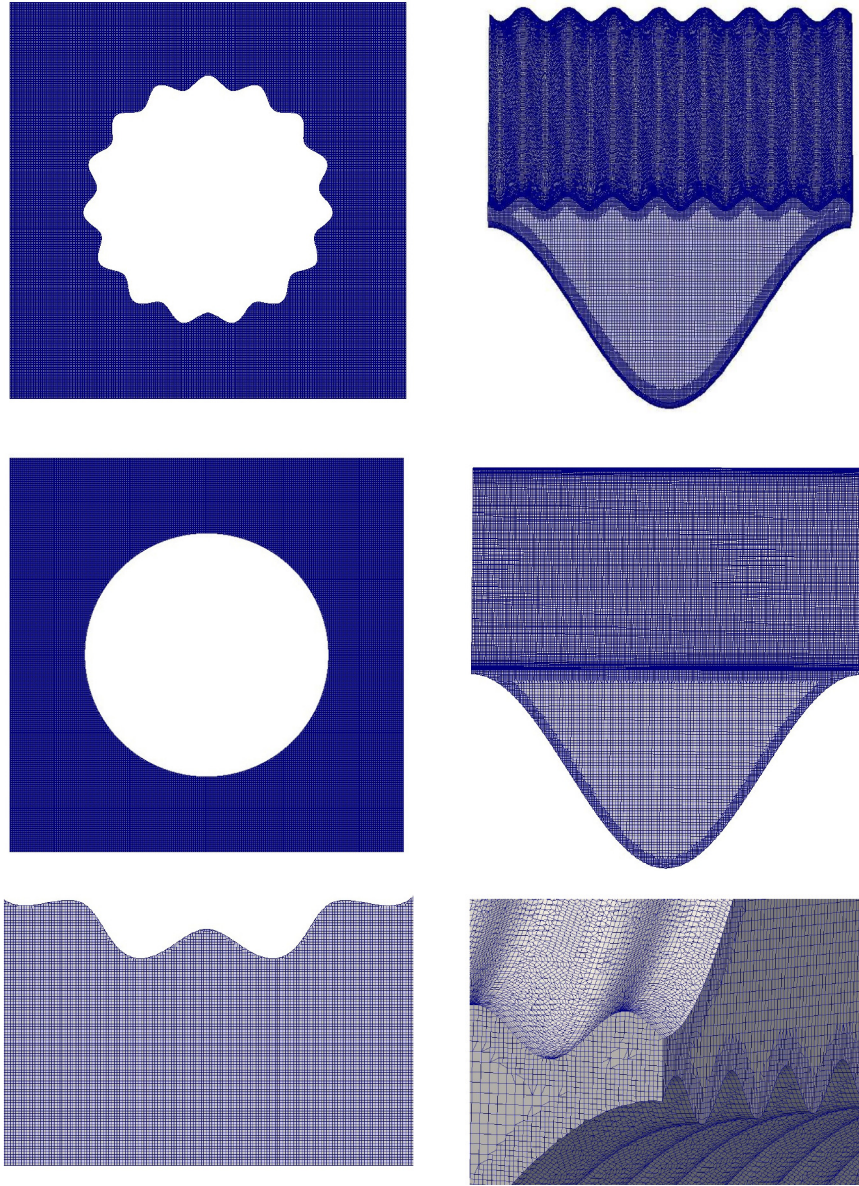


Figure A.1 – Meshes for the unit-cell of the array of beads (left) and for the element of packings (right). Domains Ω_γ and Ω_s are given. The element of packings corresponds to the geometry a .

Appendix B

Appendix - Chapter 4

B.1 Closure problems: two-phase flows

The closure problems derived in Chapter 4 are given in the following. These problems must be solved over a representative unit-cell of the system with periodic conditions. The expressions of the effective parameters can be computed based on the integrals Eqs . The velocity fields \mathbf{u}_i and \mathbf{u}_j of the phases i and j at the microscale are involved, meaning that the initial resolution of the flow over the representative unit-cell is required in order for the computation of the closure problems. Also, an other formulation can be written following a change of variable, see Lasseux et [103] [101] for futher information.

Problem I :

Conservation equations for the variable $(\mathbf{a}_{ii}, \mathbf{A}_{ii})$

$$\nabla \cdot \mathbf{A}_{ii} = 0 \quad \text{in } \Omega_i, \quad (\text{B.1a})$$

$$\rho_i \mathbf{u}_i \cdot \nabla \mathbf{A}_{ii} = -\nabla \mathbf{a}_{ii} + \mu_i \nabla^2 \mathbf{A}_{ii} - \frac{1}{V_i} \int_{\Gamma_{i\sigma} \cup \Gamma_{ij}} \mathbf{n}_i \cdot \left(-\mathbf{a}_{ii} \mathbf{I} + \mu_i \left(\nabla \mathbf{A}_{ii} + \nabla \mathbf{A}_{ii}^T \right) \right) d\Gamma \quad \text{in } \Omega_i, \quad (\text{B.1b})$$

Boundary conditions at $\Gamma_{j\sigma}, \Gamma_{i\sigma}, \Gamma_{ij}$

$$\mathbf{A}_{ii} = -\mathbf{I} \text{ at } \Gamma_{i\sigma}, \quad (\text{B.1c})$$

$$\mathbf{A}_{ii} = \mathbf{A}_{ji} - \mathbf{I} \text{ at } \Gamma_{ij}, \quad (\text{B.1d})$$

$$\mathbf{A}_{ji} = -\mathbf{I} \text{ at } \Gamma_{j\sigma}, \quad (\text{B.1e})$$

$$0 = -\mu_j \mathbf{n}_{ij} \cdot \left(-\mathbf{a}_{ji} \mathbf{I} + \left(\nabla \mathbf{A}_{ji} + \nabla \mathbf{A}_{ji}^T \right) \right) + \mu_i \mathbf{n}_{ij} \cdot \left(-\mathbf{a}_{ii} \mathbf{I} + \left(\nabla \mathbf{A}_{ii} + \nabla \mathbf{A}_{ii}^T \right) \right) \text{ at } \Gamma_{ij}, \quad (\text{B.1f})$$

Conservation equations for the variable $(\mathbf{a}_{ji}, \mathbf{A}_{ji})$

$$\nabla \cdot \mathbf{A}_{ji} = 0 \quad \text{in } \Omega_j, \quad (\text{B.1g})$$

$$\rho_j \mathbf{u}_j \cdot \nabla \mathbf{A}_{ji} = -\nabla \mathbf{a}_{ji} + \mu_j \nabla^2 \mathbf{A}_{ji} - \frac{1}{V_j} \int_{\Gamma_{j\sigma} \cup \Gamma_{ij}} \mathbf{n}_j \cdot \left(-\mathbf{a}_{ji} \mathbf{I} + \mu_j \left(\nabla \mathbf{A}_{ji} + \nabla \mathbf{A}_{ji}^T \right) \right) d\Gamma \quad \text{in } \Omega_j. \quad (\text{B.1h})$$

Average

$$\langle \mathbf{A}_{ii} \rangle = 0, \quad \langle \mathbf{A}_{ji} \rangle = 0.$$

Periodicity conditions for \mathbf{A}_{ii} and \mathbf{A}_{ji}

$$\mathbf{A}_{ii}(\mathbf{r}) = \mathbf{A}_{ii}(\mathbf{r} + \mathbf{l}_k), \quad (\text{B.1i})$$

$$\mathbf{a}_{ii}(\mathbf{r}) = \mathbf{a}_{ii}(\mathbf{r} + \mathbf{l}_k), \quad (\text{B.1j})$$

$$\mathbf{A}_{ji}(\mathbf{r}) = \mathbf{A}_{ji}(\mathbf{r} + \mathbf{l}_k), \quad (\text{B.1k})$$

$$\mathbf{a}_{ji}(\mathbf{r}) = \mathbf{a}_{ji}(\mathbf{r} + \mathbf{l}_k). \quad (\text{B.1l})$$

Problem II :

Conservation equations for the couple $(\mathbf{a}_{jj}, \mathbf{A}_{jj})$

$$\nabla \cdot \mathbf{A}_{jj} = 0 \quad \text{in } \Omega_j, \quad (\text{B.2a})$$

$$\rho_j \mathbf{u}_j \cdot \nabla \mathbf{A}_{jj} = -\nabla \mathbf{a}_{jj} + \mu_j \nabla^2 \mathbf{A}_{jj} - \frac{1}{V_j} \int_{\Gamma_{j\sigma} \cup \Gamma_{ij}} \mathbf{n}_j \cdot \left(-\mathbf{a}_{jj} \mathbf{I} + \mu_j \left(\nabla \mathbf{A}_{jj} + \nabla \mathbf{A}_{jj}^T \right) \right) d\Gamma \quad \text{in } \Omega_j, \quad (\text{B.2b})$$

Boundary conditions at $\Gamma_{j\sigma}, \Gamma_{i\sigma}, \Gamma_{ij}$

$$\mathbf{A}_{jj} = -\mathbf{I} \text{ at } \Gamma_{j\sigma}, \quad (\text{B.2c})$$

$$\mathbf{A}_{ij} = -\mathbf{I} \text{ at } \Gamma_{i\sigma}, \quad (\text{B.2d})$$

$$\mathbf{A}_{ij} = \mathbf{A}_{jj} + \mathbf{I} \text{ at } \Gamma_{ij}, \quad (\text{B.2e})$$

$$0 = -\mu_j \mathbf{n}_{ij} \cdot \left(-\mathbf{a}_{jj} \mathbf{I} + \left(\nabla \mathbf{A}_{jj} + \nabla \mathbf{A}_{jj}^T \right) \right) + \mu_i \mathbf{n}_{ij} \cdot \left(-\mathbf{a}_{ij} \mathbf{I} + \left(\nabla \mathbf{A}_{ij} + \nabla \mathbf{A}_{ij}^T \right) \right) \text{ at } \Gamma_{ij}, \quad (\text{B.2f})$$

Conservation equations for the couple $(\mathbf{a}_{ij}, \mathbf{A}_{ij})$

$$\nabla \cdot \mathbf{A}_{ij} = 0 \quad \text{in } \Omega_i, \quad (\text{B.2g})$$

$$\rho_i \mathbf{u}_i \cdot \nabla \mathbf{A}_{ij} = -\nabla \mathbf{a}_{ij} + \mu_i \nabla^2 \mathbf{A}_{ij} - \frac{1}{V_i} \int_{\Gamma_{i\sigma} \cup \Gamma_{ij}} \mathbf{n}_i \cdot \left(-\mathbf{a}_{ij} \mathbf{I} + \mu_i \left(\nabla \mathbf{A}_{ij} + \nabla \mathbf{A}_{ij}^T \right) \right) d\Gamma \quad \text{in } \Omega_i. \quad (\text{B.2h})$$

Average

$$\langle \mathbf{A}_{jj} \rangle = 0, \quad \langle \mathbf{A}_{ij} \rangle = 0.$$

Periodicity conditions for $\mathbf{a}_{jj}, \mathbf{a}_{ij}, \mathbf{A}_{jj}$ and \mathbf{A}_{ij}

$$\mathbf{A}_{jj}(\mathbf{r}) = \mathbf{A}_{jj}(\mathbf{r} + \mathbf{l}_k), \quad (\text{B.2i})$$

$$\mathbf{a}_{jj}(\mathbf{r}) = \mathbf{a}_{jj}(\mathbf{r} + \mathbf{l}_k), \quad (\text{B.2j})$$

$$\mathbf{A}_{ij}(\mathbf{r}) = \mathbf{A}_{ij}(\mathbf{r} + \mathbf{l}_k), \quad (\text{B.2k})$$

$$\mathbf{a}_{ij}(\mathbf{r}) = \mathbf{a}_{ij}(\mathbf{r} + \mathbf{l}_k). \quad (\text{B.2l})$$

Appendix C

Appendix - Chapter 6

The model resulting from the splitting of the liquid phase in four pseudo-phases is given here in its complete form. This means that the momentum conservation equations for the five phases (gas + 4 liquid phases, introduced in Chapter 6), include the additional inertial and cross-terms from Chapters 4 and 5 . The permeabilities are tensorial but the inertial and cross-terms are scalars, since inertial and coupling effects do not bring further anisotropy to the system [163, 61].

The mass conservation equations especially involve mass exchanges \dot{m}_1 , \dot{m}_2 and \dot{m} and read

$$\varepsilon \frac{\partial S_g}{\partial t} + \nabla \cdot \mathbf{U}_g = 0, \quad (\text{C.1a})$$

$$\varepsilon \frac{\partial S_{l_1^\theta}}{\partial t} + \nabla \cdot \mathbf{U}_{l_1^\theta} = \dot{m}_1, \quad \varepsilon \frac{\partial S_{l_1^{\theta_{\min}}}}{\partial t} + \nabla \cdot \mathbf{U}_{l_1^{\theta_{\min}}} = -\dot{m}_1 + \dot{m}, \quad (\text{C.1b})$$

$$\varepsilon \frac{\partial S_{l_2^\theta}}{\partial t} + \nabla \cdot \mathbf{U}_{l_2^\theta} = \dot{m}_2, \quad \varepsilon \frac{\partial S_{l_2^{\theta_{\min}}}}{\partial t} + \nabla \cdot \mathbf{U}_{l_2^{\theta_{\min}}} = -\dot{m}_2 - \dot{m}. \quad (\text{C.1c})$$

The momentum conservation equations read

$$\mathbf{U}_g = -\frac{\mathbf{K}_g}{\mu_g} \cdot (\nabla P_g - \rho_g \mathbf{g}) - F_g \mathbf{U}_g + (K_{gl} - F_{gl}) \mathbf{U}_l, \quad (\text{C.2a})$$

$$\mathbf{U}_{l_1^\theta} = -\frac{\mathbf{K}_{l_1^\theta}}{\mu_l} \cdot (\nabla P_{l_1^\theta} - \rho_l \mathbf{g}) - F_{l_1^\theta} \mathbf{U}_{l_1^\theta} + (K_{l_1^\theta g} - F_{l_1^\theta g}) \mathbf{U}_g, \quad (\text{C.2b})$$

$$\mathbf{U}_{l_1^{\theta_{\min}}} = -\frac{\mathbf{K}_{l_1^{\theta_{\min}}}}{\mu_l} \cdot (\nabla P_{l_1^{\theta_{\min}}} - \rho_l \mathbf{g}) - F_{l_1^{\theta_{\min}}} \mathbf{U}_{l_1^{\theta_{\min}}} + (K_{l_1^{\theta_{\min}} g} - F_{l_1^{\theta_{\min}} g}) \mathbf{U}_g, \quad (\text{C.2c})$$

$$\mathbf{U}_{l_2^\theta} = -\frac{\mathbf{K}_{l_2^\theta}}{\mu_l} \cdot (\nabla P_{l_2^\theta} - \rho_l \mathbf{g}) - F_{l_2^\theta} \mathbf{U}_{l_2^\theta} + (K_{l_2^\theta g} - F_{l_2^\theta g}) \mathbf{U}_g, \quad (\text{C.2d})$$

$$\mathbf{U}_{l_2^{\theta_{\min}}} = -\frac{\mathbf{K}_{l_2^{\theta_{\min}}}}{\mu_l} \cdot (\nabla P_{l_2^{\theta_{\min}}} - \rho_l \mathbf{g}) - F_{l_2^{\theta_{\min}}} \mathbf{U}_{l_2^{\theta_{\min}}} + (K_{l_2^{\theta_{\min}} g} - F_{l_2^{\theta_{\min}} g}) \mathbf{U}_g. \quad (\text{C.2e})$$

For the application in the modeling of the distillation process, the correlations of the inertial and cross-terms of the pseudo-liquid phases can be deduced from the ones used in Chapter 5 . K_{gl} and F_{gl} are in particular computed from $S_l = S_{l_1^g} + S_{l_1^{g_{\min}}} + S_{l_2^g} + S_{l_2^{g_{\min}}}$.

Bibliography

- [1] Packing characterization: Mass transfer properties. *Energy Procedia*, 23:23 – 32, 2012.
- [2] Packing characterization for post combustion co2 capture: Mass transfer model development. *Energy Procedia*, 63:1727 – 1744, 2014.
- [3] A. Arani A. Ahmadi and D. Lasseux. Numerical simulation of two-phase inertial flow in heterogeneous porous media. *Transport in Porous Media*, 84(1):177–200, 2010.
- [4] S.R. Shadizadeh A. Hashemi. The impact of reservoir properties on pseudo functions: Upscaling of relative permeability. *Petroleum Science and Technology*, 32:772–782, 2005.
- [5] Y. Achdou, O. Pironneau, and F. Valentin. Effective boundary conditions for laminar flows over periodic rough boundaries. *Journal of Computational Physics*, 147(1):187 – 218, 1998.
- [6] Y. Achdou, P. Le Tallec, F. Valentin, and O. Pironneau. Constructing wall laws with domain decomposition or asymptotic expansion techniques. *Computer Methods in Applied Mechanics and Engineering*, 151(1-2):215 – 232, 1998. Containing papers presented at the Symposium on Advances in Computational Mechanics.
- [7] M. Agnaou, D. Lasseux, and A. Ahmadi. From steady to unsteady laminar flow in model porous structures: an investigation of the first hopf bifurcation. *Computers & Fluids*, 136:67–82, 2016.
- [8] R. Agrawal and D. Herron. *Encyclopedia of Separation Science*, chapter Air liquefaction : Distillation, pages 1895–1910. Oxford: Academic Press, New York, NY, 2000.
- [9] S. V. Alekseenko, D. M. Markovich, A. R. Evseev, A. V. Bobylev, B. V. Tarasov, and V. M. Karsten. Experimental investigation of liquid distribution over structured packing. *AIChE Journal*, 54(6):1424–1430, 2008.
- [10] S.V. Alekseenko, S.P. Aktershev, A.V. Cherdantsev, S.M. Kharlamov, and D.M. Markovich. Primary instabilities of liquid film flow sheared by turbulent gas stream. *International Journal of Multiphase Flow*, 35(7):617 – 627, 2009.
- [11] J. S. Andrade, U. M. S. Costa, M. P. Almeida, H. A. Makse, and H. E. Stanley. Inertial effects on fluid flow through disordered porous media. *Phys. Rev. Lett.*, 82:5249–5252, Jun 1999.
- [12] R. T. Armstrong, N. Evseev, D. Koroteev, and S. Berg. Modeling the velocity field during haines jumps in porous media. *Advances in Water Resources*, 77:57 – 68, 2015.
- [13] A. Aroonwilas, A. Chakma, P. Tontiwachwuthikul, and A. Veawab. Mathematical modelling of mass-transfer and hydrodynamics in co2 absorbers packed with structured packings. *Chem Eng Sci.*, 58:4037–4053, 2003.

- [14] A. Aroonwilas and P. Tontiwachwuthikul. Mechanistic model for prediction of structured packing mass transfer performance in co₂ absorption with chemical reactions. *Chem Eng Sci.*, 55:3651–3663, 2000.
- [15] A. Attou, C. Boyer, and G. Ferschneider. Modelling of the hydrodynamics of the cocurrent gas-liquid trickle flow through a trickle-bed reactor. *Chemical Engineering Science*, 54(6):785–802, 1999.
- [16] J.-L. Auriault. Nonsaturated deformable porous media: Quasistatics. *Transport in Porous Media*, 2(1):45–64, 1987.
- [17] G. R. Barrenechea, P. Le Tallec, and F. Valentin. New wall laws for the unsteady incompressible navier-stokes equations on rough domains. *ESAIM: Mathematical Modelling and Numerical Analysis*, 36(2):177–203, 2002.
- [18] A. Basson and D. Gérard-Varet. Wall laws for fluid flows at a boundary with random roughness. *Communications on Pure and Applied Mathematics*, 61(7):941–987, 2008.
- [19] G. Baveye, P. Sposito. The operational significance of the continuum hypothesis in the theory of water movement through soils and aquifers. *Water Resources Res.* 20(5), pages 521–530, 1984.
- [20] J. Bear. *Dynamics of fluids in porous media*. Elsevier, New York, 1972.
- [21] G. Beavers and D. Joseph. Boundary conditions at a naturally permeable wall. *Journal of Fluid Mechanics*, 30(1):197–207, 1967.
- [22] P. Bedrikovetsky. *Mathematical Theory of Oil and Gas Recovery*. Springer, 1993.
- [23] A. Bensoussan, G. Papanicolau, and J.-L. Lions. *Asymptotic Analysis for Periodic Structures*. North Holland, Amsterdam, 1978.
- [24] R. G. Bentsen and A. A. Manai. On the use of conventional cocurrent and countercurrent effective permeabilities to estimate the four generalized permeability coefficients which arise in coupled, two-phase flow. *Transport in Porous Media*, 1993.
- [25] R. Billet and M. Schultes. Predicting mass transfer in packed columns. *Chem. Eng. Technol.*, 16(1):1–9, 1993.
- [26] B. J. Bourbiaux and F. J. Kalaydjian. Experimental study of cocurrent and countercurrent flows in natural porous media. *SPE*, 5:361–368, 1990.
- [27] C Boyer and B Fanget. Measurement of liquid flow distribution in trickle bed reactor of large diameter with a new gamma-ray tomographic system. *Chemical Engineering Science*, 57(7):1079 – 1089, 2002.
- [28] J. L. Bravo, J. A. Rocha, and J. R. Fair. Mass transfer in gauze packing. *Hydrocarbon Processing*, 64(1):91 – 95, 1985.
- [29] A Brooks, R. Corey. Hydraulic properties of porous media. *Hydrology Papers* 3, 1964.
- [30] E. Brunazzi and A. Paglianti. Mechanistic pressure drop model for columns containing structured packings. *AIChE Journal*, 43(2):317–327, 1997.
- [31] S.E. Buckley and M.C. Leverett. Mechanism of fluid displacement in sands. *Society of Petroleum Engineers*, pages 107–116, 1942.

- [32] Clément Cancès. Finite volume scheme for two-phase flows in heterogeneous porous media involving capillary pressure discontinuities. *ESAIM: Mathematical Modelling and Numerical Analysis*, 43(5):973 – 1001, 2009.
- [33] N. Chikhi, R. Clavier, J.-P. Laurent, F. Fichot, and M. Quintard. Pressure drop and average void fraction measurements for two-phase flow through highly permeable porous media. *Annals of Nuclear Energy*, 2016.
- [34] R. Clavier. *Étude expérimentale et modélisation des pertes de pression lors du renoyage d’un lit de débris*. PhD thesis, LE2M, IRSN Cadarache, 2015.
- [35] R. Clavier, N. Chikhi, F. Fichot, and M. Quintard. Experimental investigation on single-phase pressure losses in nuclear debris beds: Identification of flow regimes and effective diameter. *Nuclear Engineering and Design*, 292:222 – 236, 2015.
- [36] R. Clavier, N. Chikhi, F. Fichot, and M. Quintard. Modeling of inertial multi-phase flows through high permeability porous media: Friction closure laws. *International Journal of Multiphase Flow*, 91:243 – 261, 2017.
- [37] F.A. Coutelieiris, M.E. Kainourgiakis, A.K. Stubos, E.S. Kikkinides, and Y.C. Yortsos. Multiphase mass transport with partitioning and inter-phase transport in porous media. *Chemical Engineering Science*, 61(14):4650–4661, 2006.
- [38] L. Cueto-Felgueroso and R. Juanes. A phase field model of unsaturated flow. *Water Resources Research*, 45(10):n/a–n/a, 2009.
- [39] A. Bejan D. A. Nield. *Convection in Porous Media*, chapter Mechanics of Fluid Flow Through a Porous Medium, pages 1–29. Springer New York, New York, NY, 2013.
- [40] P. V. Danckwerts. *Gas-Liquid Reactions*. McGraw-Hill, 1970.
- [41] M. Danis and M. Quintard. Modélisation d’un écoulement diphasique dans une succession de pores. *Rev. Institut Français du Pétrole*, 39(1):37–46, 1984.
- [42] Y. Davit, C. G. Bell, H. M. Byrne, L. A.C. Chapman, L. S. Kimpton, G. E. Lang, K. H.L. Leonard, J. M. Oliver, N. C. Pearson, R. J. Shipley, S. L. Waters, J. P. Whiteley, B. D. Wood, and M. Quintard. Homogenization via formal multiscale asymptotics and volume averaging: How do the two techniques compare? *Advances in Water Resources*, 62, Part B(0):178 – 206, 2013. A tribute to Stephen Whitaker.
- [43] Y. Davit and M. Quintard. Comment on "frequency-dependent dispersion in porous media". *Physical Review E*, 86(1, Part 1):1–4, July 2012.
- [44] Y. Davit and M. Quintard. Technical notes on volume averaging in porous media i: How to choose a spatial averaging operator for periodic and quasiperiodic structures? *Submitted for publication in Transport in Porous Media*, 2017.
- [45] P.-G. de Gennes, F. Brochard-Wyart, and D. Quéré. *Gouttes, bulles, perles et ondes*. Belin, 2005.
- [46] P.G. de Gennes. Theory of slow biphasic flows in porous media. *Physico. Chem. Hydrodan.*, 4:175 – 185, 1983.

- [47] M. J.S. de Lemos. In M. J.S. de Lemos, editor, *Turbulence in Porous Media*, pages vii – viii. Elsevier Science Ltd, Oxford, 2006.
- [48] S. Diehl. On scalar conservation laws with point source and discontinuous flux function. *Journal on Mathematical Analysis*, 26:1425–1451, 1993.
- [49] G. F. Dietze and C. Ruyer-Quil. Wavy liquid films in interaction with a confined laminar gas flow. *Journal of Fluid Mechanics*, 722:348–393, 5 2013.
- [50] F. Doster and R. Hilfer. Generalized buckley-leverett theory for two-phase flow in porous media. *New Journal of Physics*, 13:33, 2011.
- [51] D. A. Edwards, M. Shapiro, P. Bar-Yoseph, and M. Shapira. The influence of reynolds number upon the apparent permeability of spatially periodic arrays of cylinders. *Physics of Fluids A*, 2(1):45–55, 1990.
- [52] E.V. Evans and R.D. Evans. Influence of an immobile or mobile saturation on non-darcy compressible flow of real gases in propped fractures. *J. Petrol. Technol.*, 40(10):1343–1351, 1988.
- [53] Torres F. E. Closure of the governing equations for immiscible, two-phase flow: A research comment. *Transport in Porous Media*, 2(4):383–393, 1987.
- [54] J. Fernandes, P. F. Lisboa, P. C. Simoes, J. P.B. Mota, and E. Saatchian. Application of cfd in the study of supercritical fluid extraction with structured packing: Wet pressure drop calculations. *The Journal of Supercritical Fluids*, 50(1):61 – 68, 2009.
- [55] A. Ferrari and I. Lunati. Inertial effects during irreversible meniscus reconfiguration in angular pores. *Advances in Water Resources*, 74:1 – 13, 2014.
- [56] L.L. Ferrás, J.M. Nóbrega, and F.T. Pinho. Implementation of slip boundary conditions in the finite volume method: new techniques. *International Journal for Numerical Methods in Fluids*, 72(7):724–747, 2013.
- [57] F Fichot, F Duval, N Trégourès, C Béchaud, and Michel Quintard. The impact of thermal non-equilibrium and large-scale 2d/3d effects on debris bed reflooding and coolability. *Nuclear engineering and design*, 236(19):2144–2163, 2006.
- [58] M. Firdaouss, J.L. Guermond, and P. Le Quéré. Nonlinear corrections to darcy’s law at low reynolds numbers. *Journal of Fluid Mechanics*, 343:331–350, 7 1997.
- [59] M. Fourar and R. Lenormand. A viscous coupling model for relative permeabilities in fractures. *SPE Annual Technical Conference and Exhibition*, 1998.
- [60] M. Fourar, R. Lenormand, M. Karimi-Fard, and R. Horne. Inertia effects in high-rate flow through heterogeneous porous media. *Transport in Porous Media*, 60(3):353–370, 2005.
- [61] M. Fourati, V. Roig, and L. Raynal. Experimental study of liquid spreading in structured packings. *Chemical Engineering Science*, 80(0):1 – 15, 2012.
- [62] M. Fourati, V. Roig, and L. Raynal. Liquid dispersion in packed columns: Experiments and numerical modeling. *Chemical Engineering Science*, 100:266 – 278, 2013. 11th International Conference on Gas-Liquid and Gas-Liquid-Solid Reactor Engineering.

- [63] W. G. Gray. A derivation of the equations for multi-phase transport. *Chemical Engineering Science*, 30(2):229 – 233, 1975.
- [64] W. G. Gray and S. M. Hassanizadeh. Macroscale continuum mechanics for multiphase porous-media flow including phases, interfaces, common lines and common points. *Advances in Water Resources*, 21(4):261 – 281, 1998.
- [65] C.W. Green, J. Farone, J.K. Briley, R.B. Eldridge, R.A. Ketcham, and B. Nightingal. Novel application of x-ray computed tomography: Determination of gas-liquid contact area and liquid holdup in structured packing. *Ind. Eng. Chem*, (0):5734–5753, 2007.
- [66] J. Guo, S. Veran-Tissoires, and M. Quintard. Effective surface and boundary conditions for heterogeneous surfaces with mixed boundary conditions. *Journal of Computational Physics*, 305:942 – 963, 2016.
- [67] J. Hagoort. Oil recovery by gravity drainage. *Society of Petroleum Engineers Journal*, 20(03):139 – 150, 1980.
- [68] W. D. Harkins and A. Feldman. Films. the spreading of liquids and the spreading coefficient. *Journal of the American Chemical Society*, 44(12):2665–2685, 1922.
- [69] Y. Haroun, D. Legendre, and L. Raynal. Direct numerical simulation of reactive absorption in gas-liquid flow on structured packing using interface capturing method. *Chemical Engineering Science*, 65(1):351 – 356, 2010. 20th International Symposium in Chemical Reaction Engineering-Green Chemical Reaction Engineering for a Sustainable Future.
- [70] Y. Haroun, L. Raynal, and P. Alix. Prediction of effective area and liquid hold-up in structured packings by cfd. *Chemical Engineering Research and Design*, 92(11):2247 – 2254, 2014.
- [71] M. Hassanizadeh and W. G. Gray. General conservation equations for multi-phase systems: 2. mass, momenta, energy, and entropy equations. *Advances in Water Resources*, 1979.
- [72] M. Hassanizadeh and W. G. Gray. General conservation equations for multi-phase systems: 3. constitutive theory for porous media flow. *Advances in Water Resources*, (1), 1980.
- [73] M. Hassanizadeh and W. G. Gray. Toward an improved description of the physics of two-phase flow. *Advances in Water Resources*, 16(1):53–67, 1993.
- [74] F. Hecht. New development in freefem++. *Journal of Numerical Mathematics*, 20:251–266, 2013.
- [75] R. Higbie. The rate of absorption of a pure gas into a still liquid during short periods of exposure. *Trans. Am. Inst. Chem. Engrs*, 31:365–389, 1935.
- [76] R. Hilfer. Macroscopic equations of motion for two-phase flow in porous media. *Phys. Rev. E*, 58:2090–2096, Aug 1998.
- [77] M. Honarpour, L. Koederitz, and A. H. Harvey. *Relative Permeability of Petroleum Reservoirs*. CRC Press, Boca Raton, FL, 1986.
- [78] P. Horgue. *Modélisation multi-échelle d'un écoulement gaz-liquide dans un lit fixe de particules*. PhD thesis, IMFT, 2012.

- [79] P. Horgue, C. Soulaire, J. Franc, R. Guibert, and G. Debenest. An open-source toolbox for multiphase flow in porous media. *Computer Physics Communications*, 187:217 – 226, 2015.
- [80] F. A. Howes and S. Whitaker. The spatial averaging theorem revisited. *Chemical Engineering Science*, 40(8):1387 – 1392, 1985.
- [81] F. Larachi I. Iliuta, M. Fourar. Hydrodynamic model for horizontal two-phase flow through porous media. *The Canadian Journal of Chemical Engineering*, 81(5), 2003.
- [82] I. Iliuta, M. Fourar, and F. Larachi. Hydrodynamic model for horizontal two-phase flow through porous media. *The Canadian Journal of Chemical Engineering*, 81(5), 2003.
- [83] I. Iliuta, C.F. Petre, and F. Larachi. Hydrodynamic continuum model for two-phase flow structured-packing-containing columns. *Chemical Engineering Science*, 59(4):879 – 888, 2004.
- [84] C. Introini, M. Quintard, and F. Duval. Effective surface modeling for momentum and heat transfer over rough surfaces: Application to a natural convection problem. *International Journal of Heat and Mass Transfer*, 54(15-16):3622 – 3641, 2011.
- [85] R. I. Issa. Solution of the implicitly discretised fluid flow equations by operator-splitting. *Journal of Computational Physics*, 62(1):40–65, January 1986.
- [86] M. Izoz. Effects of surface textures on gravity driven liquid flow on inclined plate. 2016.
- [87] S. Thibeau J. Barker. A critical review of the use of pseudorelative permeabilities for upscaling. *SPE Reservoir Engineering*, 12:138–143, 1997.
- [88] Y. Jin, M.-F. Uth, A. V. Kuznetsov, and H. Herwig. Numerical investigation of the possibility of macroscopic turbulence in porous media: a direct numerical simulation study. *Journal of Fluid Mechanics*, 766:76–103, 3 2015.
- [89] E.F. Kaasschieter. Solving the buckley–leverett equation with gravity in a heterogeneous porous medium. *Computational Geosciences*, 3(1):23–48, 1999.
- [90] F. Kalaydjian. A macroscopic description of multiphase flow in porous media involving spacetime evolution of fluid/fluid interface. *Transport in Porous Media*, 1987.
- [91] F. Kalaydjian. Origin and quantification of coupling between relative permeabilities for two-phase flows in porous media. *Transport in Porous Media*, 1990.
- [92] K. Kamrin, M. Z. Bazant, and H. A. Stone. Effective slip boundary conditions for arbitrary periodic surfaces: the surface mobility tensor. *Journal of Fluid Mechanics*, 658:409–437, July 2010.
- [93] D. L. Koch and A. J. C. Ladd. Moderate Reynolds number flows through periodic and random arrays of aligned cylinders. *Journal of Fluid Mechanics*, 349:31–66, October 1997.
- [94] N. Kofman. *Films liquides tombants avec ou sans contre-écoulement de gaz : application au problème de l'engorgement dans les colonnes de distillation*. PhD thesis, UPMC - Laboratoire FAST, 2014.
- [95] J. L. Lage, B. V. Antohe, and D.A. Nield. Two types of nonlinear pressure-drop versus flow-rate relation observed for saturated porous media. *Journal of fluids engineering*, 119(3):700–706, 1997.

- [96] J.L. Lage. The fundamental theory of flow through permeable media from darcy to turbulence. In D. B. Inghamian I. Pop, editor, *Transport Phenomena in Porous Media*, pages 1 – 30. Pergamon, Oxford, 1998.
- [97] J.L. Lage and B.V. Antohe. Darcy’s experiments and the deviation to nonlinear flow regime. *Journal of Fluids Engineering*, 122:619 – 625, 2000.
- [98] L. W. Lake. *Enhanced Oil Recovery*. Prentice Hall, Englewood Cliffs, New Jersey, 1989.
- [99] K. Lappalainen, E. Gorshkova, M. Manninen, and V. Alopaeus. Characteristics of liquid and tracer dispersion in trickle-bed reactors: Effect on {CFD} modeling and experimental analyses. *Computers Chemical Engineering*, 35(1):41–49, 2011.
- [100] D. Lasseux, A. A. Abbasian Arani, and A. Ahmadi. On the stationary macroscopic inertial effects for one phase flow in ordered and disordered porous media. *Physics of Fluids*, 23(7), 2011.
- [101] D. Lasseux, A. Ahmadi, and A. Arani. Two-phase inertial flow in homogeneous porous media: A theoretical derivation of a macroscopic model. *Transport in Porous Media*, 75(3):371–400, 2008.
- [102] D. Lasseux, F. J. Valdes Parada, J. A. Ochoa Tapia, and B. Goyeau. A macroscopic model for slightly compressible gas slip-flow in homogeneous porous media. *Physics of Fluids (1994-present)*, 26(5):–, 2014.
- [103] D. Lasseux, M. Quintard, and S. Whitaker. Determination of permeability tensors for two-phase flow in homogeneous porous media: Theory. *Transport in Porous Media*, 1996.
- [104] G. Lavalle, J.-P. Vila, G. Blanchard, C. Laurent, and F. Charru. A numerical reduced model for thin liquid films sheared by a gas flow. *J. Comput. Phys.*, 301(22):119–140, 2015.
- [105] P. Lax. *Hyperbolic Systems of Conservation Laws and the Mathematical Theory of Shock Waves*. Society for Industrial and Applied Mathematics, 1973.
- [106] R. Lenormand, E. Touboul, and C. Zarcone. Numerical models and experiments on immiscible displacements in porous media. *J. Fluid Mechanics*, (189):165–187, 1988.
- [107] W. K. Lewis and W. G. Whitman. Principles of gas absorption. *Industrial & Engineering Chemistry*, 16(12):1215–1220, 1924.
- [108] R.J. Lipinski. Model for boiling and dryout in particle beds. *Technical Report*, 1982.
- [109] B. Liu, Y. Wen, C. Liu, B. Sun, and X. Yuan. Multiscale calculation on perforated sheet structured packing to predict the liquid distribution based on computational fluid dynamics simulation. *Industrial & Engineering Chemistry Research*, 55(28):7810–7818, 2016.
- [110] X. Liu, F. Civan, and R.D. Evans. Correlations of the non-darcy flow coefficient. *J. Can. Petrol. Technol.*, 34(10):50–54, 1995.
- [111] D. Vincent M. Andro. Ecoulement tangentiel sur une surface rugueuse et loi de navier. *Annales mathématiques Blaise Pascal*, 9(2):313–327, 2002.
- [112] I. Panfilova M. Panfilov. Phenomenological meniscus model for two-phase flows in porous media. *Transport in porous media*, 58:87–119, 2005.

- [113] B. Mahr and D. Mewes. {CFD} modelling and calculation of dynamic two-phase flow in columns equipped with structured packing. *Chemical Engineering Research and Design*, 85(8):1112 – 1122, 2007.
- [114] B. Mahr and D. Mewes. Two-phase flow in structured packings: Modeling and calculation on a macroscopic scale. *AIChE Journal*, 54(3):614–626, 2008.
- [115] C. M. Marle. Ecoulements monophasique en milieu poreux. *Rev. Inst. Français du pétrole*, 22(10):1471–1509, 1967.
- [116] C.M. Marle. On macroscopic equations governing multiphase flow with diffusion and chemical reactions in porous media. *International Journal of Engineering Science*, 20(5):643 – 662, 1982.
- [117] G. Matheron. *Les variables régionalisées et leur estimation : une application de la théorie des fonctions aléatoires aux sciences de la nature*. Masson, Paris, 1965.
- [118] GG. McGlamery. *Liquid Film Transport Characteristics of Textured Metal Surfaces*. PhD thesis, University of Texas at Austin, 1988.
- [119] M. Muskat. The flow of homogeneous fluids through porous media. *International series in physics, York The Mapple Press Company*, 1946.
- [120] A. Nakayama and F. Kuwahara. A general macroscopic turbulence model for flows in packed beds, channels, pipes, and rod bundles. *Journal of Fluids Engineering*, 130, 2008.
- [121] M.R. Khosravi Nikou and M.R. Ehsani. Turbulence models application on cfd simulation of hydrodynamics, heat and mass transfer in a structured packing. *International Communications in Heat and Mass Transfer*, 35(9):1211 – 1219, 2008.
- [122] J.A. Ochoa-Tapia and S. Whitaker. Momentum transfer at the boundary between a porous medium and a homogeneous fluid - i. theoretical development. *Int. J. Heat Mass Transfer*, 38(14):2635–2646, 1995.
- [123] Z. Olujic. Effect of column diameter on pressure drop of a corrugated sheet structured packing. *Chemical Engineering Research and Design*, 77(6):505 – 510, 1999.
- [124] Z. Olujic, M. Jodecke, A. Shilkin, G. Schuch, and B. Kaibel. Equipment improvement trends in distillation. *Chemical Engineering and Processing: Process Intensification*, 48(6):1089 – 1104, 2009.
- [125] S.A. Owens, M.R. Perkins, R.B. Eldridge, K.W. Schulz, and R.A. Ketcham. Computational fluid dynamics simulation of structured packing. *Industrial & Engineering Chemistry Research*, 52(5):2032–2045, 2013.
- [126] S. Pasquier, M. Quintard, and Y. Davit. Modeling flow in porous media with rough surfaces: effective slip boundary conditions and application to structured packings. *Chemical Engineering Science*, 165:131 – 146, 2017.
- [127] S. Pasquier, M. Quintard, and D. Yohan. Modeling two-phase flow of immiscible fluids in porous media: Buckley-leverett theory with explicit coupling terms. *Phys. Rev. Fluids*, 2:104101, Oct 2017.
- [128] S. V. Patankar. *Numerical Heat Transfer and Fluid Flow*, page 214. CRC Press, New York, NY, 1980.

- [129] C.F. Petre, F. Larachi, I. Iliuta, and B.P.A. Grandjean. Pressure drop through structured packings: Breakdown into the contributing mechanisms by cfd modeling. *Chemical Engineering Science*, 58(1):163 – 177, 2003.
- [130] D. A. Pham, Y-I Lim, H. Jee, E. A., and Y. Jung. Porous media eulerian computational fluid dynamics (cfd) model of amine absorber with structured-packing for {CO₂} removal. *Chemical Engineering Science*, 132:259 – 270, 2015.
- [131] Wlodzimierz Proskurowski. A note on solving the buckley-leverett equation in the presence of gravity. *Journal of Computational Physics*, 41(1):136 – 141, 1981.
- [132] M. Quintard. Two-phase flow in heterogeneous porous media i: The influence of large spatial and temporal gradients. *Transport in Porous Media*, 5, 1990.
- [133] M. Quintard, L. Bletzacker, D. Chenu, and S. Whitaker. Nonlinear, multicomponent, mass transport in porous media. *Chemical Engineering Science*, 61(8):2643–2669, 2006.
- [134] M. Quintard and S. Whitaker. Two-phase flow in heterogeneous porous media: the method of large-scale averaging. *Transport in Porous Media*, 3:357–413, 1988.
- [135] M. Quintard and S. Whitaker. Two-phase flow in heterogeneous porous media i: the influence of large spatial and temporal gradients. *Transport in Porous Media*, 5:341–379, 1990.
- [136] M. Quintard and S. Whitaker. Transport in ordered and disordered porous media i: The cellular average and the use of weighting functions. *Transport in Porous Media*, 14:163–177, 1994.
- [137] M. Quintard and S. Whitaker. Transport in ordered and disordered porous media ii: Generalized volume averaging. *Transport in Porous Media*, 14:179–206, 1994.
- [138] M. Quintard and S. Whitaker. Transport in ordered and disordered porous media iii: Closure and comparison between theory and experiment. *Transport in Porous Media*, 15:31–49, 1994.
- [139] M. Quintard and S. Whitaker. Transport in ordered and disordered porous media iv: Computer generated porous media for three-dimensional systems. *Transport in Porous Media*, 15:51–70, 1994.
- [140] P.A.C. Raats. Applications of the theory of mixtures in soil science. *Mathematical Modelling*, 9(12):849 – 856, 1987.
- [141] L. Raynal and A. Royon-Lebeaud. A multi-scale approach for cfd calculations of gas-liquid flow within large size column equipped with structured packing. *Chemical Engineering Science*, 62(24):7196 – 7204, 2007. 8th International Conference on Gas-Liquid and Gas-Liquid-Solid Reactor Engineering.
- [142] Ludovic Raynal, Christophe Boyer, and Jean-Pierre Ballaguet. Liquid holdup and pressure drop determination in structured packing with cfd simulations. *The Canadian Journal of Chemical Engineering*, 82(5):871–879, 2004.
- [143] P.C. Reeves and M.A. Celia. A functional relationship between capillary pressure, saturation, and interfacial area as revealed by a pore-scale network model. *Water Resources Research*, 32(8):2345–2358, 1996.
- [144] A. Riaz and H. Tchelepi. Stability of two-phase vertical flow in homogeneous porous media. *Physics of Fluids*, 19(7):072103, 2007.

- [145] J. A. Rocha, J. L. Bravo, and J. R. Fair. Distillation columns containing structured packings: a comprehensive model for their performance. 1. hydraulic models. *Industrial & Engineering Chemistry Research*, 32(4):641–651, 1993.
- [146] J. A. Rocha, J. L. Bravo, and J. R. Fair. Distillation columns containing structured packings: a comprehensive model for their performance. 1. hydraulic models. *Industrial & Engineering Chemistry Research*, 32(4):641–651, 1993.
- [147] J. A. Rocha, J. L. Bravo, and J. R. Fair. Distillation columns containing structured packings: A comprehensive model for their performance. *Ind. Eng. Chem. Res.*, 35(5):1660–1667, 1996.
- [148] W. Rose. Measuring transport coefficients necessary for the description of coupled two-phase flow of immiscible fluids in porous media. *Transport in Porous Media*, 3(2), 1988.
- [149] W. Rose. Coupling coefficients for two-phase flow in pore spaces of simple geometry. *Transport in Porous Media*, 5(1), 1990.
- [150] D. H. Rothman. Macroscopic laws for immiscible two-phase flow in porous media: Results from numerical experiments. *Journal of Geophysical Research: Solid Earth*, 1990.
- [151] G. Ahmadi S. H. Hosseini, S. Shojaee and M. Zivdar. Computational fluid dynamics studies of dry and wet pressure drops in structured packings. *Journal of Industrial and Engineering Chemistry*, 18(4):1465 – 1473, 2012.
- [152] W. G. Gray S. M. Hassanizadeh. Toward an improved description of the physics of two-phase flow. *Advances in Water Resources*, 16(1):53 – 67, 1993.
- [153] W. Said, M. Nemer, and D. Clodic. Modeling of dry pressure drop for fully developed gas flow in structured packing using cfd simulations. *Chemical Engineering Science*, 66(10):2107 – 2117, 2011.
- [154] S. Schug and W. Arlt. Imaging of fluid dynamics in a structured packing using x-ray computed tomography. *Chemical Engineering and Technology*, 39(8):1561–1569, 2016.
- [155] T. Schulenberg and U. Müller. An improved model for two-phase flow through beds of coarse particles. *International Journal of Multiphase Flow*, 1987.
- [156] J.W. Sheldon, B. Zondek, and W.T. Cardwell. One-dimensional, incompressible, noncapillary, two-phase fluid flow in a porous medium. *Society of Petroleum Engineers*, 216:290–296, 1959.
- [157] A. Shilkin and E.Y. Kenig. A new approach to fluid separation modelling in the columns equipped with structured packings. *Chemical Engineering Journal*, 110(1-3):87 – 100, 2005.
- [158] E. Skjetne and J-L. Auriault. High-velocity laminar and turbulent flow in porous media. *Transport in Porous Media*, 36(2):131–147, 1999.
- [159] C. Soulaïne. *Modélisation des écoulements dans les garnissages structurés : de l'échelle du pore à l'échelle de la colonne*. PhD thesis, IMFT, 2012.
- [160] C. Soulaïne, Y. Davit, and M. Quintard. A two-pressure model for slightly compressible single phase flow in bi-structured porous media. *Chemical Engineering Science*, 96(0):55 – 70, 2013.
- [161] C. Soulaïne, G. Debenest, and M. Quintard. Upscaling multi-component two-phase flow in porous media with partitioning coefficient. *Chem Eng Sci*, 66:6180–6192, 2011.

- [162] C. Soullaine, P. Horgue, J. Franc, and M. Quintard. Gas-liquid flow modeling in columns equipped with structured packing. *AIChE Journal*, pages 3665–3674, 2014.
- [163] C. Soullaine and M. Quintard. On the use of a darcy-forchheimer like model for a macro-scale description of turbulence in porous media and its application to structured packings. *International Journal of Heat and Mass Transfer*, 74(0):88 – 100, 2014.
- [164] L. Spiegel and W. Meier. Distillation columns with structured packings in the next decade. *Chemical Engineering Research and Design*, 81(1):39 – 47, 2003. International Conference on Distillation and Absorption.
- [165] J. Sternberg. A theory for the viscous sublayer of a turbulent flow. *Journal of Fluid Mechanics*, 13:241–271, 6 1962.
- [166] J. Stichlmair, J.L. Bravo, and J.R. Fair. General model for prediction of pressure drop and capacity of countercurrent gas/liquid packed columns. *Gas Separation & Purification*, 3(1):19 – 28, 1989.
- [167] P. Suess and L. Spiegel. Hold-up of mellapak structured packings. *Chemical Engineering and Processing: Process Intensification*, 31(2):119 – 124, 1992.
- [168] B. Sun, L. He, B.T. Liu, F. Gu, and C.J. Liu. A new multi-scale model based on cfd and macroscopic calculation for corrugated structured packing column. *AIChE J.*, 59:3119–3130, 2013.
- [169] B. Szulczewska, I. Zbicinski, and A. Gorak. Liquid flow on structured packing: Cfd simulation and experimental study. *Chemical Engineering and Technology*, 26(5):580–584, 2003.
- [170] R. Taylor and R. Krishna. *Multicomponent Mass Transfer*. John Wiley & Sons, 1993.
- [171] E. F. Toro. *Riemann solvers and numerical methods for fluid dynamics : a practical introduction*. Springer, Berlin, New York, 1997.
- [172] Y.Y. Trifonov. Flooding in two-phase counter-current flows: Numerical investigation of the gas-liquid wavy interface using the navier-stokes equations. *International Journal of Multiphase Flow*, 36(7):549 – 557, 2010.
- [173] R. E. Tsai. *Mass Transfer Area of Structured Packing*. PhD thesis, University of Texas, Austin, May 2010.
- [174] R.E. Tsai, A.F. Saibert, R.B. Eldridge, and G.T Rochelle. Influence of viscosity and surface tension on the effective mass transfer area of structured packings. *Energy Procedia*, (0):1197 – 1204, 2009.
- [175] N. K. Tutu, T. Ginsberg, and J. C. Chen. Interfacial drag for two-phase flow through high permeability porous beds. *Journal of Heat Transfer*, 106(4):865–870, 1984.
- [176] N. K. Tutu, T. Ginsberg, T. Klein, J. Klages, and C. Schwarz. Debris bed quenching under bottom flood conditions (in-vessel degraded core cooling phenomenology). *Technical Report*, 1986.
- [177] V. Dhir V. Tung. On fluidization of a particulate bed during quenching by flooding from the bottom. *Proceedings of the 6th Information Exchange Meeting on Debris Bed coolability*, 1986.
- [178] R. Vellingiri, D. Tseluiko, N. Savva, and S. Kalliadasis. Dynamics of a liquid film sheared by a co-flowing turbulent gas. *International Journal of Multiphase Flow*, 56(0):93–104, 2013.

- [179] S. Veran, Y. Aspa, and M. Quintard. Effective boundary conditions for rough reactive walls in laminar boundary layers. *International Journal of Heat and Mass Transfer*, 52(15-16):3712 – 3725, 2009.
- [180] S. Veran, Y. Aspa, and M. Quintard. Effective boundary conditions for rough reactive walls in laminar boundary layers. *International Journal of Heat and Mass Transfer*, 52(15-16):3712 – 3725, 2009.
- [181] A. Viva, S. Aferka, E. Brunazzi, P. Marchot, M. Crine, and D. Toye. Processing of x-ray tomographic images: A procedure adapted for the analysis of phase distribution in mellapakplus 752.y and katapak-sp packings. *Flow Measurement and Instrumentation*, 22(4):279 – 290, 2011.
- [182] C. Wang. *Mass Transfer Coefficients and Effective Area of Packing*. PhD thesis, University of Texas, Austin, May 201.
- [183] C. Wang, D. Song, F. A. Seibert, and G. T. Rochelle. Dimensionless models for predicting the effective area, liquid-film, and gas-film mass-transfer coefficients of packing. *Industrial & Engineering Chemistry Research*, 55(18):5373–5384, 2016.
- [184] S. Whitaker. Diffusion and dispersion in porous media. *AIChE Journal*, 13(3):420–427, 1967.
- [185] S. Whitaker. Advances in theory of fluid motion in porous media. *Industrial & Engineering Chemistry*, 61(12):14–28, 1969.
- [186] S. Whitaker. Flow in porous media i: A theoretical derivation of darcy’s law. *Transport in Porous Media*, 1(1):3–25, 1986.
- [187] S. Whitaker. Flow in porous media ii: The governing equations for immiscible, two-phase flow. *Transport in Porous Media*, 1986.
- [188] S. Whitaker. The forchheimer equation: A theoretical development. *Transport in Porous Media*, 25(1):27–61, 1996.
- [189] S. Whitaker. *The Method of Volume Averaging*, volume 13. Springer Netherlands, 1999.
- [190] F. Zami-Pierre, R. de Loubens, M. Quintard, and Y. Davit. Transition in the flow of power-law fluids through isotropic porous media. *Physical Review Letters*, vol. 117:074502/1–074502/5, August 2016.
- [191] A. Zapke and D.G. Kröger. Countercurrent gas-liquid flow in inclined and vertical ducts - i: Flow patterns, pressure drop characteristics and flooding. *International Journal of Multiphase Flow*, 26(9):1439 – 1455, 2000.
- [192] C. Zarcone and R. Lenormand. Détermination expérimentale du couplage visqueux dans les écoulements diphasiques en milieu poreux. *Soil Mechanics and Porous Media*, 1994.